A rock physics modeling approach in analysis and integration of well logs and ultrasonic velocities for characterizing the reservoir facies of the Viola Limestone in southwestern Kansas

by

Victor Cimino

B.S., University of South Florida, 2016

A THESIS

submitted in partial fulfillment of the requirements for the degree

MASTER OF SCIENCE

Department of Geology
College of Arts and Sciences

KANSAS STATE UNIVERSITY
Manhattan, Kansas

2020

Approved by:

Major Professor
Dr. Abdelmoneam Raef

Copyright

Abstract

Seismic facies analysis is the focus when utilizing seismic attributes in reservoir characterization, especially in cases of significant lithological and petrophysical heterogeneities. This project targets an understanding of lithofacies and petrophysical properties effects of the Viola Limestone carbonates with the aim of evaluating viability of seismic attributes in Viola reservoir-facies characterization, in Clark County, Kansas. To this end, this study integrates ultrasonic laboratory data, analysis of well-logs, and fluid replacement modeling. This study uses ultrasonic rock physics measurements to determine core elastic properties and how they relate to in situ values from well logs. Elastic moduli such as Poisson's coefficient, Young's modulus, Bulk modulus, and Shear modulus were calculated based on lab-measured ultrasonic values. These lab values were used along with in-situ well log values for Gassman's fluid replacement modeling calculations to evaluate sensitivity of elastic properties to reservoir pore-fluid composition. These calculations were targeted in the known productive Viola B zone which is known for its hydrocarbon richness. Estimations from fluid replacement modeling were then used to compare producing Viola and non-producing Viola wells within the Morrison Northeast Field in Clark County, Kansas. Well to well evaluations using rock physics and lab tested data provide a deeper insight to well performance and hydrocarbon accumulation.

Table of Contents

List of Figures

List of Tables

List of Equations

Acknowledgements

I first would like to thank Dr. Abdelmoneam Raef for his unwavering support throughout this process. I would not have been able to make it this far without his guidance and belief. Thank you to Dr. Matthew Totten for being a great mentor and teacher through my graduate career. Thank you to Dr. Karin Goldberg for your support on my thesis committee and thank you to Dr. Pamela Kempton for her patience and support throughout my graduate career. I would also like to thank Hagood (2019) for being an exceptional colleague. I look forward to presenting with you at the 2020 AAPG Annual Conference and Expo.

Thank you to the KGS and their flexibility with the loaning of the Rich C-7 core. April and her team were very accommodating and always helpful. Thank you to Paul and Deanna Strunk, Kansas State University Geology Alumni Association, and the K-State student Union for their financial support. Without their help, this would not have been possible.

Lastly, I would like to thank Dom and Vera Cimino, I have been blessed to have parents like you. You never stopped supporting me and always believed in me. Thank you to Hannah Maddy as well, you have been my rock through this journey. Finally thank you to Adam Layne (PhD Candidate), Dr. Hagood (2019) Loufman, Michael Marinari PA-C, Adam Clark MBA., Beth Bailey, Austin Collins, Phillip Davis, and the Maddy family for all of your support.

Chapter 1 - Introduction

1.1 Introduction to the Study

Understanding discrete characteristics of reservoir rock has been of main emphasis in various disciplines over the years (Smith et al., 2003; Wang, 2001). Reservoir characterization through optimizing geophysical data and conducting lab-based studies to understand seismic resolution and the utility of seismic attributes have been adopted in case studies around the world (Sayers and Chopra, 2009; Simm and Bacon et al., 2014). There are several aspects of reservoir rocks relevant to reservoir characterization undertakings; hydrocarbon saturation, CO_2 monitoring, porosity, lithofacies controls, pore geometry effects, permeability, matrix rigidity, and fracture toughness and density (Han and Batzle, 2004; Simm and Bacon et al., 2014). Better characterization of a reservoir reduces drilling risks and help boosting ultimate recovery of a field development plan. Many studies have taken place, approaching how to best characterize reservoir properties. For example, Besheli et al. (1998) used rock physics to validate well log information for formation evaluation. Adam et al. (2006) studied Gassmann's fluid replacement effects and shear modulus variability in carbonate reservoirs. Castagna et al. (1985) sought to understand the relationship between shear and compressional wave velocities in clastic silicate rocks. All of these are various examples involving rock physic studies of reservoir properties.

The Viola Limestone is hydrocarbon-bearing Ordovician in age. There are three major facies with the Viola (Raef et al., 2017) which have distinct well-log characteristics. Vohs (2016) discussed how only the Viola "A" and "B" zones are considered productive while the Viola "C" zone is non-productive. Productive facies of the Viola in recent studies have shown to fall below the tuning thickness of seismic (Raef et al., 2017) which prove to be an issue regarding well placement and well economics in Clark and Comanche Counties, KS. This study uses ultrasonic

P-wave and S-wave velocity measurements to better understand the relationship between elastic moduli and in-situ log values, as well as fluid replacement modeling, to understand the effects of pore fluid composition on P-wave and S-wave velocities, which allows to evaluate seismic response to changes in pore fluid composition.

Gassmann's fluid replacement modeling can be used to predict P and S wave velocities within a specific reservoir after changes in fluid saturations have taken place. This enable modeling what seismic response to changes in pore fluid composition (Mavko et al. 2009).

1.2 Research Significance

Integration of lab tested ultrasonic frequency data and geophysical data not only provides valuable information, but also enhances exploration techniques (Grochau et al., 2009). This study aims to better understand the relationship between laboratory-measured ultrasonic frequencies with well-log data, specifically sonic logs. Their relationship provides insight on specific trends found in various sections of the Viola as it relates to mineral composition, dolomitization, pore geometry, porosity, hydrocarbon saturation, chert content, and seismic tuning thicknesses.

Although Gassmann's theory is peer reviewed and accepted across the industry, there still are several unknown and ambiguities in the aspects of geophysics and rock physics; in particular, the applicability to carbonate reservoirs. This study focuses on correlation of in-situ to lab results, velocity variation with increasing stress, and fluid replacement modeling. The main concern, when using ultrasonic frequency measurements, is the higher elastic moduli calculated and attenuation effects. When using Poisson's ratio at dry sample conditions the attenuation effects are not of concern; there is no Biot squirt flow.

Fluid replacement modeling in this study may provide a means for estimating the viability of 3D seismic data as it relates to the Viola Limestone characterization. Specifically,

thin areas of production controlled by paleotopographic traps which determine reservoir thickness. Not only will this study benefit Kansas oil and gas exploration due to potential increased understanding in Viola seismic exploration techniques, but it will also broaden the understanding of Gassmann's modeling as it relates to carbonate reservoirs. The topic of fluid replacement modeling is always evolving and this study may shine light specifically on dolomitized reservoirs and intervals with high chert content.

1.3 Prior Research

Isham (2012) and Lueck (2017) both utilized Gassmann's fluid replacement modeling to evaluate CO_2 seismic effects on depleted reservoir seismic signature for carbon sequestration. Both studies utilized laboratory measured P- and S- wave velocities. This study focuses only on dry rock measurement however. Dry measurements remove effects of velocity dispersion when samples are tested at various frequencies. This study estimates in situ S-wave velocities by using Poisson's ratio based the ultrasonic P-wave and S-wave velocity measurements. This is because di-pole sonic is not available in the Rich C-7 well used as the foundation of this study.

Vohs (2016) studied the Viola Limestone and specific seismic characteristics which discretely determine productive facies from non-producing facies. This was done by running a seismic attribute workflow to quality-check the accuracy of seismic horizon tracking within a study area. Richardson (2013) explained the presence of varying thickness in the Viola and its importance in preserving porosity within these paleotopographic traps. These thickness variations are very subtle and difficult to determine when visualizing amplitude data, easily impacted by porosity variability and the type of hydrocarbon present. This impacts the resolution of the seismic data, therefore making it more difficult to determine hydrocarbon bearing facies of the Viola.

Instantaneous phase was one of the seismic characteristics extracted by Vohs (2016). Phase angle homogeneity is apparent throughout the top of the Viola which is covered by the Maquoketa Shale. This phase angle can be seen to split around the location of a borehole (Figure 1-1) (Raef et al., 2017). The split in the angle indicates a velocity anomaly associated with increased porosity at the top of the Viola and/or the presence of hydrocarbons (Raef et al., 2017).

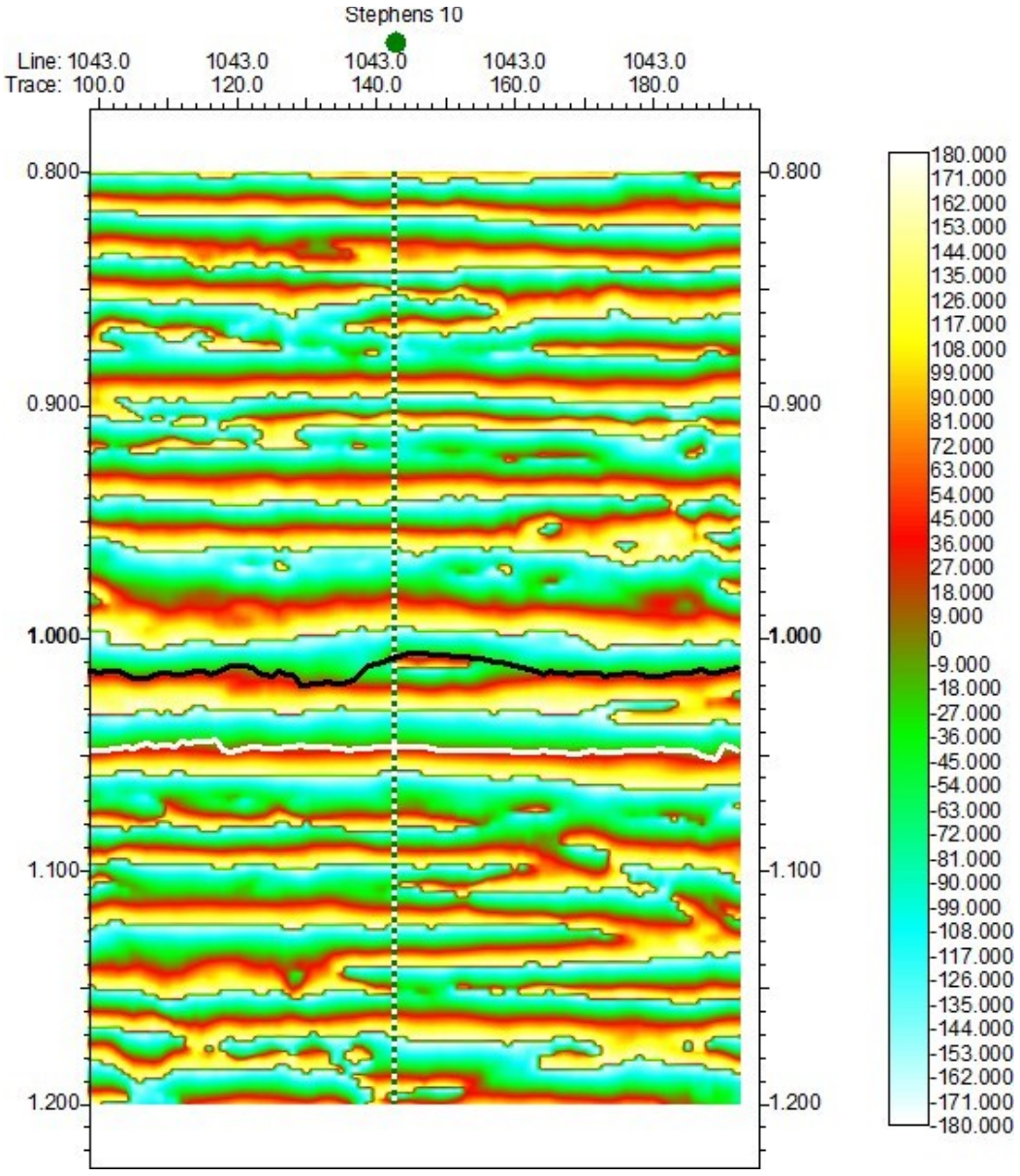

Figure 1-1: Instantaneous phase cross section across Stephens 10 well. The black line displays the Viola Limestone. The change in phase angle to the right of the borehole can be represented by the red/yellow color indicating a velocity anomaly. (Raef et al., 2017).

Within these zones, velocity anomalies are interpreted as increased porosity. When comparing this information to the top of the section in the well-log of Rich C-7, the highest amount of porosity is present at the top of the Viola. Rich C-7 is in the adjacent county to the east of Stephens 10 (Fig. 3-1, 3-2, 3-3, and 3-4), the well used in Vohs' (2016) description. This higher porosity correlates with the paleotopographic trap that is a target for hydrocarbon exploration. Our study is relevant to understand more accurately the seismic response in terms of hydrocarbon accumulation not just the occurrence of porosity.

The 3D seismic Vohs (2016) shows a distinct difference in velocity anomalies at the Viola "C" zone, in comparison to the "A" and "B" zones. Figure 1-2 depicts a time structure map of the Viola "C" top constructed from the extracted seismic characteristics. Figure 1-3 displays the Viola top including the presence of paleotopographic traps within the section, potential areas of hydrocarbon charged reservoirs (Vohs, 2016).

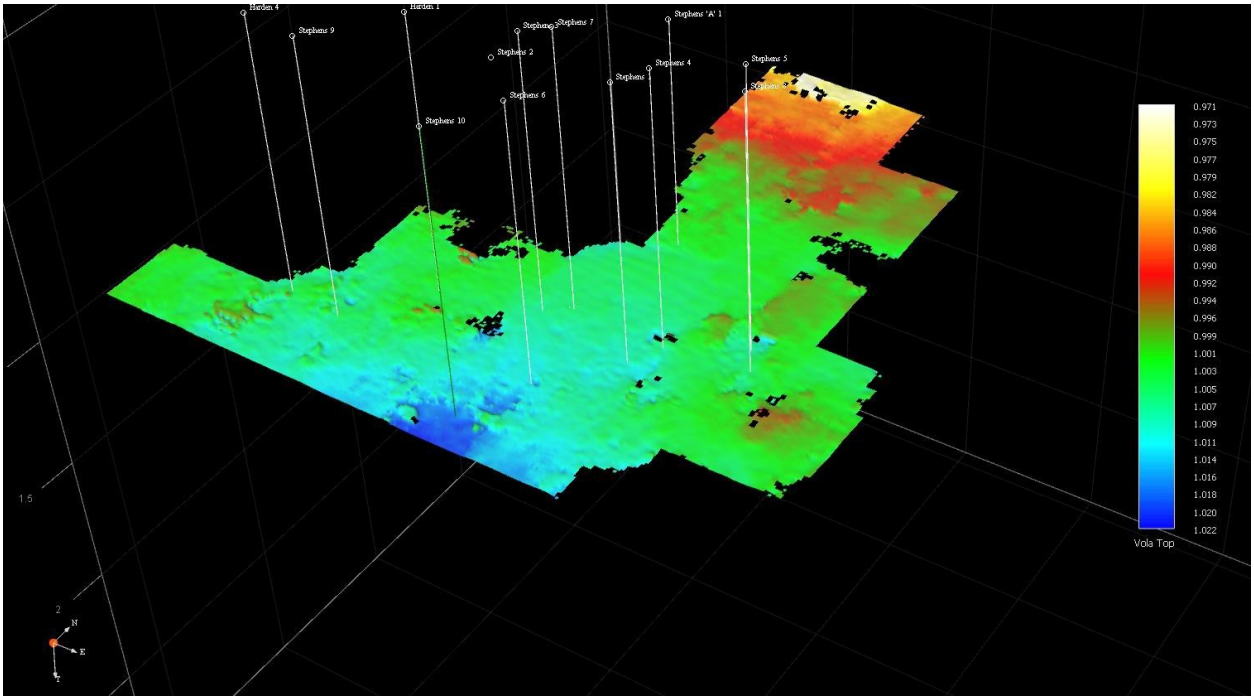

Figure 1-1: Time structure map of the Viola "C" zone (Vohs, 2016).

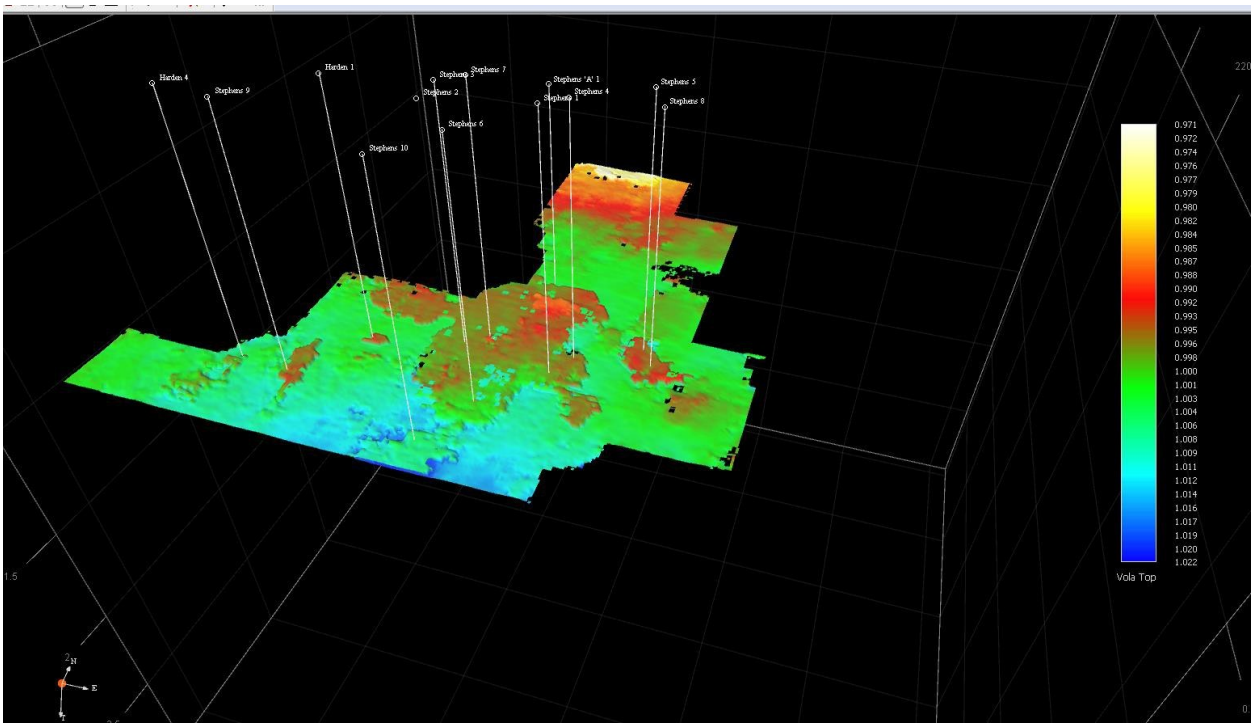

Figure 1-2: Time structure map of the Viola Top and locations of potential paleotopographic traps (warm colors) (Vohs, 2016).

The next attribute extraction carried out by Vohs (2016) was of amplitude maps. This was the most effective attribute to discriminate productive from non-productive well locations. Producing wells in the Viola had consistently lower amplitude values than dry holes (Vohs, 2016) (Fig. 1-4 and 1-5). Hydrocarbon presence would decrease the variation in acoustic impedance between the Viola and overlying horizon.

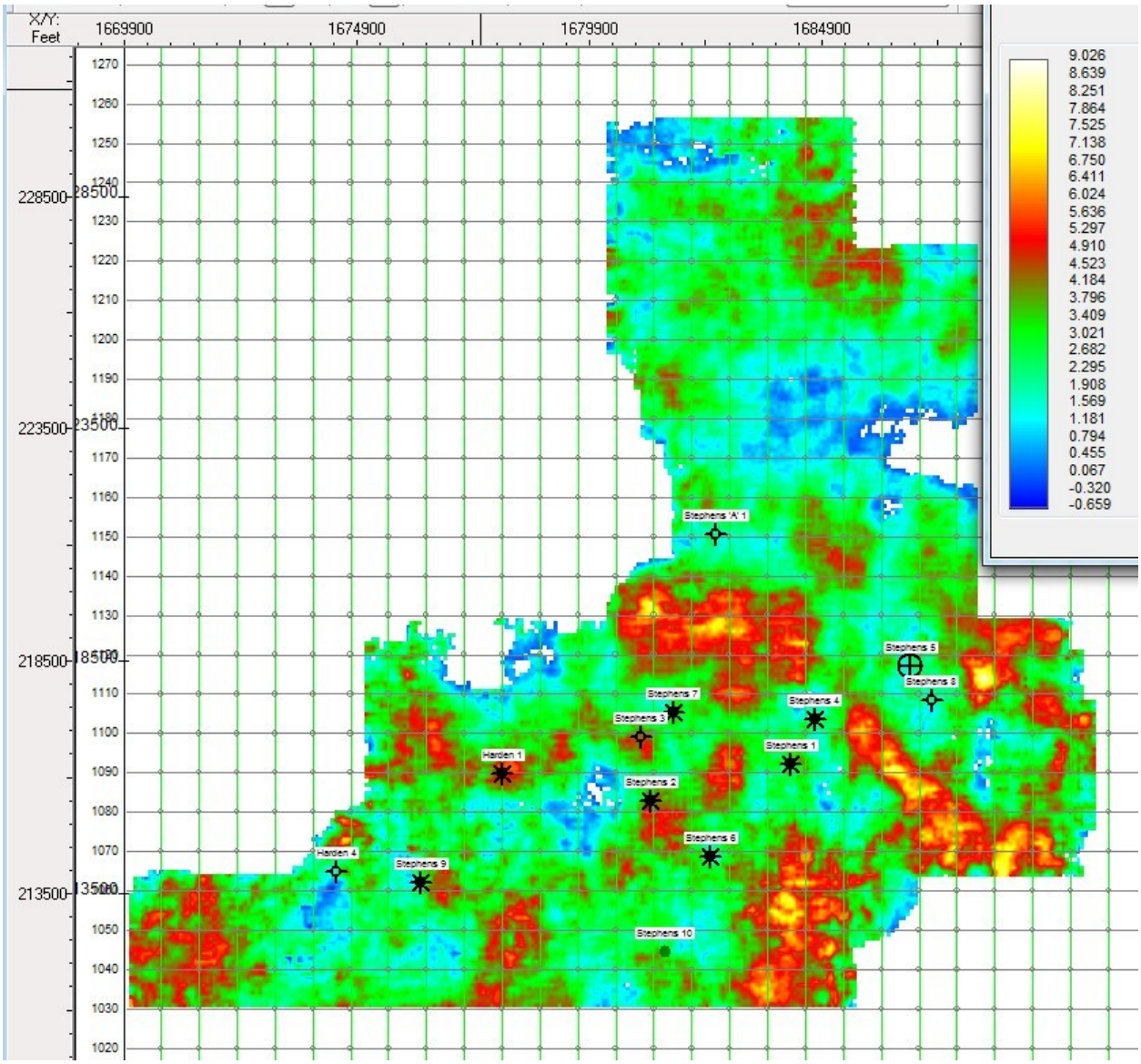

Figure 1-3: Viola "C" amplitude map showing lower amplitude anomalies (cooler colors) compared to higher velocity anomalies (warmer colors) (Vohs, 2016).

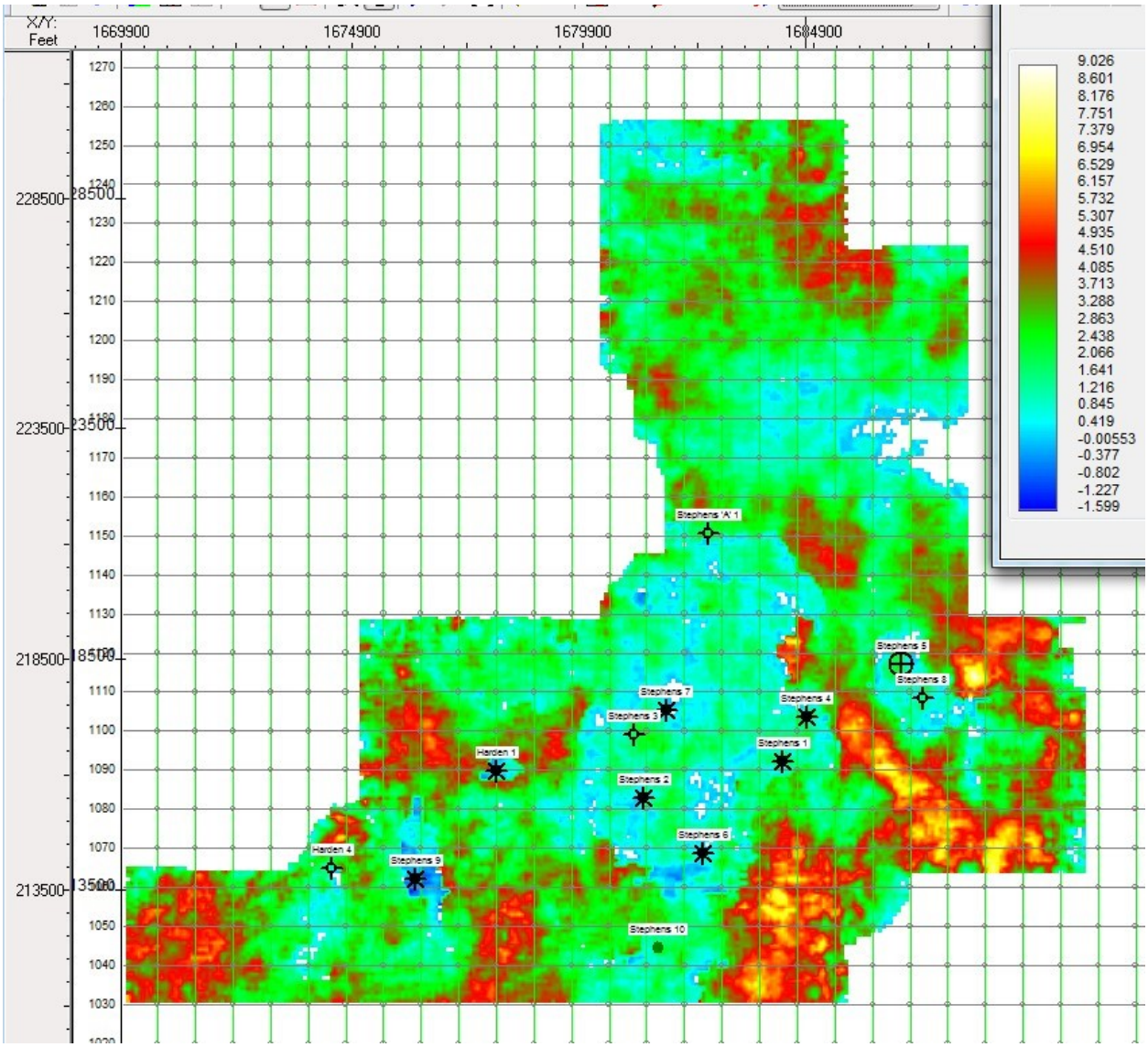

Figure 1-4: Viola top amplitude map showing slower velocities around hydrocarbon producing wells (cooler colors) compared to non-productive zone with faster velocities (warmer colors) (Vohs, 2016).

The instantaneous frequency correlates with amplitudes near zero, specifically in producing wells (Vohs, 2016). Raef et al. (2017) mentioned that instantaneous frequency peaks with tuning effects in zones of decreasing amplitudes. This observation strengthens the assumption of tuning effects being used as thin bed indicators when occurring within the zone of decreasing amplitude correlating with productive wells.

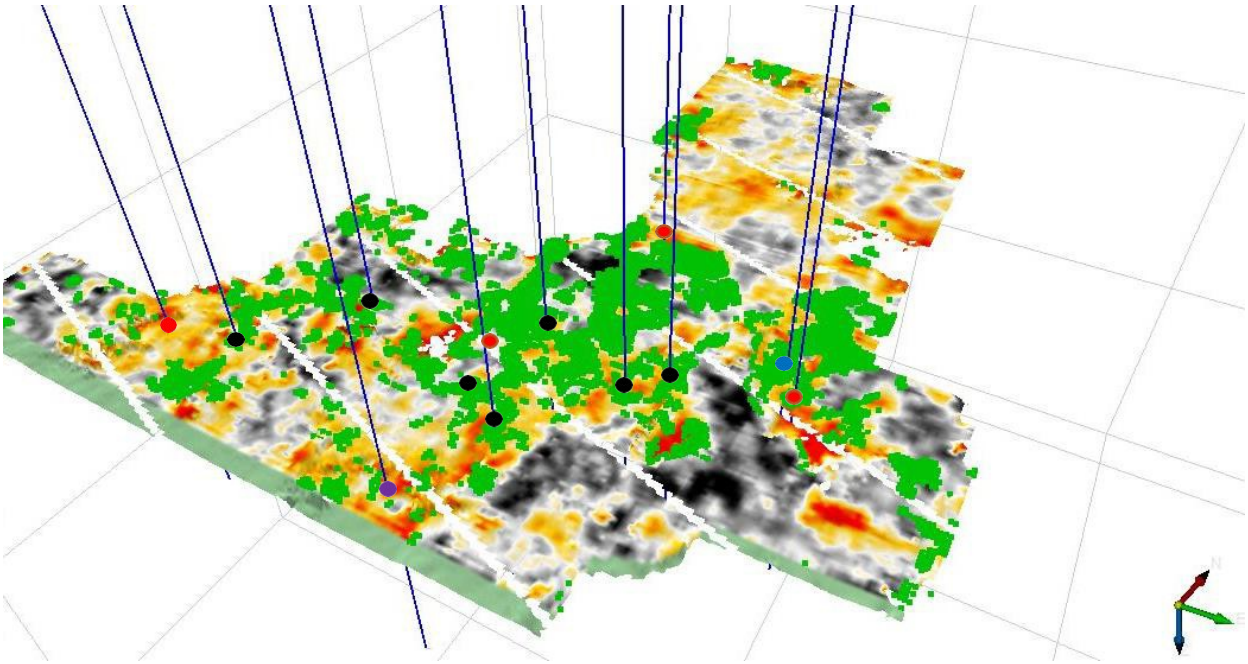

Figure 1-5: A map of high quality reservoir facies (green) corresponding to higher instantaneous frequency and lower amplitude effects of the upper Viola. (Vohs, 2016).

In conclusion Vohs (2016), showed that potentially productive zones within the Viola can be identified by instantaneous frequency and amplitude anomalies. Low velocity anomalies increase the resolution of the seismic data, resulting in doublets. Instantaneous phase and normalized amplitude are helpful attributes to identify these velocity anomalies. These seismic attributes were used to determine hydrocarbon production potential within locations of paleotopographic traps in the upper Viola. Slower velocities at constant frequencies generate shorter wavelengths which can produce near zero amplitude values. Thus, Gassmann's modeling in our study identifies post-saturation velocities to predict hydrocarbon saturation within the Viola. It provides us with a range of values that can be used within seismic exploration to determine favorable reservoir facies.

Chapter 2 - Background

2.1 Seismic Attributes

3-D reflection seismology is used to map geologic features that are associated with migration, hydrocarbon entrapment, and deposition, while characterizing static and dynamic properties of hydrocarbon reservoirs. Some seismic attributes can be directly correlated to the geologic feature or specific reservoir property of interest (Chopra & Marfurt 2005). One is seismic amplitude which can display "bright spots" that often correlate with the presence of hydrocarbons. However, amplitude is also effected by other physical properties such as porosity.

Specific attributes to be used in this study to evaluate fluid replacement are instantaneous phase, amplitude, instantaneous frequency, and thin bed indicators. Instantaneous phase is the orientation angle of the amplitude vector at a time in the seismic column. Phase is effective when used to visualize bedding configurations or indicate lateral continuity (Jaiswal et al., 2014). The phase angle is a physical attribute that can describe a geometric shape of the seismic wave passing through different facies.

Amplitude can be used to directly identify zones of high hydrocarbon saturations (low amplitude) (Vohs, 2016). This attribute is so commonly used because of its correlation with porosity and saturation. Amplitude is simply the height of the wave as the wavelet responds to impedance, and the peaks or troughs coincide with increasingly positive or negative amplitude values. Thin bed indicators are computed as a difference between instantaneous frequency and time average frequencies.

Lastly, instantaneous frequency (i.e. the rate of change of phase over time) can be used to better identify the top of the Viola Limestone (Raef et al., 2017) and help indicate low impedance thin beds, relating them to turning thickness (Widess, 1973; Zeng, 2009). In zones of

decreasing amplitude, instantaneous frequency will peak indicating below-resolution response (Simm and Bacon, 2014).

2.2 Well Log Data

Well logging is done to collect various data types by measuring different parameters geoscientists and engineers would find useful in the exploration, completions, and production. Methods for well logging on shore can be done in two different ways. The first one, most common in Kansas and specifically used in this study, is called Wireline logging (sometimes referred to as an open-hole log). Wireline logging employs an electrical cable downhole to lower tools into the borehole to transmit data (Schlumberger 2019). The tools used in this study are gamma ray, neutron density and neutron porosity, resistivity, bulk density, and sonic logs.

The other method is called Measurements While Drilling (MWD), in which electrical tools are arranged along a Bottom Hole Assembly (BHA) (Figure 2-1). MWD measurements are taken while drilling, as the name states. These tools sit at specific lengths behind the tip of the drill bit where measurements are continuously taken during drilling operations and are received through binary signals sent as pulses through the drilling mud. MWD measurements are abundantly used when drilling and geosteering lateral wells during the kick of point, curve build, and lateral portion of the well.

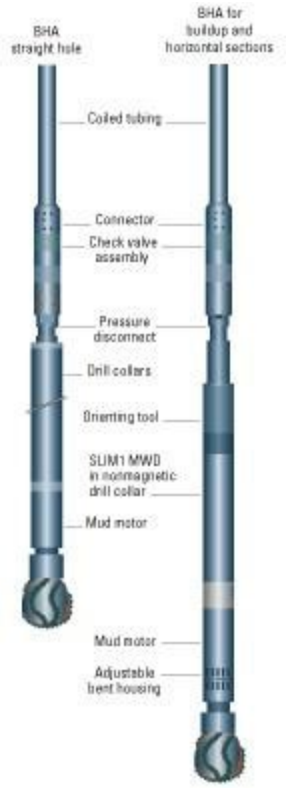

Figure 2-1: Generic Diagram of a bottom hole assembly (Schlumberger 2019).

Gamma ray logs measure the total natural radioactivity at a specific depth in API units (Schlumberger 2019). They are used for lithology identification and correlation between wells. Higher API values indicate rocks that have a higher radioactivity, such as shales, some carbonates, feldspar-rich rock, and bentonites. Lower API values indicate clean sands, chalks, and chert.

Induction logs also known as resistivity logs, measure the resistivity of a formation in ohms. This is used in identifying hydrocarbons within a formation, or water content. Water and brine are more conductive than oil so resistivity for water and brine is negligible, while the resistivity of oil is high, resulting in positive values in log data. Higher resistivity values can indicate large oil saturation.

Compensated neutron logs measure the slowing of neutrons between a source and one or more detectors that measure at the epithermal level where the particle energy is above that of their surrounding matter (Schlumberger 2019). This slowing process is dominated by hydrogen within the formation. These values are then calculated to provide porosity values in percentages

for the given acute measurement at that specific depth. These logs are evaluated across a field or basin to understand porosity trends within a formation, to assess formation heterogeneity, or to identify possible hydrocarbon reservoirs.

Sonic logs measure P-wave velocities at specific depths. Sonic logs are recorded by pulling a tool that emits an acoustic signal from a source along a wireline, which travels through the formation and then returns to the receiver (Schlumberger 2019). This process is very similar to reflection seismology acquisition for geophysical studies. Today, P- and S- wave velocities are being measured either from a di-pole wireline tool, or through borehole seismic imaging logs done with MWD assemblies. The sonic log is one of the most important logs in this study since it is used in Gassmann's fluid replacement modeling.

The last well log used in this study is a density log. Bulk density measurements are based on the reduction in gamma ray flux between a source and a detector due to Compton scattering (Schlumberger 2019). A Cesium-137 sources is chosen so that gamma ray energies are high enough to be read as detectors take an average bulk density between two receivers measuring for gamma rays scattered from the formation. After calculations from calibrated values are completed, the final value per half a foot or foot is given in grams per cubic-centimeter.

Well	County	Viola (ft)	Perforation (ft)	Production	LAS	Status
Rich C-7	Comanche	5804	5807-5814 5819-5822	367,197 bbls	Yes	Producing
Herd 1	Comanche	5765	-	106,609 mcf	No	Producing
ACRE 5-21	Comanche	5650	5652-5692	68,372 bbls	Yes	Producing
Stephens 1	Clark	6383	6384-6396	56,273 bbls	Yes	Producing
Stephens 4	Clark	6370	6382-6388	82,713 bbls	Yes	Producing
Stephens 8	Clark	6342	-	-	Yes	Abandoned
Stephens 10	Clark	6409	-	-	Yes	Abandoned

Table 2-1: This tables identifies and provides an overview of the wells used in this study.

Rich C-7

Rich C-7 ran open hole wireline logs throughout the borehole. Sonic and resistivity logs were run from surface to total depth while density and porosity logs were only run from 4200 feet to total depth. Gamma ray logs are presented in the left track of all three log read-outs. Figures 2-2, 2-3, and 2-4 show the repeat sections over areas of interest for the compensated density and neutron porosity logs, sonic log, and resistivity log.

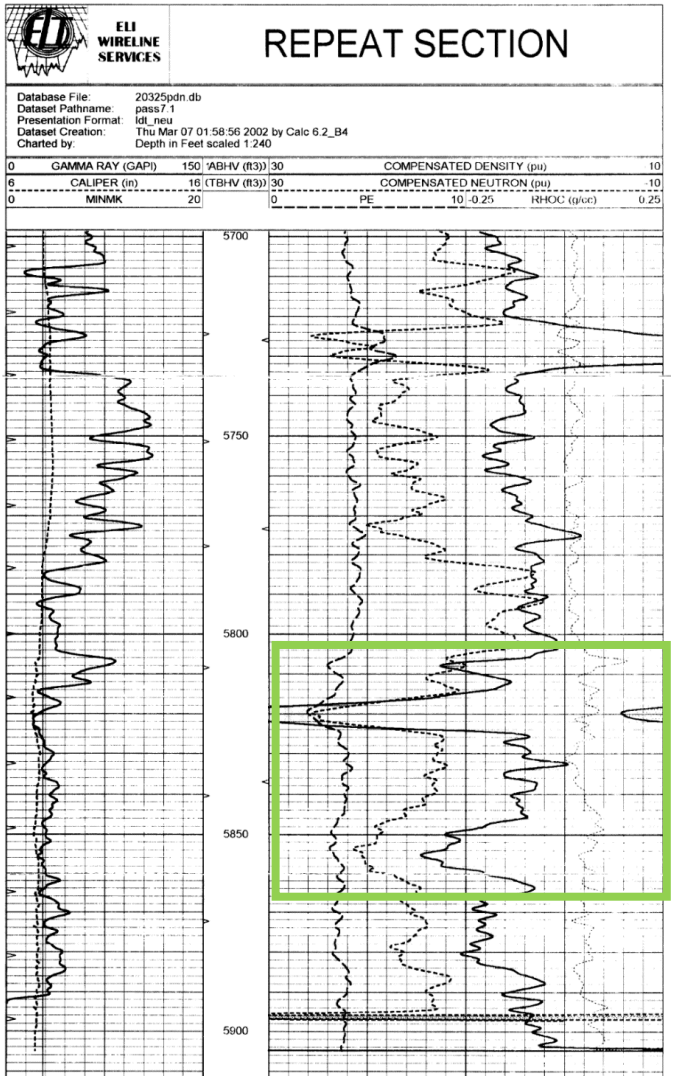

Figure 2-2: Rich C-7's compensated neutron density and porosity logs measure estimated porosity values (%) in the right track, gamma ray values (API) in the left track, and bulk density values (g/cm^3) in the far right (solid line). The green box indicates the area of interest (Viola "B") and location of study core within the well.

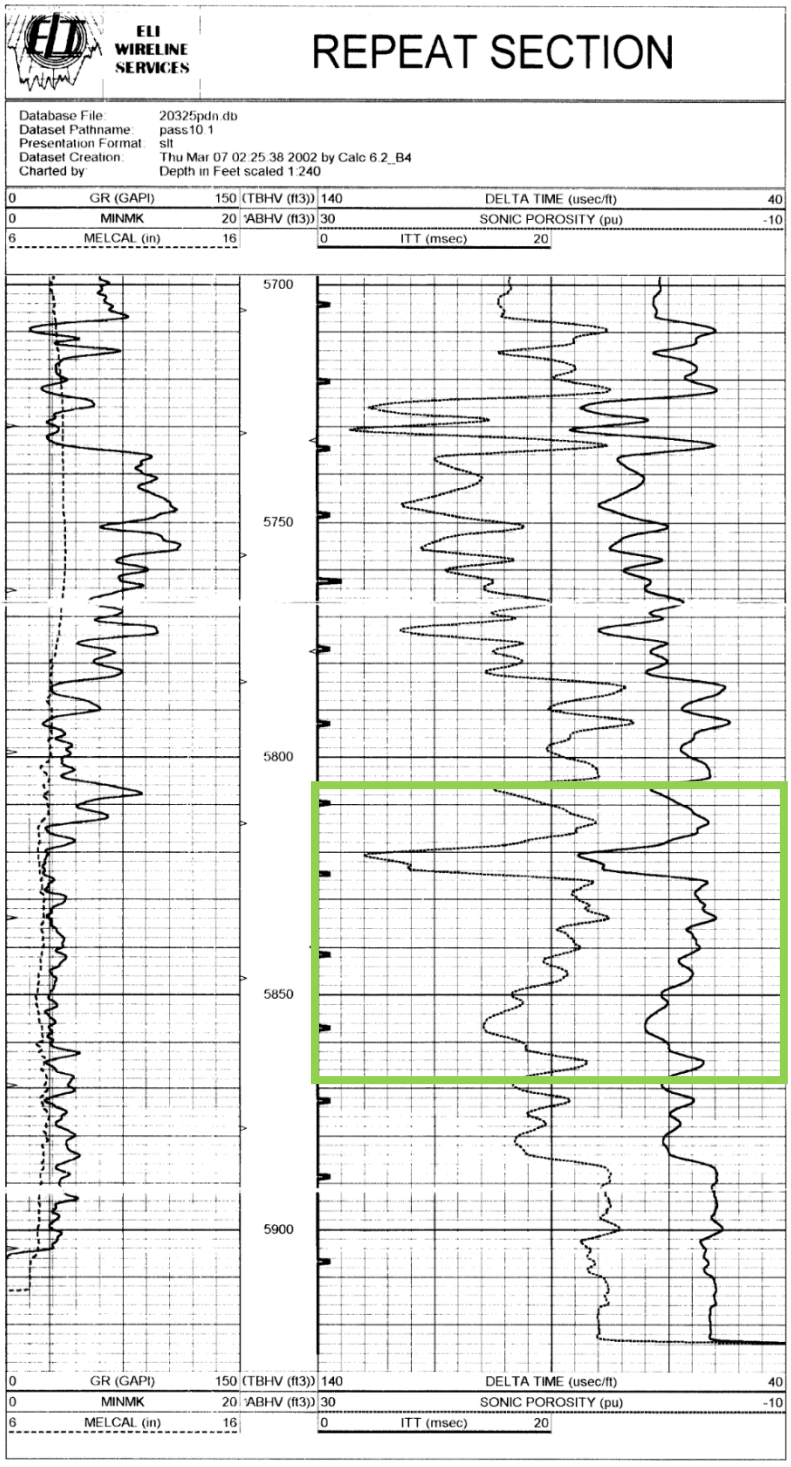

Figure 2-3: Rich C-7's sonic log indicates P-wave velocity values in the right track along the "delta time" (solid line). The left track shows the gamma ray log. The green box indicates the location within the well where Viola is present and location of study core. Notice the anomaly at 5820', which is a dramatic slowing of P-wave velocity since microseconds per foot is higher.

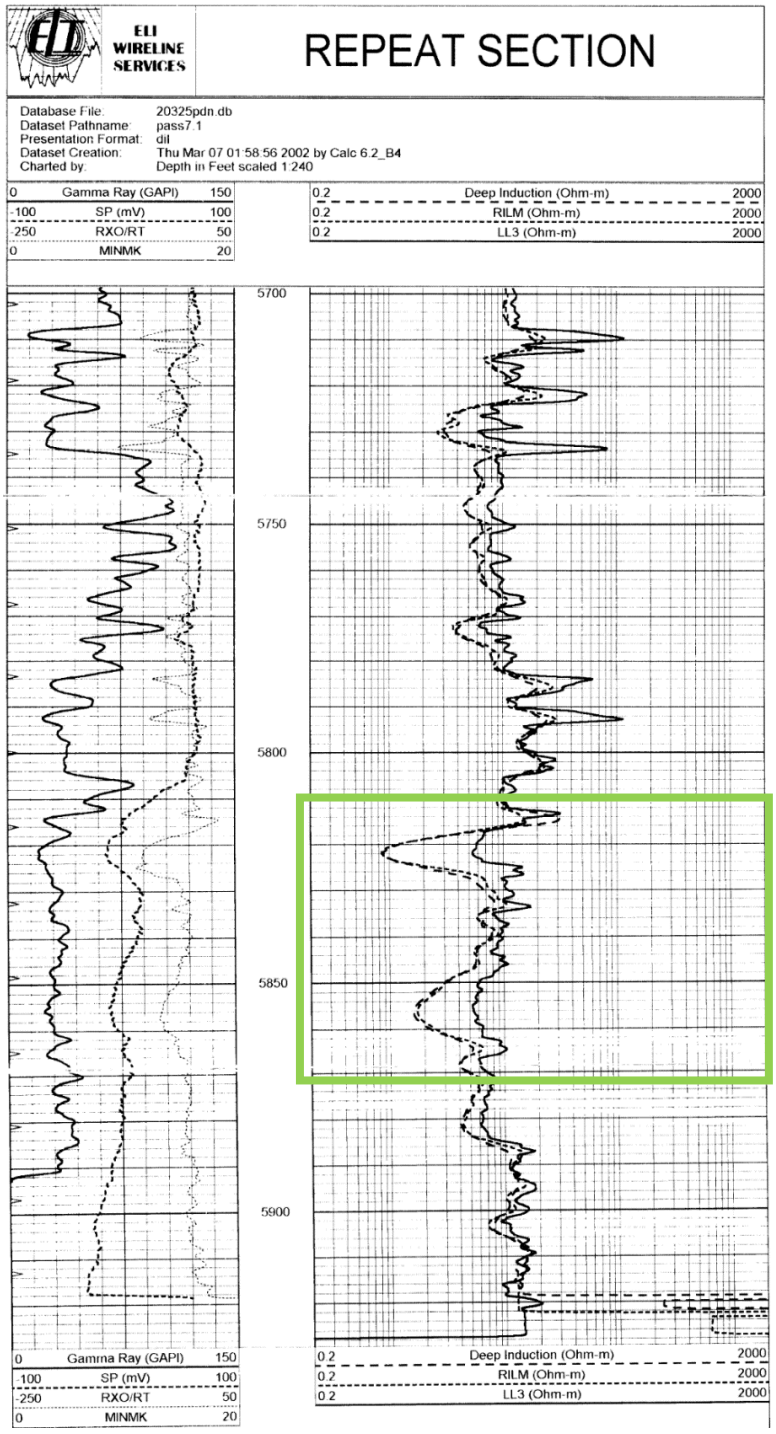

Figure 2-4: Rich C-7's resistivity log indicates potential locations of hydrocarbon accumulation in the right track along the "RILM" (solid line). RILM resembles medium observance induction while, deep induction indicates a deeper reading of resistivity spanning further into the formation, away from the borehole. The left track shows gamma ray. The green box indicates the location within the well where the Viola is present and location of the study core.

2.3 Geomechanics

Geomechanics is the study of soil and rocks interaction with temperature, pressure, and stress as it occurs geologically. Rock mechanics is the study of mechanical behaviors and physical characteristics of rock masses and their response to forces. It has emphasis in rock mass characterization, including the analysis of joints and faults, rock fabrics, rock-forming minerals, stresses and strains, rock surface friction, failing rock deformation, linear elasticity including Hooke's law, inelastic behavior, wave propagation in rocks, poroelasticity and thermoelasticity (Simm and Bacon, 2014). Rock mechanics is used in the petroleum industry to reduce the risk of drilling and optimize reservoir characterization which in turn benefits well economics. Rock mechanics today is studying fracture propagation in specific parts of tight-oil plays to better understand where to place a frack, and how much force is needed to maximize reservoir performance (El-Bahiry et al., 2017).

This study uses rock mechanics in the form of elastic moduli through rock physics. Rock physics is the relationship between measurements of elastic parameters made from the surface, well, and lab equipment (Chopra, 2009). Intrinsic properties such as mineralogy, porosity, pore shape, pore fluid, viscosity, and stress can all be analyzed using rock physics (Chopra 2009). The goal of rock physics is to better understand the physical properties of a reservoir and how those properties are linked to seismic data, and to infer the variation of these properties in a lateral or vertical sense (Chopra 2009).

2.4 Rock Physics

Typical rock physics areas of inquiry include fluid substitution, fluids and saturation, pressure, pore fluid properties, porosity, clay content, density, lithology, Vp ad Vs, Vp/Vs ratio, shale property and anisotropy (Wang, 2001) These values can be of significance when

constructing synthetic sonic logs, creating links between amplitude and rock properties, and evaluating elastic properties (Mavko et al., 2009). Through laboratory measured values combined with seismic data, physical rock properties can be linked to seismic expressions. Gassmann's fluid replacement model is a perfect example of the use of elastic properties to estimate and determine what a seismic response with look like after the substitution of a current fluid for a different one within the same lithology. In areas where drilling has not yet occurred, this helps reducing risk.

Chopra (2009) describes rock physics in five main areas: (1) laboratory measurements (made with rock samples under different conditions); (2) interpretation of borehole measurements (including well logging and borehole seismic); (3) modeling (theoretical models developed for establishing elastic properties of rocks under appropriate conditions and estimating the expected seismic properties from available reservoir properties); (4) deformation analysis (studies aimed at quantifying the sensitivity of rocks to stress); and (5) seismic reservoir characterization (application of rock physics knowledge to seismic data for reservoir characterization). Amongst these five areas, this study focuses primarily on 1, 2, and 3 with a goal of seismic reservoir characterization to strengthen the results reported by Vohs' (2016) work.

For laboratory measurements uniaxial stress was applied to specific core intervals of Rich C-7 to produce elastic properties tested at *in situ* pressure. These elastic properties are utilized in interpretation of borehole measurements where wireline values are cross plots with elastic property values. Some cross plots may include bulk modulus by porosity, Poisson's ratio by porosity, P-wave (dry) velocity by sonic *in situ*, Poisson's ratio by acoustic impedance, and density by P-wave velocity. Evaluations of other rock physics data against themselves are also

used such as Vp/Vs to understand lithology (Greenberg and Castagna, 1992). In this study the focus is on five specific elastic moduli: bulk modulus, shear modulus, Young's modulus, Poisson's ratio, and bulk compressibility modulus.

2.5 Elastic Moduli

Bulk Modulus

Bulk modulus (K) is the rocks response to normal stress applied in all directions on a unit of rock. Bulk modulus is calculated using equation (1).

Equation 1: Bulk Modulus

$$\boldsymbol{k = p(V_p^2 - \frac{4V_s^2}{3})}$$

In equation (1), *p* represents bulk density, *Vp* represents P-wave velocity, and *Vs* represents S-wave velocity. (Simm and Bacon 2014). Values are typically measured in Giga Pascals (GPa), and larger values indicate the existence of higher resistance to compressional forces.

Shear Modulus

Shear Modulus (*u*) (equation 2) is a measure of the response to a shear or tangential stress where the shear strain is measured through the shear angle. Shear modulus indicates the rigidity of a rock or the resistance to shaking motions. Fluids are not assumed to have shear deformation, so the shear modulus of most fluids is zero (Simm and Bacon 2014). In shear modulus' equation *p* is density and V_s as S-wave velocity.

Equation 2: Shear Modulus

$$\boldsymbol{u = pV_s^2}$$

Young's Modulus

Young's Modulus (*E)* (equation 3) describes elasticity and tensile strength, which is an object's tendency to deform along an axis when force is applied along the axis. This is a

materials ability to resist extensional deformation (Watt et al., 1976). A high Young's modulus value indicates a high resistance to extensional forces. In the equation, p represent density, V_p is P-wave compressional velocities, and V_s is S-wave shear velocities.

Equation 3: Young's Modulus

$$E = \frac{pV_s^2(3V_p^2 - 4V_s^2)}{V_p^2 - V_s^2}$$

Poisson's Ratio

Poisson's Ratio (σ) (equation 4) is a fractional change in width to the fractional change of length under uni-axial compression (Simm and Bacon 2014). A way to visualize Poisson's ratio is thinking how much a material will contract in all other directions other than the direction in which pressure is being directly applied. A high Poisson's ratio indicates a large difference between measured V_p and V_s velocities. In the equation V_p is compressional velocity and V_s is shear velocity.

Equation 4: Poisson's Ratio

$$\sigma = \frac{V_p^2 - 2V_s^2}{2(V_p^2 - V_s^2)}$$

Bulk Compressibility

Bulk compressability modulus is the reciprocal of bulk modulus (1/K).

2.6 Fluid Substitution Theory

Within the study of rock physics, fluid substitution is one of the most important topics vastly studied as it highly concerns the study of hydrocarbon reservoirs. Predicting velocities after fluid substitution is very complex and requires several assumptions, based upon the method used. In this study, Gassmann's equation is used for fluid replacement modeling. Gassmann's relation can estimate the change of a porous media's elastic moduli, at low frequencies, when there is a change in the pore fluid saturation (Mavko et al., 2009). While using both

compressional and shear velocities with rocks saturated with an initial pore fluid or gas, bulk and shear modulus can be calculated. Then, using Gassmann's equation velocities can be predicted with the bulk modulus of the rock with pore space occupied by a substituted fluid (Mavko et al., 1998).

The concept of fluid substitution is important when establishing a relationship between physical rock properties, material occupying pore space, and seismic expressions. Rock physics requires information regarding the rock frame and pore fluid (mineral composition, density, moduli) to achieve accurate results. A known initial fluid is used to begin the model, in our case we are using water which is easily calculated using our dry-core lab-measured properties. Fluid replacement modeling then predicts the expected elastic moduli based on porosity and how much of a certain fluid is replacing the initial fluid. The resulting elastic moduli allow for the calculation of expected P-wave, S-wave, and Bulk Density values which are useful when describing reservoir facies or interpreting seismic signature of enhanced oil recovery (EOR) processes and Amplitude versus offset (AVO) analysis (Mavko et al., 1995).

Using fluid replacement models on carbonates is challenging due to their non-homogenous nature of their mineral matrix and pore density. The velocity-porosity relationship becomes scattered and less predictable which makes establishing concrete evidence of reservoir properties challenging (Xu and Payne, 2009). Current theories such as Gassmann and Biot-Gassmann are effective due to the frequency range they cover. Gassmann fluid substitution is ideal for this study because of its effectiveness on carbonates with moderate to high porosity along with the low frequency of sonic logs and its relation to 2D and 3D seismic survey frequencies (Simm and Bacon, 2014).

Gassmann

For Gassmann's equation to be acceptable, there are basic assumptions that must be met. Wang et al. (2001) describes them as the following five requirements: (1) The rock (both the matrix and frame) is macroscopically homogeneous, which assures the wavelet is long compared to the grain and pore size. 2) All the pores are interconnected or communicating. Porosity and permeability must be high without poorly connected pores. This assumption is frequently met due to the high frequency used in sonic logs and in lab settings, to ensure equilibrium of the pore fluid flow, induced by the passing wave (Wang et al., 2001). 3) The pores are filled with a frictionless fluid (liquid, gas, or mixture). This is again assumed to ensure full equilibrium of the pore fluid flow. (4) The rock-fluid system under study is closed (undrained), meaning, the volume of said rock-fluid-system cannot allow fluid to flow when a passing wave foes not cause any appreciable fluid to flow through the frame. (5) The pore fluid does not interact with the solid in a way that would soften or harden the frame. Inevitably the fluid will interact with the rock, it is more so for fluid that causes a chemical reaction between the pore fluid and rock matrix.

Requirement 1 is met by observing figure 2-5. In the photo of the core sample taken at the highest point of porosity on the "B" Zone (figure 2-6), there is homogeneity of the dolomite and consistency of chert nodules throughout the sample.

Figure 2-5: Core sample taken at where porosity is the highest within the Viola "B" Zone.

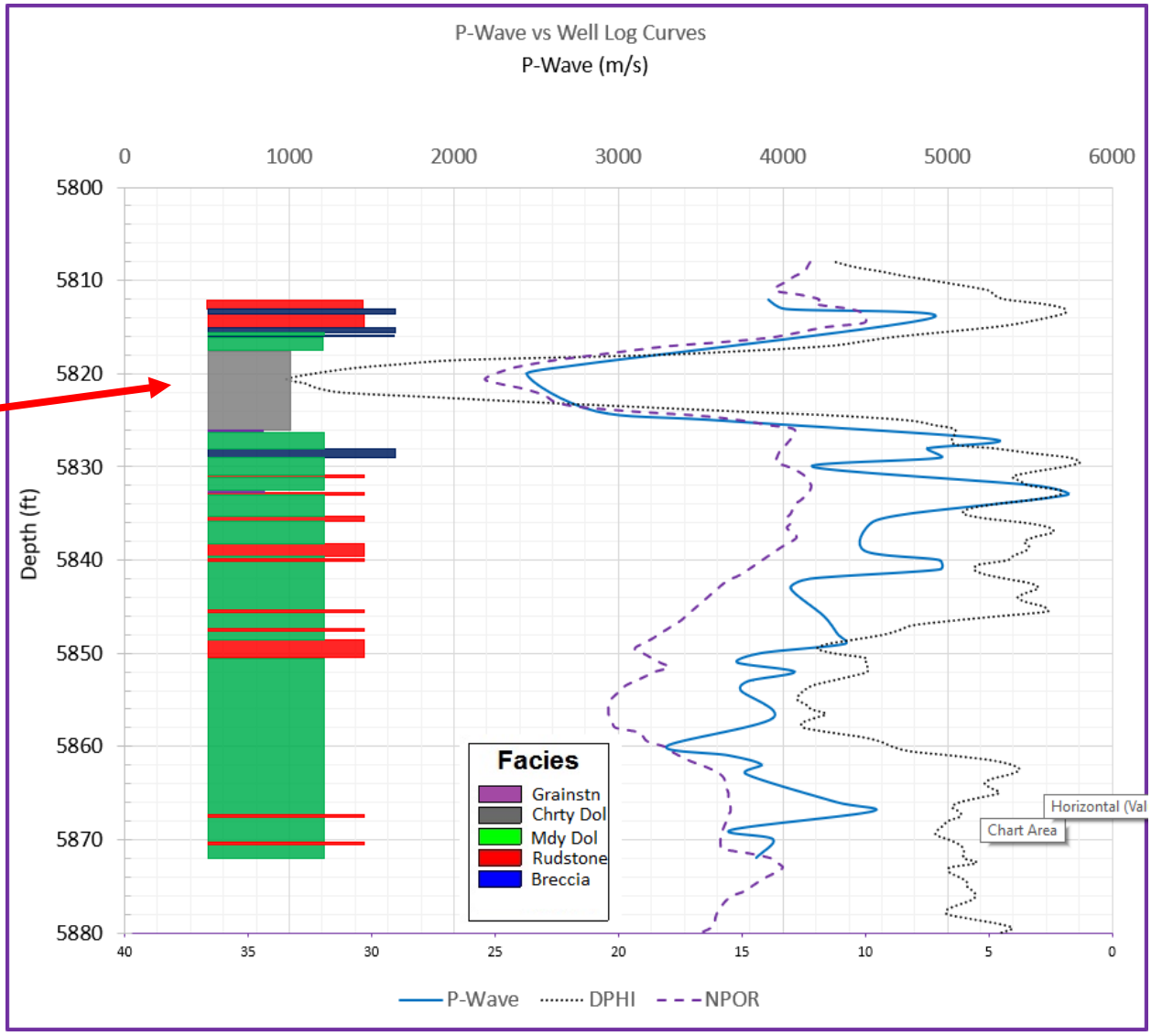

Figure 2-6: Facies diagram of Rich C-7 (left) and a comparison of laboratory-measured values to log-measured values (right). The red arrow indicates where the photo in figure 2-5 was taken (From Hagood, 2019).

Requirement 2 is achieved through the known vuggy porosity within the Viola A and B zones (Raef et al., 2019). Especially within a dolostone, crystal dissolution can overall increase the permeability and porosity, aiding in the validation of requirement 2 (Adam et al., 2006).

Assumption 3 is met with the fluid present *in situ* being on oil production data provided by the KGS. The samples were tested in the lab dry. Thus the samples are calculated to be water-saturated initially, and then substituted for oil to increase seismic interpretation accuracy. Assumption 4 is met through the rock fluid system being undrained when the well log data was acquired. Lastly, assumption 5 is achieved by assuming brine and oil will not physically change the Viola "B" zone rock.

Gassmann's model calculates and predicts change in compressional and shear wave velocities after fluid substitution has taken place. The model describes the rock through the bulk moduli as a fluid and mineral matrix (Simm and Bacon, 2014). Variables used based on Gassmann's (1951) equation are K_{sat} as the fluid saturated rock bulk modulus, K_o as the bulk modulus of the mineral matrix, K^* as the porous rock frame bulk modulus (all fluid removed), K_{fl} as the pore fluid bulk modulus, and Φ as fractional porosity (Mavko et al., 2009).

Equation 5: Gassmann's fluid replacement theory equation (Simm and Bacon, 2014).

$$K_{sat} = K^* + \frac{\left(1 - \frac{K^*}{K_o}\right)^2}{\frac{\Phi}{K_{fl}} + \frac{(1-\Phi)}{K_o} - \frac{K^*}{(K_o)^2}}$$

There are five steps that are necessary to complete the process of using core samples with *in situ* well log values (Avseth et al., 2006). (1) Calculate and extract the bulk and shear moduli in the core sections from acquired compressional velocity, shear velocity, and density. Using equations 1, 2, 3, and 4, bulk modulus, shear modulus, Young's modulus, and Poisson's ratio can be calculated. (2) Transform the bulk modulus from dry to saturated through the rock-forming

minerals bulk moduli, the dry-rock bulk modulus, the fluid bulk modulus, and the rock porosity. The transformation of dry bulk moduli to a saturated bulk moduli uses the equation 5 above. K* is the dry bulk modulus, K_o is the mineral bulk modulus, K_{fl} is the bulk modulus of the wanted fluid (in this case, water), and Φ is porosity of the sample. This will yield $K_{sat,}$ which is bulk modulus (in GPa) of the dry rock frame, now saturated with fluid. (3) Because the shear modulus, or rigidity, is not affected by fluid saturations or fluid type filling the pores (since shear waves do not travel through fluids), keep the shear modulus unchanged. (4) Correct the bulk density for the change in fluid [$\rho_{core} + (\Phi * \rho_w) = \rho_{sw}$]. (5) Recalculate the newly-substituted fluid velocities by reversing the bulk modulus equation but using K_{sw}.

This study, a multi-scale rock physics study using core samples, well log data, and 3D seismic data to compare ultrasonic lab measurements, *in situ* well log values, and seismic exploration values, is done within the Viola "B" Zone, a productive facies of the Viola Limestone in southwest Kansas. Additionally, this study contributes to carbonate rock physics, sicne there is a lack of understanding involving Gassmann's equation and carbonate rock facies. Studying the Viola for hydrocarbon saturation leads to a better understanding of mineral matrix's effect on reservoir characteristics, and of porosities effect on seismic wavelets.

2.7 Ultrasonic to Sonic Transformation

Translating geophysical information collected at ultrasonic frequencies (lab measurements) to lower frequencies (seismic and sonic well log), is an unsolved issue within the discipline (Grochau and Gurevich, 2009). Dipole sonic logs are acquired down hole measuring both P- and S-wave velocities unlike traditional monopole tools such as sonic acoustic logs (Wang, 2001). Measurement taken at different frequencies can cause dispersion effects when fluids are in play. This is where there is a vast change in velocities within P-wave values from

the ultrasonic and sonic frequencies. In this study, laboratory P- and S-waves were tested along with the acquisition of P-wave values from well logs.

2.8 Velocity Dispersion

Velocity dispersion (dependent on frequency) occurs when measurements of a single sample is taken at two different frequencies where water/fluid is present within the pores and vastly different velocities are measured at higher pressures (Mavko et al., 1995). The fluid within the pores consume and dampen then energy of the wave thus altering the true velocity. This study was cautious of dispersion as all samples were fan dried prior to being tested for P- and S-wave velocities. Also, under larger amounts of pressure, dispersion effect seems to be less (Mavko et al., 1995). The samples in this study were exposed to pressure from 1,000 lbf to 10,000 lbf, thus limiting the amount of dispersion at the higher pressures when measurement were taken at ultrasonic frequencies.

2.9 Poisson's Ratio

Since in this study Vs data were not collected from well log measurements, an empirical relationship can be made between Poisson's ratio of the lab measured cores, to the P-wave velocity of the *in situ* log measurement. Since Poisson's ratio is indeed a ratio between Vp and Vs, the ratio should stay relatively constant regardless of the frequency in which measurement were taken in (Adam et al, 2006). Any variations in results would be due to a different amount of stress applied to the core samples than what is present *in situ* within the rock column. As long as effective pressure is applied and velocity measurement are taken at that pressure, these variations in results should be negligible or non-existent. Thus, shear waves are predicted in this study from the empirical relationship published by Adam et al. (2006) (Fig. 2-7 and 2-8).

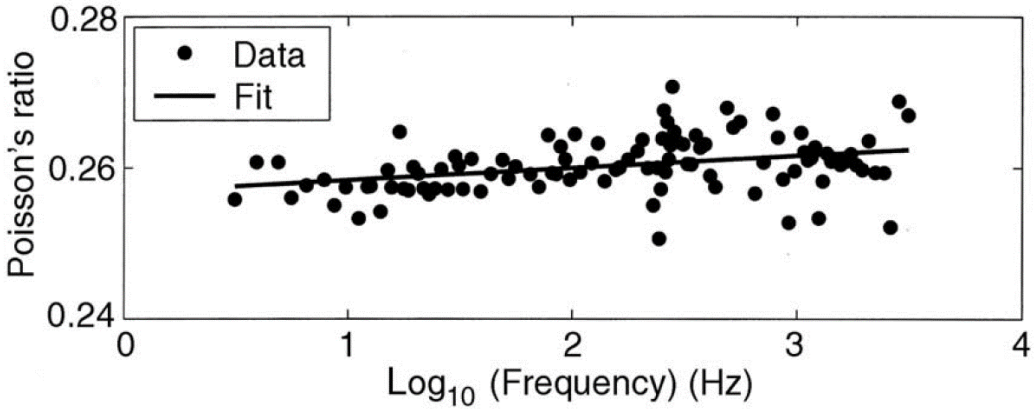

Figure 2-7: Figure from Adam 2006 showing how minimal Poisson's ratio changes as frequency increased. (After Adam et al,, 2006)

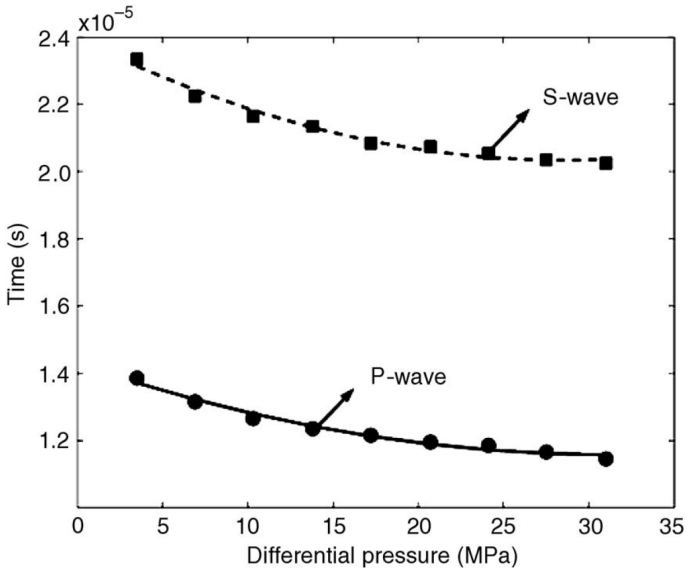

Figure 2-8: Relationship of Ultrasonic Measurements in time in relation do increase of differential pressure. As pressure increases, first arrival time decreases (velocity increases). After Adam et al., 2006.

Chapter 3 - Petroleum Geology, Regional Tectonic, and Stratigraphic Setting

3.1 Clark & Comanche Counties Production Overview

Clark County

Oil and gas production in Clark County is relevant to this study due to the 3D seismic data being located in the Morrison North-East field in this county. The first well in the area was drilled in 1954 and produced oil from zones within the Morrowan formation. From 1954 to 1966 19,734 barrels of oil were produced from the field. Lesser amounts of oil and gas were produced between 1973 and 2011 with a spike in gas production from the mid 80's through the early 90's. In 2011 Coral Coast Petroleum began production from the Viola Limestone with great success. Seven wells drilled within the area covered by the seismic survey done by Coral Coast targeting the Viola were successful in producing oil and gas (Vohs, 2016). Tables 3-1, 3-2, and 3-3 show oil and gas production for the last ten years and production platforms active within Clark county from the Morrison North-West, Morrison, and Morrison North-East Fields. Figure 3-1 shows the location of Clark County in Kansas, and figure 3-2 identifies the location of the three listed oil and gas fields mentioned above.

Year	Oil bbls	Oil Wells	Cumulative Oil bbls	Gas mcf	Gas Wells	Cumulative Gas mcf
2011	2,327	1	404,726	-	-	110,531
2012	2,411	1	407,137	-	-	110,531
2013	1,996	1	409,133	-	-	110,531
2014	1,992	1	411,125	-	-	110,531
2015	1,662	1	412,787	-	-	110,531
2016	819	1	413,606	-	-	110,531
2017	1,306	1	414,912	-	-	110,531
2018	1,632	1	416,544	-	-	110,531

Table 3-1: Hydrocarbon production for the Morrison Northwest field, Clark County Kansas.

Year	Oil bbls	Oil Wells	Cumulative Oil bbls	Gas mcf	Gas Wells	Cumulative Gas mcf
2011	-	-	430,274	-	-	118,395
2012	-	-	430,274	-	-	118,395
2013	14,053	1	444,327	-	-	118,395
2014	1,512	1	445,839	-	-	118,395
2015	137	1	445,976	-	-	118,395

Table 3-2: Hydrocarbon production for the Morrison field, Clark County Kansas.

Year	Oil bbls	Oil Wells	Cumulative Oil bbls	Gas mcf	Gas Wells	Cumulative Gas mcf
2011	47,065	2	74,450	34,163	2	3,820,972
2012	105,605	5	180,055	121,659	4	3,942,631
2013	68,568	6	248,623	179,069	5	4,121,700
2014	30,148	6	278,771	92,610	5	4,214,310
2015	15,258	7	294,029	46,869	5	4,261,179
2016	11,176	5	305,205	22,084	4	4,283,263
2017	8,649	6	313,854	3,309	3	4,286,572
2018	6,493	6	320,347	-	-	4,286,572

Table 3-3: Hydrocarbon production for the Morrison Northeast field, Clark County Kansas.

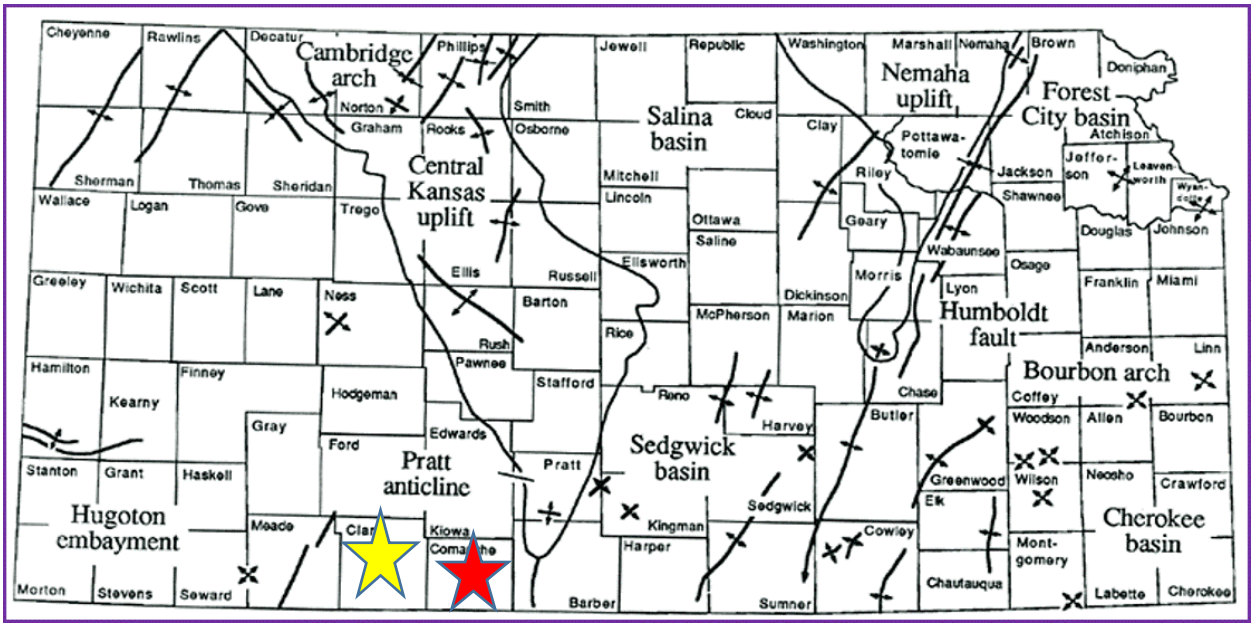

Figure 3-1: Location of Clark (yellow star) and Comanche (red star) Counties within the state of Kansas, along with the main structural features.

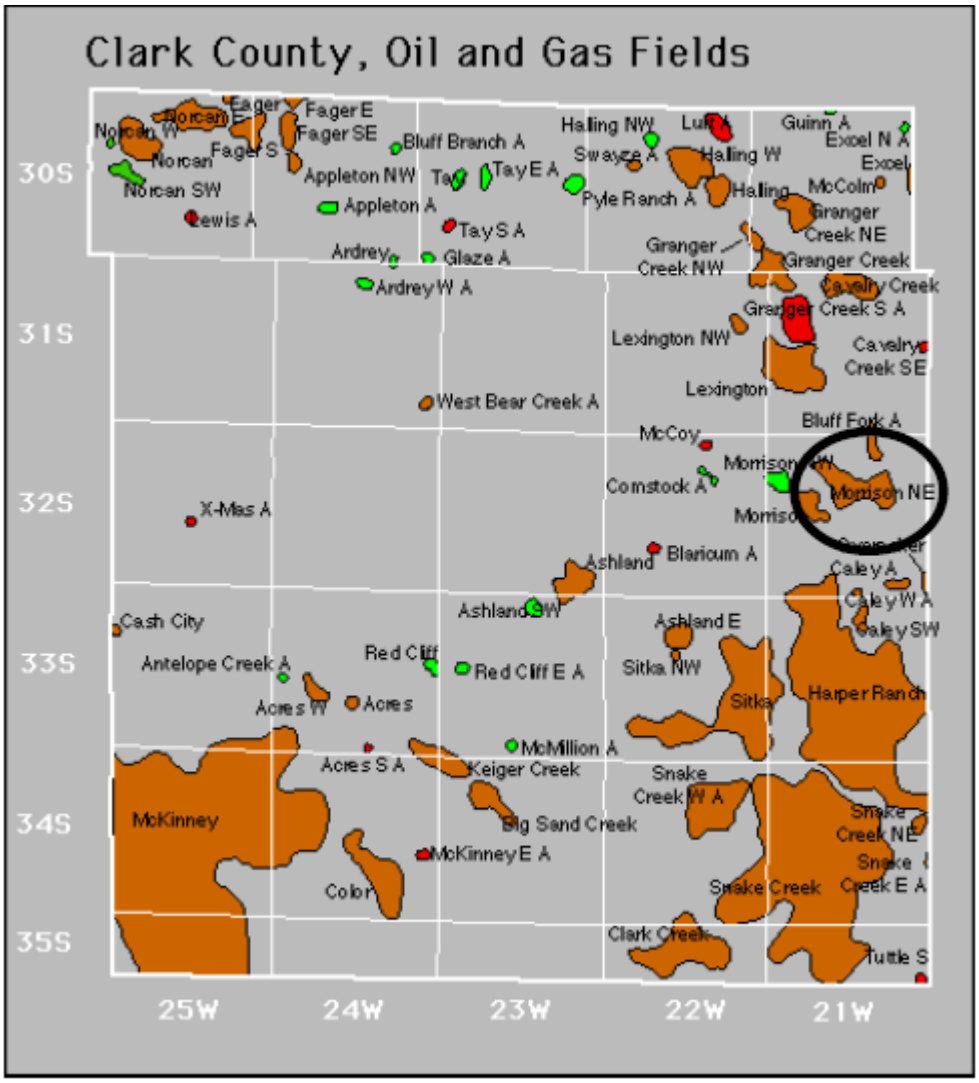

Figure 3-2: Location of the Morrison, Morrison Northwest, and Morrison Northeast oil and gas fields in Clark County, KS.

Comanche County

The oil and gas production of the Herd field in Comanche County, KS (Figure 3-1) is relevant due to the Herd-1 well logs being used as a comparative well for well log measurements in this study. Table 3-4 shows the oil and gas production data for the last ten years within Comanche County's Herd field. Figures 3-3 shows the location of the Herd oil and gas fields in Comanche County.

Year	Oil bbls	Oil Wells	Cumulative Oil bbls	Gas mcf	Gas Wells	Cumulative Gas mcf
2011	18,173	4	1,094,693	137,367	11	2,750,175
2012	15,581	4	1,110,274	129,825	11	2,880,000
2013	16,330	4	1,126,604	101,468	11	2,981,468
2014	10,026	4	1,136,630	86,798	9	3,068,266
2015	5,854	3	1,142,484	52,291	9	3,120,557
2016	5,633	3	1,148,117	46,318	9	3,166,875
2017	7,608	3	1,155,725	45,064	6	3,211,939
2018	4,955	2	1,160,680	43,626	7	3,255,565

Table 3-4: Oil and gas production per year, cumulative production values over time, and active wells each year within the Herd field within Comanche County, KS.

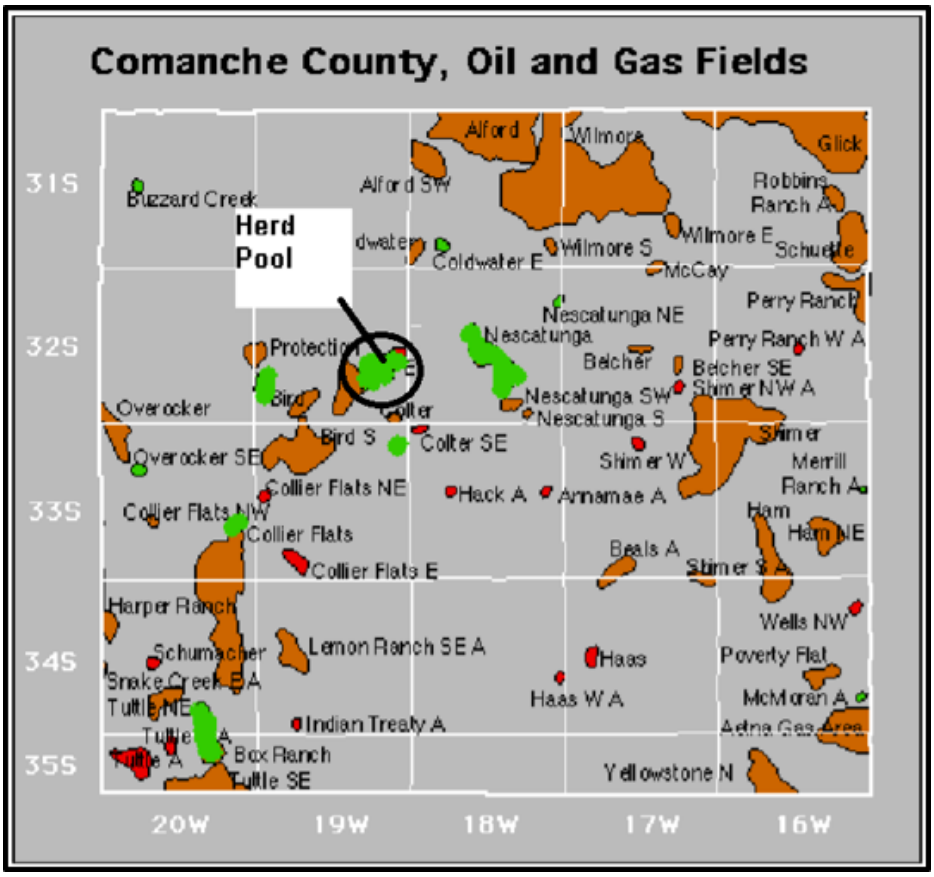

Figure 3-3: Depicts the location of the Herd oil and gas field within Comanche County, KS.

3.2 Core Data

A single barrel core taken from the Rich C-7 well in Herd Field, Kansas, was borrowed from the Kansas Geological Survery. Its depth ranged from 5808' to 5868', crossing the Viola A, B, and C Zones along with the transitional zones between each distinct facies. The core was broken down into 44 individual core samples which were measured and tested for various physical and elastic properties.

Hagood (2019) described individual facies along the core length which was paired with ultrasonic velocity measurements to understand the relationships between well log values, ultrasonic measurements, and core lithologic descriptions. Data collected from these core samples were used to compare and contrast relationships between elastic and *in situ* well log values.

3.3 Paleotopographic Traps

Production within the upper Viola is controlled by paleotopographic traps. The upper Viola was preserved by an erosional unconformity separating it from the overlaying Maquoketa Shale (figure 3-4) (Richardson, 2013). These erosional unconformities generated the paleotopographic highs and lows within the Viola, which determine how much "A" and "B" is present. Below the productive zone the Viola has no porosity labeled as the "C" zone.

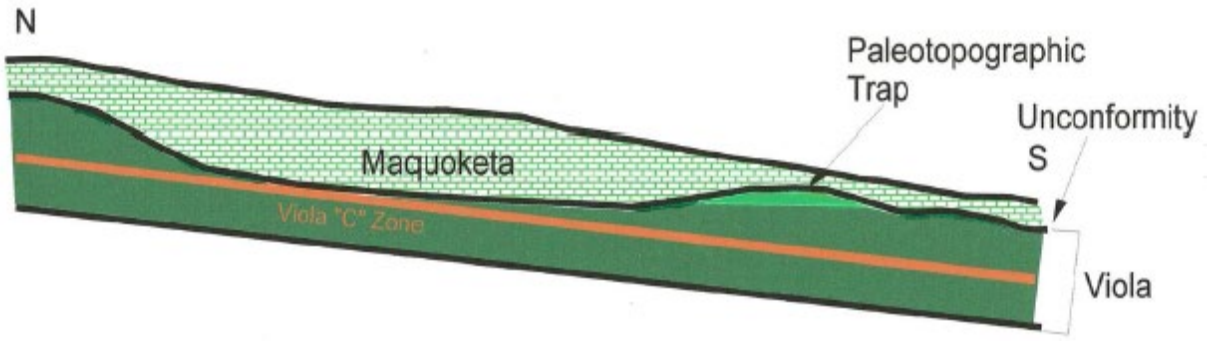

Figure 3-4: Ideal reservoir model showing a paleotopographic trap in the Viola A top (Richardson, 2013).

3.4 Stratigraphic Overview

The Viola Limestone is of Middle and Late Ordovician age and has as much as 239 feet of carbonate sequence in Comanche County (Adkison, 1972). The Kansas Viola Limestone has been correlated with the Viola Limestone in southern Oklahoma (Adkison, 1972).

Over the course of geologic time the Viola has gone through several erosional events. Prior to Devonian carbonate deposition, the Viola experienced an erosional event in the late Devonian that cut through four major locations in the central area in Kansas, about 14 miles west of Wichita. Evidence of this erosion is found at the Chautauqua arch (Figure 3-5) (Adkison, 1972). Lee (1956) wrote, “The Viola sequence does not lend itself to accurate regional zoning”. This is due to facies variation, a leading challenge when tracking the Viola “A” zone as a potential reservoir.

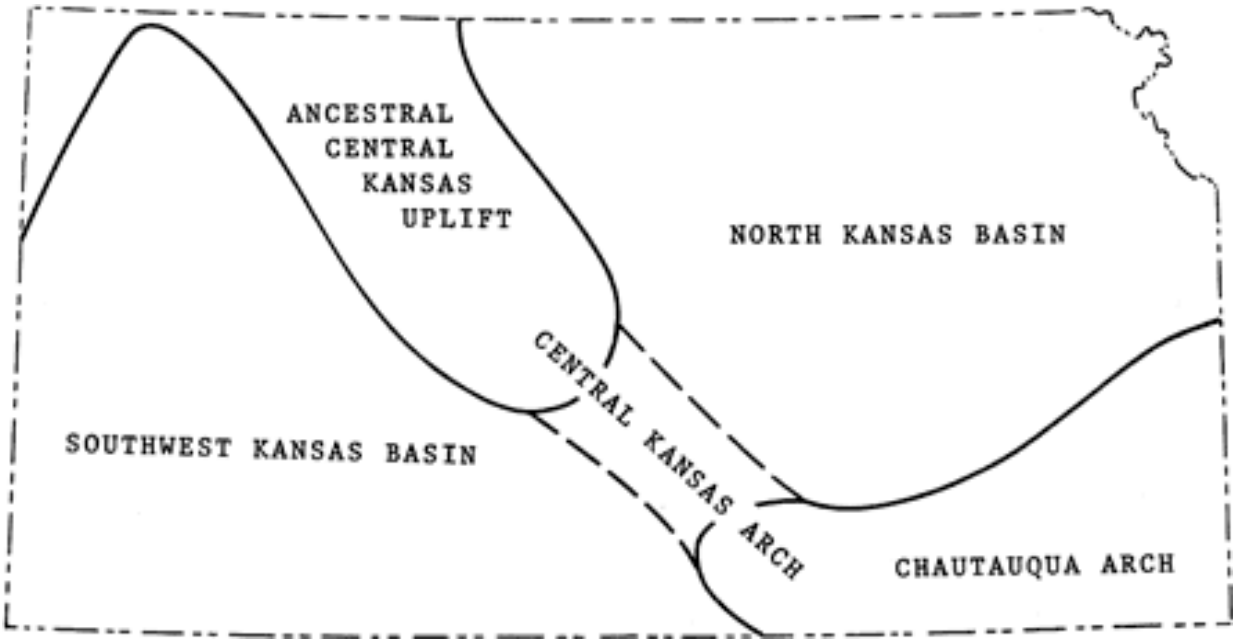

Figure 3-5: Structures present in Kansas during Viola deposition (Merriam, 1963)

The Viola Limestone includes dolostone, limestone, and chert (Adkison, 1972). According to Adkison (1972) there is an abundance of dolostone in locations where the Viola is extremely thin. Vohs (2016) explained that productive zones of the Viola are in locations which are very thin, and Linares (2016) stated these productive locations are dolomitic reservoirs. Production occurs in the vuggy dolostones the lie below the erosional unconformity separating the Viola from the Maquoketa Shale (Vohs, 2016) (Figure 3-6).

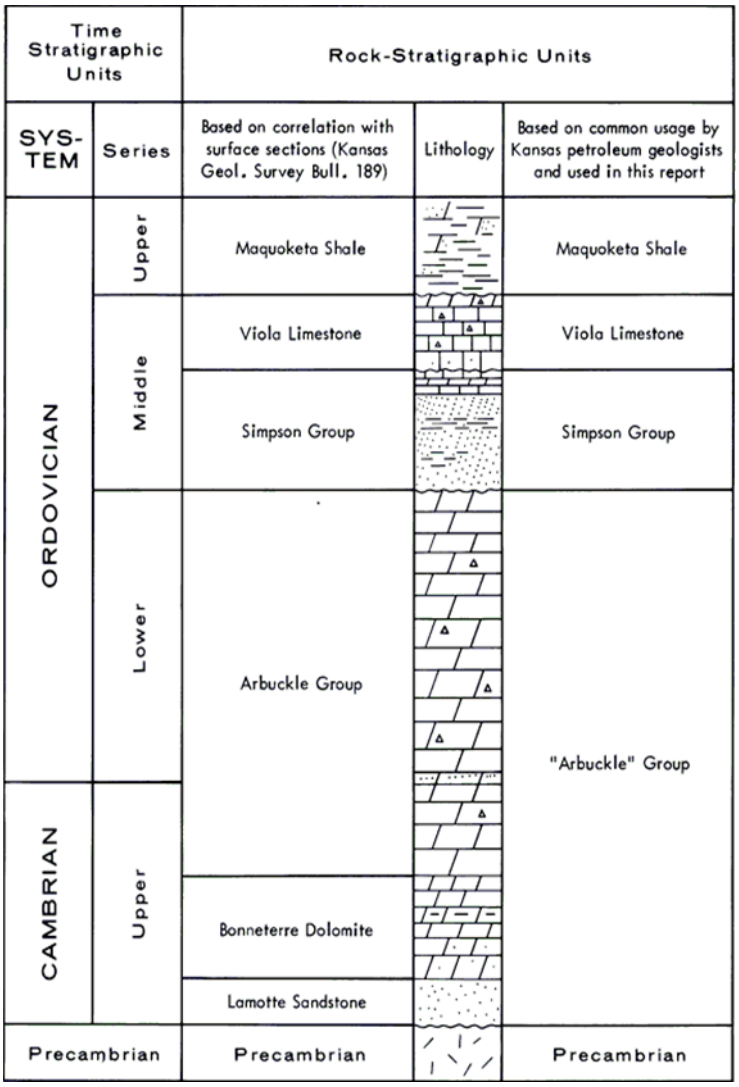

Figure 3-6: Stratigraphic column showing the Cambrian and Ordovician units in the study area, including the Middle Ordovician Viola Limestone (Cole, 1975)

Maquoketa Shale

The reservoir seal is defined as the Maquoketa Shale which is upper Ordovician in age and comprises a limestone within the study area. The limestone is has a thickness of about 20 to 25 feet in the study area (KGS, 2020). There is no visible porosity and due to it, the Maquoketa makes an excellent seal.

Viola Limestone

Between the Maquoketa Shale and Simpson Group lies the Viola Limestone, with hydrocarbon reservoirs within its top. This unit comprises of a medium to coarse vuggy dolostone containing scattered chert throughout with a thickness of about 175 to 200 feet. The upper Viola contains the vuggy porosity and sits below an erosional unconformity separating it from the Maquoketa. Vugs are pores that are somewhat equant, not markedly elongated, with diameters greater than 1/16 mm, and is not fabric selective (Choquette and Pray, 1970). During the Middle Ordovician an epicontinental sea covered present-day Kansas (Figure 3-7), which experienced two marine transgressions and regressions (Bornemann et al., 1982). During this time interval, sub aerial exposure of the Viola allowed dissolution that resulted in secondary vuggy porosity to form, as well as the paleotopographic highs and lows within the upper Viola.

Simpson Group

Underlying the Viola Limestone, the Middle Ordovician Simpson Group is divided into three parts represented by a limestone unconformity at the top of the formation, followed by the upper Simpson, and concluded with the lower Simpson. The upper Simpson is comprised of two hard shale bodies and the rest of the Simpson is comprised of fine and medium-coarse grained sandstones. Within the study area the Simpson is about 15 feet thick (KGS, 2020).

Arbuckle Group

Beneath the Simpson is the Arbuckle Group, which consists of carbonates. The seismic signature of the Arbuckle Group is very distinctive, which allows accurate picking of horizons above this unit (Vohs, 2016).

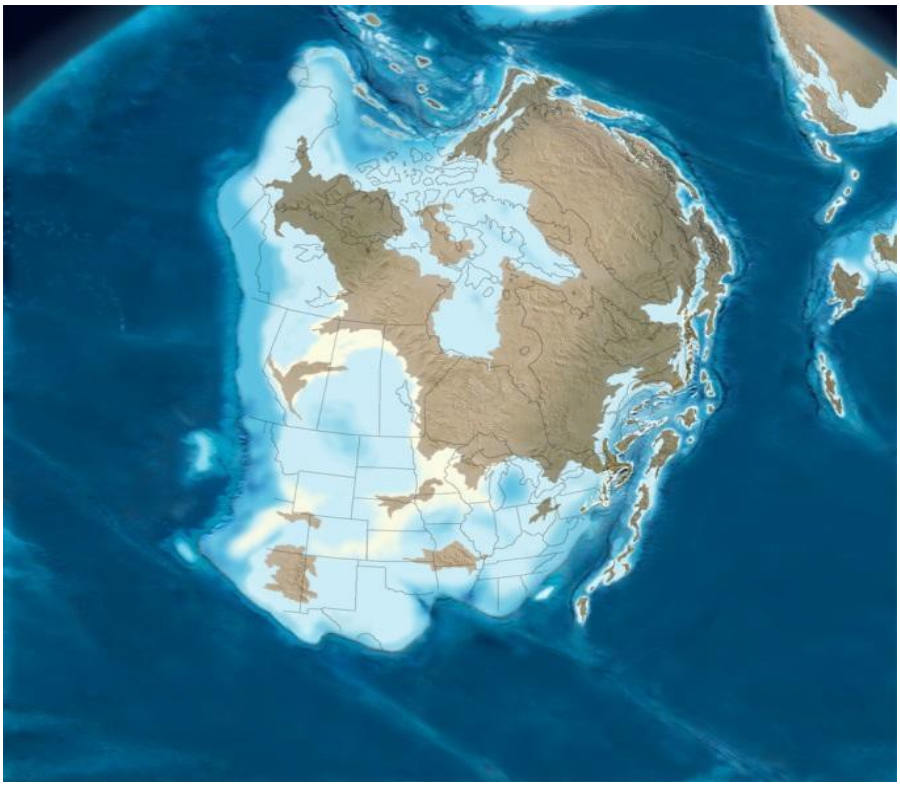

Figure 3-7: Paleotopographic reconstruction showings the epicontinental sea responsible for deposition the of the Middle Ordovician Viola in Kansas (Blakey, 2015).

3.5 Hagood's (2019) Stratigraphic Analysis

Hagood (2019) completed a high-resolution facies study of the Viola using Rich C-7 and neighboring wells. Various facies comprise the Viola "B" Zone, providing a deeper understanding of the lithofacies and rock textures as it applies to fluid replacement modeling. Lithological composition of the Viola includes Cherty Dolomite, Intra-clastic Breccia, Intra-clastic Rudstone, Bioclastic Grainstone, and Muddy Dolostone (Hagood, 2019). The targeted section within the Viola this study covers includes Cherty Dolomite, Muddy Dolostone, Rudstone, and the Interclastic Breccia.

The productive "B" zone consists of cherty dolomite that contributes to such high porosity within the formation. Atop the "B" zone contains about a foot of rudstone with

alternating thin beds of breccia and muddy dolostone (Hagood, 2019). The “B” zone is marked by a transition to cherty dolomite facies. The “C” zone contains primarily muddy dolostone facies, with the top of the “C” zone being marked with a thin rudstone (Hagood, 2019). Figure 3-8 shows the identification of the “C” zone and “B” zone through the suite of well logs and petrophysical data.

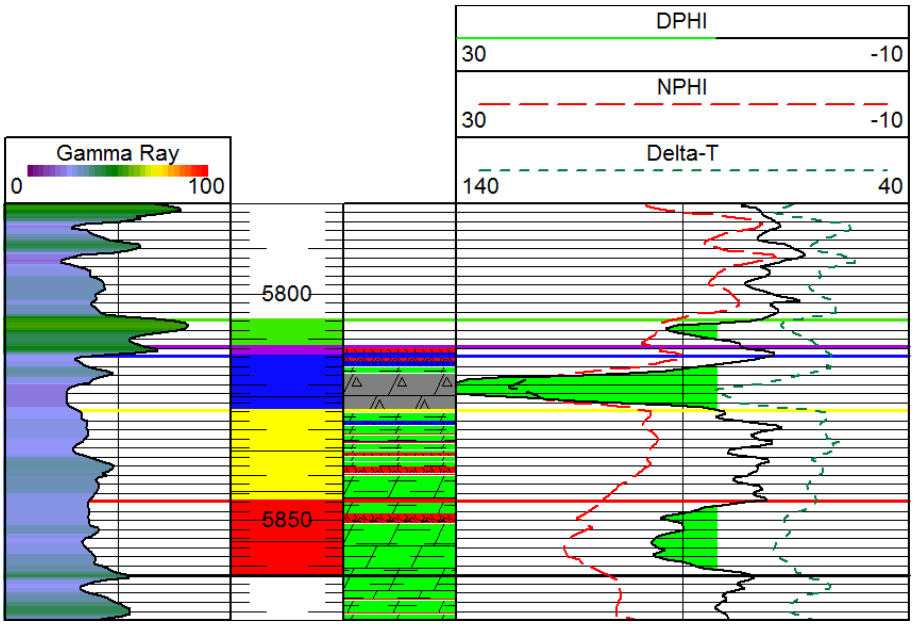

Figure 3-8: The “B” Zone highlighted in blue along the depth track is where slower Vp velocities and higher neutron porosity values are present, corresponding with the cherty dolomite. A, B, and C zones are highlighted in green, blue, and red respectively. Green highlighting along the right log track depicts porosity above 15% (Hagood et al., 2019).

As mentioned before, paleotopographic highs are targeted when exploring the Viola for fossil fuel production. These highs are important in sealing the dolomite reservoirs and are compromised of the Maquoketa Shale. However, these paleotopographic reservoirs may not be laterally continuous throughout a region providing challenges for exploration. As seen in Hagood (2019), density porosity (DPHI), neutron porosity (NPHI), and sonic (DT) well log traces have strong correlation with P-wave velocities, and thus will also be used in this study. The

relationship betweek low density and porouos cherty dolomite may be useful in determining P-wave velocities and productive zones within the Viola Limestone. Hagood (2019) provided essential data for the lithological composition of Viola productive facies and how they interact with well logs.

Chapter 4 - Methods & Procedures

Rock physics ultrasonic measurements is conducted to analyze geologic and geophysical data jointly to determine reservoir facies. By using elastic laboratory and *in situ* properties, this study aims to achieve a deeper level of understanding about the Viola A and B productive facies and their seismic characteristics. Grochau and Gurevich (2009) conducted a study using both ultrasonic laboratory velocity measurements and sonic log measurements to understand and utilize Gassmann's fluid substitution. Elements from their methods have been adopted in this study.

4.1 Core Testing Procedures

The study core from the KGS was sixty feet thick. Forty two sections were selected from the core for study, ranging from six to 14 inches in length. All of the sections were split in half lengthwise, but not all were perfect cuts. Each core was bored at 150 cm in diameter. In the lab volume was measured to calculate density, weight was measured on a digital scale, height was measured for ultrasonic testing accuracy, and diameter was measured for each section as well. Since each section was not perfect the following equations were used to determine the proper density.

$Density = \frac{Mass}{Volume}$. Volume was measured using a 3-gallon clear tub which was calibrated by first pouring 5 liters of water into the tub. Next, water was added to the tub in 200 ml increments. Once any motion disturbance dissipated a mark was made at the meniscus. This was done from 5 liters to 8 liters of water calibrated every 200 ml. Each core section was weighed on the scale first and had its weight recorded in grams (g). Next, each section of core was submerged in the water. Once the wave disturbance settled, a measurement was taken, and the water displaced was then calculated to provide volume (g/cm^3) for each core section. Each

sample was then dried with a fan for 64 hours before being tested for ultrasonic velocities so velocity dispersion could be avoided.

The mass and volume of each Rich C-7 Core sample were estimated to calculate the density. The height and volume correction factor as percentage of diameter was applied to account for samples shapes deviating from a complete cylinder. Each core was measured for a percent value of diameter since each core was not cut perfectly at 52.5mm for the 110mm barrel core.

4.2 ULT 100 Ultrasonic System

To obtain P-wave and S-wave velocities of our core samples, the ULT 100 Ultrasonic System is used in conjunction with a standard computer, the CATS Ultrasonic software, and a controller used to emit ultrasonic waves through the intended sample. Tests were run on 42 core samples of the Viola Limestone sampled from the Rich C-7 well in Comanche County Kansas. The core was lent by the KGS. Air humidified samples were exposed to overburdening pressures so ultrasonic measurement could be taken. These high frequency waves have short enough wavelengths to sample specimens such as core samples.

The GCTS CATS Ultrasonic system is composed of two main components: a ULT controller, and a GUI (Graphic User Interface) to the controller called the CATS Ultrasonic Software. The controller is an embedded microprocessor that is running the control program in a real time environment. It controls the High Speed Input Board and Ultrasonic Pulser which executes the tests. The user only interacts with the controller through the CATS software, although the controller is independent from the software and the CATS software does not need t be running in order for the controller to operate. Within the lab, the setup consists of one

Windows Computer running the CATS software, the ULT controller, a hydraulic press to apply overburdening stress, and a digital sensor to read and display the amount of overburdening stress in ft/lbs (Figure 4-1). The system is non-destructive which makes it ideal for this study.

Figure 4-1: The Geophysics Laboratory in Thompson Hall at Kansas State University in Manhattan, KS.

The software determines shear and compressional wave velocities and stores the waveforms digitally to determine compressional (P) wave and shear (S) wave velocities along with an associated waveform. First arrival times must be selected for both the Compressional and Shear waveforms through the software either automatically or manually. First arrival times of waves is the amount of time it takes a wave pulse (P or S), to travel through the core sample. From those values elastic constants can be calculated. These are the elastic moduli that are used later when conducting fluid replacement theory.

To obtain these unique wavelets, two platens are used to emit and measure the wave energy. Before testing a sample with the platens, they must be calibrated in a "face to face" test to determine how long it takes P and S waves to pass through the platens. These "face to face" arrival times are subtracted from the observed compressional and shear first arrival times of the test specimen to give correct arrival times. The shear and compressional velocity is calculated using the following equation: $\frac{Specimen\ Heigh}{arrival\ time - face\ to\ face\ arrival\ time} = Velocity$. The GCTS provides an aluminum core sample to test, ensuring the controller sends a strong signal to the software to be processed.

Core samples are tested once all calibrations are complete. First, the user needs to ensure each sample is smooth and flat on the bottom. The samples also need to have a diameter larger than the platens to ensure proper emission of the wave energy. This all can be done using a rock saw and patience when cutting, to ensure a leveled and smooth surface. Next, an acoustic medium is used to ensure the best fit is achieved between the sample and the platen. Any air between the platen and the sample can hamper the ability of the system to emit a full signal or inhibit the reading of the signal. The medium used during this study was honey due to its high viscosity to prevent intrusion into the pore spaces of the samples.

In situ pressure is ideal when testing for compressional and shear waves. This can be calculated using the assumptions of an average grain density of 2.71 g/cm^3 and each foot of overburdening rock to be equivalent to 1 pound per square inch (psi). Since the sensor measures in lbf, psi needed to be converted: $psi = \frac{lbf}{\pi r^2}$ where r is the radius of each sample being tested. Above in section 4.1, the method for estimating the "true radius" of each sample is expanded upon since each core sample was half of a 115cm diameter barrel core. Unfortunately *in situ* pressures were not achieved during the study. The target pressure was roughly 17,000 lbf when

the pressure gauge of the equipment initially used could only safely achieve 10,000 lbf. However, new equipment used later during the study could measure well above 20,000 lbf. Samples were exposed to *in situ* pressure gradually and each sample would become structurally compromised roughly 5000 lbf before the reaching the desired *in situ* pressure. Due to this limitation, this study only uses velocities measured at 10,000 lbf which is 7,000 lbf less than *in situ* pressure. Velocity results should still follow sonic trends, but will have values lower than *in situ*. Thus, all results are assessed as relative to *in situ* variables.

Once the samples were loaded between the platens the CATS software required initial inputs related to the physical nature of each specimen, along with configuration of the board. For this study the board used a sampling rate of 1.25MHz, set within the software along with other parameters. External manual gain was kept off, input automatic gain was kept at the default of 20, and energy output was kept at the default of 100%. Specimen characteristics input included mass of the sample, diameter, height in millimeters, lithology type, and the types of platens used. Density and volume were then calculated by the software based upon the users inputs. From here a "test" was created to induce 8 P-wave and S-wave pulses every 30 seconds. This was done so the user could increase the overburdened pressure to the next step and the system would then take the average of all 8 waves for each when building the wavelet. Doing so, provided that each sample taken as lbf is increased by 500 each time can be consolidated within one file and overburden pressure never need to be released before taking the next sample contributing to the degrading of the core samples.

The CATS software provides an automatic and manual picking parameter to obtain P and S wave velocities from the wave forms. Automatic picking was inconsistent with our samples so manual procedures were followed. Within the digital window, a grid where the X-Axis depicts

time in milliseconds and the Y-Axis provides limits for energy in Volts which are used to plot the wavelet. Figure 4-3 (P-wave) and 4-4 (S-wave) show how the waveforms are displayed by the ULT 100 system which are later used to pick first arrival times.

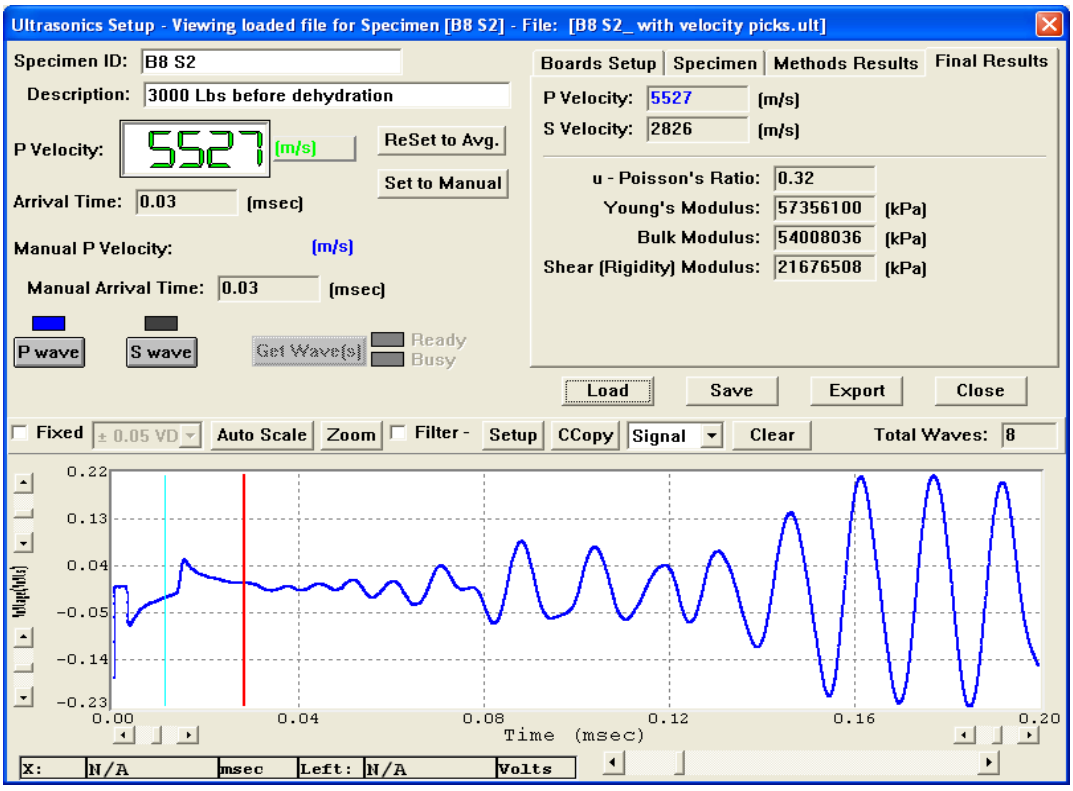

Figure 4-2: Compressional wave waveform displayed within the ULT 100 system. Elastic properties are established from manually picked first arrival times providing P-wave values.

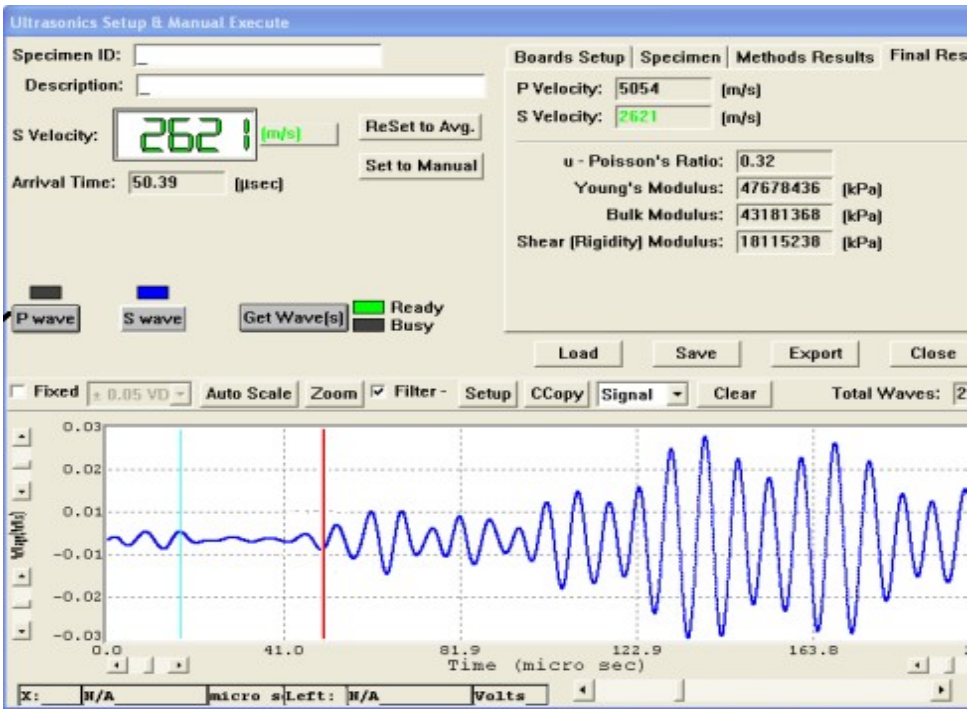

Figure 4-3: Shear wave waveform displayed within the ULT 100 system. Elastic properties are established from manually picked first arrival times providing S-wave values.

Selecting a first arrival time can be very challenging with the amount of noise absorbed with each sample. The automatic methods used within the software are ineffective and do not provide consistent or correct results. At each stress interval starting at 500 lbs and going to 10,000 lbs with 500 lb steps between reading, a compressional and shear-wave velocity are taken. These wave velocities can be exported into text files where the data can be visualized either by using code or Microsoft excel. For this study, Microsoft excel was used to stack waveforms (Figure 4-4) for each sample to assist in determining the correct location along the wavelet. This method proved to be the most accurate in user generated first arrival times. A visualization of the dispersion of energy as force is applied provides an accurate method to separate the signal of each wavelet from its noise. Once first arrival times are selected the system

calculates velocity using the equation: $V = \frac{L}{Tf}$, where V is velocity (m/s), L is length of the sample (mm), and Tf is the first arrival time of the signal (milliseconds).

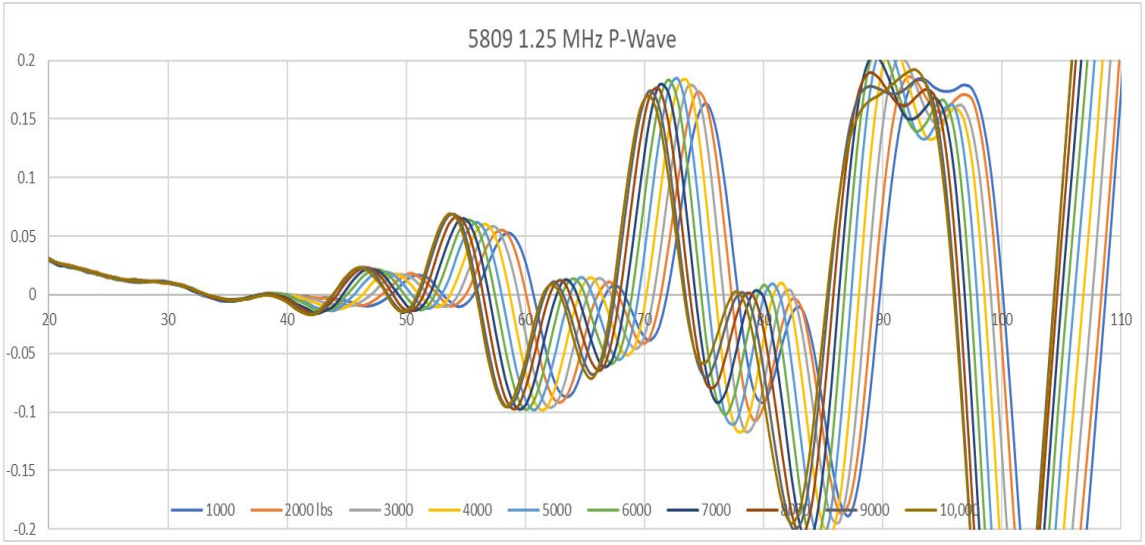

Figure 4-4: P-wave wavelets are superimposed in 1000 lb increments for sample 5809. It can be seen at around 40 milliseconds the waveform begins to diverge indicating a start of "true signal" providing an accurate selection for first arrival time.

Once correct first arrival times are determined, the CATS software calculates the velocity for each wave. Although the CATS software can also calculate elastic moduli (in units of kPa), elastic moduli were calculated using an Excel spreadsheet for best adjustment of elastic moduli. When collecting data in this way, the highest priority is to A) collect good data initially when testing each sample and applying force; B) ensuring accurate superposition and establishment of first arrival times when picking for each sample. Any inaccuracy in first arrival time selection would subsequently alter P and S wave velocities, extensively used throughout this study.

4.3 Well Log Data Extraction

P-wave velocity (Vp), neutron porosity (NPHI), density porosity (DPHI), deep induction resistivity (ResD), and bulk density (Rho) were all extracted from electric well logs in LAS. File

format. Acoustic Impedance was calculated using Vp and Rho, and porosity was calculated using Doveton's (2017) PE calculator with the addition of neutron porosity and bulk density as other variable parameters.

Sonic log values are not digestible by Gassmann modeling straight off the log. Acoustic log's display data in a time per length format. Log slowness is recorded at microseconds/foot. Whereas ultrasonic P-waves and Gassmann modeling use meters per second as their unit for both velocity values. The higher the log value the slower the P-wave, whereas the lower the value, the faster the wave propagates through the rock. To convert log slowness to velocity use $velocity = \frac{1000000}{\log slowness}$, where *log slowness is in* $\frac{us}{ft}$. Once this is accomplished a conversion of $\frac{ft}{s}$ to $\frac{m}{s}$ is required to achieve values comparable to the ultrasonic values.

4.4 Gassmann Modeling

Gassmann Modeling

Wang et al. (2001) described Gassmann modeling as follows. The Gassmann (1951) equations calculate the bulk modulus of a fluid-saturated porous medium using the known bulk moduli of the solid matrix, the frame, and the pore fluid. The solid matrix consists of the rock-forming minerals, the frame refers to the skeleton rock sample, and the pore fluid can be a gas, oil, water, or mixture of all three.

The first step (Equation 6) is using densities (Rho), P-wave velocities (Vp), and S-wave velocities (Vs) from a specimen that contains an initial set of fluids. In section 2.6, K_{sat1} was solved for along with ρ_{sw1}. They represent the bulk modulus of a core sample saturated with water, and bulk density of the water saturated sample respectively. One other variable needed to achieve Vp_2 and Vs_2 are K_d which is the bulk modulus of the rock frame. Units are normalized during fluid substitution, bulk moduli in GPa, all velocities in km/s, and density in g/cc. The

following 5 steps outlined by Mavko et al. (1995), Avseth (2005), and Downton and Gunderson (2005) are used in a practical workflow to solve for p_{b2}, Vp_2, and Vs_2.

Equation 6: Moduli Calculation. (a-shear modulus) (b-fluid saturated bulk modulus)

$$\text{a.}\quad \mu = Vs^2\rho_b \qquad \text{b.}\quad K_{sat} = Vp^2 p_b - \frac{4}{3}\mu$$

Equation (a) solves for shear modulus which is used as a variable within the saturated bulk modulus equation (b) (K_{sat}). Saturated bulk modulus of an initial fluid is needed when calculating for bulk modulus of the rock frame (K_d).

Equation 7: Dry Rock Inversion. (a - integer used in b) (b - bulk modulus of the mineral matrix)

$$a.\ K_\Phi = \frac{\Phi}{\frac{1}{K_{sat}} - \frac{1}{K_0}} - \frac{K_0 K_{fl}}{K_0 - K_{fl}} \qquad \text{b.}\ K_d = \frac{1}{\frac{\Phi}{K_\Phi} + \frac{1}{K_0}}$$

In equation 7, (a) provides an integer used in (b) to solve for bulk modulus of the dry rock frame (K_d). K_0 is the bulk modulus of the mineral matrix, Φ is porosity, and K_{fl} is the bulk modulus of the initial fluid saturating the rock being tested with fluid substitution. Obtaining the bulk mineral matrix can be achieved through data tables and known constants. For this study Dolomite has a mineral density of 2.87 g/cc, Calcite has a mineral density of 2.71 g/cc, and Chert has a mineral density of 2.35 g/cc. Additionally Dolomite has a bulk modulus of 94.9 GPa, Calcite has a bulk modulus of 76.9 GPa, and Chert has a bulk modulus of 26.0 GPa. Calculating concentrations of each mineral can be done in a few ways, the most popular being X-Ray Diffraction which provides weight percent's of specific minerals. This study uses a composition calculator created by Doveton (2017) (equation 8). K_{fl}, the bulk density of the initial fluid uses constants such as 2.38 GPa for water, 1.59 GPa for oil, and 0.07 GPa for gas. A mixture or two or all three can be used within fluid replacement modeling. Fractional proportions would be used

to calculate an average bulk density if multiple fluids were used. Throughout this study, the initial fluid (fl_1) is always water and the replacement fluid (fl_2) is always assumed to be oil.

Equation 8: Fluid Substitution - Density. (a - bulk density of the rock with substituted fluid; b - density of the substitution fluid; c – bulk density of the rock with substituted fluid lacking bulk density but having matrix density)

$$a.\ p_{b2} = p_{b1} - [(\phi p_{fl1}) - (\phi p_{fl2})] \qquad b.\ p_{fl2} = (p_w S_w) + (1 - S_w)p_h$$

$$c.\ p_{b2} = (p_{fl2}\phi) + (1 - \phi)p_0$$

Equation 8 corrects bulk density to reflect the second fluid in-place after the initial one. P_{b2} is the bulk density of the substituted solution, P_{fl1} is the density of the initial fluid, P_{fl2} is the density of the substituting fluid, P_w is the density of water (1.09 g/cc), S_w is water saturation, P_h is the density of the substituted hydrocarbon, and P_0 is the density of the mineral matrix. Equation (a) solves for the bulk density of the substituted specimen using known fluid densities, porosity, and bulk density of the initial specimen. Equation (b) differs for it no longer contains bulk density of the initial specimen but now contains the matrix density of the rock. Lastly, equation (c) solves for the density of the substituted fluid which is used in both equation (a) and (b).Obtaining S_w can be done by either manually entering various values between 0 and 1 since it a fractional value, or it can be determined by using *Archie's Equation* to solve for Sw.

Equation 9: Fluid Substitution - Shear Velocity

$$a.\ V_{s2} = \sqrt{\frac{\mu}{p_{b2}}}$$

Equation 9 provides the solution for the velocity of the shear wave (Vs_2), where μ is equation 2 and P_{b2}, equation 8a. The reason there is no "fluid substituted shear modulus" is due to fluid having no effect on shear waves. However, when calculating for V_{s2}, it is necessary,

since shear waves change due to bulk density even though the wave does not interact with the fluid filling the pore space.

Equation 10: Fluid Substitution - Compressional Velocity

$$V_{p2} = \sqrt{\frac{p_{b1}}{p_{b1} + (p_{fl2} - p_{fl1})\phi} V^2_{p1} + \beta^2 \frac{N_2 - N_1}{p_{b1} + (p_{fl2} - p_{fl1})\phi}}$$

$$Where \qquad \beta = 1 - \frac{K_d}{K_0} \qquad N_1 = \frac{1}{\frac{\phi}{K_{fl1}} + \frac{\beta - \phi}{K_0}} \qquad N_2 = \frac{1}{\frac{\phi}{K_{fl2}} + \frac{\beta - \phi}{K_0}}$$

Lastly, equation 10 provides the solution for the velocity of the compressional wave (V_{p2}), which now reflects the substituted fluid. B, N_1, and N_2 are integers calculated using bulk modulus of the rock frame (K_0), dry bulk modulus (K_d), porosity (Φ), bulk modulus of the initially saturated fluid (K_{fl1}), and bulk modulus of the newly substituted fluid (K_{fl2}). Additionally, equation 11 uses the initial bulk density (p_{b1}), bulk density of the substituted fluid (p_{fl2}), bulk density of the initial fluid (p_{fl1}), porosity (Φ), and the initially saturated P-wave velocity (Vp_1).

Calculating Mineral Composition for Gassmann Modeling

John Doveton (2017) created a calculator and visualizer to assist in using Photo-Electric Logs (PE) to determine mineral composition. Due to the lack of X-Ray diffraction data to determine mineral composition of various points along the core, Doveton's (2017) PE log calculator will be used to determine effective mineral composition within the Rich C-7 core to assist in accurate gassmann calculations along with analyzing Stephens Ranch wells used in Vohs' study to compare mineral composition between other producing and non-producing wells.

Doveton's (2017) calculator provides an apparent density and a bulk photoelectric absorption for the mineral matrix. Using these variables, percentages are calculated for Quartz (Chert), Dolomite, and Calcite (Limestone) at each depth along a log curve (Figure 4-5). The

necessary inputs are density porosity (DPHI), neutron porosity (NPHI), both in equivalent limestone fractional units, and photoelectric factor (PE). From those, bulk density is calculated, which is then used with PE to produce the volumetric photoelectric factor (U). At any depth within the Viola, the apparent density and a bulk photoelectric absorption factor of the mineral matrix can be used to calculate the proportions of calcite, dolomite, and chert (Figure 4-6).

Compositional proportions are then calculated using Doveton's (2017) method, and then applied to calculate mineral density and mineral bulk modulus. The equation to determine mineral density is $\rho_0 = (Dolomite\ \% * 2.87) + (Calcite\ \% * 2.71) + (Chert\ \% * 2.35)$. Mineral bulk modulus (in GPa) was calculated with $K_0 = (Dolomite\ \% * 94.9) + (Calcite\ \% * 76.8) + (Chert\ \% * 26)$.

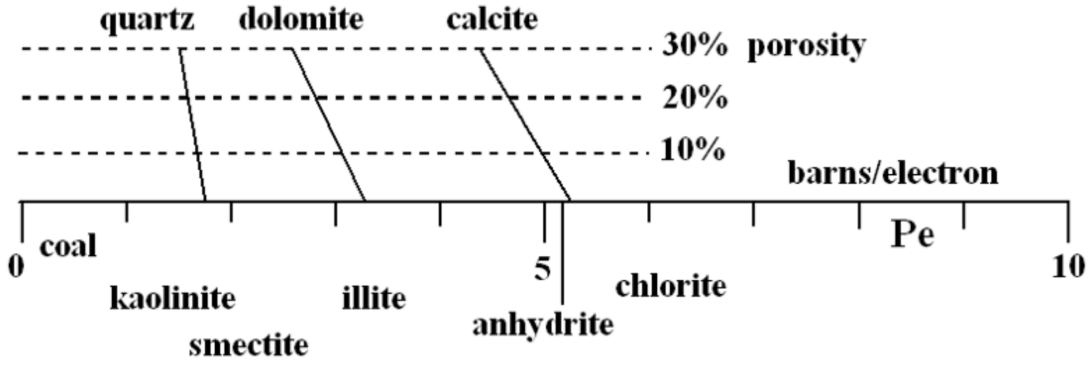

Figure 4-5: Example of how a photoelectric factor is used with porosity to determine mineral composition, according to Doveton (2017).

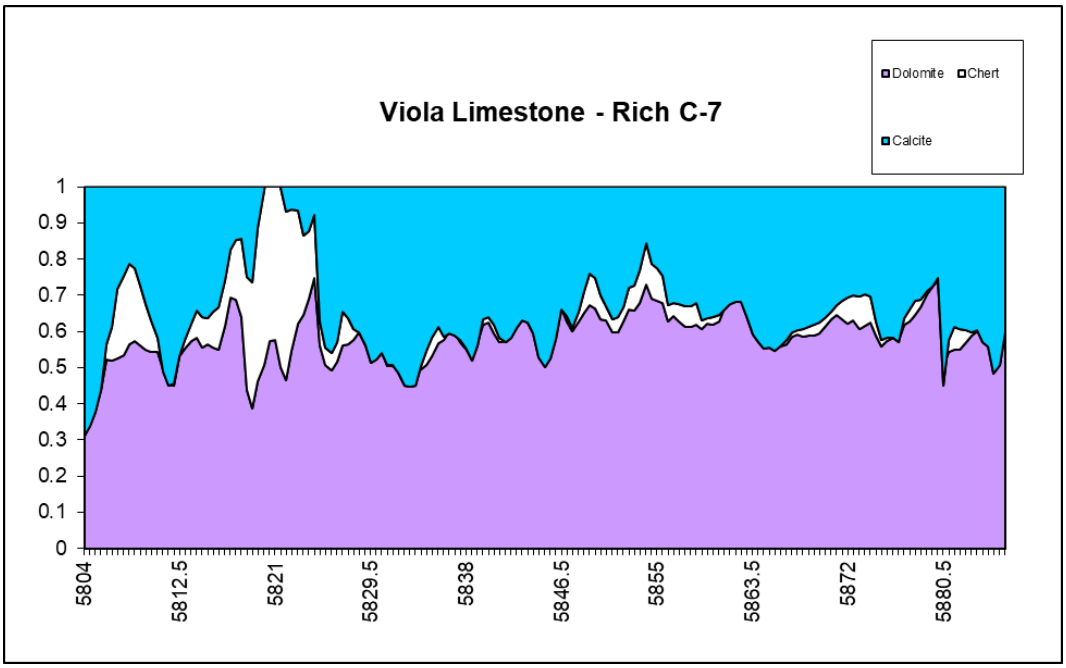

Figure 4-6: Lithological proportion profile of the Viola Limestone in the study interval from Rich C-7. The values are achieved by using PE logs along with Neutron and Density Porosity. Blue indicates calcite, purple is dolomite, and white is chert.

An additional method used within this study to check lithologic contents based on velocity data is based on the Greenberg-Castagna relationship (Castagna et al., 1985), used to solve for either Vs or Vp using an equation dependent on the lithology of the log section being tested (Equation 11). This is effective when di-pole sonic is not present, or to get an approximation of a specific point upon a log's lithology.

Equation 11: Castansa Vs transform for dolomite.

$$Vs = 0.58321Vp - 0.07775$$

The equation is defined as a dolomite trend. Along with the Greenberg-Castansa method, the Poisson method (Equation 12) was also used and applied to the same data as shown in Fig. 4-7. Using Poisson's coefficient from the lab-measured core samples, the equation can be re-organized to solve for Vp or Vs when Poisson's ratio is known. Solving for Vs is complex but also intuitive, due to Vs not being affected by fluid properties. Figure 4-7 depicts the two

methods (Castagna Dolomite trend line equation, and Poisson's ratio established from core measurements) of obtaining Vs or lithological composition using Vp and peer-reviewed trend lines.

Equation 12: Vs Transform using Poisson from Ultrasonic Core tested velocities.

$$Vs = \sqrt{\frac{Vp^2 - (2 * Vp^2 * \sigma)}{(\sigma * -2) + 2}}$$

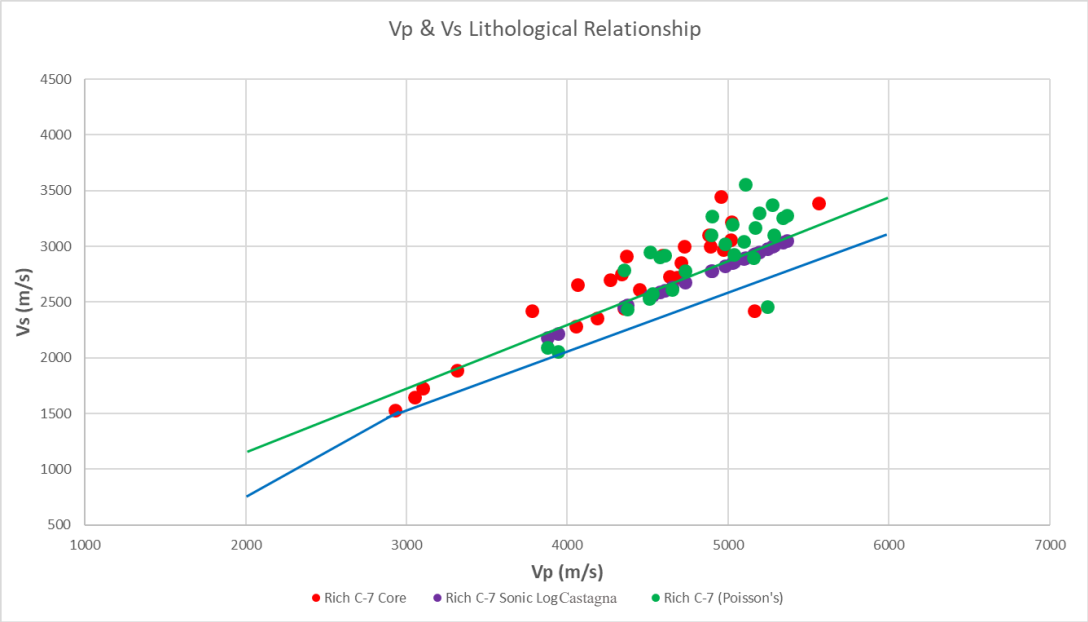

Figure 4-7: Vp & Vs cross plot to establish lithologic relationships using values aquired through lab-tested core values, Castagna Dolomite trend line equation, and Poisson's ratio established from core measurements and applie to Rich C-7 sonic log. Green trend line most closely fits dolomite while the blue line most closely fits limestone.

Lastly Figure 4-8, following an example reported by Raef et al. (2019) identifies lithological amounts specifically for the Viola Limestone. The method uses neutron porosity and sonic logs to generate a cross plot with depth, represented by a color gradient on each data point. The red points on the right side of the figure are trending along the 70% Chert/30% Dolomite line, while several of the green points are trending above any lines. However, several points at the top of the core (bottom-left corner of the figure) trend along the Dolomite line. They are at

the top of the Viola “B” zone, dominated by dolomitization. The dark red points are beneath the “B” zone, within the unconsolidated breccia overlying the “C” zone (Hagood, 2019). This suggests that Rich C-7 comprises carbonates but is not homogenous; lithology is an important reservoir quality control, as well as porosity. Fluid replacement modelling used Doveton’s (2017) PE method to identify lithological proportions of Dolomite, Chert, and Calcite.

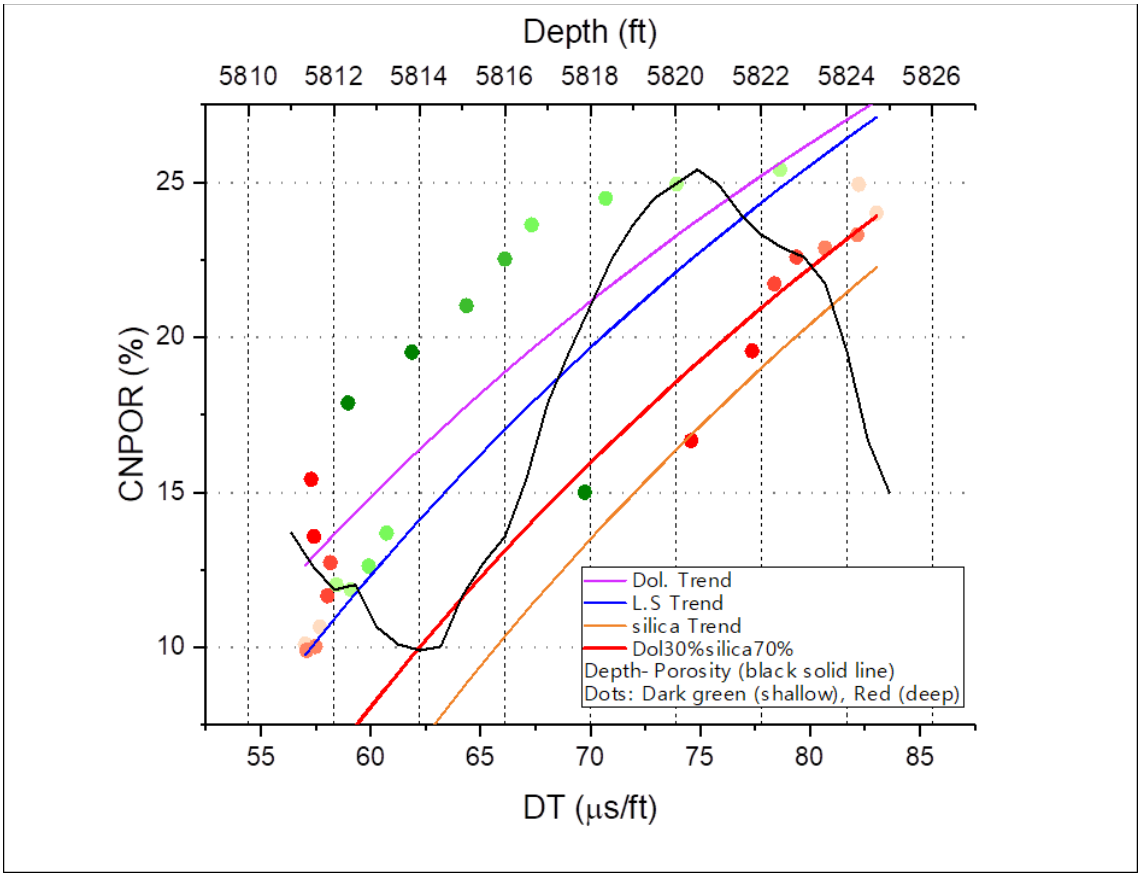

Figure 4-8: Lithology composition cross plot using neutron porosity (CNPOR) and sonic velocity logs to identify lithological trends across the Rich C-7 core. Depth can be interpreted using the color of the points. Dark green is at the shallowest point moving to the lightest green which transitions to a light red and then to the darkest red representing the deepest point interpreted.

Interactive Spreadsheet

For this study an Excel calculator (Figure 4-9) provided by Dr. Abdelmoneam Raef was used for fluid substitution modeling. Inputs include initial fluid type, substituted fluid type, the initially-saturated Vp (calculated using lab-tested Vp), the initially-saturated Vs (calculated using lab-tested Vs), the initial-saturated rock density (lab measure density corrected for brine saturation), initially-saturated bulk modulus (from laboratory measurements), rock skeleton density (from Doveton's 2017 PE method), initial fluid density, initial fluid modulus, substituted fluid density, substituted fluid modulus, and porosity (obtained from Rich C-7 wireline logs). The spreadsheet then calculates for Vp of the dry rock, Vs of the dry rock, elastic moduli of the dry rock, Poisson's ratio of the dry rock, and bulk density of the dry rock. Final values are then outputted in the spreadsheet as Vp, Vs, bulk modulus, bulk density, and Poisson's coefficient of the rock including the substituted fluid.

Constant input values used in this study were only the properties of brine and oil. The remainder of the inputs varied from sample to sample due to measurements being taken at several depths along the Rich C-7 core. Orange highlighted cells are inputs that required user input, while yellow highlighted ones, variables that needed to be selected, such as lithologic type, fluid type, and water saturation (S_w) proportions. Selected depths for this study are 5810 ft, 5815 ft, 5816 ft, 5820 ft, 5821 ft, 5823 ft, and 5824ft. These are various intervals the move systematically from above the productive facies (within the rudstone atop the Viola "B" zone), to the chert-rich productive facies, and then to two facies below targeted production zones, to evaluate various characteristics of the Viola "B" zone and its relationship with pore-fluids.

Lastly, a second page (Figure 4-10) was create within the Gassmann spreadsheet to assist in visualization of data trends as it relates to Vp, Vs, density (Rho), and Poisson's ratio. This was used primarily to increase testing efficiencies of the spreadsheet, since the interactive calculator can only process one sample at a time using inputs of specific S_{w1} and S_{w2} values. Using the add on, S_{w2} results from 0% to 100% could be obtained with a step of 5% fluid change.

SACS: Calculation of the effect of CO2-saturation

INITIAL SITUATION		NEW SITUATION		CONSTANTS			Units
Velocities from a rock with water saturation Sw and hydrocarbon saturation Shc are known		Velocities from the same rock with a new water saturation Sw2 and hydrocarbon saturation Shc2 are determined					
SAT ROCK		SAT ROCK (GASSMAN)					
Vp(Sw)	5314	Vp(Sw2)	5232				m/s
Vs(Sw)	3037	Vs(Sw2)	3046				m/s
RHO(Sw)	2760	RHO(Sw2)	2743				kg/m3
K(Sw)	4.400E+10	K(Sw2)	4.116E+10				Pa
Sw	1.00	Sw2	0.00				
Poisson(Sw)	0.257	Poisson(Sw2)	0.244				
ROCK SKELETON				SANDSTONE	SHALE	OTHER	
Lithology	OTHER			SS	SH	OTHER	
POR	0.0700						
RHOs	2774			2650	2700	2774	kg/m3
COMPs	1.201E-11			2.710E-11	2.530E-11	1.2014E-11	1/Pa
Ko	8.323E+10			3.690E+10	3.953E+10	8.323E+10	Pa
INITIAL HYDROCARBON		NEW HYDROCARBON		WATER	OIL	GAS	
Hydrocarbon	WATER	Hydrocarbon	OIL	water	oil	gas	
Shc	0.00	Shc2	1.00				
RHOhc	1090	RHOhc2	850	1090	850	660	kg/m3
COMPhc	4.200E-10	COMPhc2	6.300E-10	4.200E-10	6.3E-10	1.4286E-08	1/Pa
TOTAL FLUID (water + hc)		TOTAL FLUID 2 (water + hc2)					
COMPfl	4.200E-10	COMPfl2	6.300E-10				1/Pa
Kfl	2.381E+09	Kfl2	1.587E+09				Pa
DRY ROCK (GASSMAN)							
Vp(dry)	5042						m/s
Vs(dry)	3080						m/s
RHO(dry)	2684	**CALCULATION OF VELOCITIES AFTER FLUID SUBSTITUTION**					kg/m3
K(dry)	3.429E+10						Pa
Poisson(dry)	0.202						
		AUTHOR: Rob Arts					

Figure 4-9: Gassmann interactive spreadsheet used in fluid substitution modeling.

Fluid 1	Fluid 2	Sw1	Vp2	Vs2	Rho2	K2	Poisson Copy	Sw2	Poisson
1	0	0	5314	3037	2760	4.400E+10	0.26	1	0.257
0.95	0.05	0.05	5308	3037	2759	4.380E+10	0.26	0.95	0.257
0.9	0.1	0.1	5302	3038	2758	4.361E+10	0.26	0.9	0.256
0.85	0.15	0.15	5297	3038	2757	4.343E+10	0.25	0.85	0.255
0.8	0.2	0.2	5292	3039	2757	4.326E+10	0.25	0.8	0.254
0.75	0.25	0.25	5287	3039	2756	4.309E+10	0.25	0.75	0.253
0.7	0.3	0.3	5282	3040	2755	4.293E+10	0.25	0.7	0.252
0.65	0.35	0.35	5278	3040	2754	4.277E+10	0.25	0.65	0.252
0.6	0.4	0.4	5273	3041	2753	4.262E+10	0.25	0.6	0.251
0.55	0.45	0.45	5269	3041	2752	4.248E+10	0.25	0.55	0.250
0.5	0.5	0.5	5265	3042	2752	4.234E+10	0.25	0.5	0.250
0.45	0.55	0.55	5261	3042	2751	4.220E+10	0.25	0.45	0.249
0.4	0.6	0.6	5258	3043	2750	4.207E+10	0.25	0.4	0.248
0.35	0.65	0.65	5254	3043	2749	4.194E+10	0.25	0.35	0.248
0.3	0.7	0.7	5251	3043	2748	4.182E+10	0.25	0.3	0.247
0.25	0.75	0.75	5247	3044	2747	4.170E+10	0.25	0.25	0.246
0.2	0.8	0.8	5244	3044	2747	4.159E+10	0.25	0.2	0.246
0.15	0.85	0.85	5241	3045	2746	4.148E+10	0.25	0.15	0.245
0.1	0.9	0.9	5238	3045	2745	4.137E+10	0.24	0.1	0.245
0.05	0.95	0.95	5235	3046	2744	4.126E+10	0.24	0.05	0.244
0	1	1	5232	3046	2743	4.116E+10	0.24	0	0.244

Figure 4-10: Solutions worksheet within the Gassmann workbook for fluid substitution modeling.

Chapter 5 - Results & Discussion

5.1 Dry Core Physical and Ultrasonic Measurements.

Table 5-1 shows these measurements for the interval tested within the core.

Core Depth(ft)	Height (mm)	Weight (g)	volume core (cm^3)	density core (g/cm^3)
5808	124	1708.9	603.81	2.83
5809	108	1264.7	466.53	2.71
5810	186	2092.9	803.46	2.60
5815	207	1787.1	894.18	2.00
5816	168	1318.1	725.71	1.82
5820	194	2082.1	975.15	2.14
5821	90	1097.8	494.80	2.22
5823	63	1089.4	366.15	2.98
5824	115	1826.9	623.21	2.93
5825	115	1585	569.02	2.79
5826	152	2100	799.85	2.63
5829	115	1633.3	587.09	2.78
5831	94	1302.1	465.11	2.80
5832	112	1477.7	545.38	2.71
5836	98	1323.9	469.51	2.82
5837	100	1403.5	502.65	2.79
5838	142	2095.6	747.23	2.80
5839	135	1836	678.58	2.71
5842	108	1521	542.87	2.80
5844	79	1008.1	378.48	2.66
5845	83	1082.2	410.68	2.64
5846	139	1797.6	687.77	2.61
5848	102	1261.5	488.67	2.58
5850	71	884.6	356.88	2.48
5853	99	1224.9	497.63	2.46
5856	125	1572.2	608.68	2.58

Table 5-1: Rich C-7 core physical lab measurements and density calculations.

The core was categorized into four specific lithological zones based on Hagood (2019). 5808ft – 5810ft is considered rudstone, 5811ft – 5821ft is a cherty dolomite, 5822ft – 5839ft is labeled the intermediate zone (unconsolidated breccia), and 5840ft – 5856ft is considered Muddy Dolomite. These sections will be named as such throughout this chapter. The Tested Interval (TI) identifies the zone of the core for which Gassmann's fluid replacement modeling was conducted.

Twenty-six points along the core were selected for ultrasonic velocity testing. These points were selected based on viability of node placement and structural integrity of each core. For sample consistency and to prevent estimation liberties, each sample's 10,000 pound force P-wave and S-wave velocities were used in this study. Table 5-2 identifies the in-situ pressure needed at each sample and equation 13 describes how those values were calculated.

Equation 13: Overburden Pressure Calculation

$$\boldsymbol{Lbs\ of\ Force = 3.14 \times 1.025^2 \times Depth\ (ft)}$$

The value of 3.14 is Π since the area of a circle is first being calculated; 1.025^2 is the radius of our core samples if they were to be full core samples in inches. Depth is used because the geostatic gradient of crustal rock is on average 1 PSI per foot. Therefore depth is used in place for PSI when calculating in situ pressure (Table 5-2). Equation 13 is derived from the equation of pressure being $\boldsymbol{Pressure = \frac{Force}{Area}}$. Where force is lbs force calculated by equation 13.

Depth (ft)	In-Situ Lbf
5808	19160.37

5809	19163.67
5810	19166.97
5815	19183.47
5816	19186.77
5819	19196.66
5820	19199.96
5821	19203.26
5823	19209.86
5824	19213.16
5825	19216.46
5826	19219.76
5827	19223.05
5828	19226.35
5829	19229.65
5830	19232.95
5831	19236.25
5832	19239.55
5835	19249.45
5836	19252.75
5837	19256.04
5838	19259.34
5839	19262.64
5842	19272.54
5843	19275.84
5844	19279.14
5845	19282.44
5846	19285.73
5847	19289.03
5848	19292.33
5849	19295.63
5850	19298.93
5853	19308.83
5856	19318.72

Table 5-2: In-Situ pounds per force (Lbf) throughout core.

Table 5-3 lists the ultrasonic P-wave and S-wave velocities, density, acoustic impedance, and Poisson's Coefficient for the Rudstone interval. These values are used in future sections of this chapter. Figures (5-1to 5-3) identify the first arrival times of P and S waves for this interval when using the ULT-100 System. The arrows identify the first arrival time at 10,000 lbs. of force. In each figure, the Y-axis represents Energy in voltage and the X-Axis represents time in microseconds.

Core Depth(ft)	Density core (g/cm)	P-wave Core (m/s)	P-wave (km/s)	S-wave Core (m/s)	S-wave (km/s)	Core Impedance [(g/cc)*(km/s)]	Poisson's Core
5808	2.83	4351	4.35	2444	2.44	12.31	0.27
5809	2.71	4451	4.45	2612	2.61	12.07	0.24
5810	2.60	5562	5.56	3389	3.39	14.49	0.20

Table 5-3: Rudstone ultrasonic parameters and measurements.

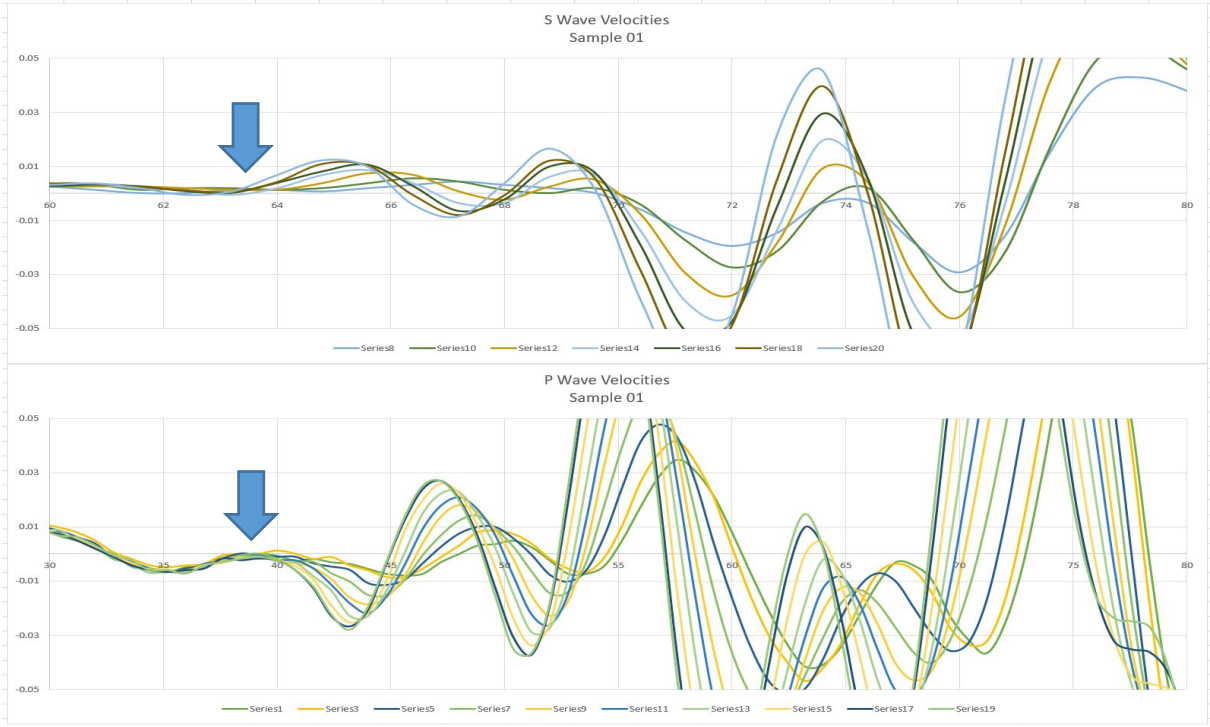

Figure 5-1: 5808ft sample P-wave and S-wave waveforms stacked from 1,000 lbs. - 10,000 lbs. of force taken at a frequency of 1.25 MHz.

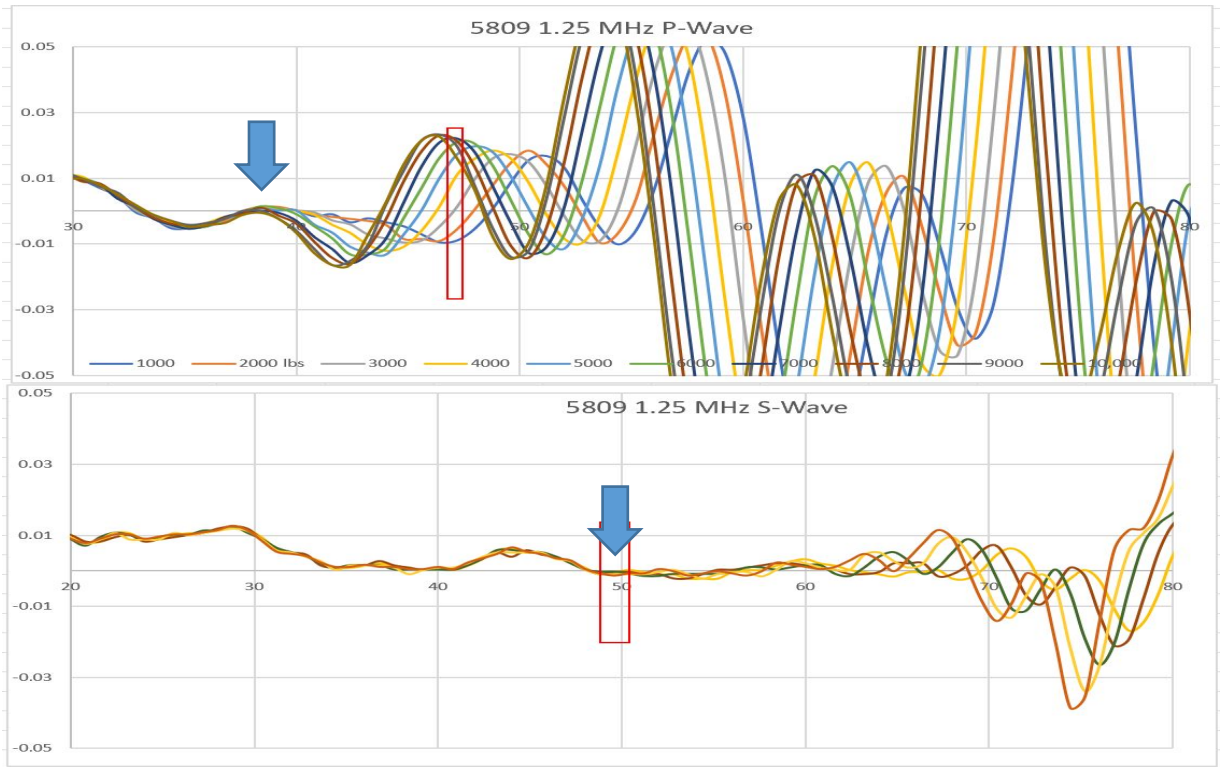

Figure 5-2: 5809ft sample P-wave and S-wave waveforms stacked from 1,000 lbs. - 10,000 lbs. of force taken at a frequency of 1.25 MHz.

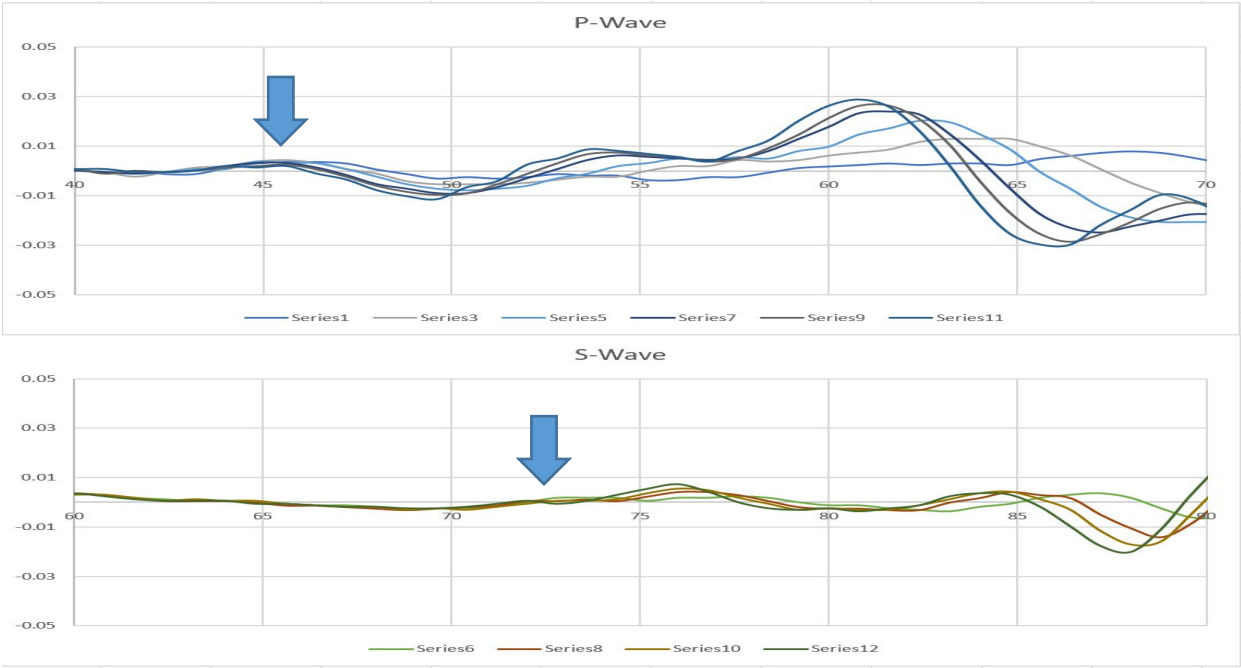

Figure 5-3: 5810ft sample P-wave and S-wave waveforms stacked from 1,000 lbs. - 10,000 lbs. of force taken at a frequency of 1.25 MHz.

Table 5-4 lists the ultrasonic P-wave and S-wave velocities, density, acoustic impedance, and Poisson's coefficient for the cherty dolomite interval. These values will be used in future sections of this chapter. Figure (5-4 to 5-7) identify the first arrival times of the P and S waves for this interval when using the ULT-100 system. The arrows identify the first arrival time at 10,000 lbs of force. In each figure, the Y-axis represents Energy in voltage and the X-axis represents time in microseconds.

Core Depth (ft)	Density core (g/cm^3)	P-wave core (m/s)	P-wave (km/s)	S-wave core (m/s)	S-wave (km/s)	Core Impedance [(g/cc)*(km/s)]	Poisson's Core
5815	2.00	3316	3.32	1886	1.89	6.63	0.26
5816	1.82	3050	3.05	1649	1.65	5.54	0.29
5820	2.14	2931	2.93	1527	1.53	6.26	0.31
5821	2.22	4119	4.12	2257	2.26	9.14	0.29

Table 5-4: Cherty dolomite ultrasonic parameters and measurements.

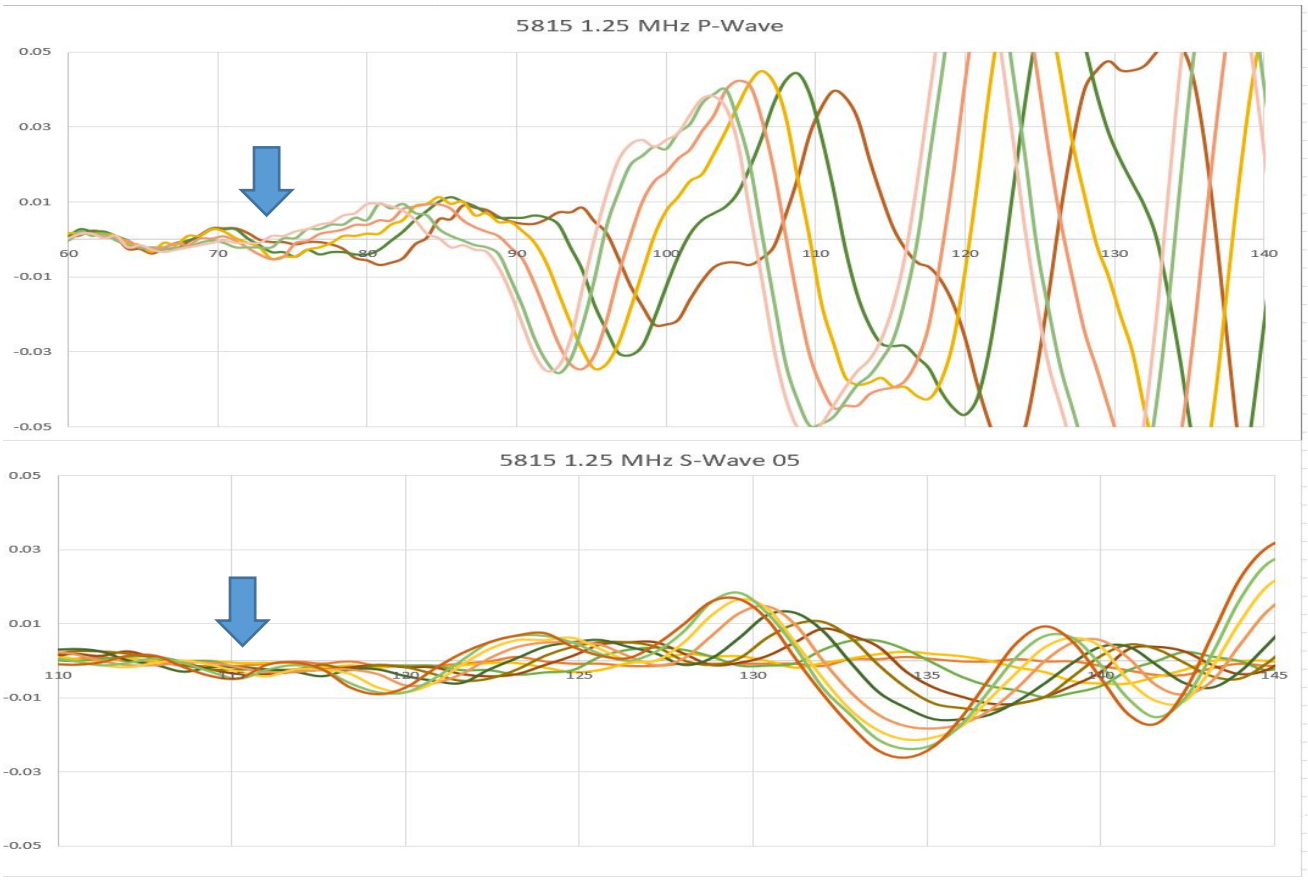

Figure 5-4: 5815ft sample P-wave and S-wave waveforms stacked from 1,000 lbs. - 10,000 lbs. of force taken at a frequency of 1.25 MHz.

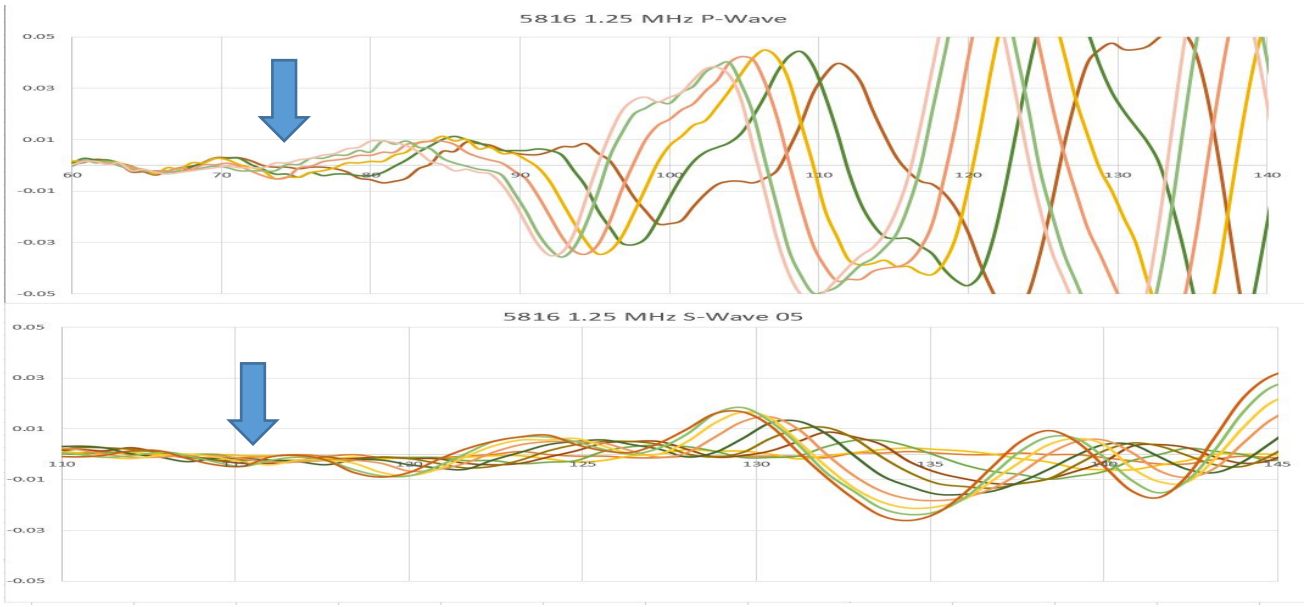

Figure 5-5: 5816ft sample P-wave and S-wave waveforms stacked from 1,000 lbs. - 10,000 lbs. of force taken at a frequency of 1.25 MHz.

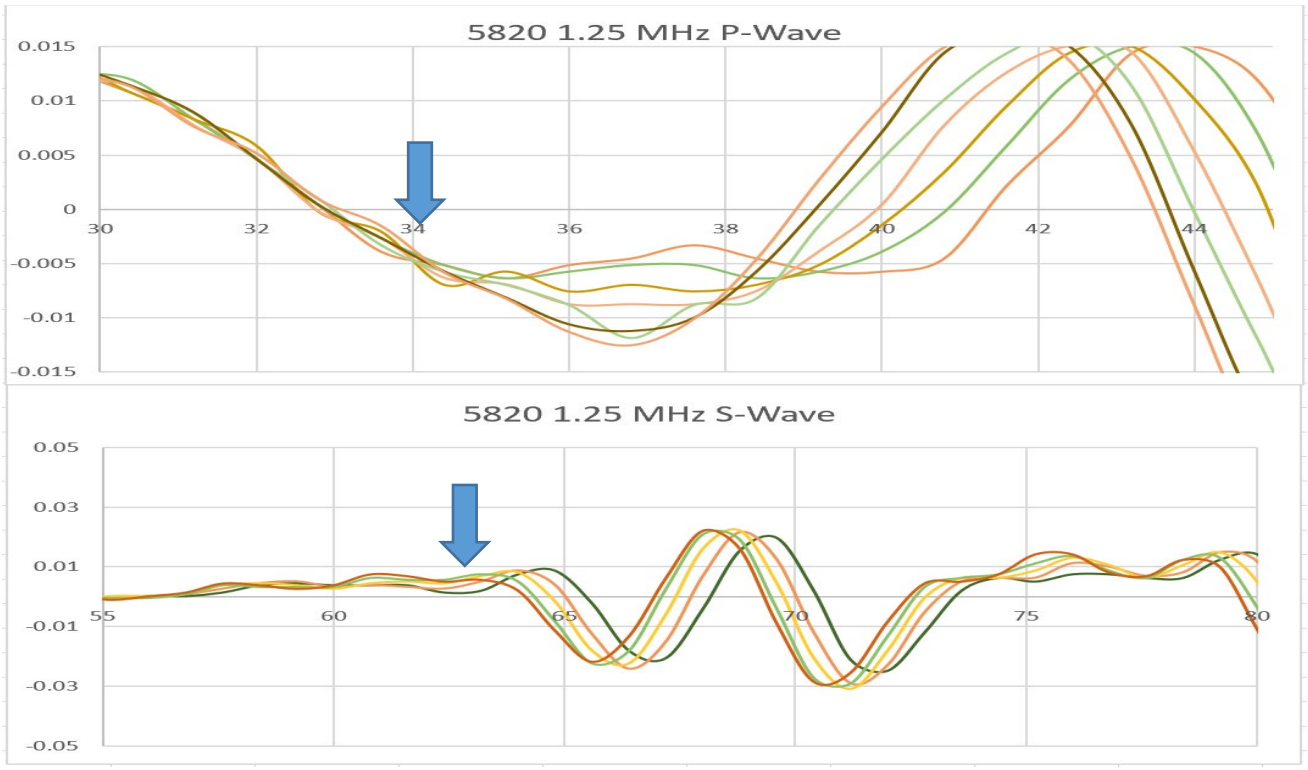

Figure 5-6: 5820ft sample P-wave and S-wave waveforms stacked from 1,000 lbs. - 10,000 lbs. of force taken at a frequency of 1.25 MHz.

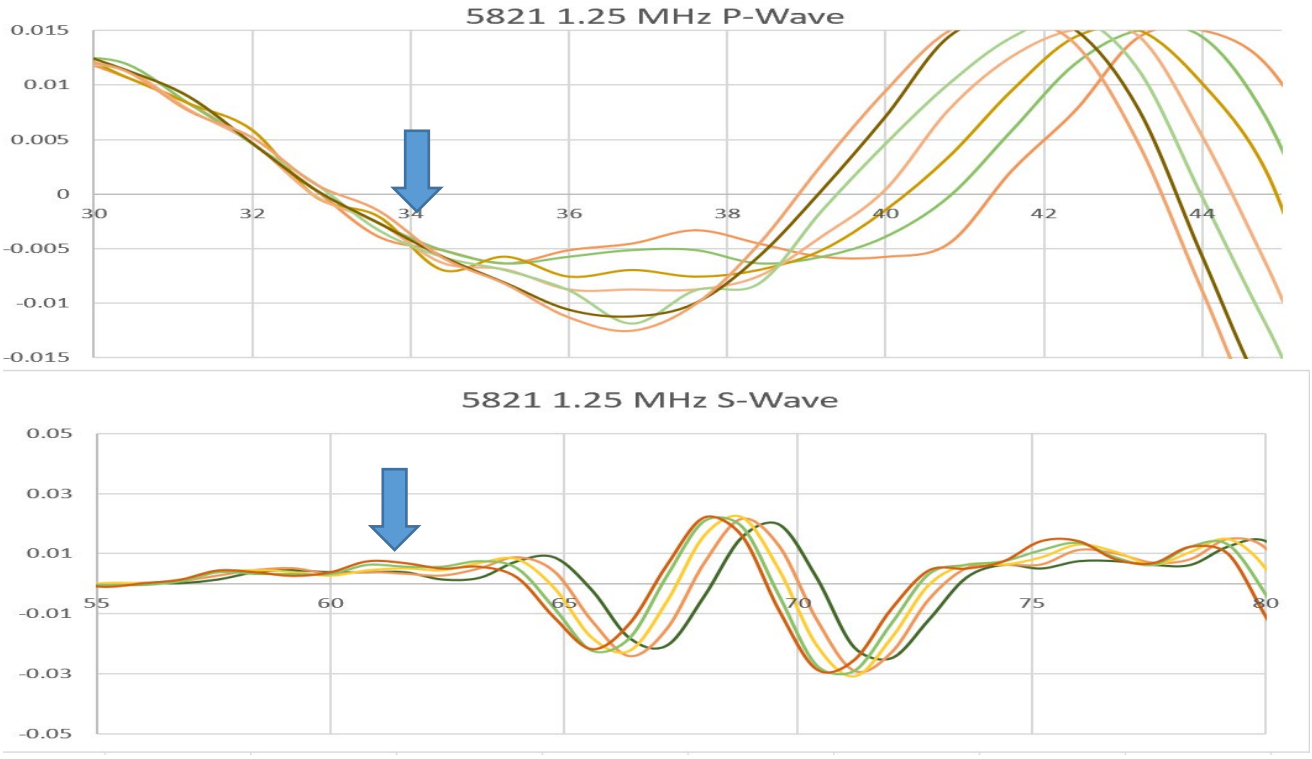

Figure 5-7: 5821ft sample P-wave and S-wave waveforms stacked from 1,000 lbs. - 10,000 lbs. of force taken at a frequency of 1.25 MHz.

Table 5-5 lists the ultrasonic P-wave and S-wave velocities, density, acoustic impedance, and Poisson's coefficient for the Intermediate interval. These values will be used in future sections of this chapter. Figures (5-8 to 5-18) identify the first arrival times of P and S waves for the interval when using the ULT-100 system. The arrows identify the first arrival times at 10,000 lbs of force. In each figure, the Y-axis represents Energy in voltage and the X-axis represents time in microseconds.

Depth (ft)	P-wave (m/s)	P-wave (km/s)	S-wave (m/s)	S-wave (km/s)	Density (g/cm^3)	Acoustic Impedance	Poisson's Coefficient
5823	5022	5.02	3217	3.22	2.98	14.94	0.15
5824	4878	4.88	3100	3.10	2.93	14.30	0.16
5825	4957	4.96	3449	3.45	2.79	13.81	0.03
5826	4890	4.89	2998	3.00	2.63	12.84	0.20
5829	5017	5.02	3062	3.06	2.78	13.96	0.20
5831	5164	5.16	2422	2.42	2.80	14.46	0.36
5832	4725	4.73	3004	3.00	2.71	12.80	0.16
5836	4969	4.97	2971	2.97	2.82	14.01	0.22
5837	4708	4.71	2854	2.85	2.79	13.15	0.21
5838	4265	4.27	2701	2.70	2.80	11.96	0.17
5839	4366	4.37	2914	2.91	2.71	11.81	0.10

Table 5-5: Lab and Ultrasonic Measurements of the Intermediate interval.

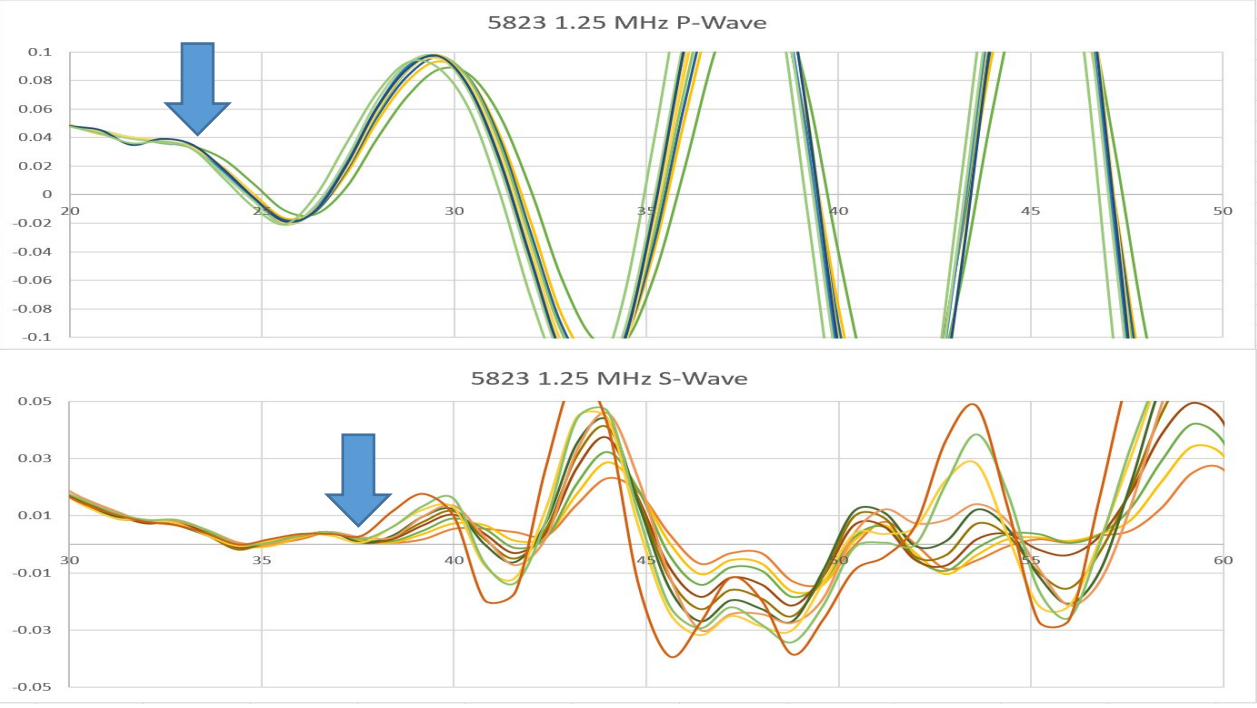

Figure 5-8: 5823ft sample P-wave and S-wave waveforms stacked from 1,000 lbs. - 10,000 lbs. of force taken at a frequency of 1.25 MHz.

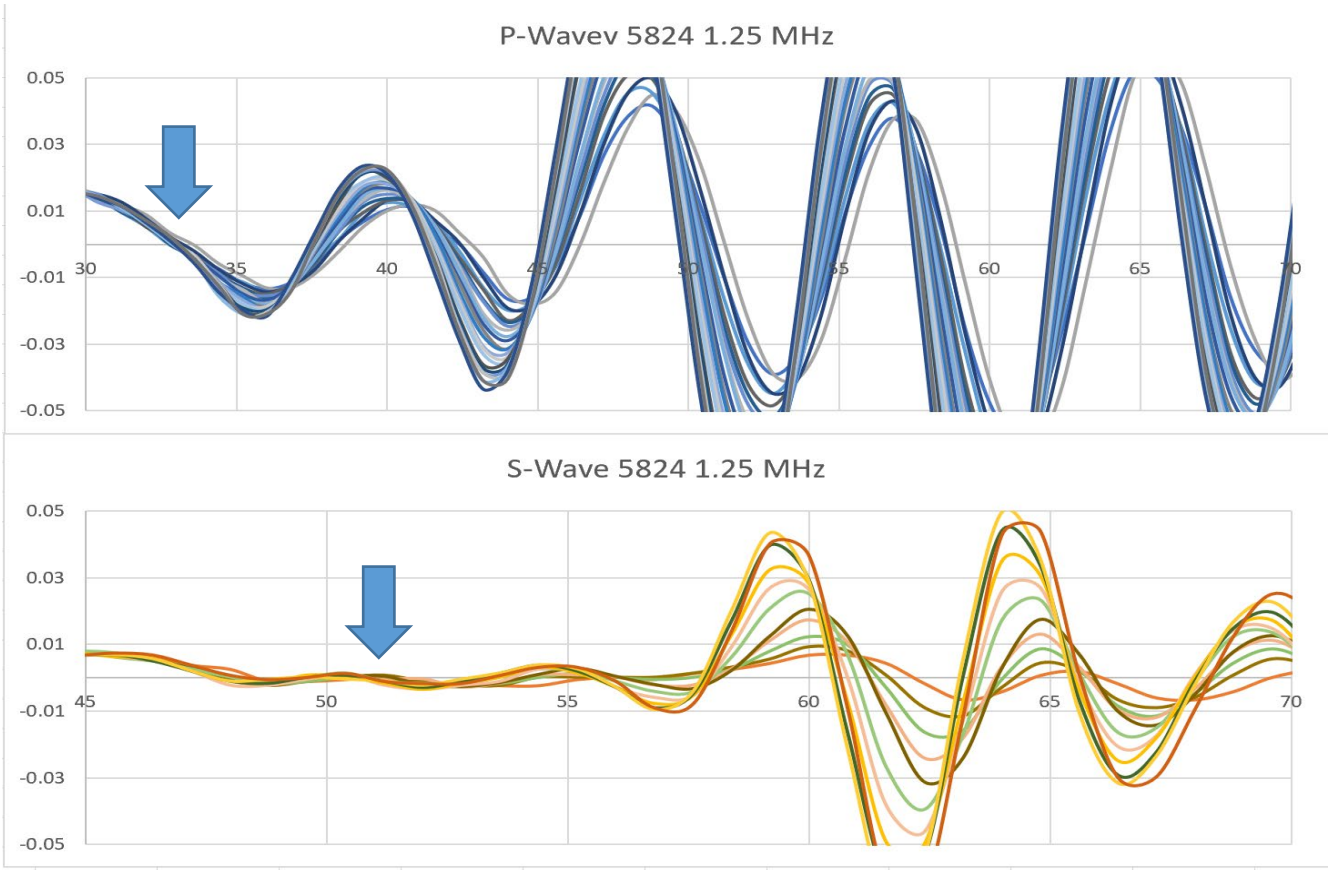

Figure 5-9: 5824ft sample P-wave and S-wave waveforms stacked from 1,000 lbs. - 10,000 lbs. of force taken at a frequency of 1.25 MHz.

.

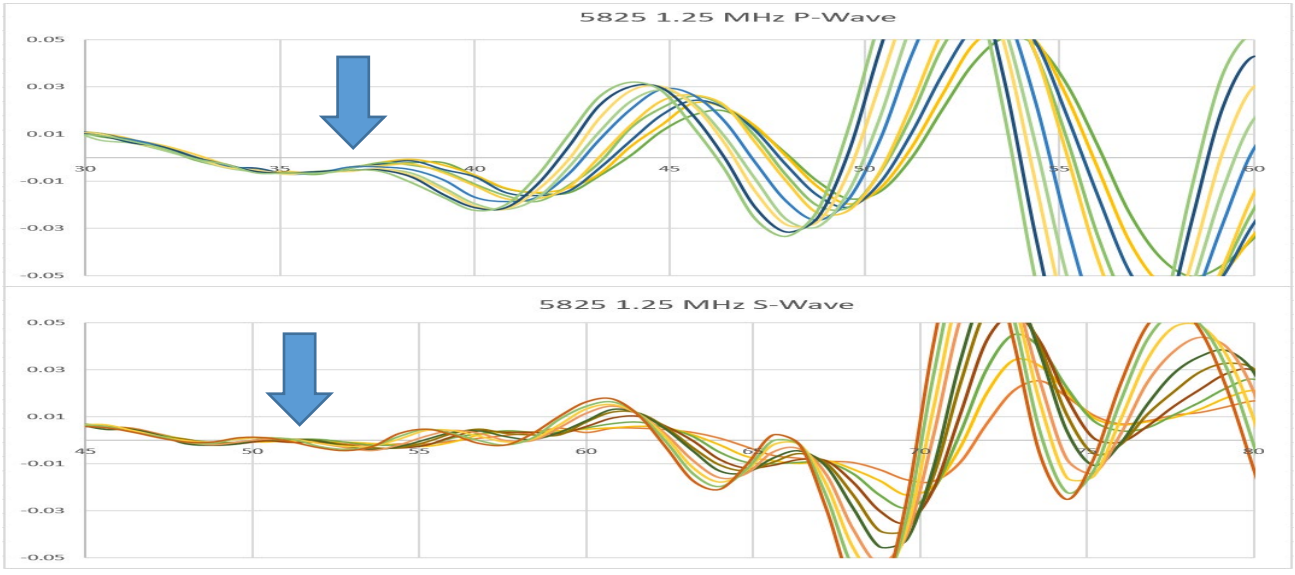

Figure 5-10: 5825ft sample P-wave and S-wave waveforms stacked from 1,000 lbs. - 10,000 lbs. of force taken at a frequency of 1.25 MHz.

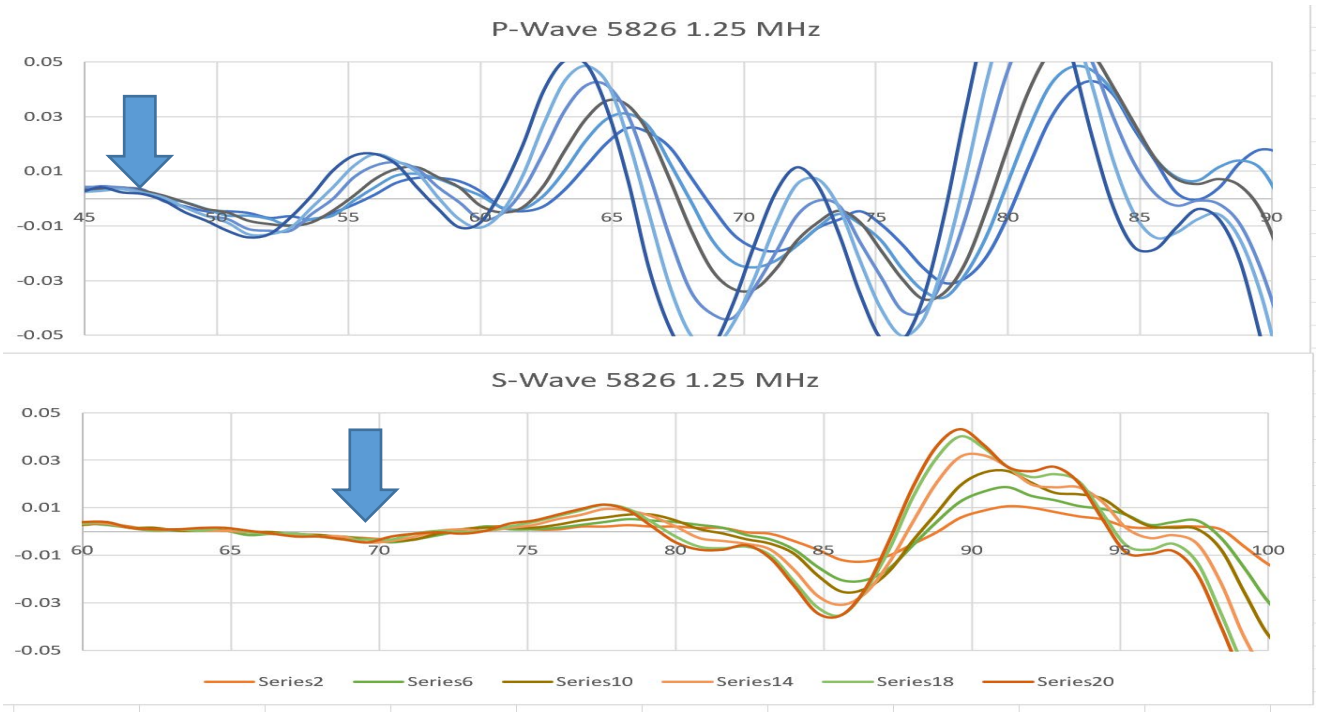

Figure 5-11: 5826ft sample P-wave and S-wave waveforms stacked from 1,000 lbs. - 10,000 lbs. of force taken at a frequency of 1.25 MHz.

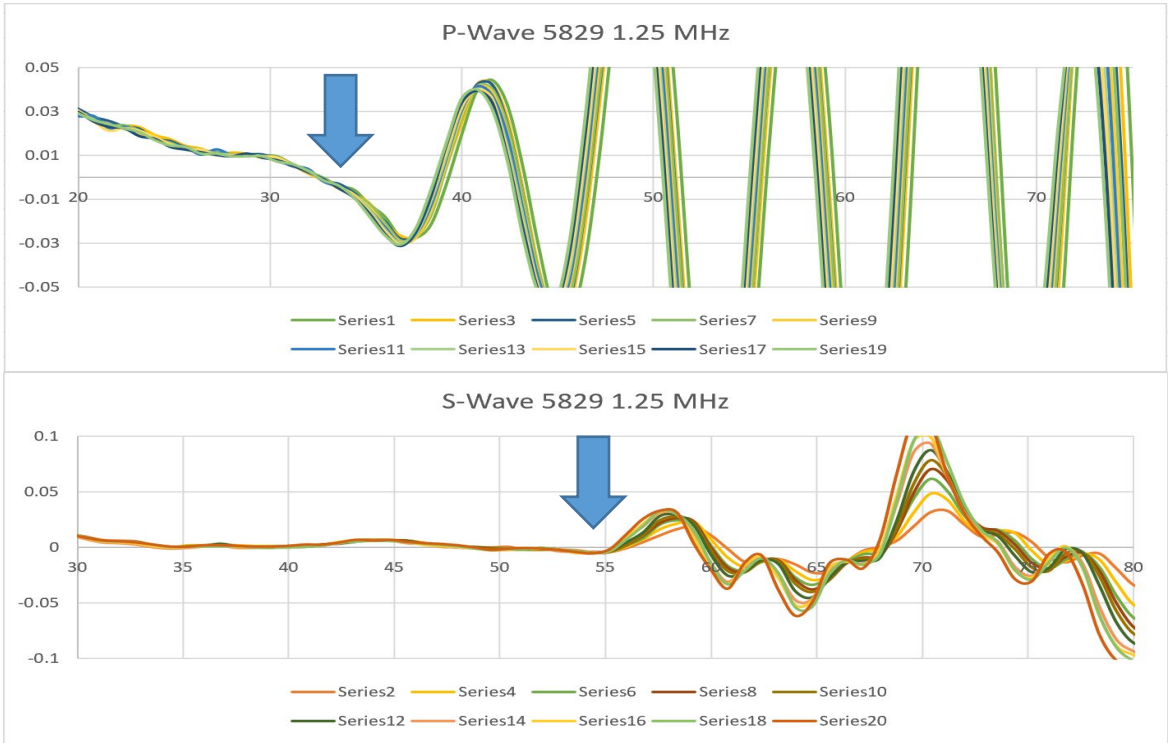

Figure 5-12: 5829ft sample P-wave and S-wave waveforms stacked from 1,000 lbs. - 10,000 lbs. of force taken at a frequency of 1.25 MHz.

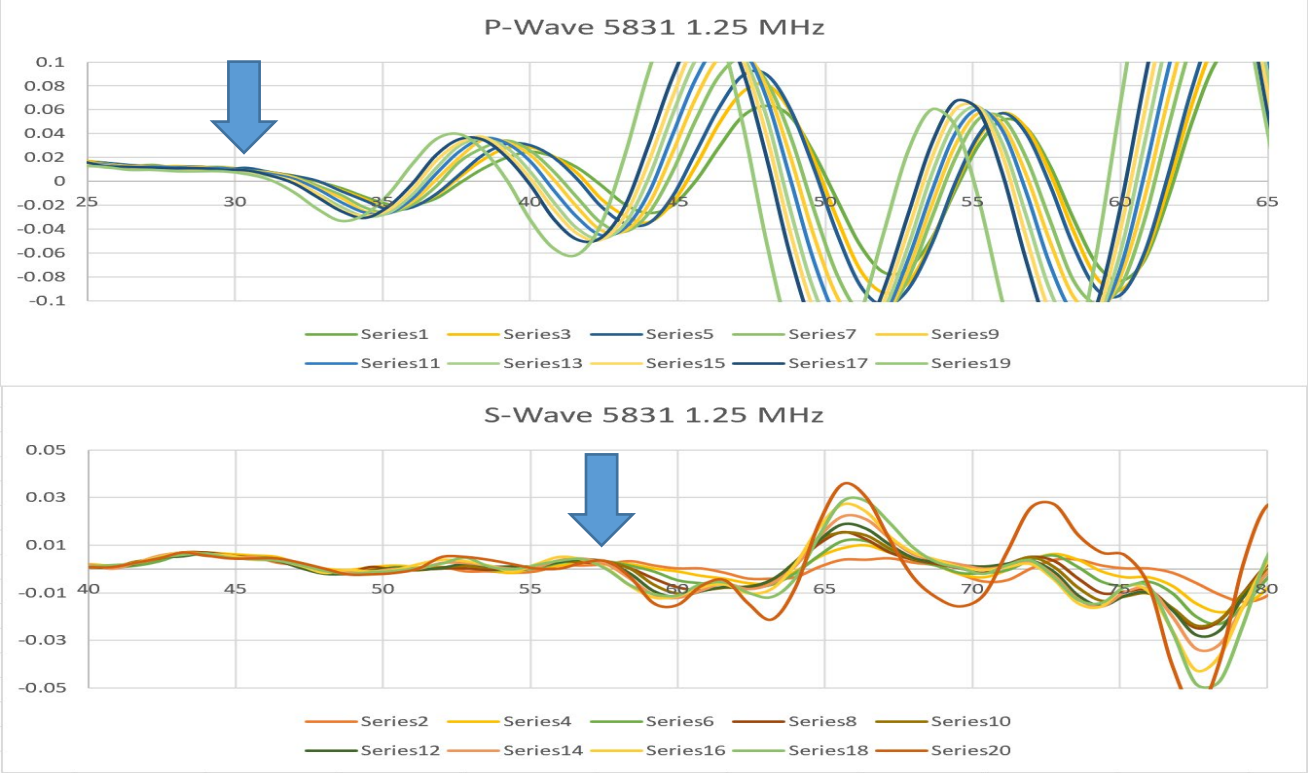

Figure 5-13: 5831ft sample P-wave and S-wave waveforms stacked from 1,000 lbs. - 10,000 lbs. of force taken at a frequency of 1.25 MHz.

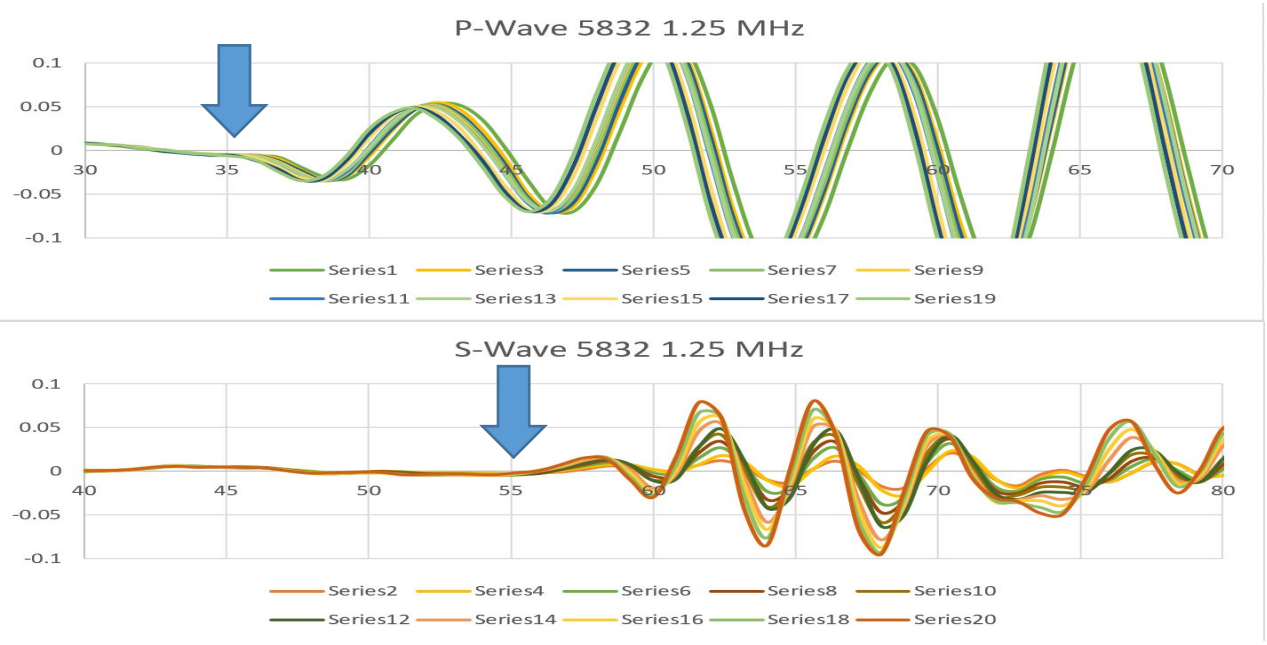

Figure 5-14: 5832ft sample P-wave and S-wave waveforms stacked from 1,000 lbs. - 10,000 lbs. of force taken at a frequency of 1.25 MHz.

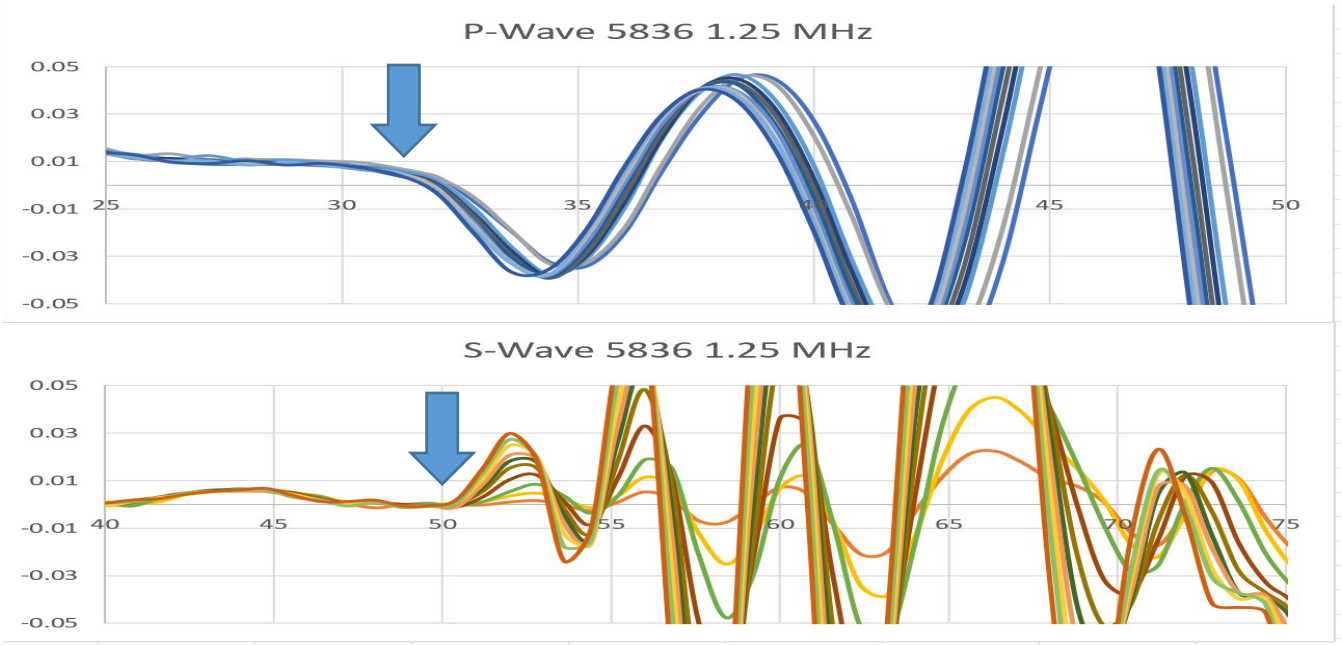

Figure 5-15: 5836ft sample P-wave and S-wave waveforms stacked from 1,000 lbs. - 10,000 lbs. of force taken at a frequency of 1.25 MHz.

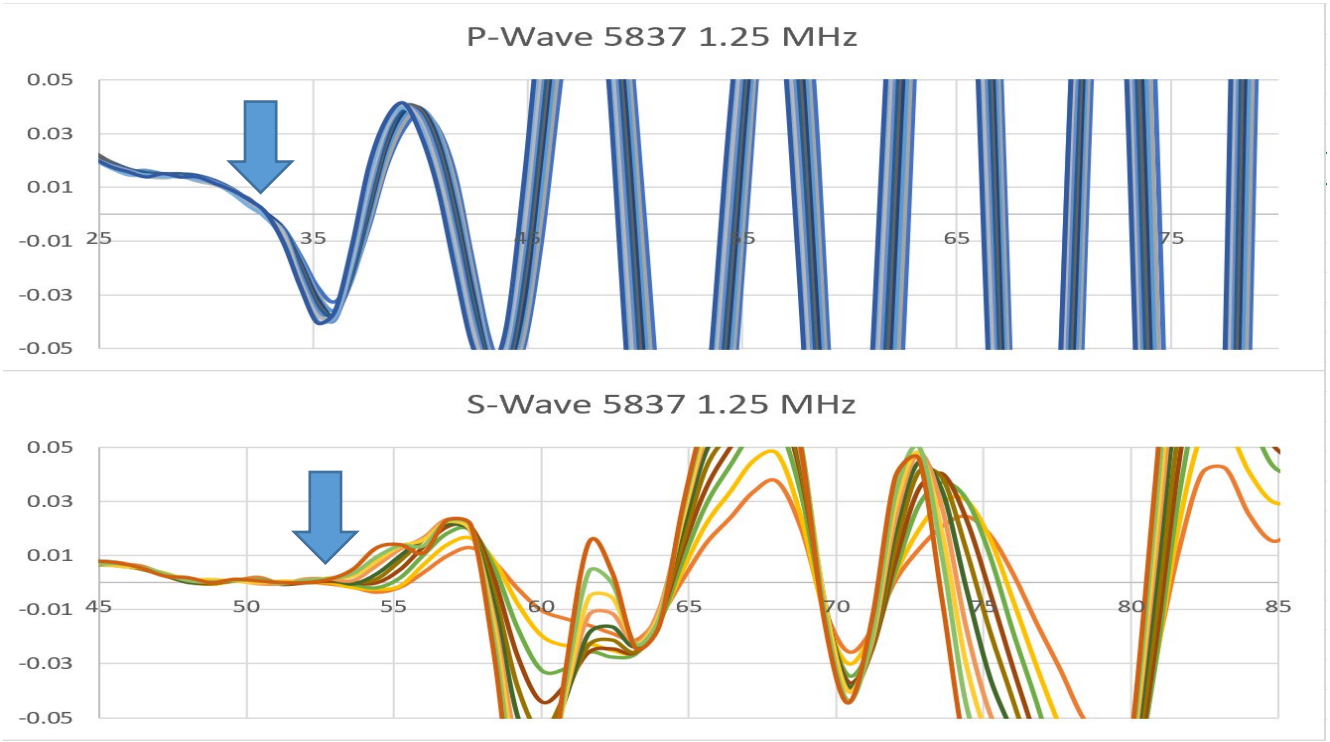

Figure 5-16: 5837ft sample P-wave and S-wave waveforms stacked from 1,000 lbs. - 10,000 lbs. of force taken at a frequency of 1.25 MHz.

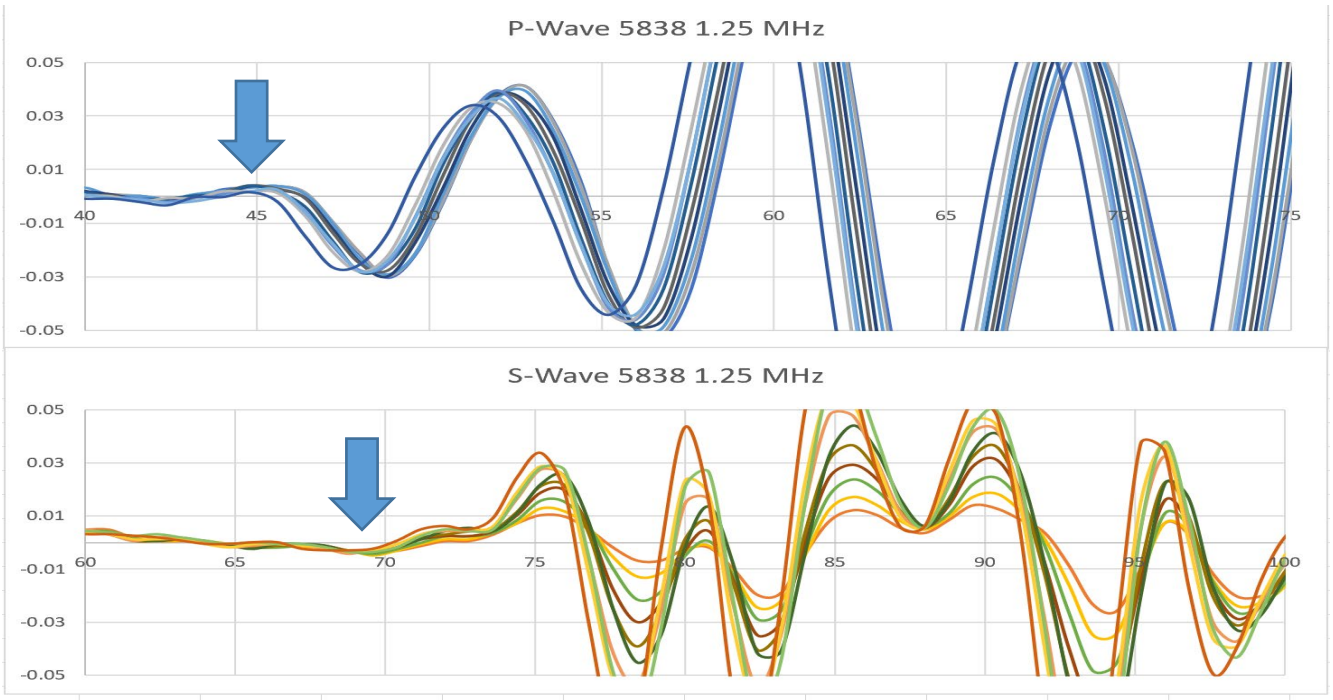

Figure 5-17: 5838ft sample P-wave and S-wave waveforms stacked from 1,000 lbs. - 10,000 lbs. of force taken at a frequency of 1.25 MHz.

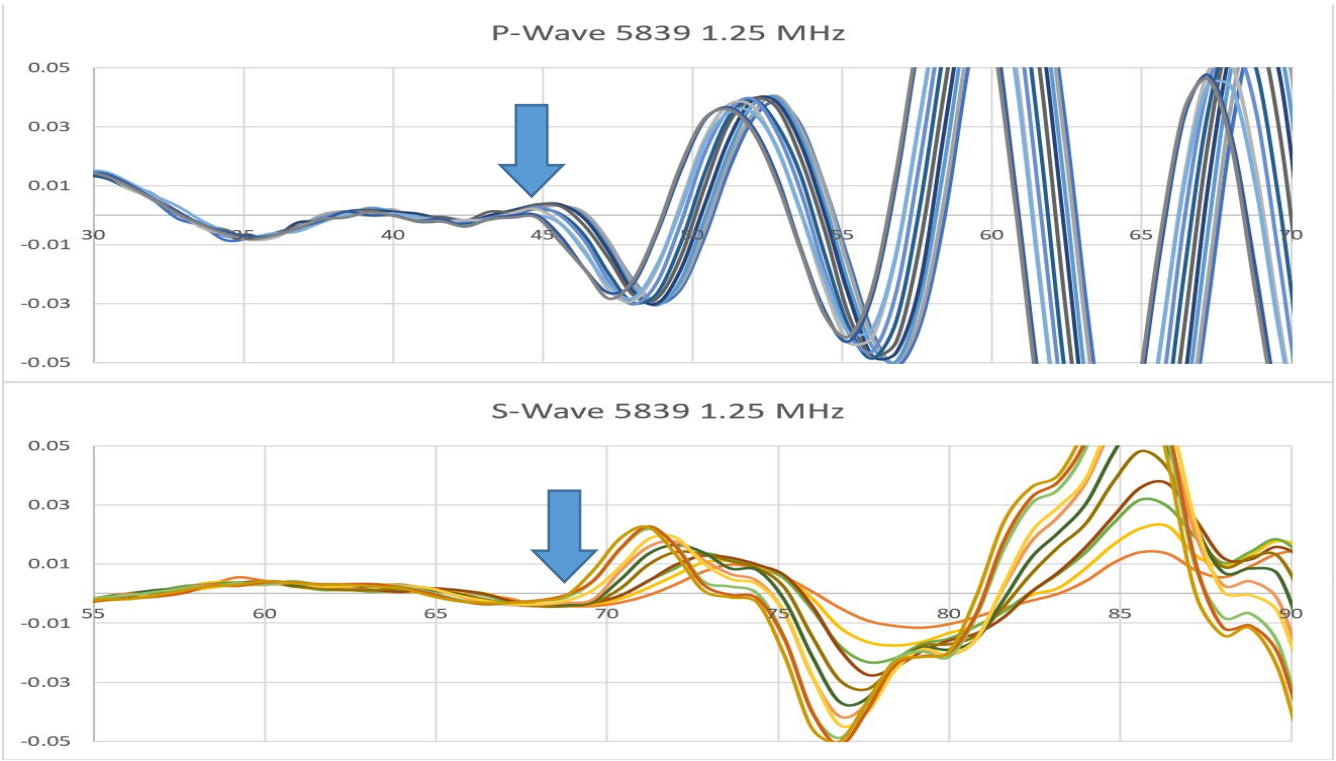

Figure 5-18: 5839ft sample P-wave and S-wave waveforms stacked from 1,000 lbs. - 10,000 lbs. of force taken at a frequency of 1.25 MHz.

Table 5-6 lists the ultrasonic velocities of P- and S- Waves, , Density, Acoustic Impedance, and Poisson's Coefficient for the Muddy Dolomite interval. These values will be used in future sections of this chapter. Figures (5-19 to 5-26) identify the first arrival times of P and S waves for this interval when using the ULT-100 system. The arrows identify the first arrival time at 10,000 lbs of force. In each figure, the Y-axis represents Energy in voltage and the X-axis represents time in microseconds.

Depth (ft)	P-wave (m/s)	P-wave (km/s)	S-wave (m/s)	S-wave (km/s)	Density (g/cm^3)	Acoustic Impedance	Poisson's Coefficiant
5842	4683	4.68	2721	2.72	2.80	13.12	0.25
5844	4635	4.64	2727	2.73	2.66	12.35	0.24
5845	4589	4.59	2918	2.92	2.64	12.09	0.16
5846	4066	4.07	2655	2.66	2.61	10.63	0.13
5848	4338	4.34	2749	2.75	2.58	11.20	0.16
5850	4186	4.19	2353	2.35	2.48	10.38	0.27
5853	3779	3.78	2423	2.42	2.46	9.30	0.15
5856	4056	4.06	2280	2.28	2.58	10.48	0.27

Table 5-6: Lab and Ultrasonic Measurements of the Muddy Dolomite interval.

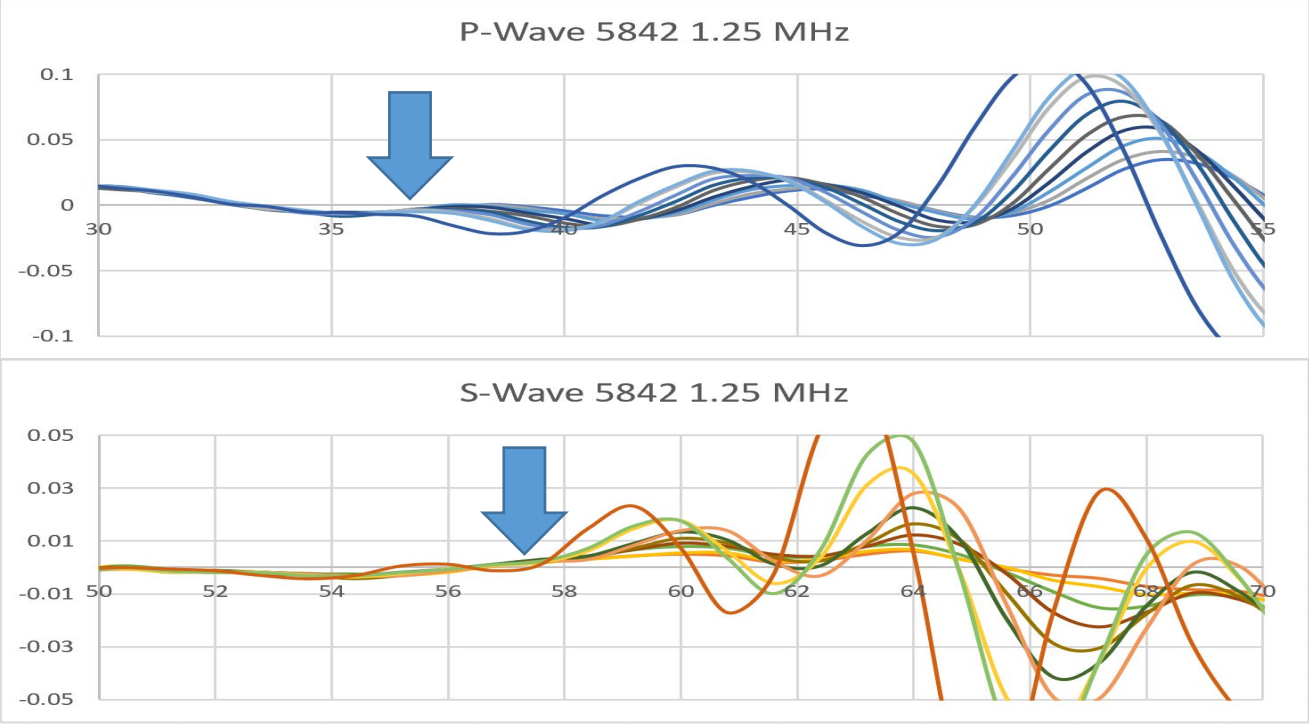

Figure 5-19: 5842ft sample P-wave and S-wave waveforms stacked from 1,000 lbs. - 10,000 lbs. of force taken at a frequency of 1.25 MHz.

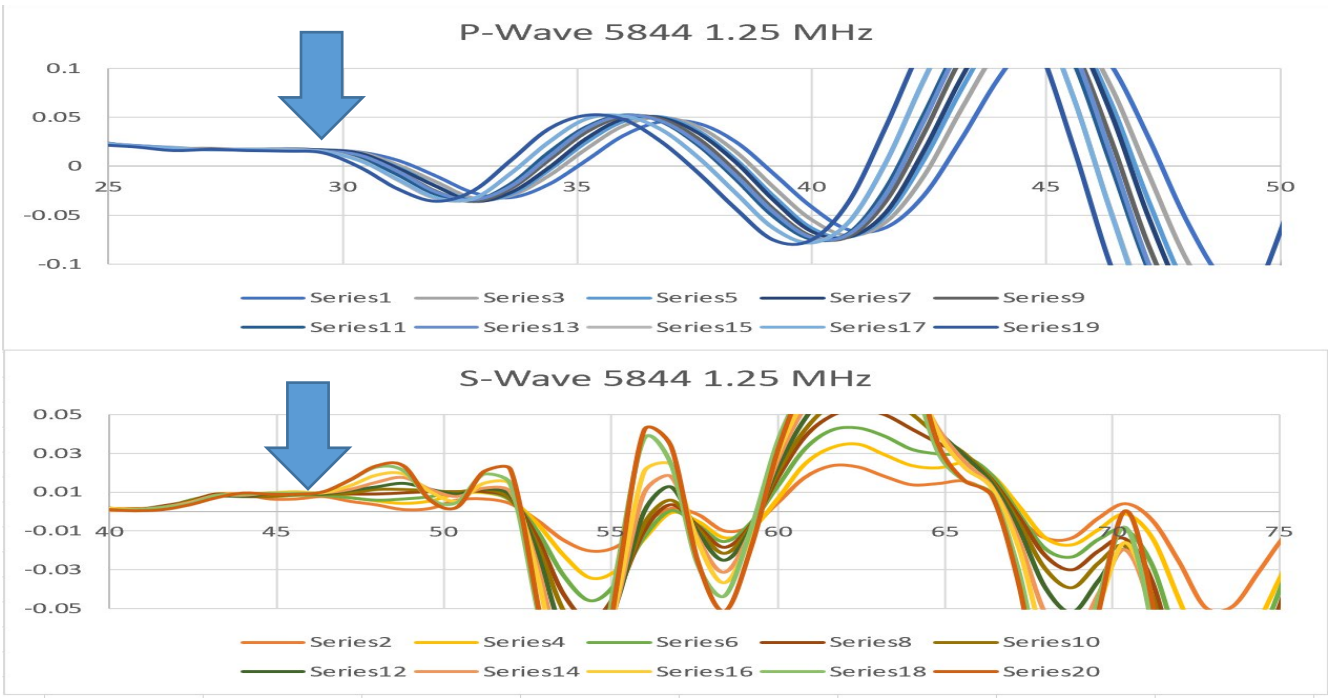

Figure 5-20: 5844ft sample P-wave and S-wave waveforms stacked from 1,000 lbs. - 10,000 lbs. of force taken at a frequency of 1.25 MHz.

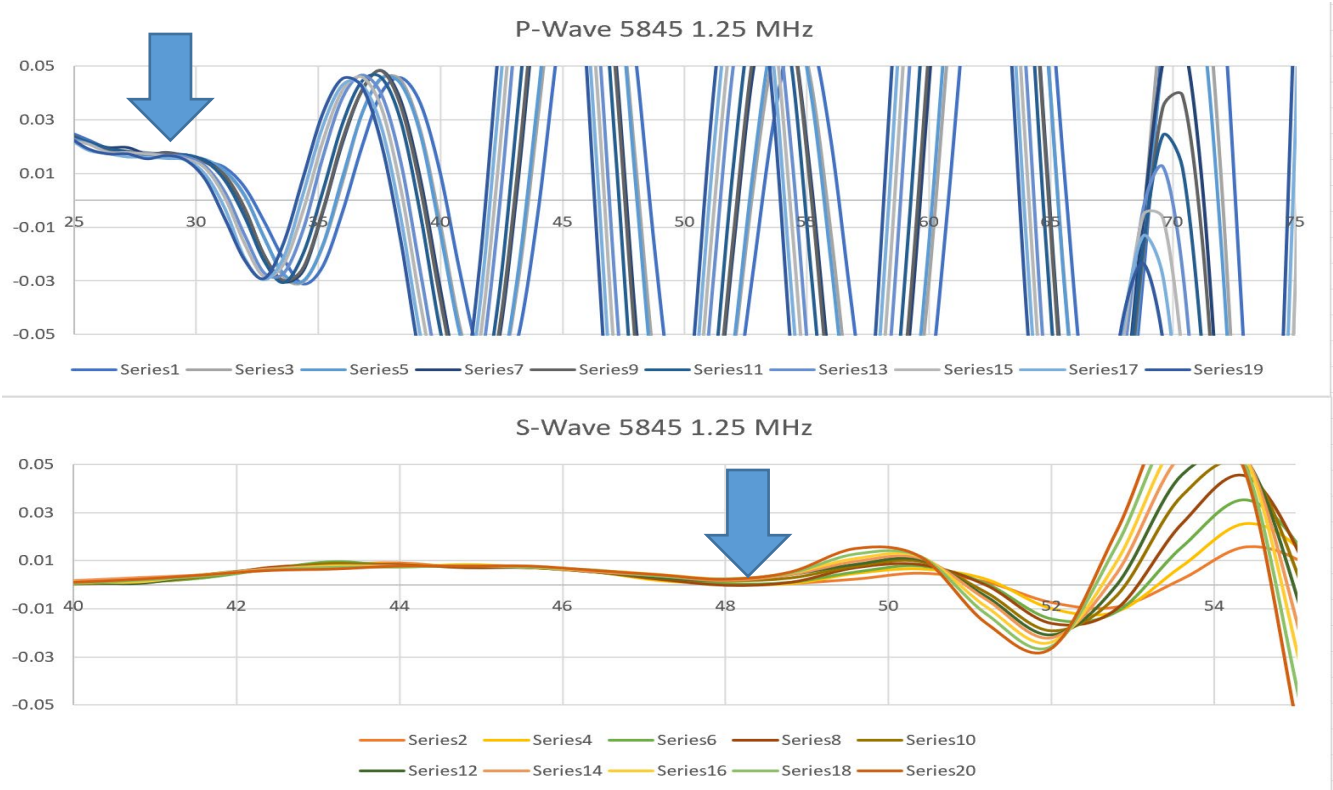

Figure 5-21: 5845ft sample P-wave and S-wave waveforms stacked from 1,000 lbs. - 10,000 lbs. of force taken at a frequency of 1.25 MHz.

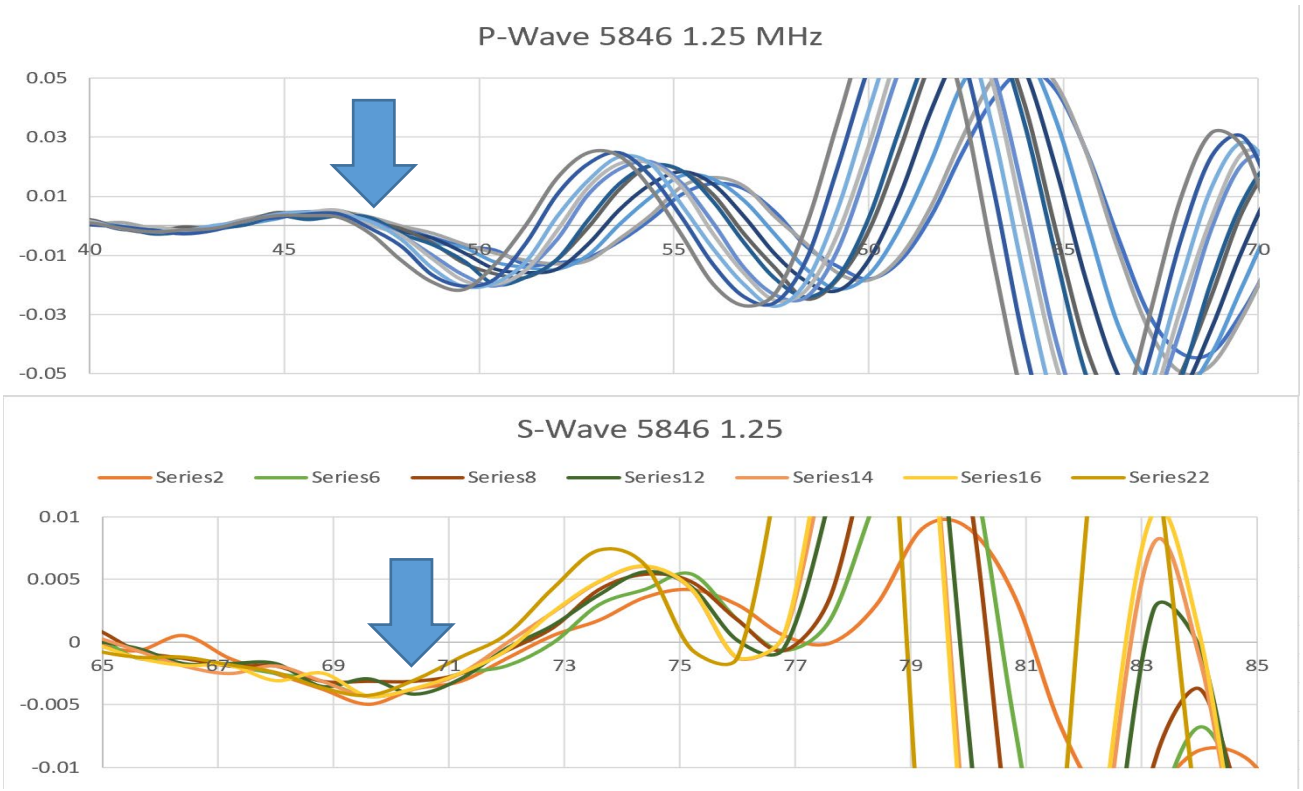

Figure 5-22: 5846ft sample P-wave and S-wave waveforms stacked from 1,000 lbs. - 10,000 lbs. of force taken at a frequency of 1.25 MHz.

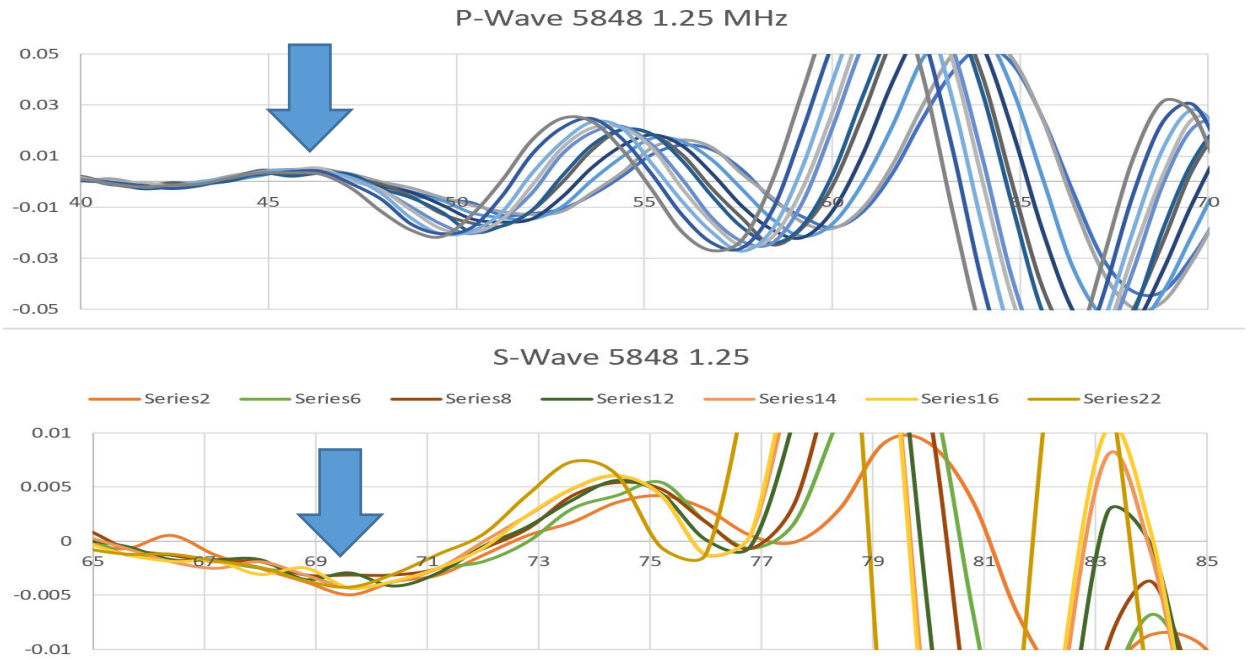

Figure 5-23: 5848ft sample P-wave and S-wave waveforms stacked from 1,000 lbs. - 10,000 lbs. of force taken at a frequency of 1.25 MHz.

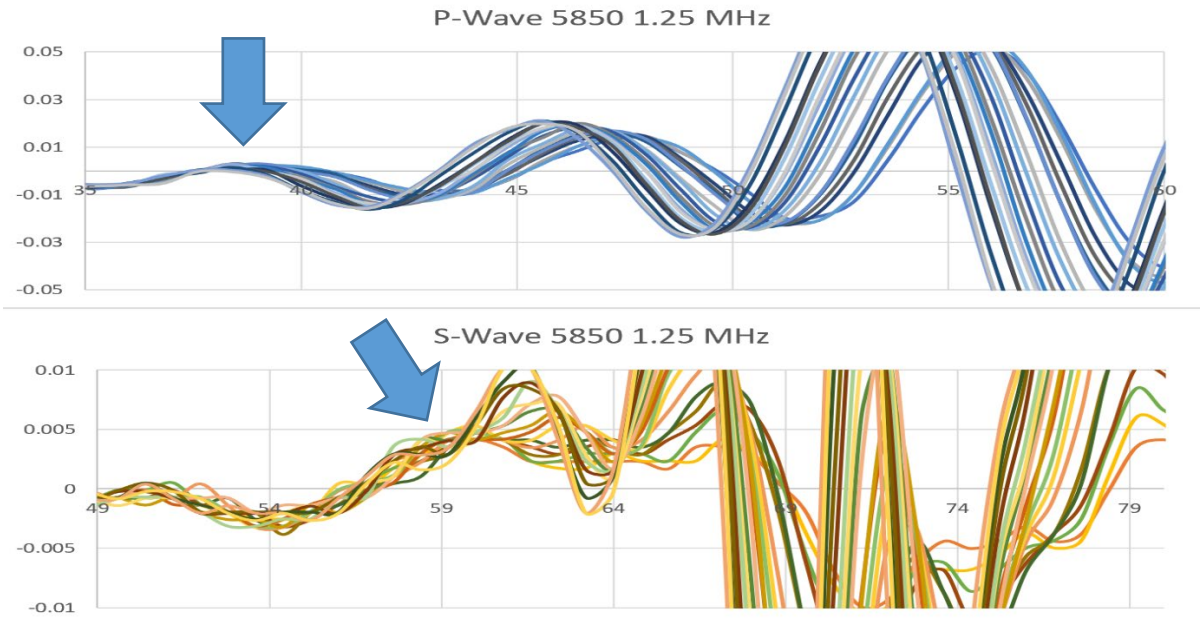

Figure 5-24: 5850ft sample P-wave and S-wave waveforms stacked from 1,000 lbs. - 10,000 lbs. of force taken at a frequency of 1.25 MHz.

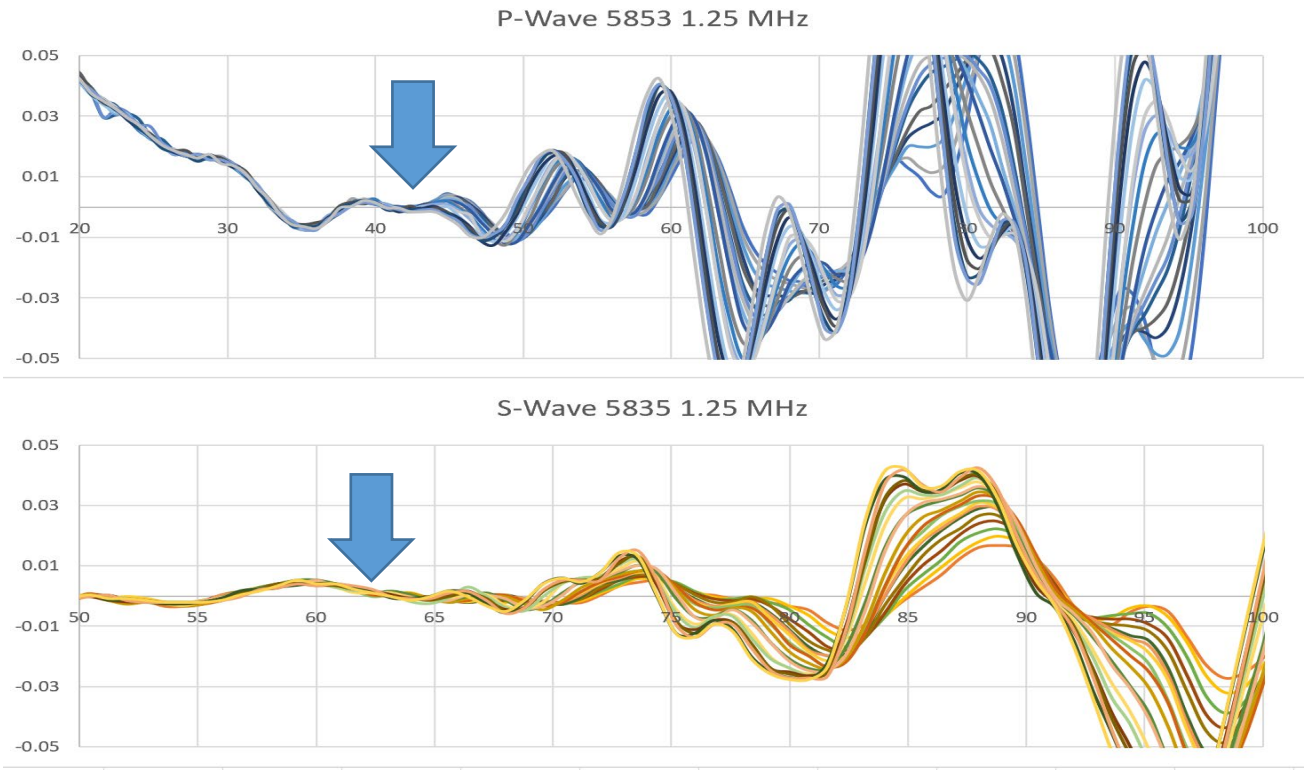

Figure 5-25: 5853ft sample P-wave and S-wave waveforms stacked from 1,000 lbs. - 10,000 lbs. of force taken at a frequency of 1.25 MHz.

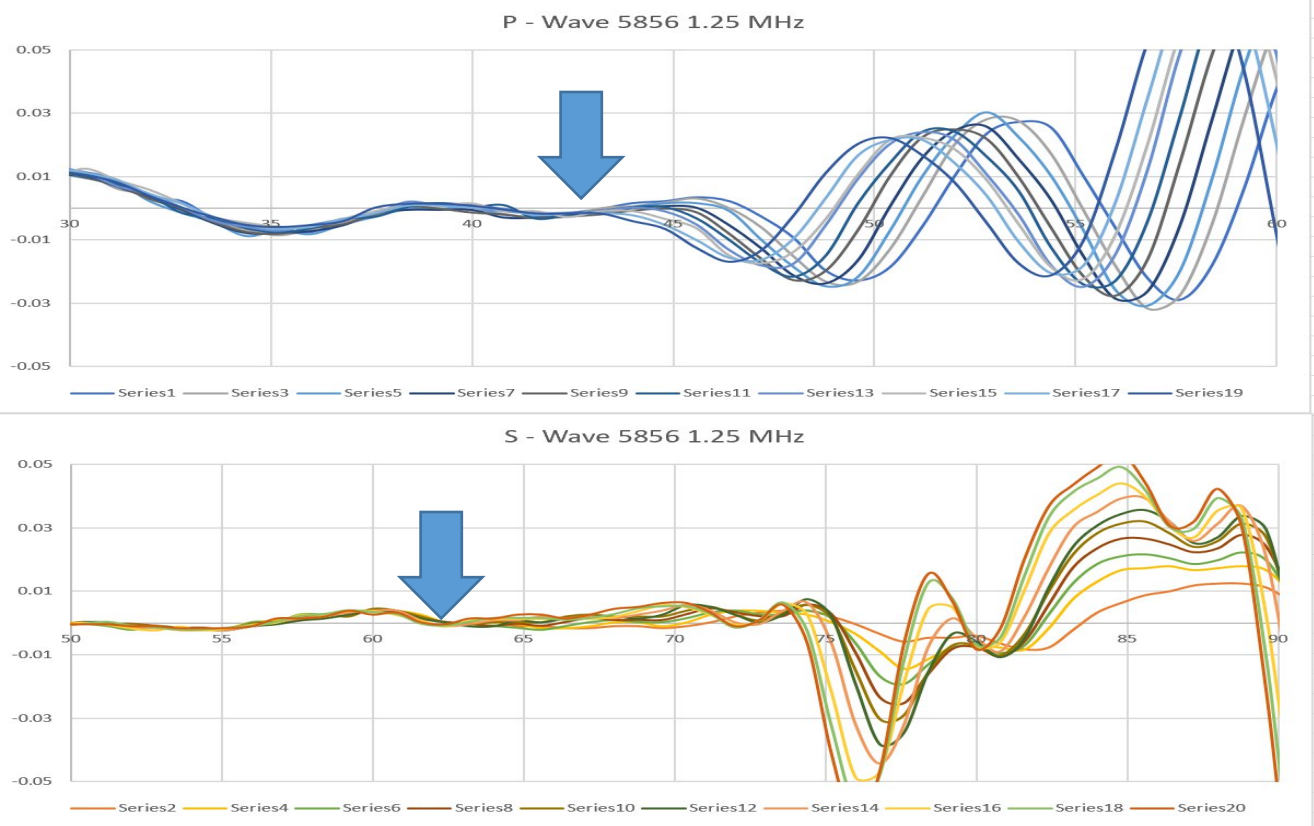

Figure 5-26: 5856ft sample P-wave and S-wave waveforms stacked from 1,000 lbs. - 10,000 lbs. of force taken at a frequency of 1.25 MHz.

5.2 Elastic sonic and ultrasonic reservoir facies properties

Sonic and ultrasonic velocities may vary greatly due to the difference in frequency which each measurement was taken at. One is done as an open-hole measurement, and the other is done within lab conditions. Figure 5-27 depicts the difference between the two measurement methods. Although values vary, the same trend can be seen in both logs, as the measurements pass through the Cherty Dolomitic section (within the blue square), and the Muddy Dolomitic section (within the red square). Variation in these values is due to the difference in frequency and overburden (or effective) pressure. Both the Cherty Dolomite (“B” Zone) and Muddy Dolomite (“C” Zone) are the more porous intervals within our core and the Viola as a whole, as seen in Figure 5-27 the neutron and density porosity logs follow the sonic log and the ultrasonic measurements trends of

porosity. The ultrasonic measurements account for high values of porosity more dramatically than the sonic values.

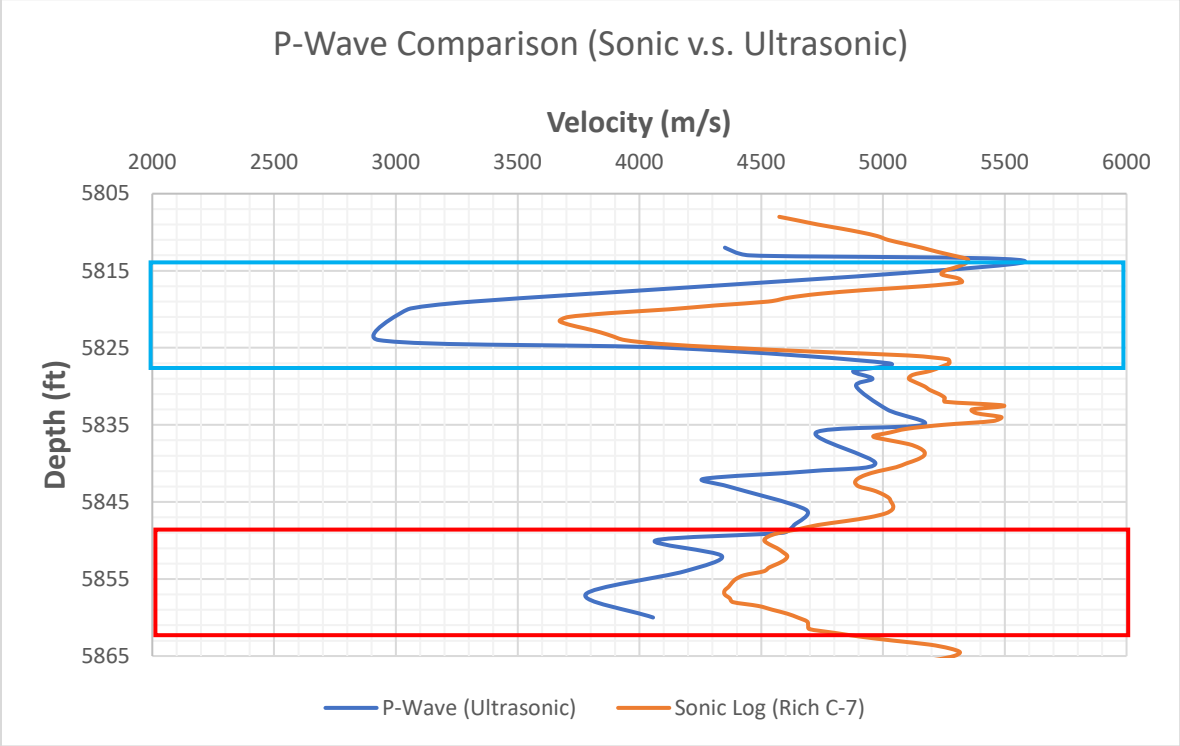

Figure 5-27: P-wave velocities taken at sonic frequencies (wireline logging) and ultrasonic frequencies (Lab compression testing) in the Rich C-7 well and core. The blue box marks the Cherty Dolomite section and the red one, the Muddy Dolomitic section.

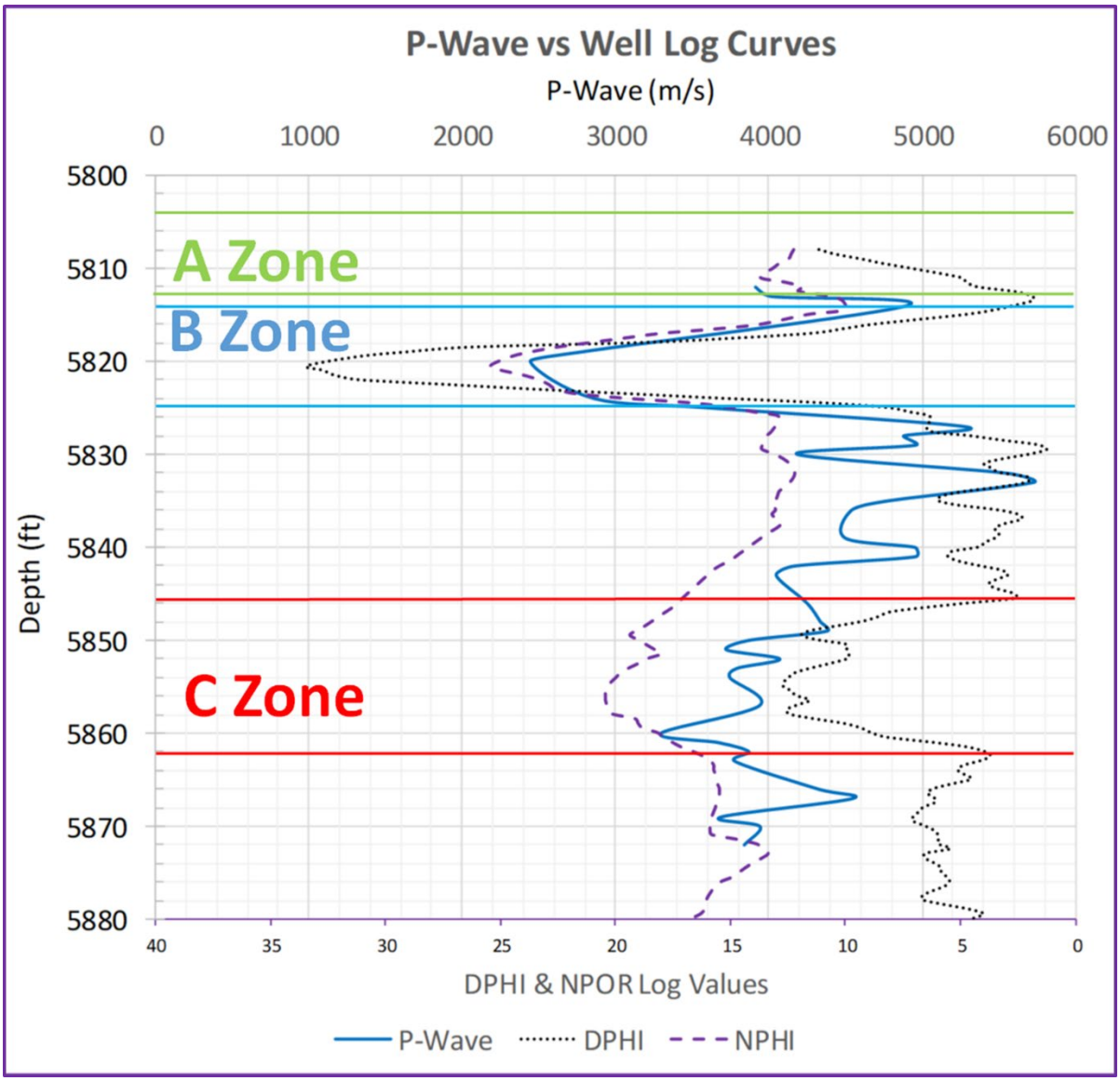

Figure 5-28: Density (DPHI) and neutron (NPHI) porosity logs compared to P-wave velocities from ultrasonic measurements obtained in the Rich C-7 Core.

Poisson's ratio being a measure of fractional compressibility of pore space (Simm and Bacon, 2014), it was used throughout the core to compare with other parameters and moduli. Figure 5-29 and 5-30 show relationships of Poisson's ratio with porosity taken from the neutron porosity log and lab-measured acoustic impedance (V_p and density measured in dry core).

The Cherty Dolomite (in green) can easily be discriminated with high Poisson values paired with high values of porosity. The higher porosity provides a lower acoustic impedance

due to porosity effects on the velocity and density of rock. Other intervals such as the "C" and Intermediate zone can also be easily grouped for they have lower velocities and higher densities, interpreted as due to a higher dolomite content along with less porosity. The "C" Zone however, has a higher average porosity than the Intermediate Zone.

These high porosity and low impedance values for the reservoir facies strongly corroborate the conclusion by Vohs (2016) that good reservoir properties correlate with lower amplitude levels. The Viola seismic event is represented as peak (low impedance shale on relatively higher impedance Viola carbonates), which gets reduced as impedance falls to levels close to that of the capping shale formation (Vohs, 2016).

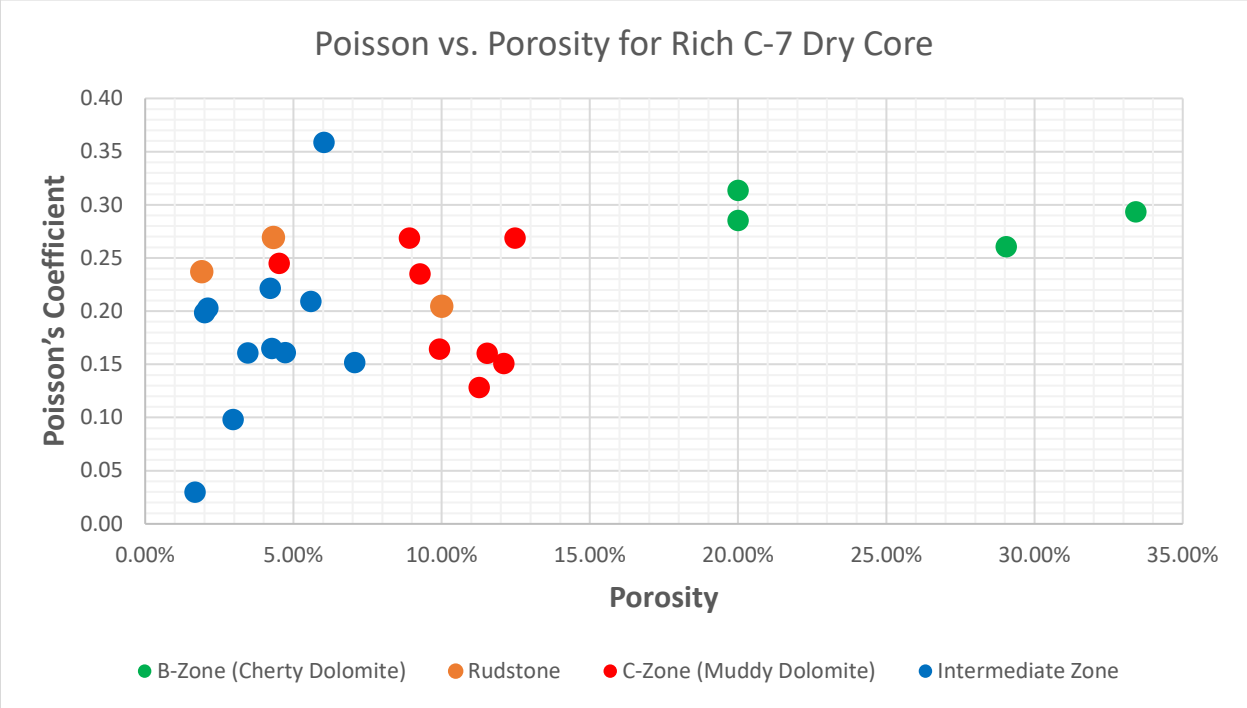

Figure 5-29: Relationship of Poisson's ratio and porosity for Rich C-7 dry core measurements.

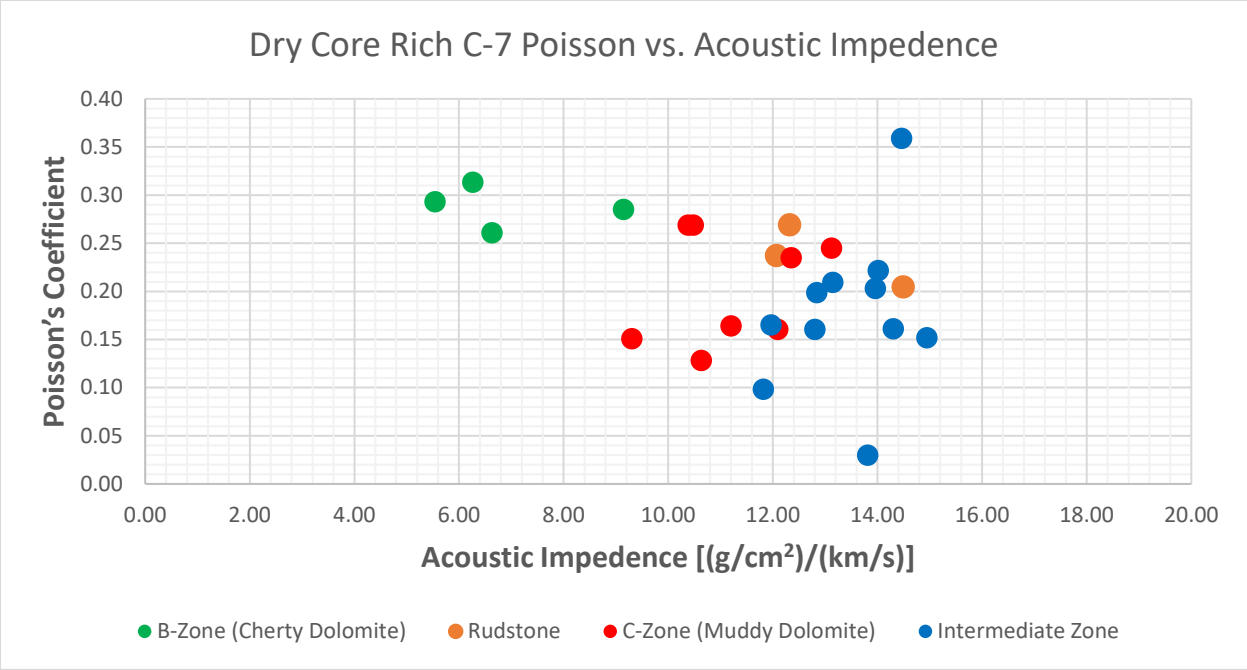

Figure 5-30: Cross plot of Poisson's coefficient and acoustic impedance of the Rich C-7 dry core.

Density is also a parameter used in rock physics to identify trends in lithology, but it is also used when calculating bulk modulus. Since the "B" Zone has a high amount of chert, it is expected to have lower density values accompanied with the higher porosity values. Figure 5-31 shows the relationship of density to velocity, taken at the core during dry conditions. The "C" Zone has lower porosity, and it can be identified for its higher velocity and density, since it comprises Muddy Dolomite intervals within the core.

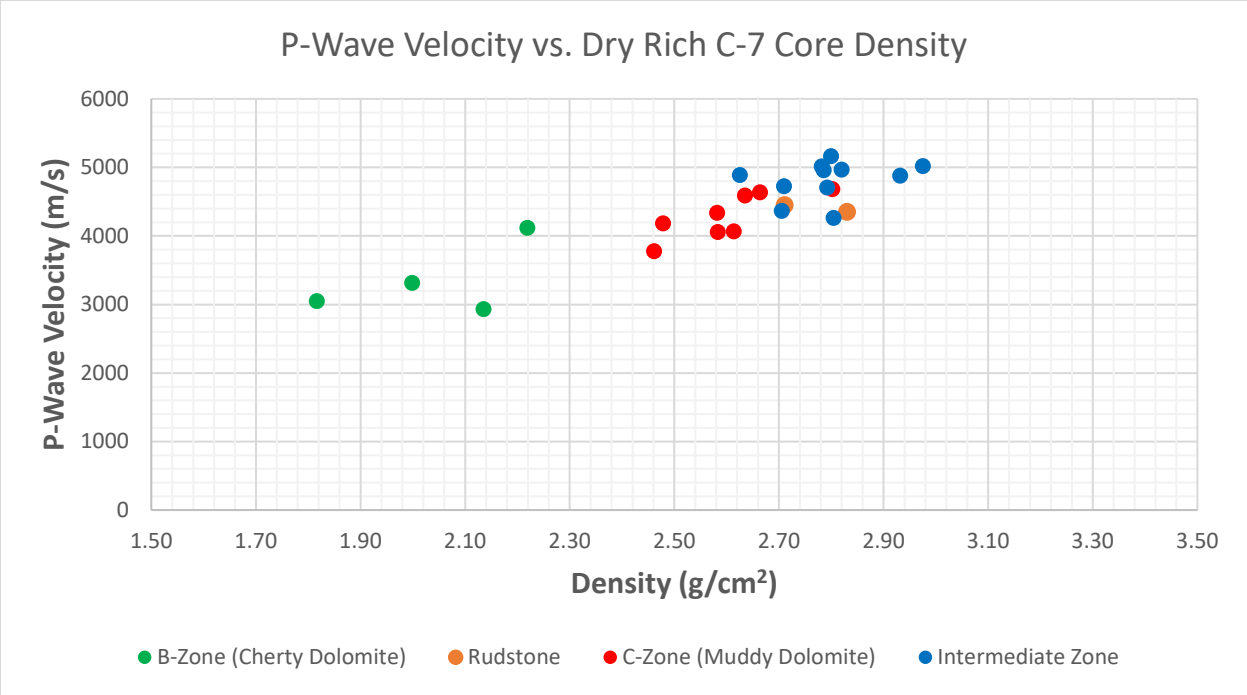

Figure 5-31: Cross plot of P-wave velocity and density measured in the Rich C-7 core.

Porosity values were used to identify specific intervals in the core. Figure 5-32 and 5-33 both show relationships of porosity in relation to V_p values obtained from ultrasonic measurements taken from Rich C-7 dry core (Figure 5-32), and sonic log values (Figure 5-33). In both figures, the "B" Zone is clearly identified by a much slower velocity and high porosity. Again, the "C" Zone can be identified for having lower porosity then the "B" zone, yet higher than the intermediate zone. A tighter grouping can be seen from all intervals in Figure 5-33. This is due to the relationship of sonic velocity to neutron porosity. Both of these measurements were taken in a static setting compared to the Ultrasonic measurements which were taken dynamically.

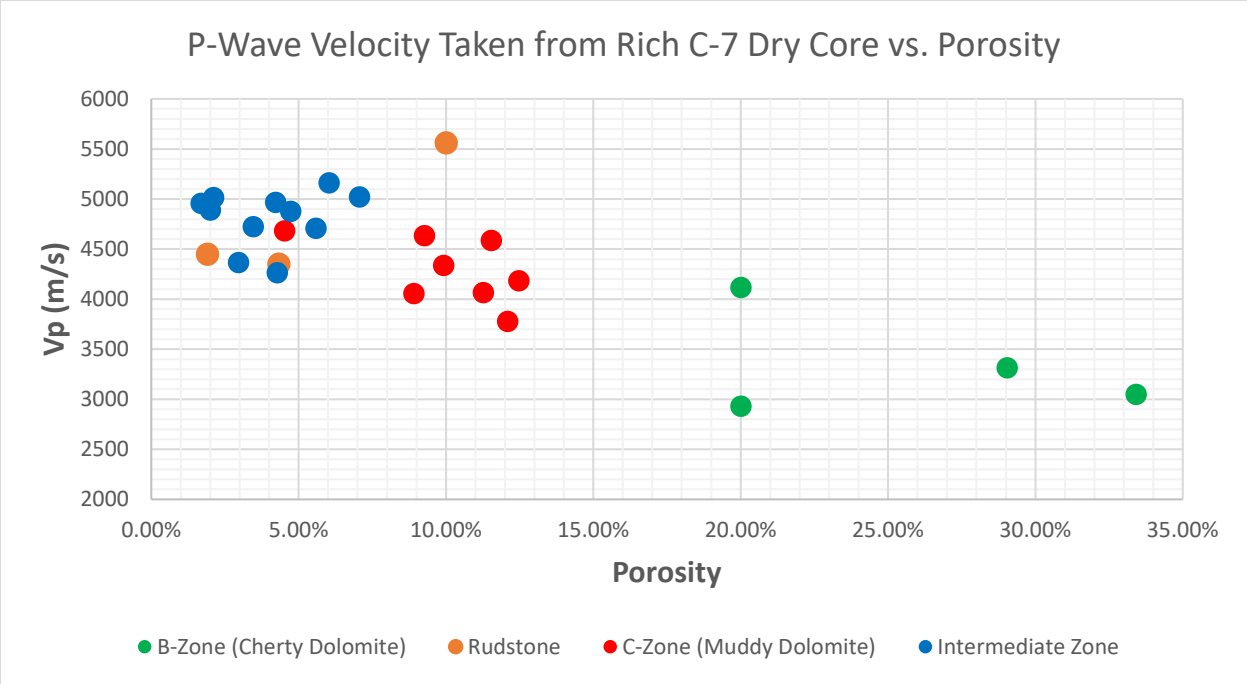

Figure 5-32: Cross plot of P-wave velocity acquired from ultrasonic measurements compared to porosity values taken from the Rich C-7 neutron porosity log.

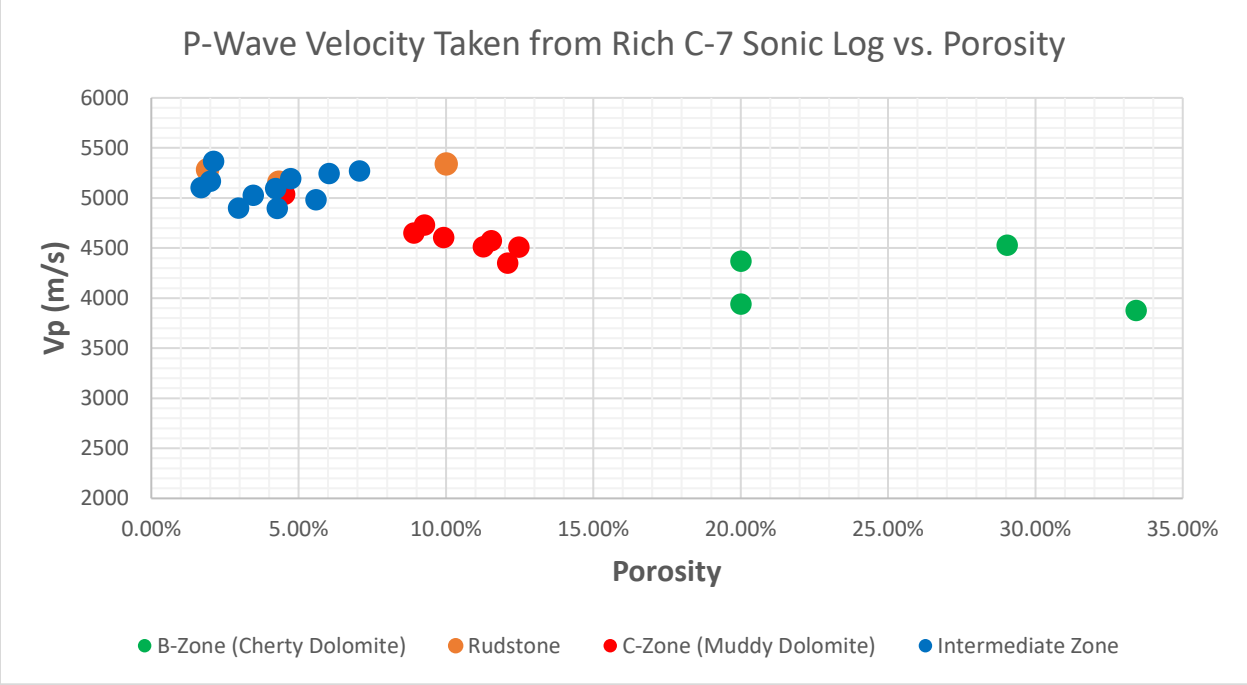

Figure 5-33: Cross plot of P-wave velocity acquired from sonic measurements compared to porosity values taken from the Rich C-7 neutron porosity log.

Figure 5-34 describes the relationship of standard elastic functions as a dual axis cross plot. Y1 contains porosity values while Y2 shows P-wave velocity values as they both are stacked in accordance with density, showing an inverse relation. “B” Zone samples are easily discernable from “C” Zone, Intermediate Zone and Rudstone samples in the stratigraphic section. Thus, porosity and density should be used as preliminary identification factors when identifying and isolating “B” Zone intervals within Viola reservoirs, since this zone contains the greatest porosity and chert concentrations.

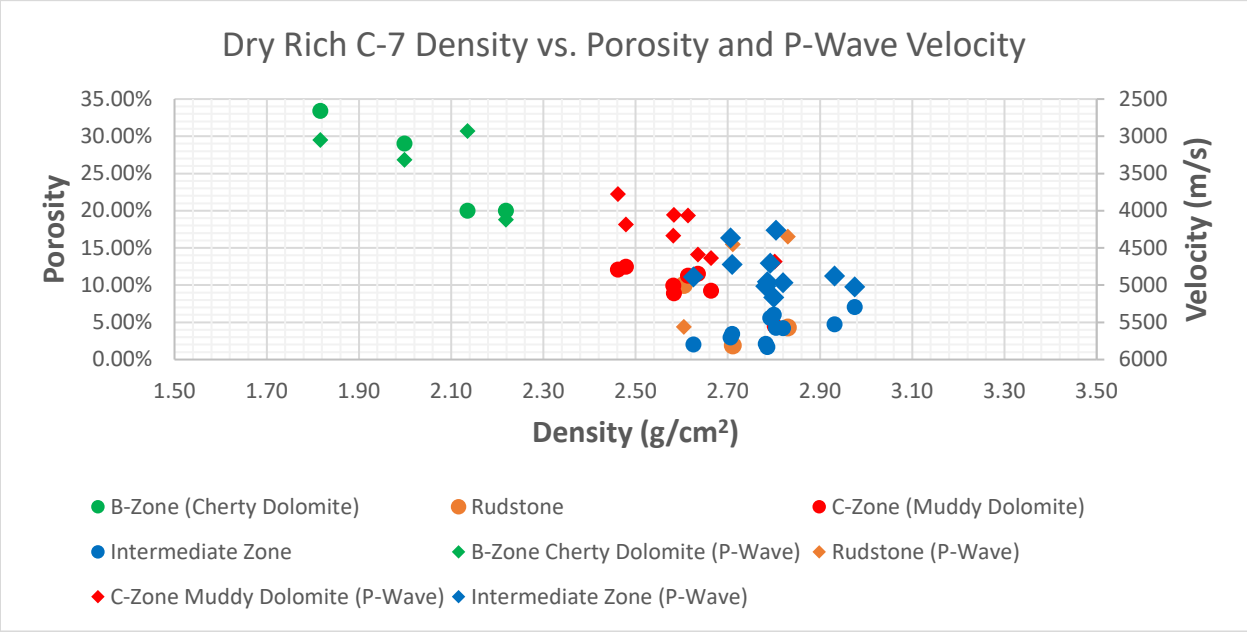

Figure 5-34: Dual Y-Axis cross plot showing relationships of porosity and P-wave vlocity as a function of density.

Other elastic moduli such as bulk and shear moduli are criteria when attempting to isolate or identify specific zones within a stratigraphic section. Bulk and shear modulus are both calculated using P-wave velocity, S-wave velocity, and density as described in Chapter 2. Velocity values are in km/s, density is in g/cm^3, and bulk and shear moduli are in Giga-Pascals (GPa). Figure 5-35 shows a relationship of bulk and shear moduli identifying the various

intervals within the Rich C-7 core. The "B" zone can be identified in this figure. The separation from other zones is not as dramatic as seen in previous figures, but Figure 5-35 does provide insight on the differences each interval has when identifying pore-fluid fill, minerology, and porosity.

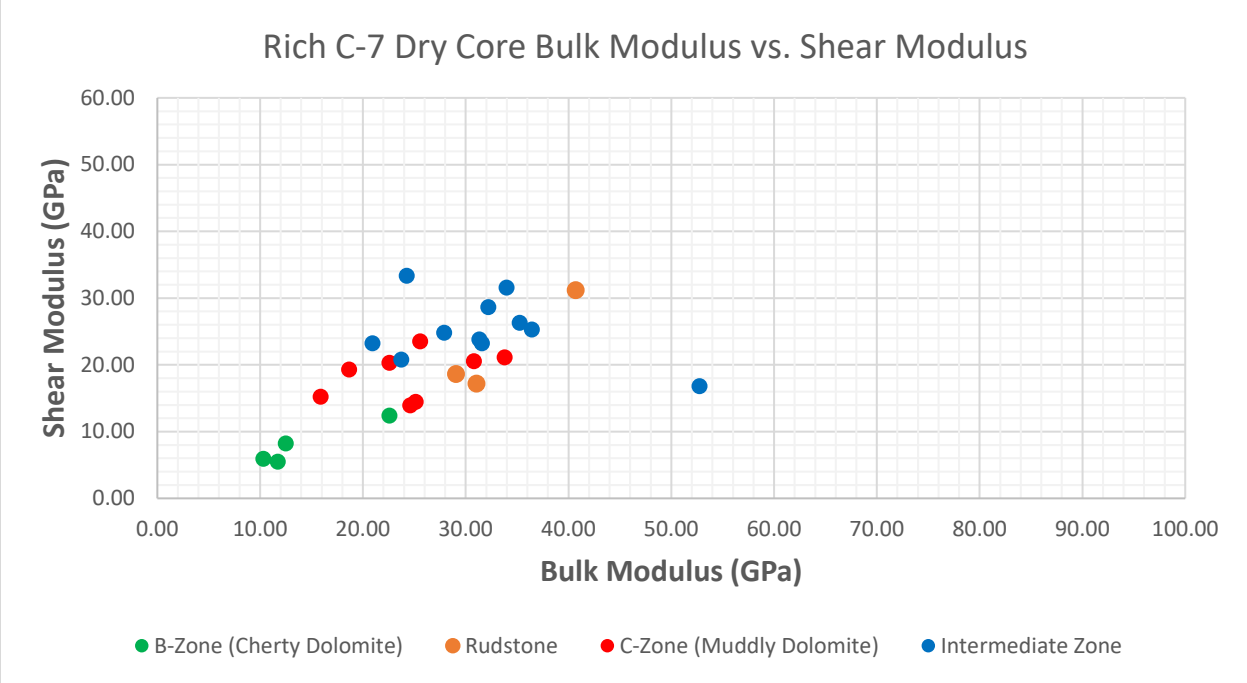

Figure 5-35: Cross plot of bulk modulus and shear modulus for the Rich C-7 core.

Where bulk modulus is a function of density, P-wave, and S-wave velocities, shear modulus is simply a function of density and S-wave velocity. Therefore, fluid substitution will have a greater effect on bulk modulus since fluid has minimal to no-effect on S-wave velocities.

Porosity being such a large factor in P-wave and S-wave velocity of our core, Figure 5-36 explores the relationship of porosity to bulk modulus, shear modulus, and poisons coefficient. Knowing the "B" Zone is a high porosity cherty dolomite, and the "C" Zone, is a muddy dolomite with a higher relative porosity to the rest of the core, it can be seen in Figure 5-39

where the “B” Zone and “C” Zone are isolated. More porous rocks have higher Poisson’s coefficient due to the compressibility ratio of their pores. However, the “B” Zone can be seen having much lower elastic moduli values than the rest of the core. This is interpreted as the “B” Zone having high chert content and secondarily due to porosity. Chert content within the “B” Zone is the greatest factor when isolating it from the rest of the core. Low density present in chert along with higher porosity provides lower velocity values, which in turn produce lower moduli values.

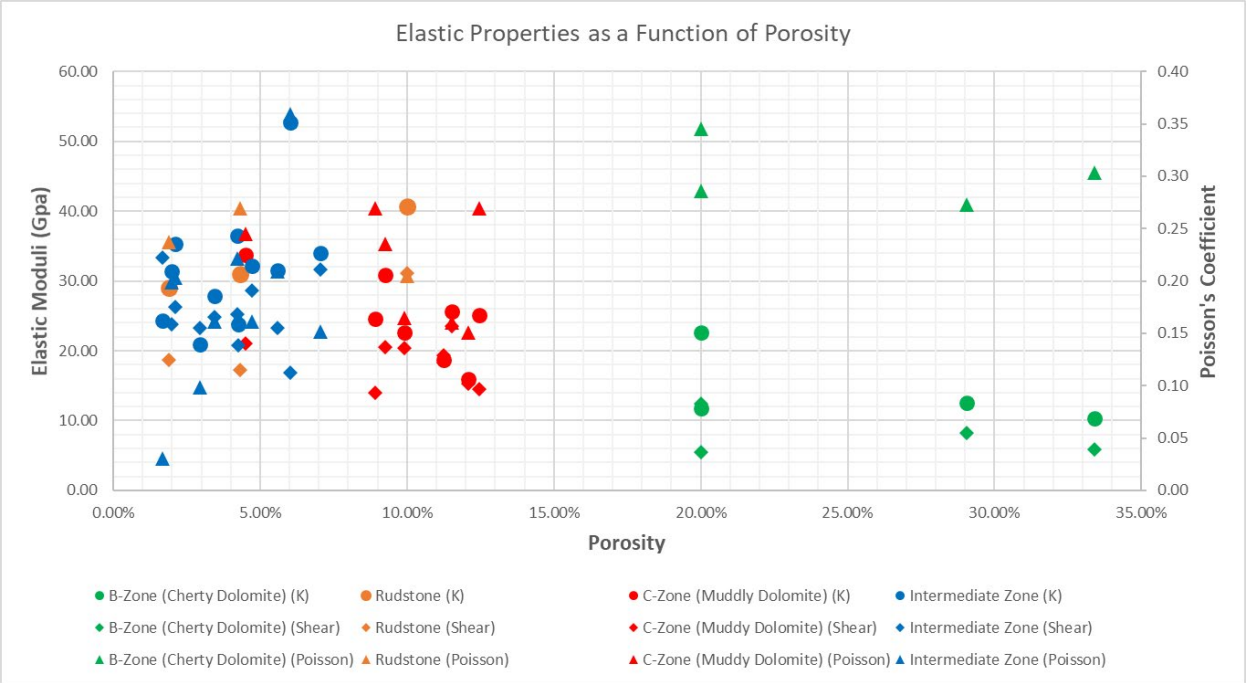

Figure 5-36: Multi-variable cross plot comparing bulk modulus, shear modulus, and Poisson’s coefficient as a function of porosity for the dry core of Rich C-7.

5.3 Contrast of Reservoir and Non-Reservoir properties within the Viola

5.3.1 Contrast in Elastic Moduli

Hagood (2019) described the Viola to have lithological composition of Cherty Dolomite, Intraclastic Breccia, Intraclastic Rudstone, Bioclastic Grainstone, and Muddy Dolostone. Above

in chapter 5.2, elastic moduli show contrast between different lithofacies. Cherty dolomite can be seen to provide higher porosity, lower elastic moduli, lower density, and lower velocity across - multiple cross-plots. Poisson's coefficient is also higher due to the compressive ratio of larger pores that can be found within the Viola "B" zone's cherty dolomite.

Comparatively lower porosity in the "Intermediate" zone's intraclastic breccia and the "C" zone's muddy dolostone yields higher seismic-wave velocities, higher elastic moduli, lower Poisson's coefficient, and higher density. There is a distinct contrast between the cherty dolomite and all other zones within the Viola. Assuming this is homogenous across the region, the cherty dolomite would comprise a reservoir with superior quality compared to the intermediate and "C" zones of the Viola. The "A" zone is considered a oil producing zone with high porosity, but due to the lack of core samples, the lithological evidence cannot be provided. Therefore, it will be assumed that the best-producing Viola reservoirs are rich in silica and dolomite.

5.3.2 Lithological Contrast

Rich C-7 is an excellent producing well with over 350,000 bbls of oil and it is used in this study with the core provided by the KGS. The red boxes superimposing figure 5-37 depicts the locations where the Viola was perforated for production. It can be seen that a zone with a high chert content was targeted in the lower section of the Viola "B". The Viola "B" comprises of up to 50% chert and dolomite from 5812 ft to 5825 ft, whereas the Viola "A" zone can be described as the first high chert accumulation from about 5805 ft to 5810 ft. The Viola "A" base was targeted in the upper perforation conducted by the operator. This most likely was done based upon what was seen on resistivity logs. Cherty intervals such as the "B" zone depicted in 5-37 correlate with the highly porous and low elastic moduli response to the Rich C-7 core tested in the lab.

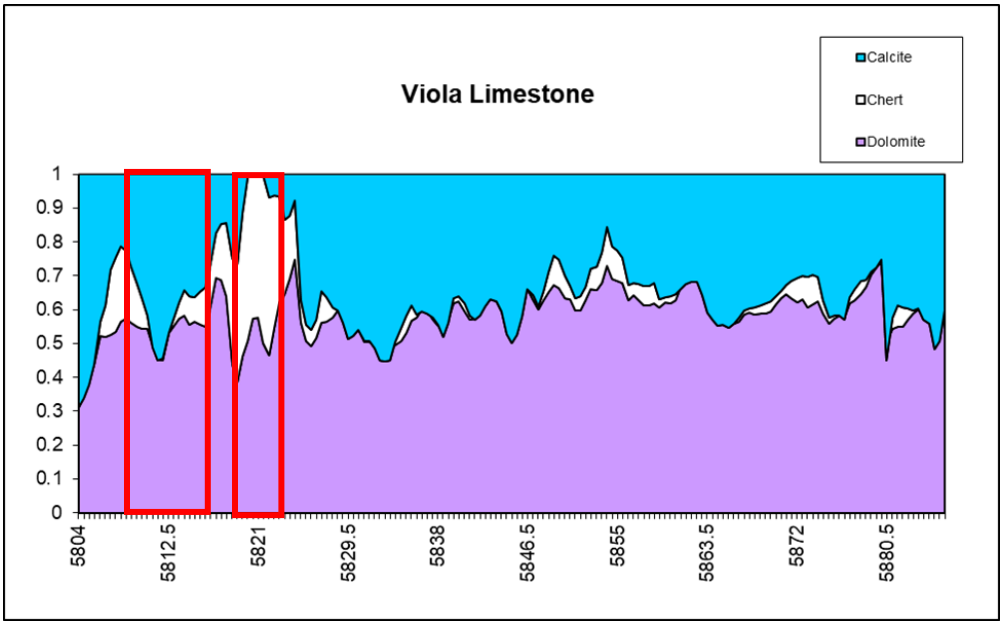

Figure 5-37: Rich C-7 PE log lithological analysis. Overlaid red boxes highlight perforated areas of the upper Viola for hydrocarbon production.

Stephens 1 and 4 are oil and gas producing wells within the North East Morrison field in Clark County, Kansas. Both wells targeted the upper Viola where chert content is higher than other sections of the well. Stephens 4 (Figure 5-38) is easily compared to Rich C-7 in it's chert content potentially indicating the Viola "B" zone composed primarily of dolomite and calcite. Stephens 1 (Figure 5-48) and Stephens 4 (Figure 5-39) both seem to be excessively modeled for chert within the Viola. Stephens 1 most likely is a result of bad wireline data due to a baseline chart content that could be observed across the well. Stephens 1 would most likely model more like Stephens 4.

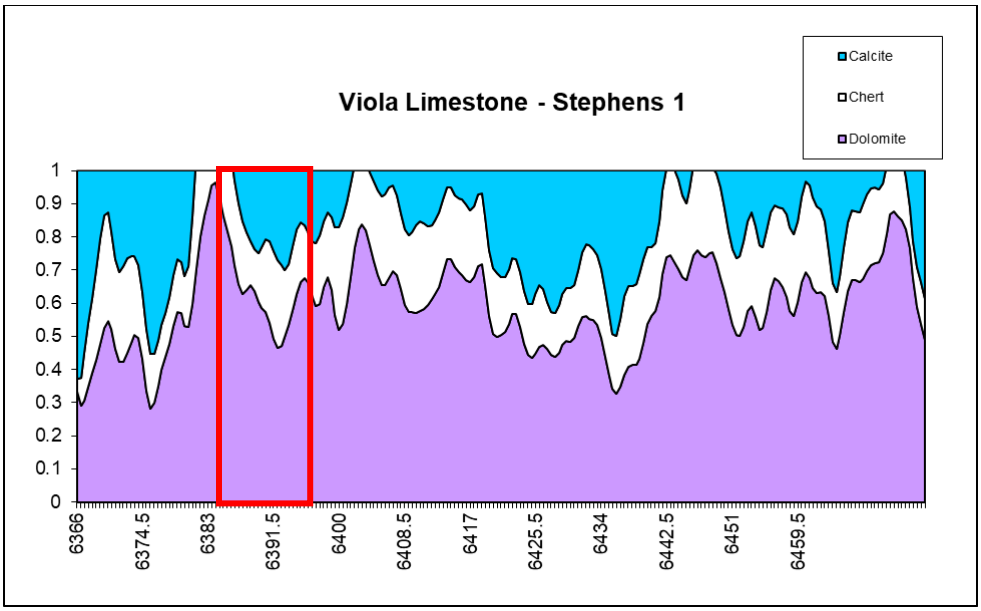

Figure 5-38: Stephens 1 PE log lithological analysis. The red boxes highlight perforated areas of the Viola for hydrocarbon production.

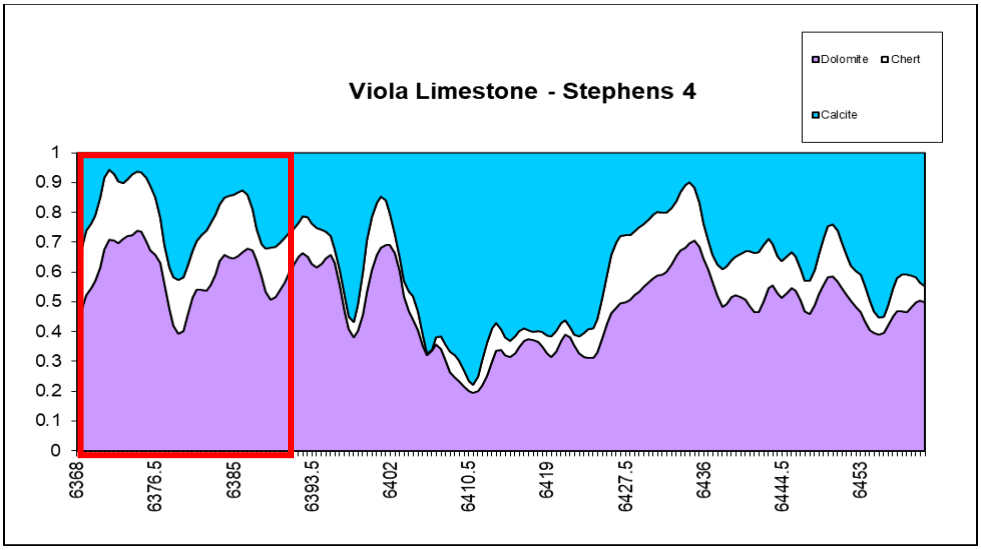

Figure 5-39: Stephens 4 PE log lithological analysis. The red boxes highlights drill stem tested areas of the Viola for hydrocarbon production.

Stephens 8 and 10 were used as non-productive examples within the Morrison Northeast field within Clark County, Kansas. Stephens 10 (Figure 5-40) shows various occurrences of cherty dolomite which can be described as the "A" and "B" zones. Stephens 8 (Figure 5-41) on the other hand contains a single thick section of cherty dolomite with almost no calcite. Both

wells ideally would provide positive reservoir rock for hydrocarbon accumulation. A lack in production could be due to a poor seal or insufficient source rock mobility of hydrocarbons.

Comparing Rich C-7 responses to the four examples given above, production can be determined due to the presence of cherty dolomite which provides higher porosity values. Thus, elastic responses within such cherty dolomite areas that indeed provide good porosity could be expected to follow similar elastic trends as seen in the Viola "B" zone cherty dolomite.

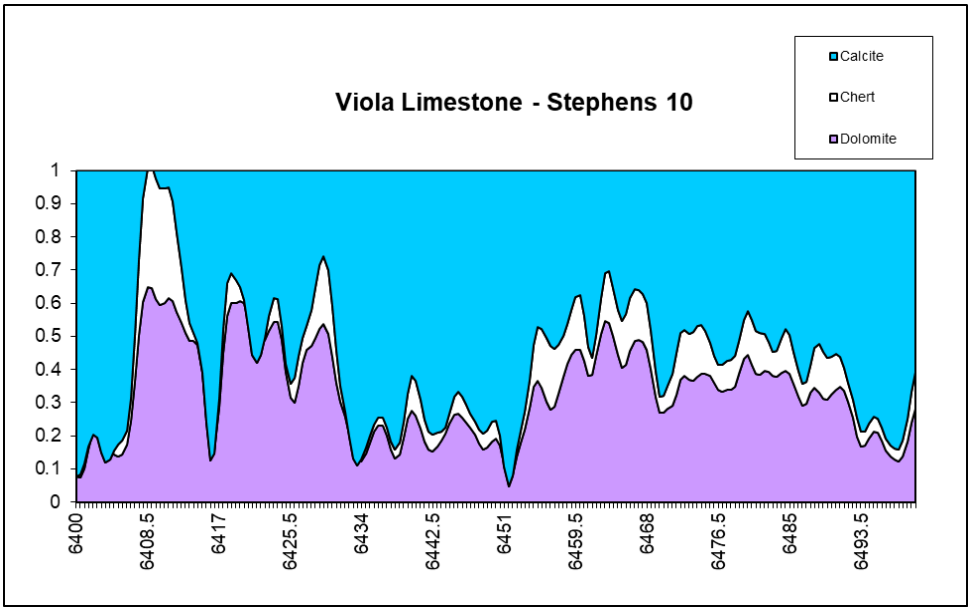

Figure 5-40: Stephens 10 PE lithological composition.

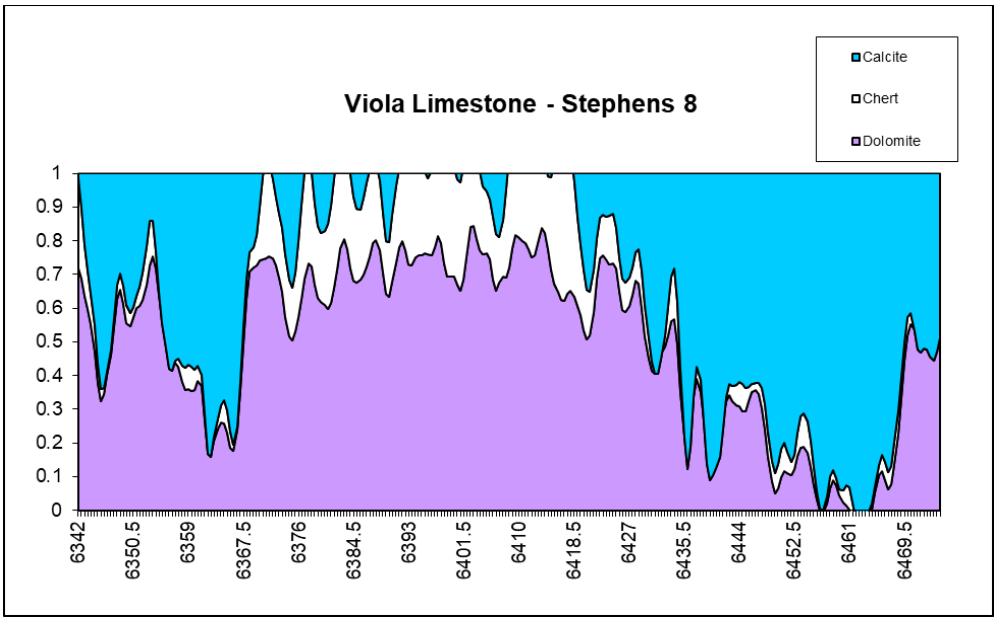

Figure 5-41: Stephens 8 PE lithological composition.

5.3.3 Well Log Contrasts

Well log cross plots were used to identify contrast in productive and non-productive wells within the Viola. Rich C-7 along with Stephens 1, Stephens 4, Stephens 8, and Stephens 10 were used to generate cross plots ,including neutron porosity (NPHI) vs. density porosity (DPHI) (Figures 5-42 and 5-43 for Rich C-7 and Stephens wells respectively),Sonic P-wave (Vp) vs, Bulk Density (Rho) (Figures 5-44 and 5-45), Porosity (Phi) vs. Sonic P-wave velocity (Vp) (figures 5-46 and 5-47), Acoustic Impedance (AI) vs. Porosity (Phi) (Figures 5-48 and 5-49), and a tri-plot with P-wave velocities (Vp) against Deep Induction Resistivity (ResD) in relation to porosity (Phi) (Figure 5-50).

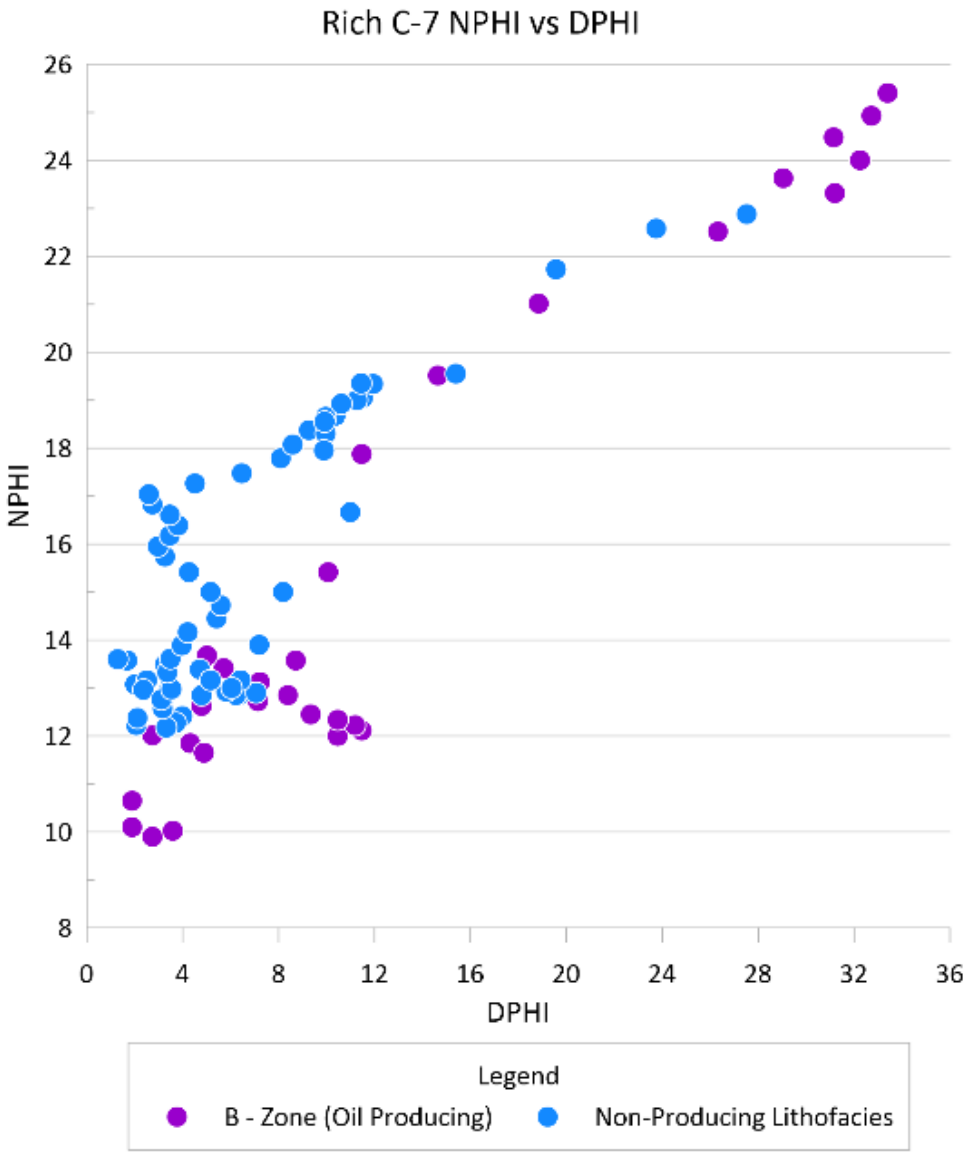

Figure 5-42: Rich C-7 NPHI vs. DPHI cross plot.

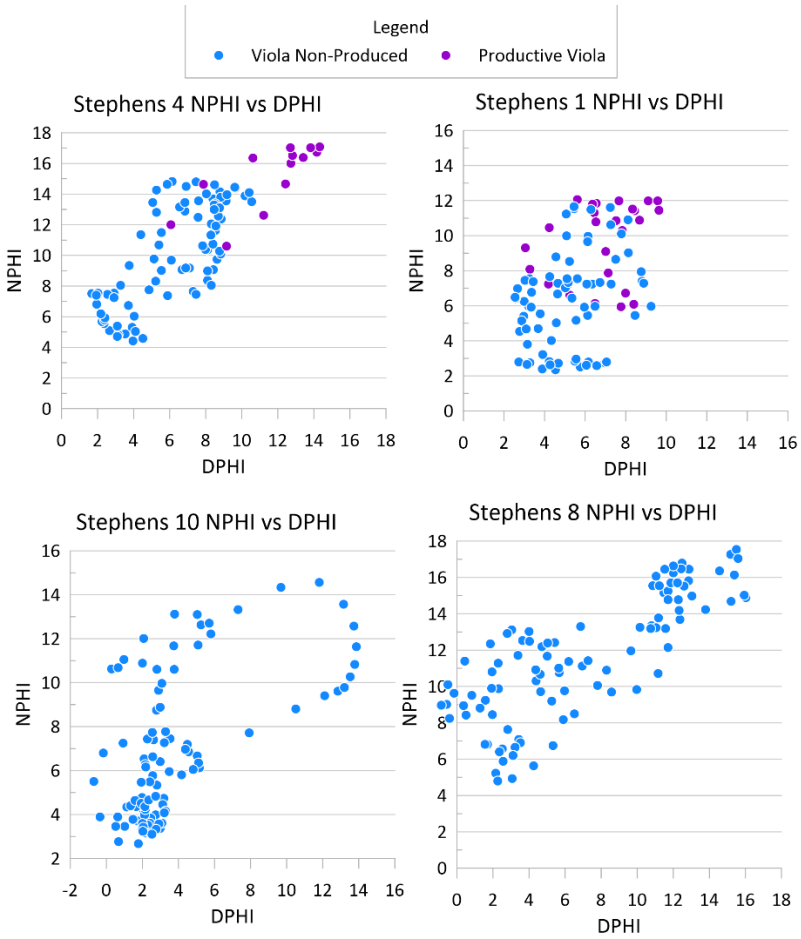

Figure 5-43: NPHI vs. DPHI cross plot in Stephens producing and non-producing Viola wells.

Figure 5-42 and 5-43 depict neutron and density porosity cross plots for the anlayzed wells (Rich C-7 and Stephens wells, respectively). The blue dots are data points in intervals of no targeted or natural production whereas the purple dots indicate areas targeted for perforation. Rich C-7 displays a trend for non-production in the lower-right quadrant of the scatter plot with low density and neutron porosity values. Other wells follow a similar (but somewhat clearer, as seen in Stephens 1 and 4) trend, despite porosity values not being as high as in Rich C-7. Stephens 1 and 4 have lower values of porosity than rich C-7 but also produced six times less oil than Rich C-7 (Table 2-1).

Rich C-7 depicts an inverse relation between sonic p-wave velocity and bulk density, (Figure 5-44) between its cross plot and those of Stephens 1, 4, 8, and 10 display a positive one (Figure 5-45). Productive facies in Rich C-7 display low sonic velocity and high density values, whereas in Stephens 1 and 4 productive facies are characterized by low sonic velocity and low density. High density values in a very porous lithofacies where low velocities occur (as in Rich C-7) might be a log response to large amounts of fluid within the pore space. Production data in Rich C-7 indicates large amounts of fluid in the well, possibly hydrocarbon or brine saturation, based on the behavior of various other elastic, seismic, core, and well-log properties that allowed identification of the Viola "B" zone producing facies. For Stephens 8 and 10, the low density and low velocity response could be due to high concentrations of chert within the lithofacies, with no hydrocarbons within the pore space.

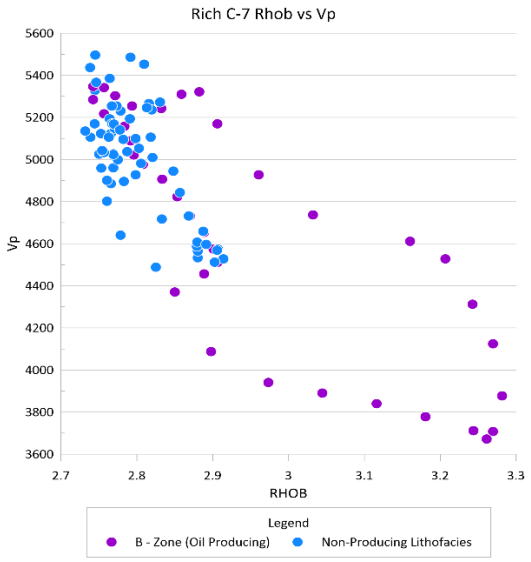

Figure 5-44: Rich C-7 sonic P-wave velocity vs. bulk density cross plot in Rich C-7.

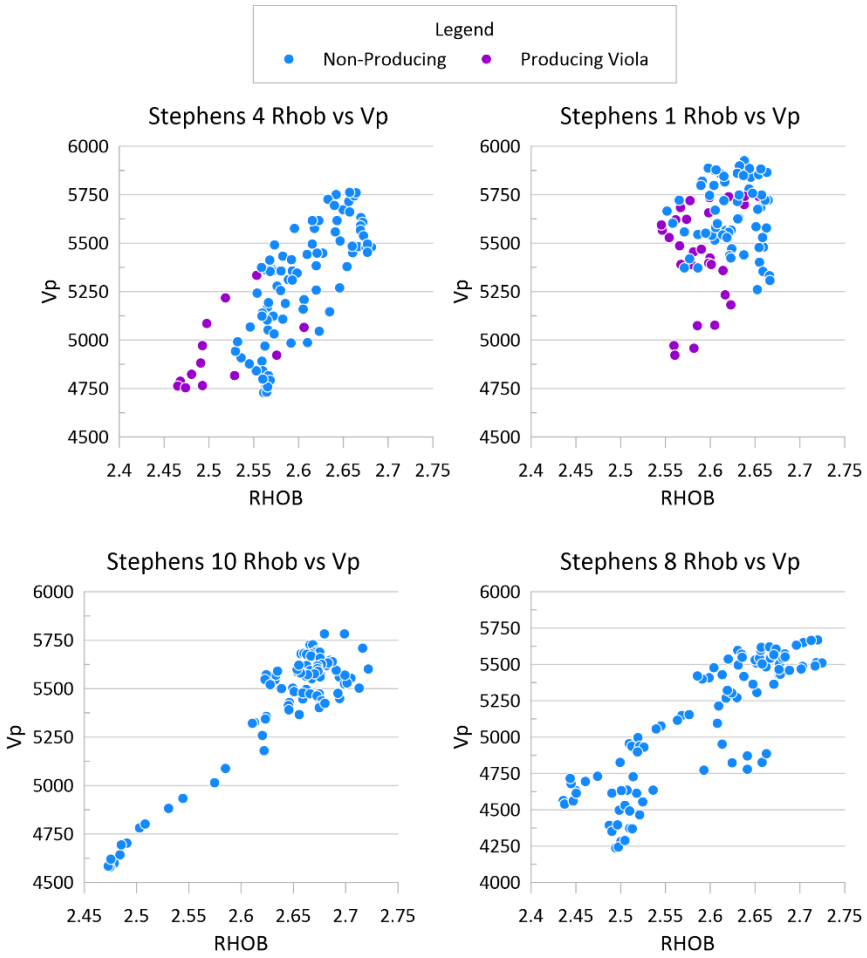

Figure 5-45: Sonic P-wave velocity vs. bulk density cross plot in Stephens wells.

Relationships between porosity and compressional velocity can identify the type of fluid due to compressional velocities response being affected by both rock frame and fluid. In both Rich C-7 (Figure 5-46) and Stephens 4 (Figure 5-47), high porosity correlated with low P-wave velocity. In Rich C-7, porosity values rise above 24% and velocity values drop below 4000 m/s. In Stephens 1 (Figure 5-47), however, the highest porosities display high P-wave velocities. This could be due to the purple marks were assigned based upon the zone perforated by the operator. Non-producing wells follow clear negative relation between porosity and P-wave velocity. The largest variance is in the productive lithofacies. In Rich C-7, data points that lie below the trend

suggest potential hydrocarbon saturation, since the relative change in velocity is minimal regardless of porosity.

Stephens 1 and 4 both display negative correlation of porosity with P-wave velocity, and although the productive purple points follow the trend, several points in both wells show significant changes in porosity with minimal velocity changes. Porosity variance at constant P-wave velocity may be due to changes in lithological properties and not a response caused by fluid. Stephens 8 and 10, on the other hand, both follow the trend.

Figures 5-48 and 5-49 depict cross-plots of acoustic impedance against porosity. This trend is very similar to the Vp and porosity crossplots, with an inverse relation where, as porosity increases, impedance decreases. In many data points for the productive facies, impedance is consistently low across a range of impedance. Especially for the non-producing wells, impedance vs. porosity graphs are almost identical to those of P-wave velocity vs. porosity. Similarities between the plot are due to minimal change in density in proportion to Vp. Rich C-7 has a slightly wider pay zone distribution, while Stephens 4 is slightly tighter along with Stephens 1. The response of these parameters in non-producing wells in both fields are nearly identical.

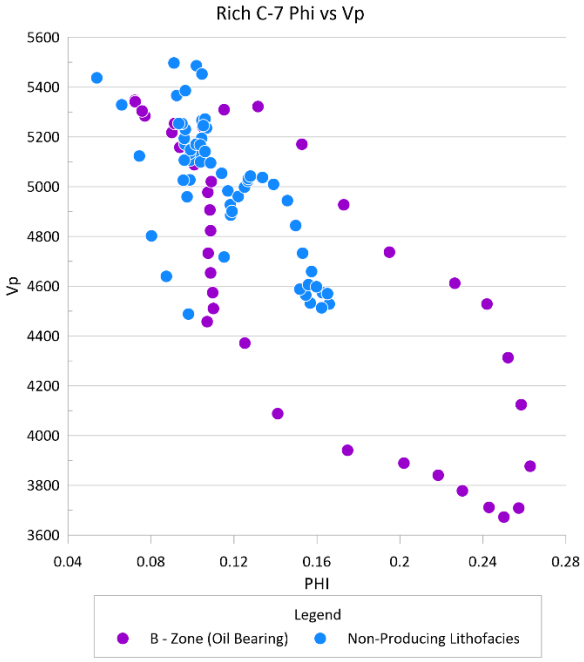

Figure 5-46: Rich C-7 porosity and P-wave velocity cross plotted.

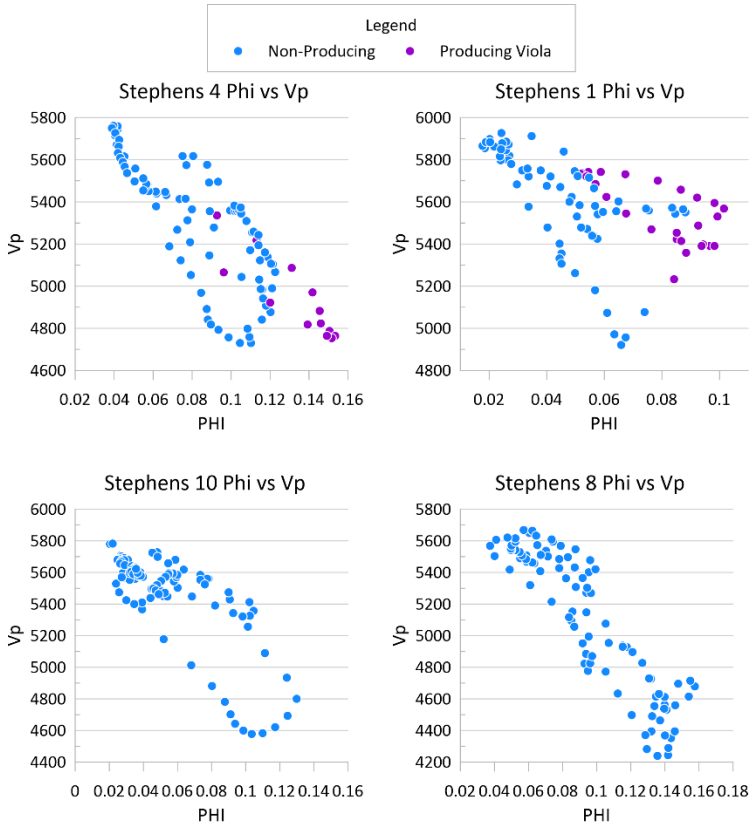

Figure 5-47: Cross plot of compressional velocity and porosity in Stephens wells.

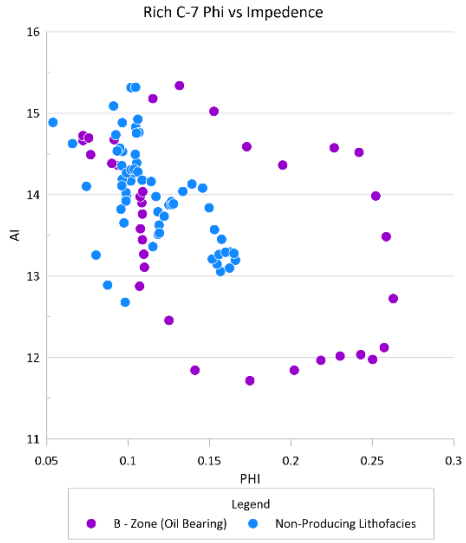

Figure 5-48: Cross-Plot of impedance and porosity in Rich C-7.

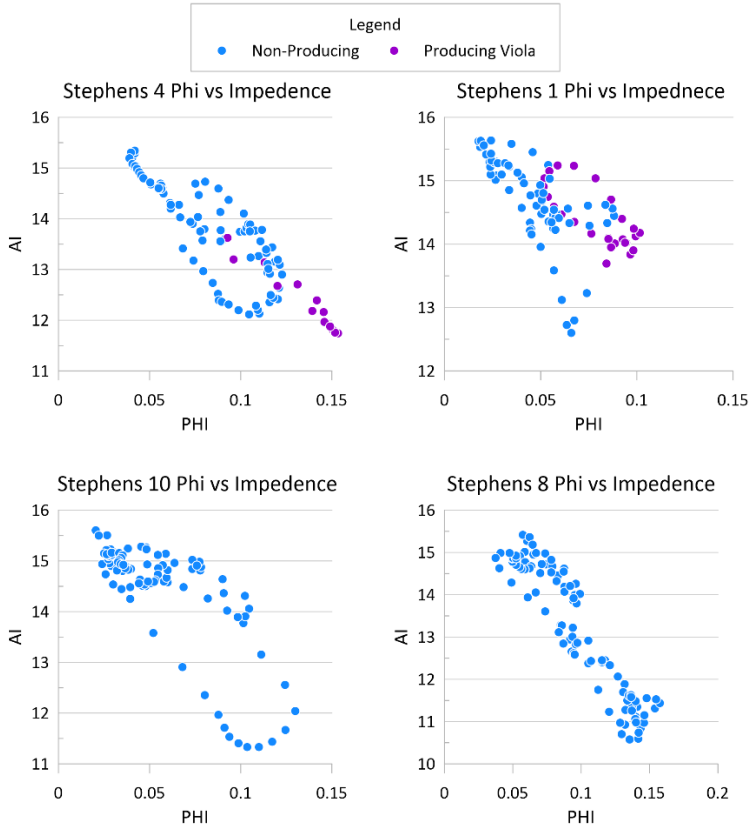

Figure 5-49: Cross-plot of impedance and porosity in Stephens wells.

Figure 5-50 shows a cross plot comparing deep-induction resistivity (ResD), P-wave velocity from sonic log (Vp), and porosity from Doveton's (2017) calculator. Porosity is modeled as a color gradient, while the differentiation of oil-producing and non-producing zones are represented by square and circle points, respectively. At lower velocities porosity is higher, as seen from the warmer colors. It appears that oil saturation is occurs at moderate porosities, with constant resistivity between 15 and 20 ohms, where porosity does not follow the velocity trend. This change in velocity could be due to lithological changes within the pay zone affecting density. Rich C-7 perforated interval consists of rudstone, unconsolidated breccia, muddy dolomite, and cherty dolomite. Figure 5-51 shows how each lithology correlates with log-measured porosity values. Changes in porosity across the square points in figure 5-50 can be visualized as a log in Figure 5-51, however, the large change in Vp occurring along constant resistivity value are due to lithologic changes and you move from the upper to middle Viola "B".

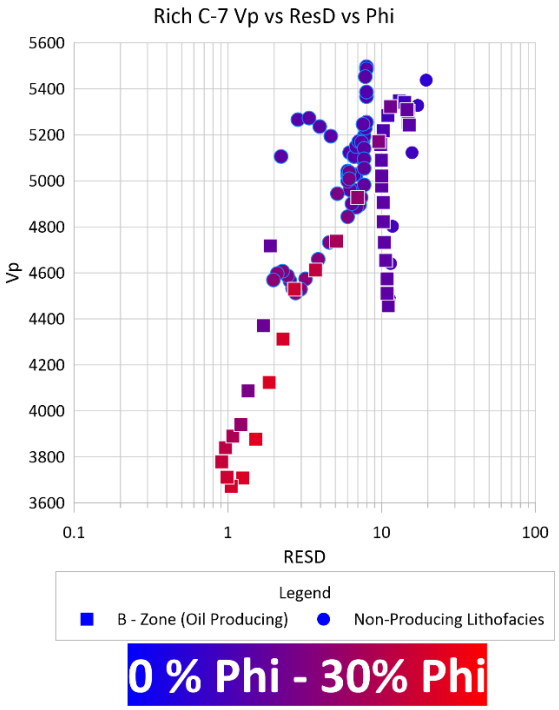

Figure 5-50: Rich C-7 tri-data cross plot.

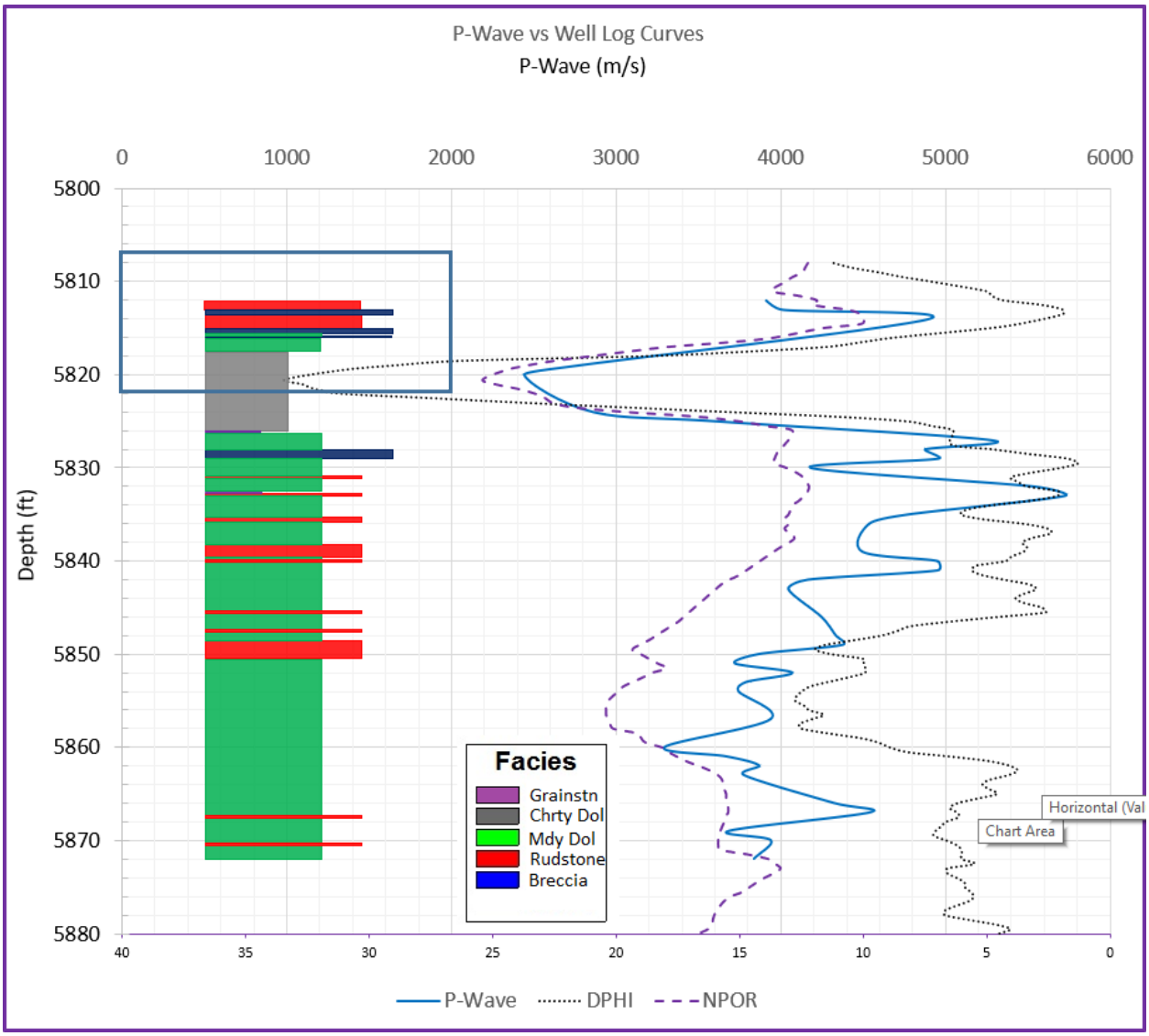

Figure 5-51: Rich C-7 perforated zone (blue square) and how it related to porosity, velocity, and lithology (Hagood, 2019).

Figure 5-52 depicts the tri-data cross plots for Stephens 1 and 4. Stephens 1 has a similar distribution of pay-zone points as Rich C-7, constant resistivity is at 20 ohms, minimal change in porosity, yet a moderate distribution of Vp across the interval. This again may be due to lithological changes, as calcite increases and decreases across the reservoir, or it can also be due to hydrocarbon saturation, where the slower points are richer in hydrocarbon. Stephens 4, however, displays lower resistivity and higher porosity, with two distinct groups of data points in

respect to resistivity (one between 4-10 ohm, with higher porosities, and another ~20 ohm, with lower porosities). This could be due to higher porosity values being wetter and producing more brine, compared to lower porosity reservoir which might be more hydrocarbon rich. Such observations may yield to better understanding the fluid properties of the hydrocarbon reservoir.

Lastly Figure 5-53 uses the same data parameters applied to the non-producing Stephens 8 and 10 wells. It shows the expected inverse relation between porosity and velocity. Higher porosity (warmer) points seem to be mostly at the bottom of the graph, correlating with slower velocity. Resistivity values for these wells resemble those from Rich C-7 and other producing wells, despite lower porosities in comparison to Stephens 1 and 4. Lack in production could be due to lower porosity values, which prevent hydrocarbons from accumulating in the pore spaces.

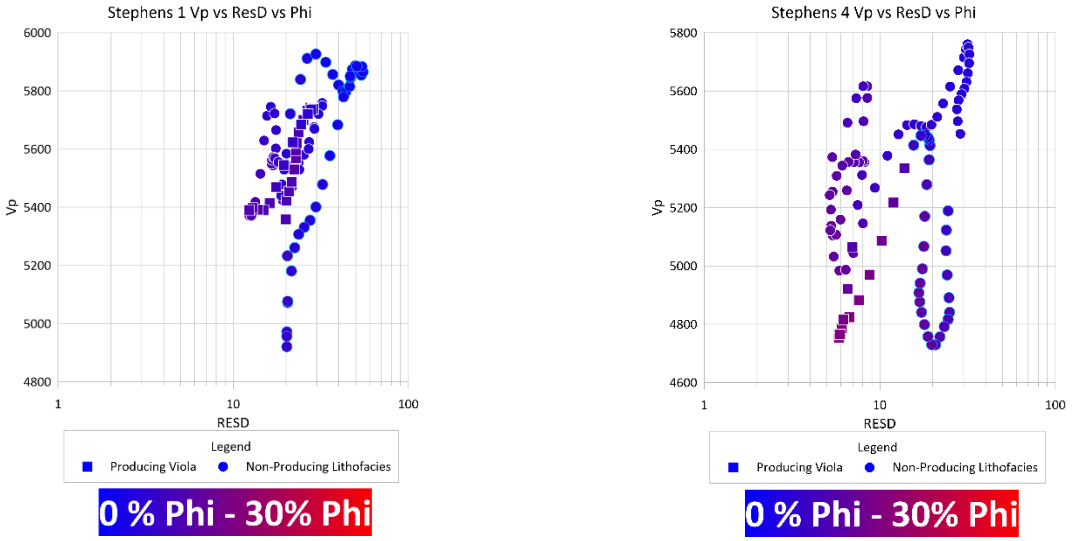

Figure 5-52: Viola producing wells Stephens 1 and 4 tri-data cross plots.

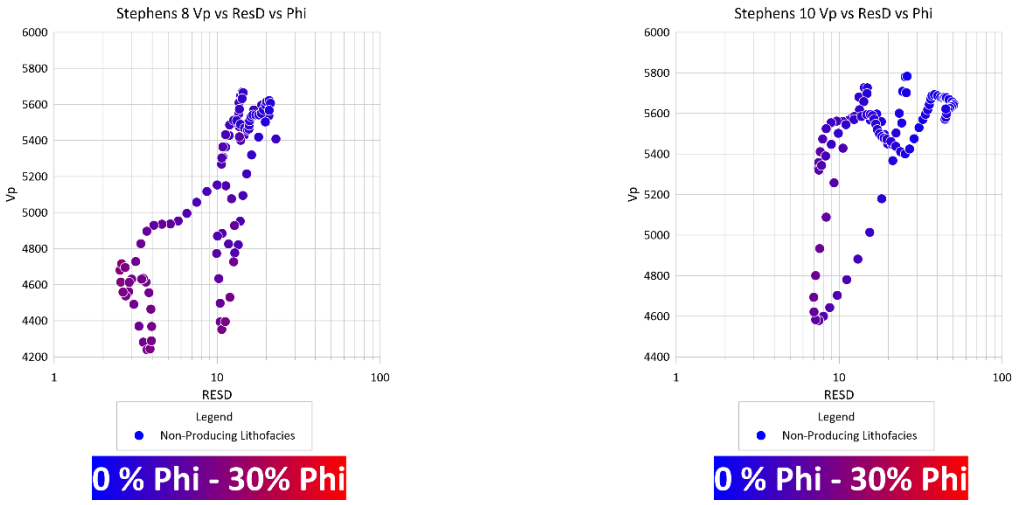

Figure 5-53: Viola non-producing wells Stephens 8 and 10 tri-data plots.

Cross plots such as the figures above provide insights to what log properties can most closely identify productive facies in a well. They also provide data to compose synthetic logs for well-to-seismic ties in 3D modeling for exploration. Most velocity responses are due to porosity variance; however, velocity occasionally will not follow porosity but move independently, which could be due to lithological changes affecting density, producing a slowing-effect on velocity, or due to a velocity response to hydrocarbon saturation (Simm and Bacon et al., 2014).

Gassmann fluid replacement modeling may identify how velocity or density changes are affected by a change in pore fluid, in terms of change in magnitude, rather than relative values. Mineral composition may also be a primary catalyst for velocity change within the Viola, depending on the amount of silica (chert) or dolomite present due to a lower mineral density (Mavko et al., 1998). Lastly, porosity effect may provide clarity on lithological composition as a function of P-wave velocity.

The results presented above provide insights into the response expected in seismic data, not only to track the Viola (which can be particularly thin in certain areas), but to also determine if fluid has a measurable effect on compressional velocity.

5.4 Effects on Effective Porosity and Mineral Composition Effects on Seismic Velocity

Changes in lithology within the Viola are associated with changes in porosity. Hagood (2019) showed the lithologic diversity of this unit, which can also be seen in elastic and well log data. Since lithologic variation within the Viola affects porosity and density usually in a linear fashion, a better understanding of the effect lithology has on porosity provides a more accurate interpretation of fluid replacement and seismic modeling.

5.4.1 Photoelectric Lithology

Lithological proportions based on Doveton's (2017) analysis are used in fluid replacement, but also provide insight on effective porosity within the Viola. In this analysis, porosity is considered as part of the total composition..

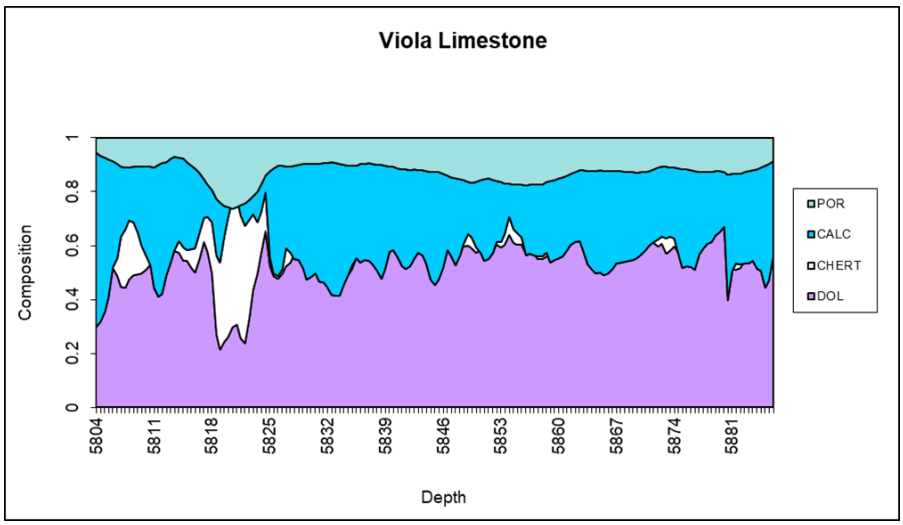

Figure 5-54: Total composition of the Viola in Rich C-7, calculated as the relative proportion of each component to a total (in the Y axis) in relation to depth (X axis).

Figure 5-54 is a total composition analysis of the Viola Limestone in Rich C-7. Chert is more abundant between 5818 and 5824 ft., representing the "B" Zone and production interval for the well. Core samples at that location indicate large amounts of porosity ranging from 16% to 28% in the physical sample (Hagood, 2019), also indicated by density and neutron log data that coincides with slowing response in sonic logs, as shown in the previous sections. Most notably, dolomite holds a relative majority across the interval which is expected seeing a majority of the "B" Zone is primarily comprised of dolomite. Calcite, however, is seen to inversely correlate to porosity. Where calcite is low, porosity increases, and porosity increases exponentially when silica is present as seen in the reservoir facies.

Porosity within the Viola "A" and "B" zones are known to be vuggy, resulting from dolomite dissolution (Hagood, 2019). Higher porosity values within this unit correlate with abundant chert, as indicated by Hagood (2019) and Richardson (2013). The seismic slowing effects in the "B" Zone, resulting from higher porosity related to chert content, provides a different result in fluid replacement than what a primarily dolomitic reservoir would provide.

Stephens 1, 4, 8, and 10 depict similar results (Figure 5-55), where Stephens 1 and 4 are producing and Stephens 8 and 10 were non-producing wells. Stephens 1 has high, above baseline porosity (i.e. porosity native to a majority of dolomite) where chert is present at 6443 ft., and below baseline porosity where calcite is more abundant. This observation is valid for all four wells, producing or not. High percentages of calcite directly correlate with lower porosity, higher dolomite provides functional porosity, and highest porosity values occur when chert is present. However, it is suspected Stephens 1 contains poorly quality controlled data by the operator from the wireline logging tool. The abundance of chert is due to incorrect baseline correction.

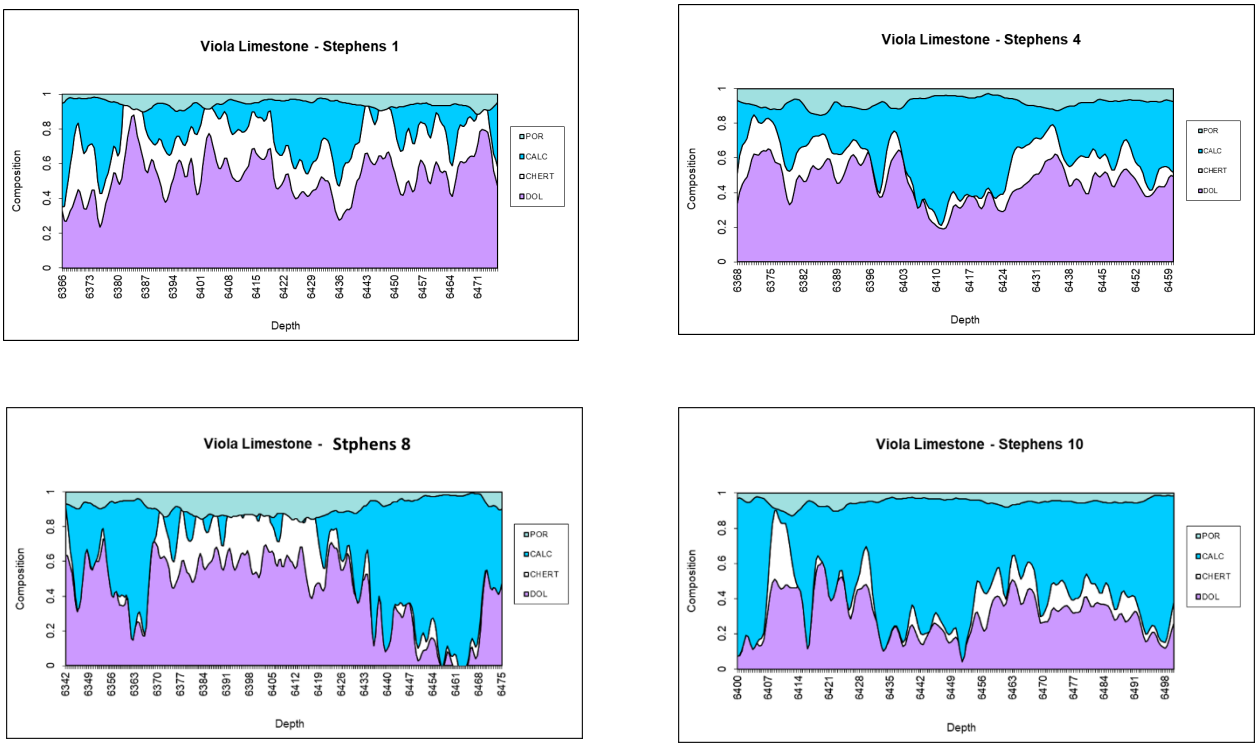

Figure 5-55: Lithological analysis (including porosity) for Stephens 1, 4, 8, and 10 wells All four components are reported as relative proportions (in percentage) relative to a total (Y axis) along well depth (X axis).

5.4.2 Lithological Effects on Effective Porosity

As shown in section 5.4.1, lithologic composition plays a major role in porosity abundance. This relation was further explored through well log analysis, evaluating neutron porosity in relation to density porosity in producing and non-producing wells (Figure 5-56). Each graph in this figure is composed of three data sets. In addition to neutron and density porosity, relative abundance of specific minerals is shown as a color gradient. Dark red indicated 0% of the mineral at that point in the log, and lighter values are closer to 50%, with light red below fifty and light blue above fifty percent. Dark blue color indicates 100% of the mineral.

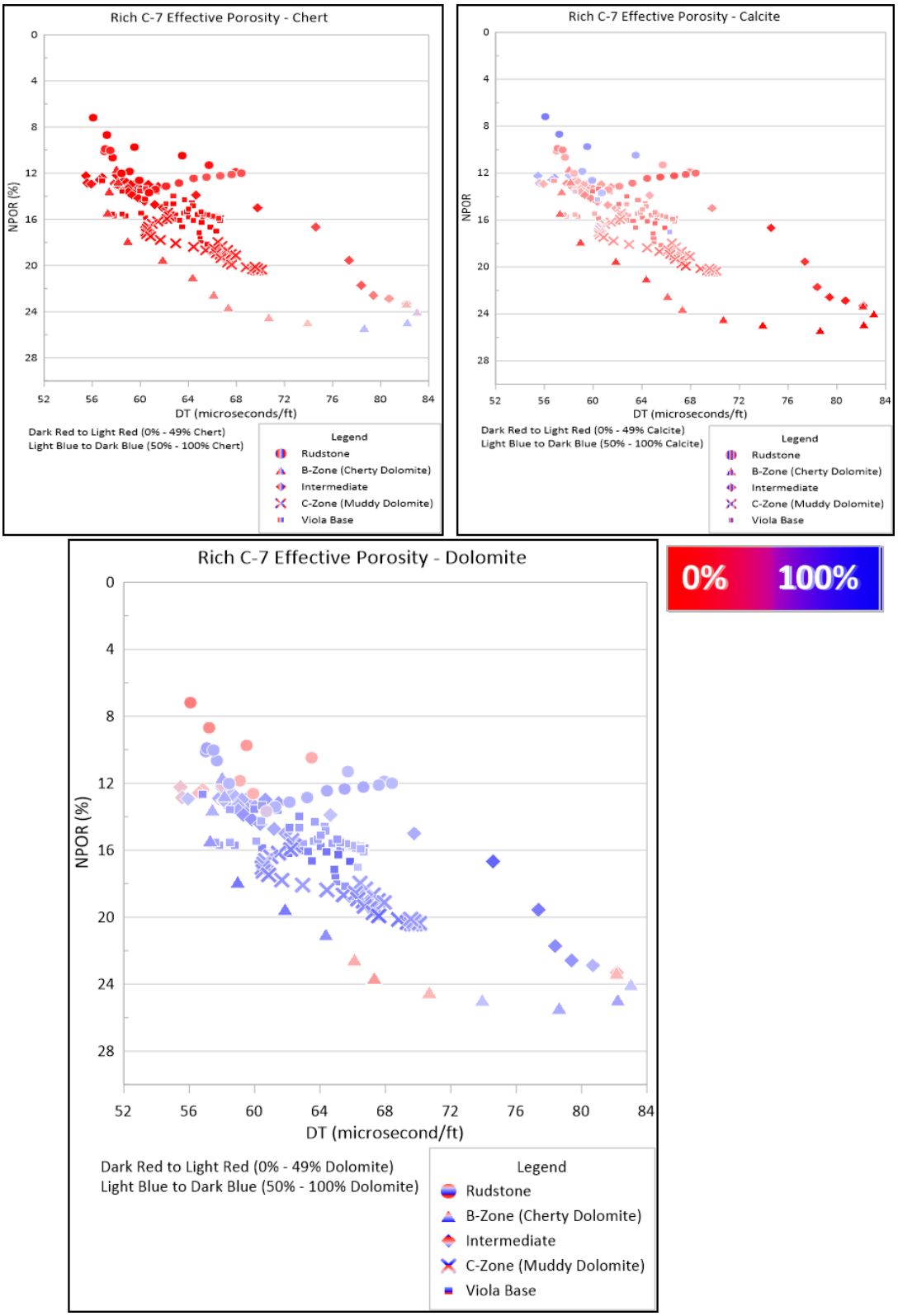

Figure 5-56: Mineral composition in relation to neutron and density porosity in Rich C-7. Mineral composition is shown as a gradient in each figure for dolomite, calcite, and chert.

Each graph in Figure 5-56 looks at a specific mineral within the total composition of the Viola. Chert occurs in higher percentages (closer to 50%) in areas of higher porosity, while the proportion of dolomite is high across the core. Calcite is inversely proportional to porosity, as calcite is lowest (dark red) in areas of high porosity and highest (light red and blue) in areas of lower porosity.

The same type of plot is done for producing wells Stephens 1 and 4 (Figures 5-57 and 5-58). Both wells display higher proportion of dolomite and lower proportion of calcite in higher porosity. Both Stephens 1 and 4 have minor chert proportions at higher porosities, with Stephens 1 displaying almost no chert in producing zones. This may explain why this well produces thirty-thousand barrels of oil less than Stephens 4. Notably, Rich C-7 outproduced all of the Stephen's wells in this project combined. Rich C-7's unique feature compared to Stephens 1 and 4 is its high chert content contributing to porosity.

The results for non-producing wells Stephens 8 and 10 can be seen in figures 5-59 and 5-60. Similar to what is seen for producing wells, in non-producing wells calcite occurs in high proportions where porosity lower porosity, while dolomite is higher where porosity is greater. Chert is slightly higher at higher porosities, though not as much as in Rich C-7. The greatest difference between the producing and non-producing wells is the abundance of calcite within the sections. Non-producing wells have higher proportions of calcite than producing wells which could play a negative role in production. Rich C-7 has very little calcite, perhaps affecting hydrocarbon saturation due to the inverse effect of porosity and calcite. Stephens producing wells, compared to Rich C-7 which also produces, have much less chert. Chert content in Rich C-7 correlates with porosity and potentially affects hydrocarbon saturation, since both Stephens

1 and 4 did not produce more than one-hundred thousand barrels of oil, while Rich C-7 produced over three-hundred thousand barrels of oil.

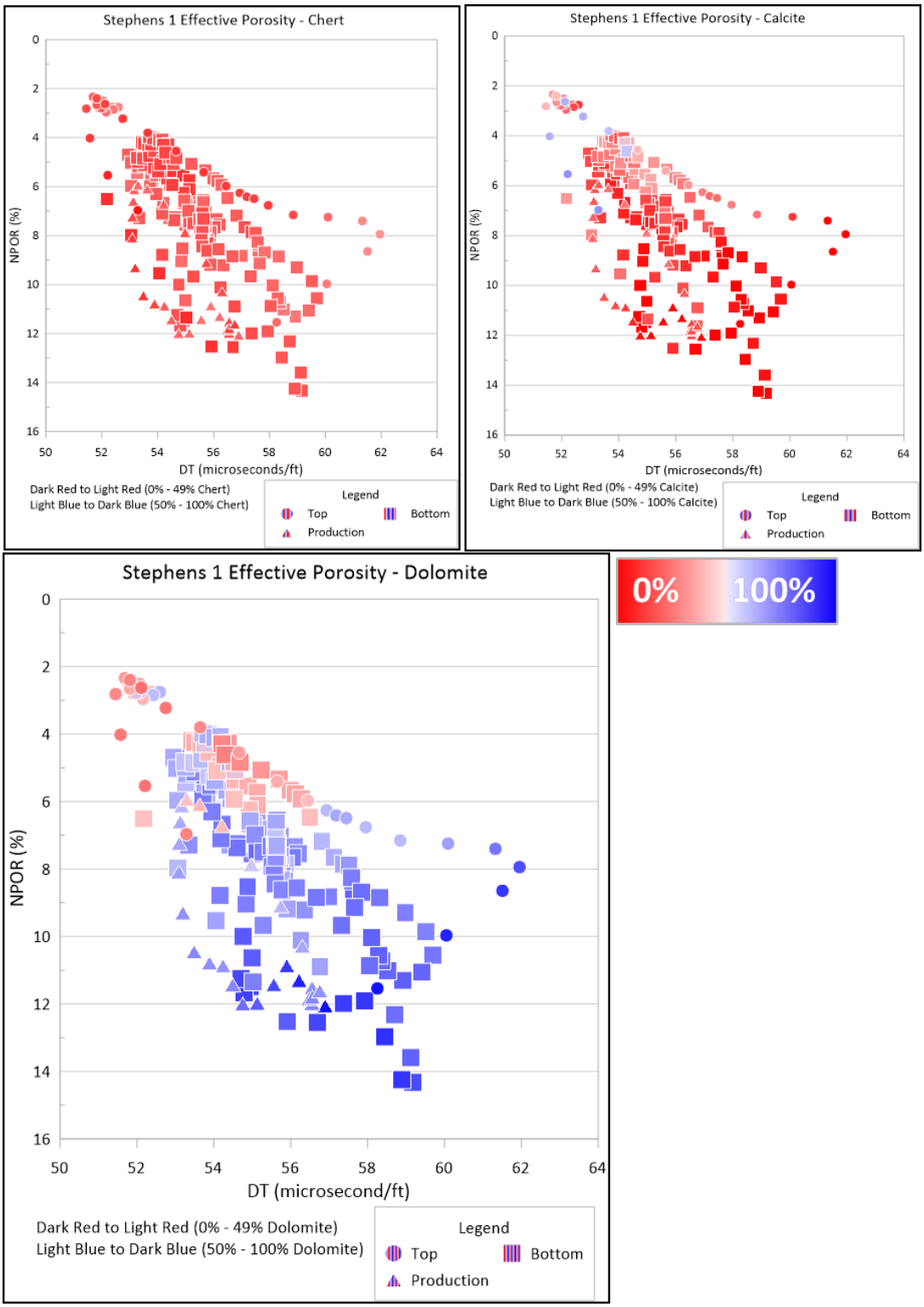

Figure 5-57: Mineral composition in relation to neutron and density porosity in Stephens 1. Mineral composition is shown as a gradient in each figure for either dolomite, calcite, or chert.

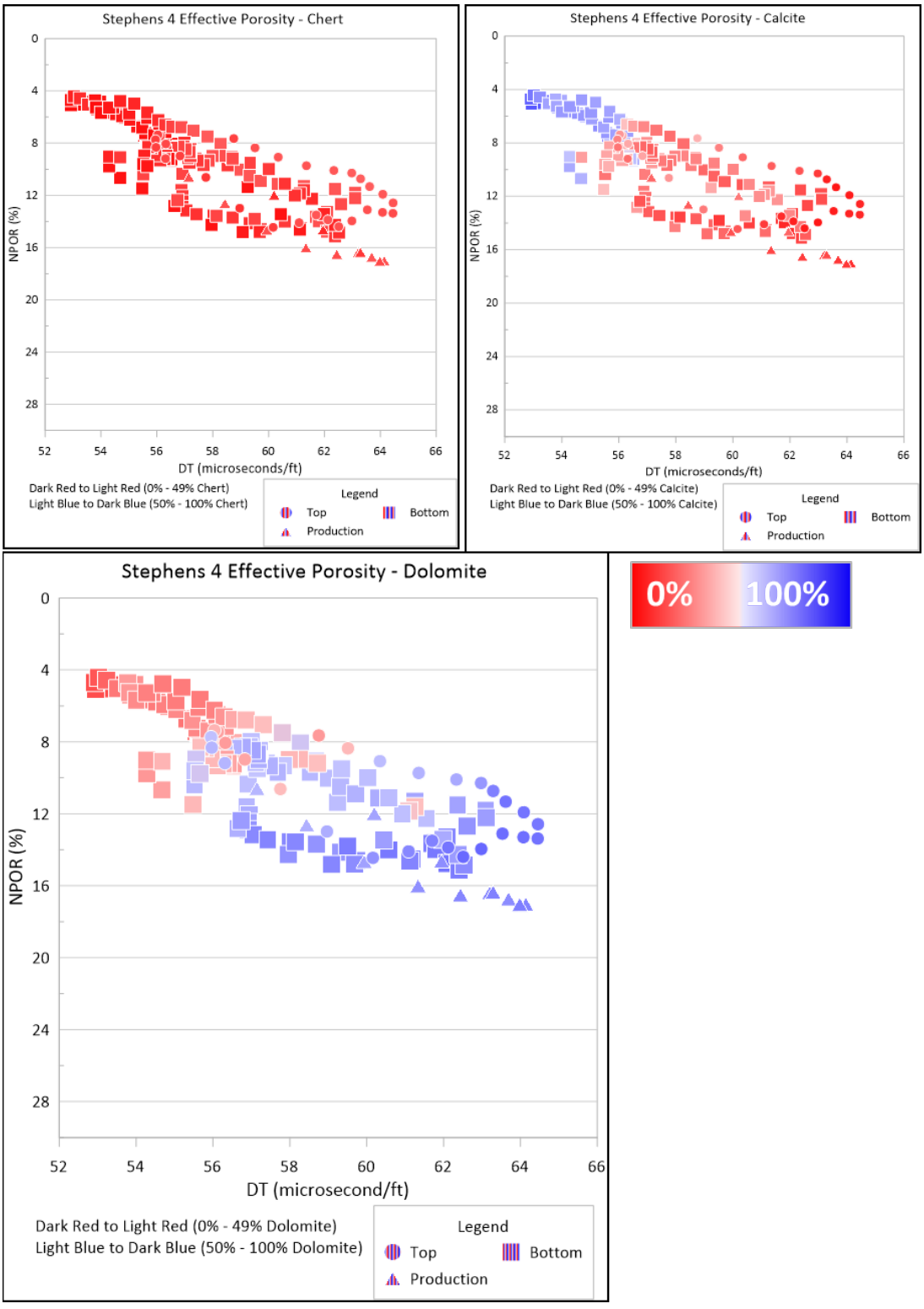

Figure 5-58: Mineral composition in relation to neutron and density porosity in Stephens 4 using neutron and density porosity. Mineral composition is shown as a gradient in each figure for either dolomite, calcite, or chert.

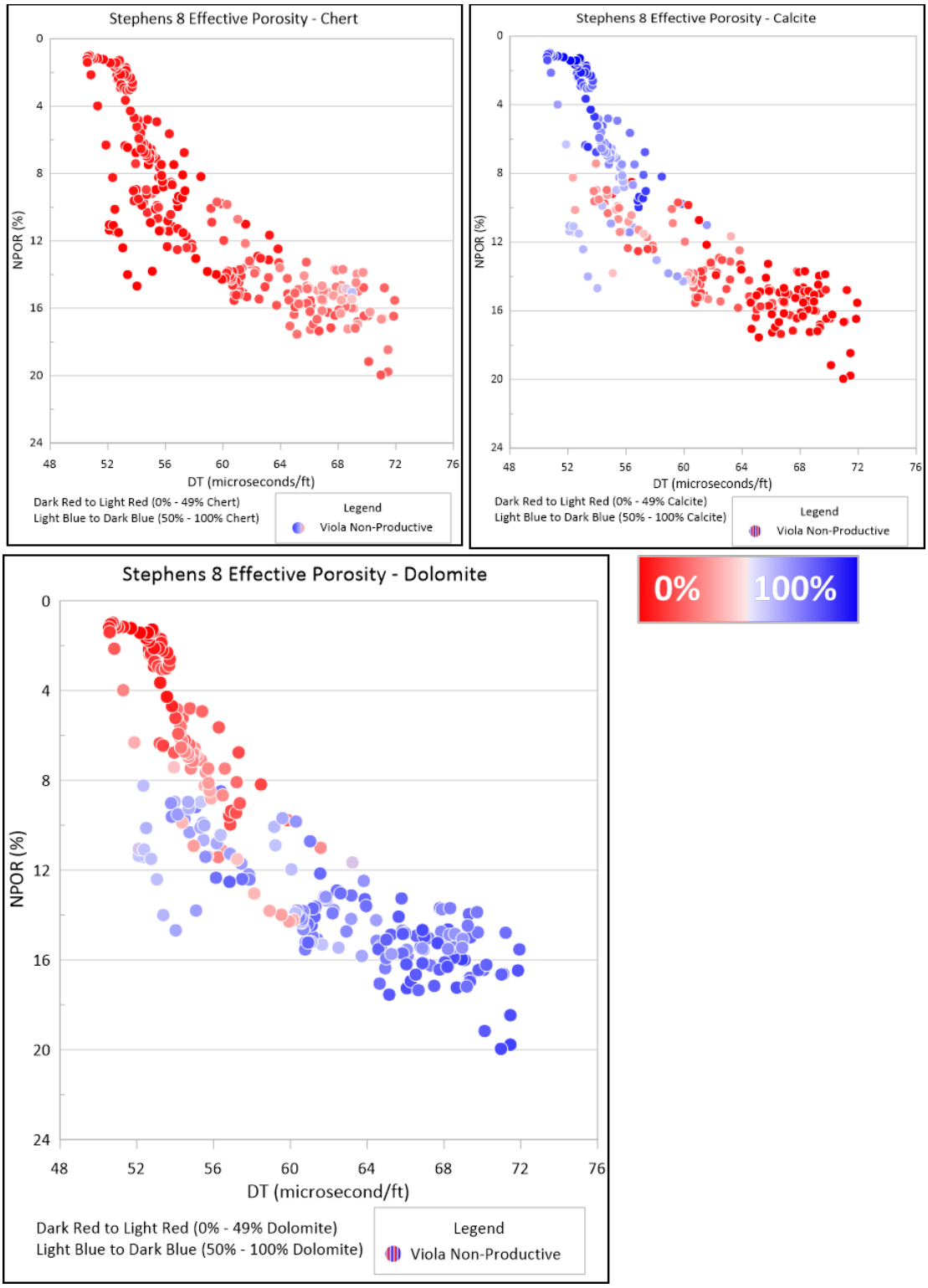

Figure 5-59: Mineral composition in relation to neutron and density porosity in Stephens 8 using neutron and density porosity. Mineral composition is shown as a gradient in each figure for either dolomite, calcite, or chert.

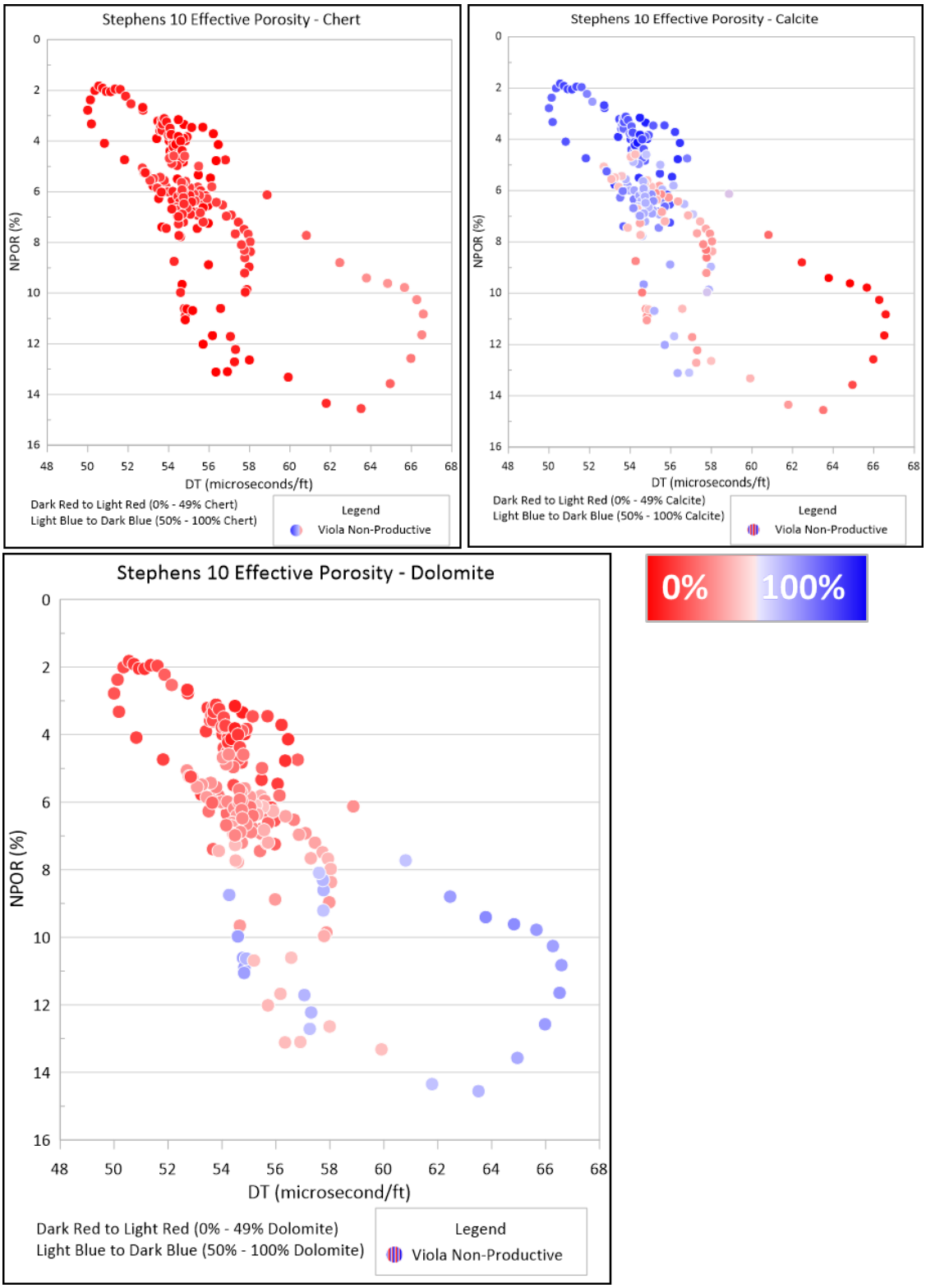

Figure 5-60: Mineral composition in relation to neutron and density porosity in Stephens 10. Mineral composition is shown as a gradient in each figure for either dolomite, calcite, or chert.

5.5 Gassmann's Substitution

The results obtained in Gassmann Fluid Replacement modeling include analysis of the 1) effective minerology, considering brine- vs. oil-bearing reservoir facies (Figures 5-61 to 5-64 & tables 5-7 to 5-9), 2) variance of velocity, density, and acoustic impedance as a function of porosity for a producing and non-producing zone within the Viola (Figures 5-65 to 5-66), 3) oil saturation contrast for dolomite, limestone, chert and a 70% chert/ 30% dolomite lithological composition (Figures 5-67 to 5-76), and 4) comparability of fluid replacement responses to well logs within the Viola for Rich C-7 (Figures 5-77 to 5-81) .

Four different depth intervals along the core were selected to conduct fluid replacement modeling. These depths were 5810 ft (above the indicated pay interval), 5815-5816 ft (within the perforated zone at the top of the "B" zone), 5820-5821 ft (at the base of the "B" zone), and 5823-5824 ft (within the muddy dolomite underlying the "B" zone). These intervals were selected to show the diverse effects that fluid replacement modeling has on the Viola, within the "B" zone and in surrounding rocks.

Interpretation of the results are focused on the change expected when hydrocarbons are present within the Viola, including the sonic and seismic response of pay zones, along with what drives porosity and hydrocarbon saturation, to better understand its production potential. Vohs (2016) showed that the Viola top can be isolated in seismic using impedance and frequency applied to 3-D seismic surveys, but an assessment of fluid effects on the seismic response provides a better understanding of velocity effects. Although the values provided by Gassmann's modeling are not exact, it provides a workflow and approximate relationship of reservoir characteristics as it applies to exploration questions. Lastly, let it be noted that all core depths are four feet below logging depth. Therefore a depth correction was applied when comparing values

obtained in Gaussman's modeling to responses in the Rich C-7 well log. The perforated depth focused on is 5818-5822 ft. log depth which is covered within testing.

5.5.1 Brine bearing vs Oil-Bearing reservoir facies (Effective Minerology)

Effective results in Gassmann fluid replacement modeling requires specific inputs. Table 5-7 lists all the inputs used for each interval modeled in Rich C-7. P-wave (Vp) and S-wave (Vs) velocities are in meters per second, bulk density is in grams per centimeter squared, porosity is in percent, compressibility is the inverse of bulk modulus in Pascals, and lithological density is in kilograms pre centimeters squared.

Depth	Vp Sw (m/s)	Vs Sw (m/s)	Rho Sw kg/m³)	Phi (%)	1/K (Pa)	Litho Rho (kg/m³)
Effective						
5810	5746	3389	2681	0.07	1.20E-11	2774
5815	3555	1886	2260	0.24	1.51E-11	2646
5816	3319	1649	2100	0.26	1.62E-11	2619
5820	3414	1527	2320	0.17	1.26E-11	2752
5821	3690	1730	2360	0.13	1.20E-11	2774
5823	5266	3217	3052	0.07	1.23E-11	2740
5824	5299	3100	2983	0.05	1.17E-11	2792

Table 5-7: Input data loaded for each sample in Gassmann's interactive spreadsheet.

Table 5-8 lists the mineral composition data used in Rich C-7. Sample 5816 ft has highest chert content, being within the "B" Zone, while samples 5821 ft and 5824 ft have the highest amount of calcite occurring at the bottom of the "B" Zone and underneath the 'B" Zone, respectively.

Depth	Dolomite %	Chert %	Calcite %	Rho_o (kg/m^3)	Rho_o (g/cm^3)	K_o (GPa)	K_o (Pa)	$1/K_o$
5810	0.58	0.08	0.34	2.77	2774.00	83.23	8.32E+10	1.20E-11
5815	0.39	0.35	0.26	2.65	2646.40	66.08	6.61E+10	1.51E-11
5816	0.51	0.48	0.01	2.62	2618.80	61.65	6.16E+10	1.62E-11
5820	0.69	0.19	0.12	2.75	2752.00	79.64	7.96E+10	1.26E-11
5821	0.56	0.07	0.37	2.77	2774.40	83.38	8.34E+10	1.20E-11
5823	0.56	0.09	0.34	2.74	2740.10	81.60	8.16E+10	1.23E-11
5824	0.58	0.03	0.39	2.79	2792.00	85.77	8.58E+10	1.17E-11

Table 5-8: Mineral composition of each depth and it's calculated inputs used in gassmann fluid replacement modeling. These values were achieved using Doveton's photoelectric composition interactive worksheet.

Table 5-9 below provides fluid replacement results for intervals within Rich C-7. The percent change in P-wave velocity (Vp), density (Rho), and Acoustic Impedance (AI) with different oil saturation is shown for each depth in Figures 5-61 to 5-66. All samples yielded lower values for the three parameters (Vp, Rho, and AI) when oil replaces brine in a system, since oil has a lower density of 0.85 g/cm^3 compared to brines, 1.09 g/cm^3. Lower densities of oil cause "slowing" and "brightening" effects in seismic due to its lower acoustic impedance compared to surrounding lithofacies. Hence, the importance of determining effective lithology within each selected depth along Rich C-7.

Depth (ft)	Vp Brine (m/s)	Vp Oil (m/s)	Rho Brine (g/cm^3)	Rho Oil (g/cm^3)	AI Brine	AI Oil
5810	5745	5687	2.68	2.66	15.41	15.15
5815	3555	3476	2.26	2.20	8.04	7.66
5816	3319	3228	2.10	2.04	6.97	6.58
5820	3414	3254	2.32	2.28	7.92	7.42
5821	3690	3501	2.36	2.33	8.71	8.15
5823	5265	5188	3.05	3.04	16.07	15.75
5824	5299	5181	2.98	2.97	15.81	15.69

Table 5-9: Rich C-7 Gassmann data across seven selected depths. Data includes P-wave for brine saturated and oil saturated, bulk density for brine and oil saturates, and acoustic impedance for brine and oil saturated.

Figure 5-61 shows fluid replacement results for the sample at 5810 feet. Porosity is relatively low compared to the rest of the “B” zone at seven percent (Table 5-7) and chert content is negligible (Table 5-8). Percent change grows along a nearly linear path, as oil is substituted into the system, with a maximum of 2% change. This is an expected response for lithofacies with non-reservoir characteristics (Simm and Bacon, 2014), since the low porosity provides a conduit for change of velocity characteristics, but with minimal seismic response..

The fluid replacement response at 5815 feet (Figure 5-62), within the hydrocarbon-bearing zone, shows a five percent change in impedance , and over two percent change in density and velocity to higher values, with density can be seen changing at a faster rate than compressional velocity. Porosity at these depths is twenty-four and twenty-six percent (Table 5-7), and the changes could be due to the fluid response of hydrocarbons within pore-space in comparison to brine (Simm and Bacon, 2014), highlighting the effects hydrocarbons have on highly porous intervals within the Viola. High percent changes in acoustic impedance provide promising results in utilizing Gassmann fluid replacement data to determine reservoir quality in the Viola Limestone, along with direct hydrocarbon indicators in 3-D seismic. These indicators would include the identification of oil-water contacts, dimming due to velocity slowing from hydrocarbon saturation, and velocity slowing due to an increase in porosity and decrease in density due to chert.

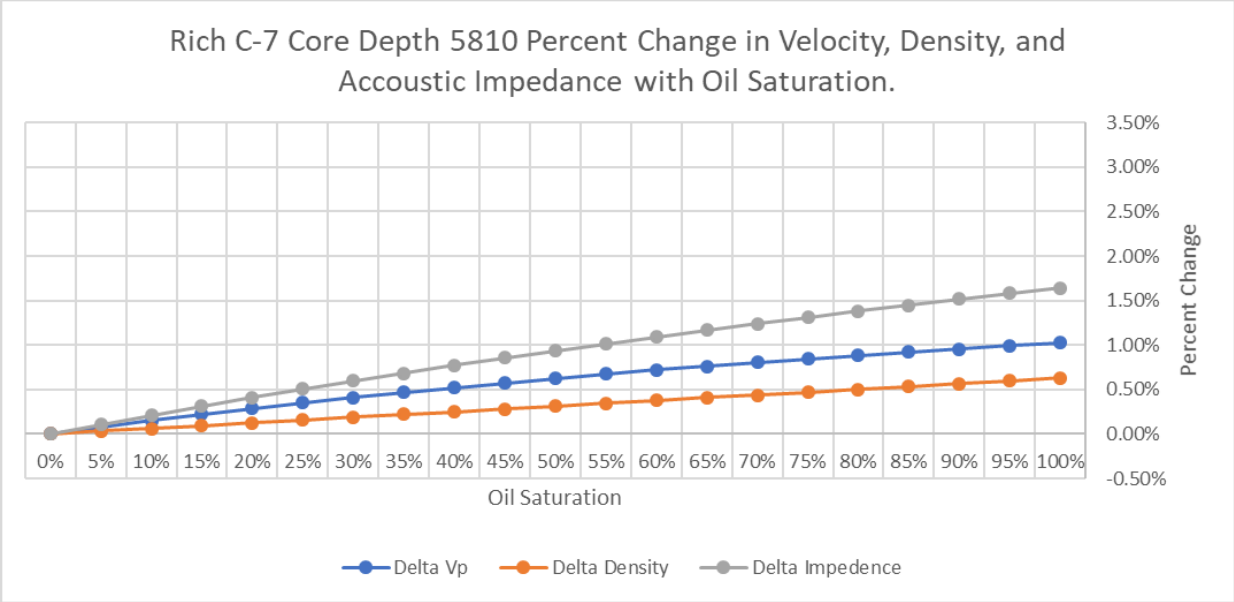

Figure 5-61: Fluid replacement percent change in Vp, density, and impedance plotted in correlation with oil saturation at 5810 ft. within Rich C-7.

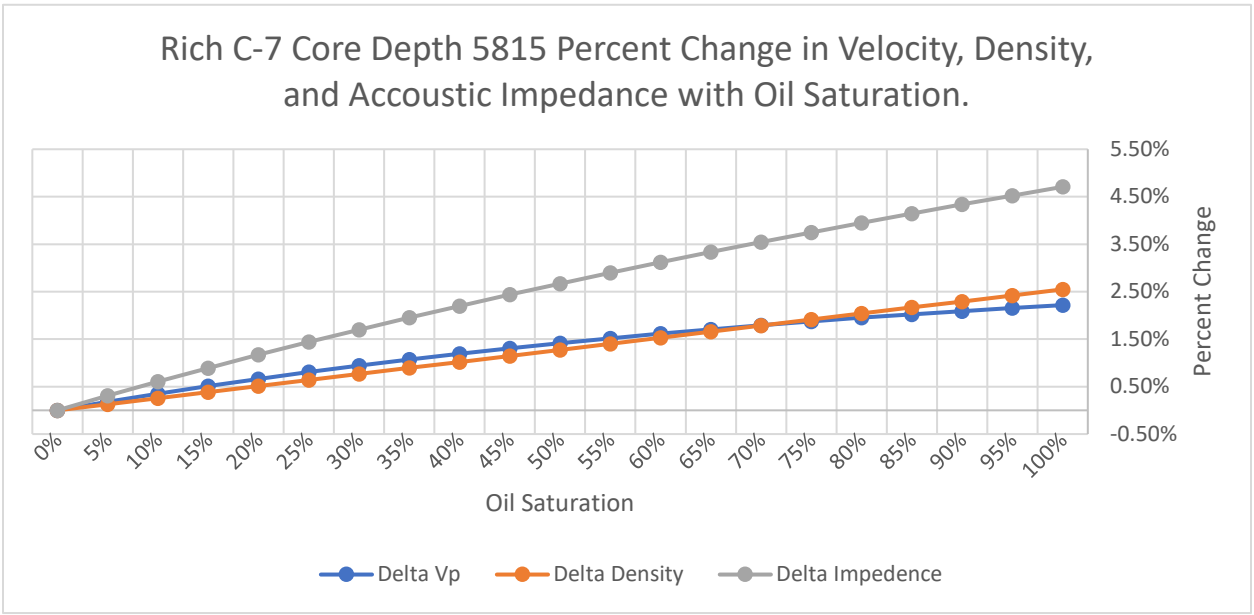

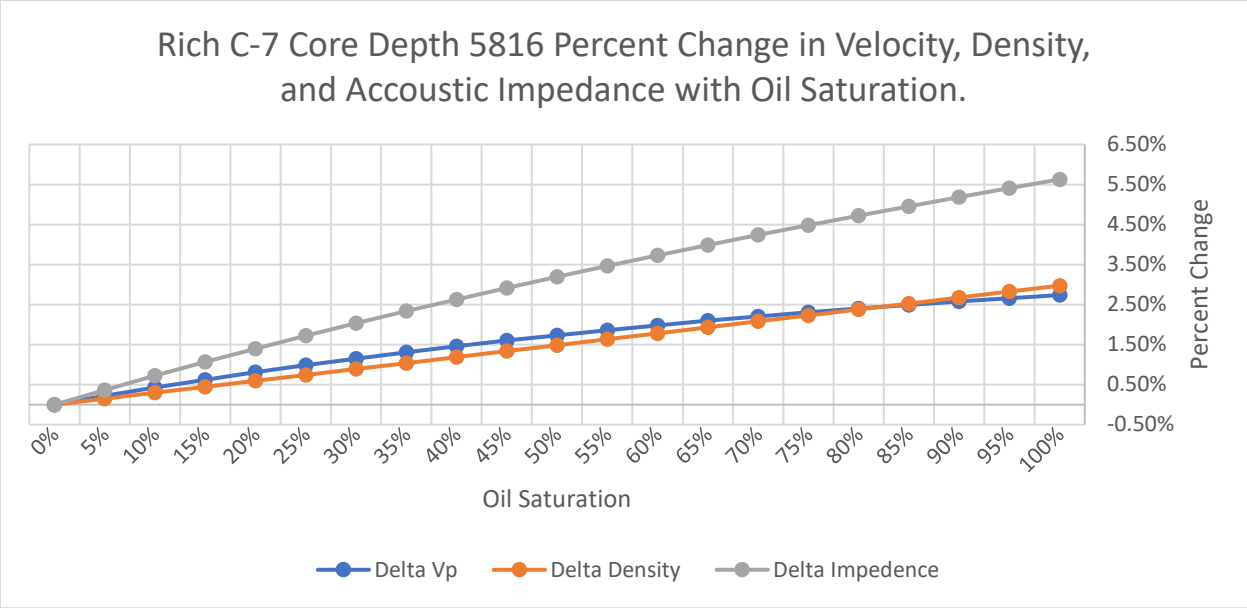

Figure 5-62: Fluid replacement percent change in Vp, density, and impedance for different oil saturation at 5815 and 5816 ft. in Rich C-7.

The results of fluid replacement in reservoir quality of the Viola at the base of the "B" zone are shown in figures 5-63 and 5-64. Porosity remains above ten percent at both depths (Table 5-7), but chert content declines as samples move out of the "B" zone. Calcite content is higher at 5821 feet, impacting porosity (Table 5-7 and 5-8). At both depths, there is significant changes in impedance (about 6%) and velocity (about 5%), with slight change in density (1.5%). This change is due to a velocity anomaly from a drop in fluid density within an abundance of porosity. At 5820 feet, density changes slightly more than 5821 feet due to higher porosity at 5821 feet allowing for more hydrocarbons. Overall change in density from hydrocarbons is smaller than the overall change in velocity. P-wave velocities change at a slightly faster rate in 5821 than in 5820 feet, possibly due to lower porosity (Table 5-7) in the former resulting from calcite cementation that provided less space for hydrocarbons. If velocity changes are related to decreased porosity due to calcite cementation, this parameter may potentially provide insights on expected responses to isolate calcite-free zones in Viola reservoir facies. This may also be a

principle due to the similar densities of calcite and dolomite in comparison to the greater difference in density of dolomite and chert. Having a sample with a lower mineral base density could be affected more by fluid than those lithofacies with higher base mineral densities.

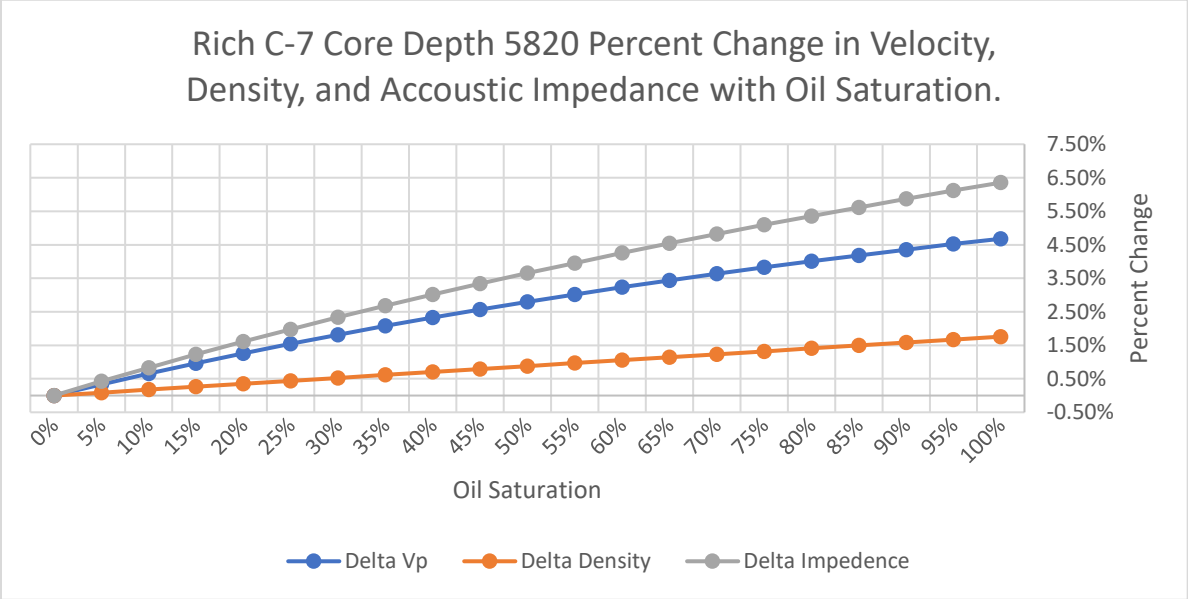

Figure 5-63: Fluid replacement percent change in Vp, density, and impedance for different oil saturation at 5820 ft in Rich C-7.

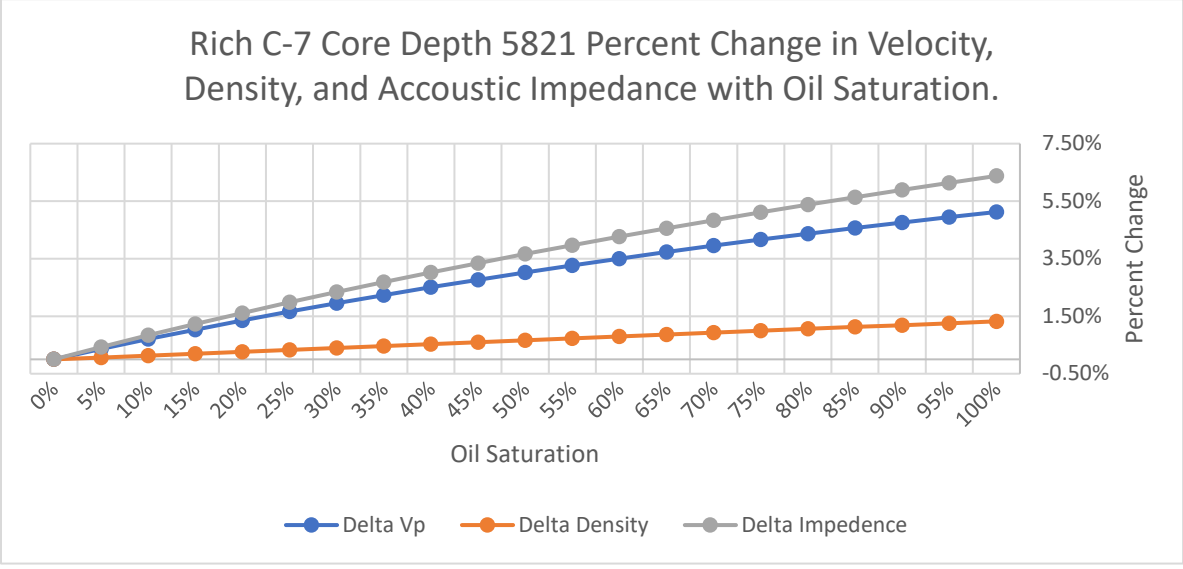

Figure 5-64: Fluid replacement percent change in Vp, Density, and Impedance plotted in correlation with oil saturation at 5821 ft. within Rich C-7.

Lastly figures 5-65 and 5-66 show the percent changes at 5823 and 5824 feet, occurring outside of the Viola “B” Zone. With porosity values lower (Figure 5-7) and density values higher than in the “B” Zone, changes in impedance are below three percent. Both samples have total density change at below a half percent and negligible velocity change. This is due to low available pore space to house fluid. The lower porosity is due to negligible chert and greater calcite contents.

The results above show that sample at 5810 feet has the lowest percent change in all three parameters. Calcite through total composition modeling and fluid replacement modeling is showing to have a negative effect on reservoir performance.

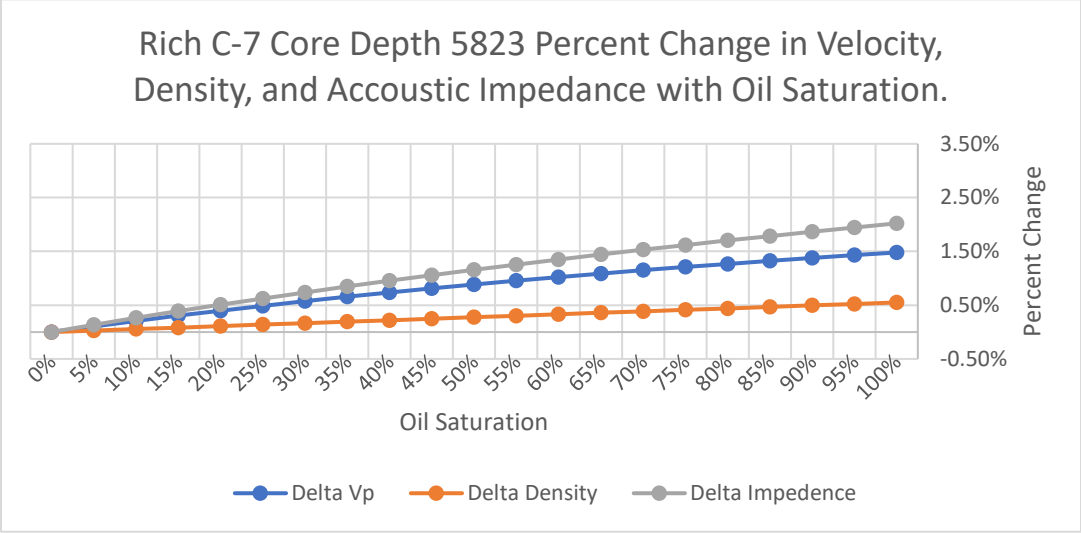

Figure 5-65: Fluid replacement percent change in Vp, density, and impedance for different oil saturation at 5823 in Rich C-7.

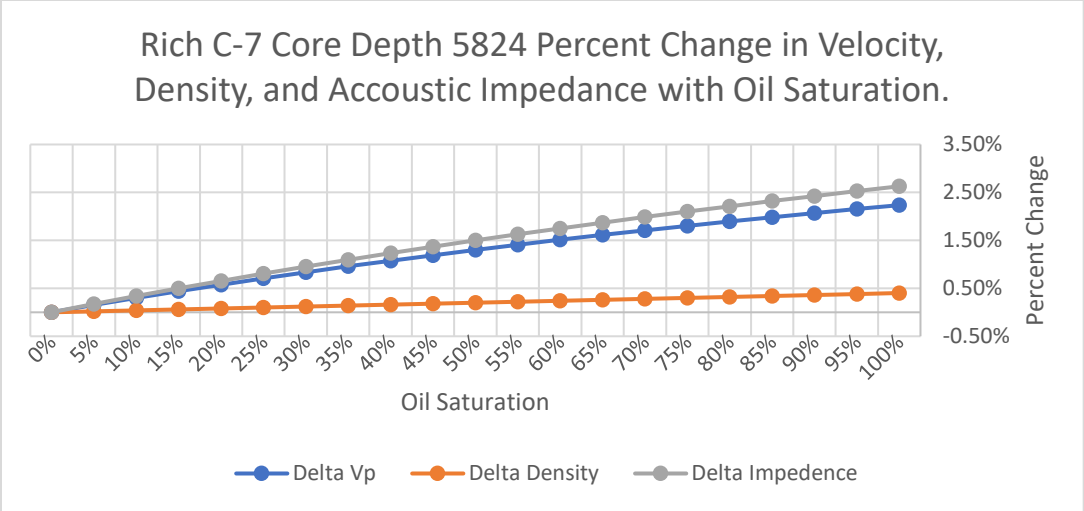

Figure 5-66: Fluid replacement percent change in Vp, Density, and Impedance plotted in correlation with oil saturation at 5824 ft. within Rich C-7.

5.5.2 Porosity Variability and Effects on Seismic Velocity

Porosities effect on fluid replacement modeling is one of the primary concerns by Wang (2001), along with quantitative effects on acoustic impedance and P-wave velocity changes within homogenous lithologies. Samples at 5815 feet and 5823 were used for the interpretation of the effect of abundance of chert and calcite in the porosity, with the former being within Viola "B" reservoir rock, and the latter being below the "B" Zone, in the low porosity muddy dolomite.

Figure 5-78 below shows results from a Gassmann porosity analysis conducted on the sample at a depth of 5815 feet within the Viola "B" Zone. Each plot symbol shape represents a different porosity, with in-situ porosity being twenty-four percent, represented by triangles. P-wave velocities taken from Gassmann analysis are cross plotted with acoustic impedance values. Hydrocarbon saturation is represented by the color gradation along the spectrum, with violet being zero hydrocarbons and all brine, and red being all hydrocarbons and no brine. In this interval, chert content is thirty-five percent and calcite is below thirty percent, with the remaining proportion being dolomite.

Porosity values (Figure 5-28) go from eighteen percent to thirty percent porosity within the Viola “B” zone. Lower porosities within the cherty section of the Viola “B” are shown to have an almost linear relationship with acoustic impedance. This is due to a proportional decrease in density as hydrocarbon saturation increases in comparison with P-wave velocity. As porosity increases linearity in the trend line begins to decay, sloping upwards into a more logarithmic trend. This trend is due to a slower change in velocity in relation to increasing impedance. Higher porosity samples experience larger changes in density when hydrocarbons are injected, in comparison to those at lower porosities at effective mineral composition. Changes in trends in relation to porosity percentages provide examples of porosity effects on acoustic impedance, density, and velocity. Seismic response would be less apparent at higher porosities but could potentially indicate hydrocarbon saturation within the Viola Limestone.

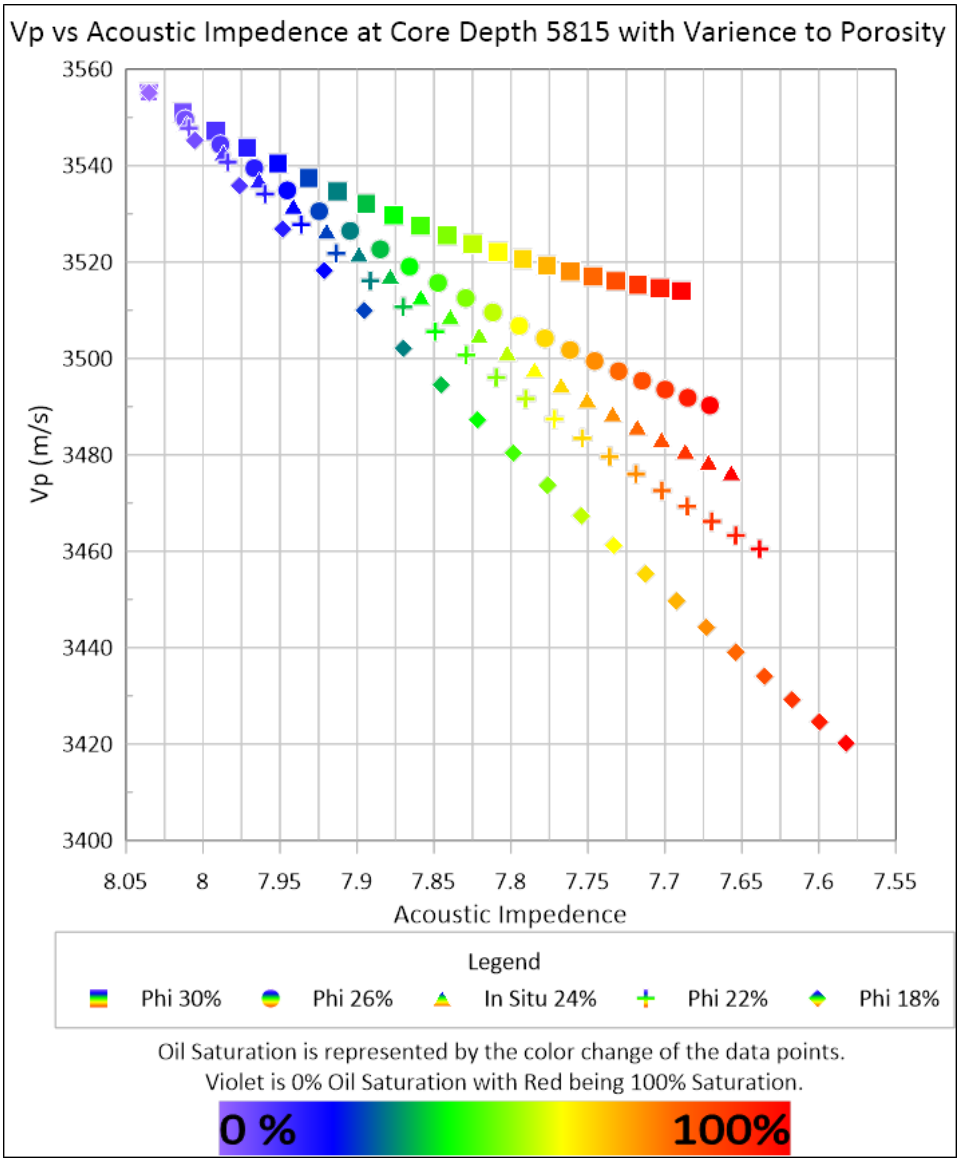

Figure 5-67: Tri-data cross plot showing the effects of changes in porosity at constant lithologies within the Viola "B" taken at 5815 feet of Rich C-7.

In comparison, the same analysis was ran from a sample at 5825 feet, below the reservoir zone. Despite similar behavior in the trend line, the magnitude of impedance change and rate of change from linear to logarithmic is significant (Figure 5-68). The linear relation continues from three to seven percent until fourteen percent, when it changes with the total change in acoustic impedance. At 5815 feet, the greatest change in impedance occurs at eighteen percent, with a

five and a half percent change in impedance, where the greatest change in impedance at 5823 feet occurs at three percent porosity at four and a half percent change in impedance. The overall change in impedance is greater within the cherty dolomite zone due to its higher porosity and mineral density compared to the muddy dolomite, which has lower porosity on average and a much lower chert content.

As shown the amount of porosity does impact fluid substitution results, however proportion of calcite and chert are seen to impact fluid substitution in relations to their respective minerology and their effects on porosity. Calcite having a negative effect on porosity and chert having a positive effect. It can also be seen that higher porosity values directly correlate to hydrocarbon saturation. Changes in density are greater than changes in velocity at higher porosities and potentially lower calcite content. Cherty dolomite makes for a superior reservoir within the Viola not only due to its high porosity, but also due to its mineralogical signature seen in impedance, density, and velocity when saturated with hydrocarbons instead of brine.

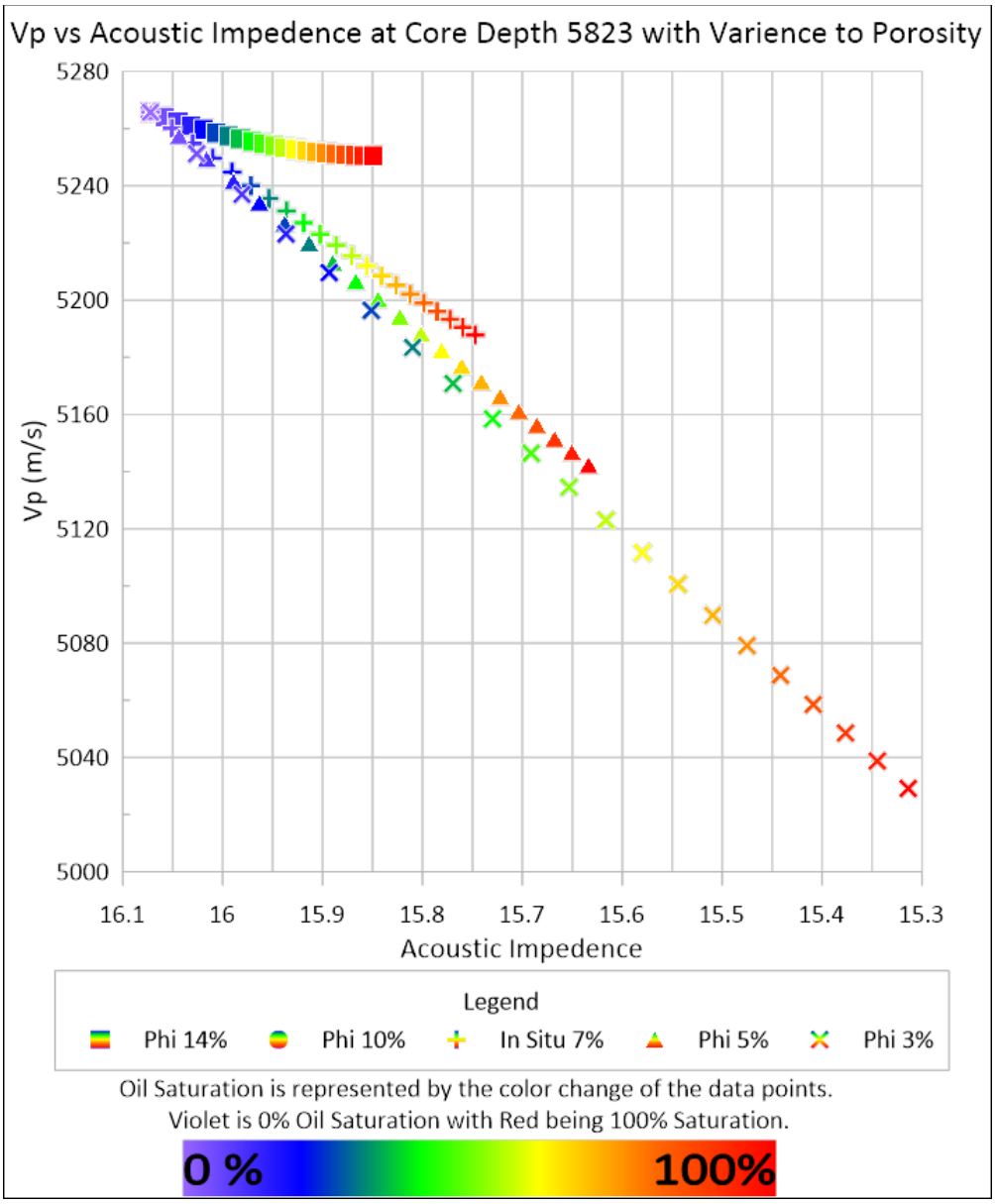

Figure 5-68: Tri-data cross plot showing the effects of changes in porosity at constant lithologies beneath the Viola "B" Zone in a muddy dolomite taken at 5823 feet within Rich C-7.

5.5.3 Lithological Control on In-Situ Porosity

With the Viola being such a mineralogically diverse formation, observing effects of different lithologic compositions in porosity at different depths is beneficial to understand the Viola “B” Zone. Figures 5-6 through 5-78 display the results of Gassmann calculations (done

with the same data and format as in the section above)for different lithological compositions at identical porosities and fluid substitution input values, applying mineral matrix density and mineral matrix compressibility. Compositions used were 100% Dolomite, 100% Calcite, 100% Chert, and a 70% Chert/ 30% Dolomite blend (Raef et al., 2019). Comparing each to effective lithology (Table 5-8) may provide more insight on P-wave velocity and density response to hydrocarbon saturation, mineral composition, and porosity. Lithofacies tested correspond to the central "B" zone at 5815 feet, and the lower "B" zone at 5820 feet.

Central "B" Zone

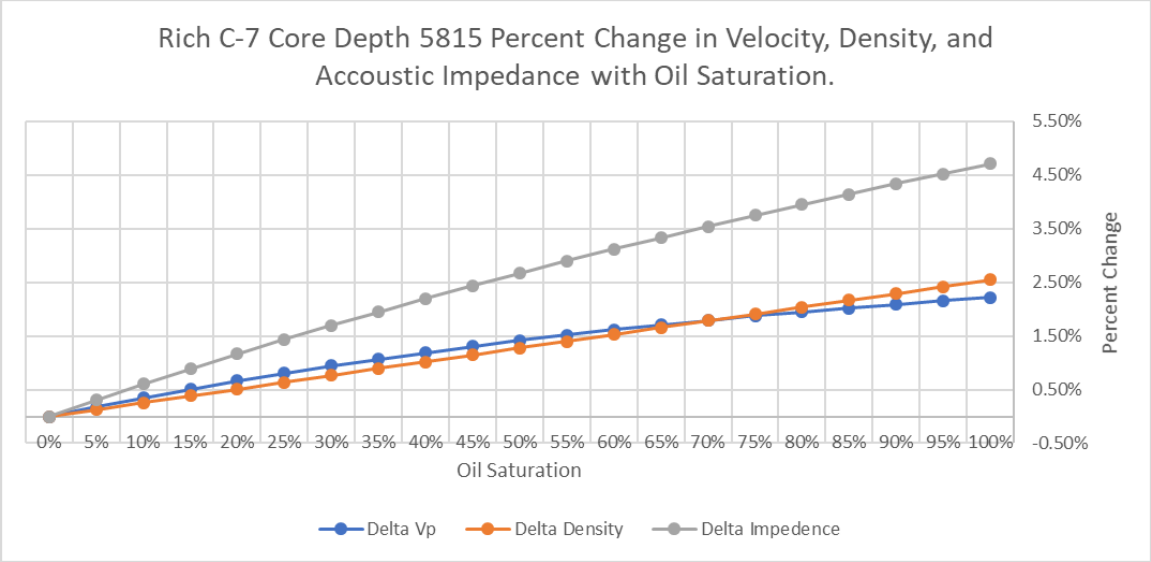

Figure 5-69: Gassmann Fluid Replacement results at effective lithology and 24% porosity (in-situ).

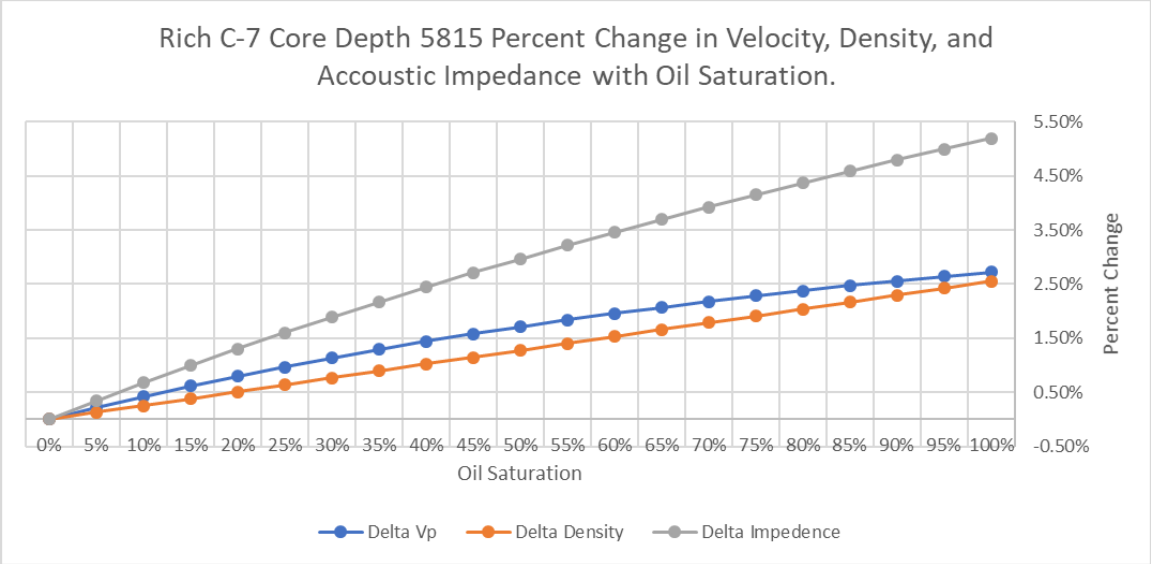

Figure 5-70: Gassmann Fluid Replacement results at 100% Dolomite and 24% porosity (in-situ).

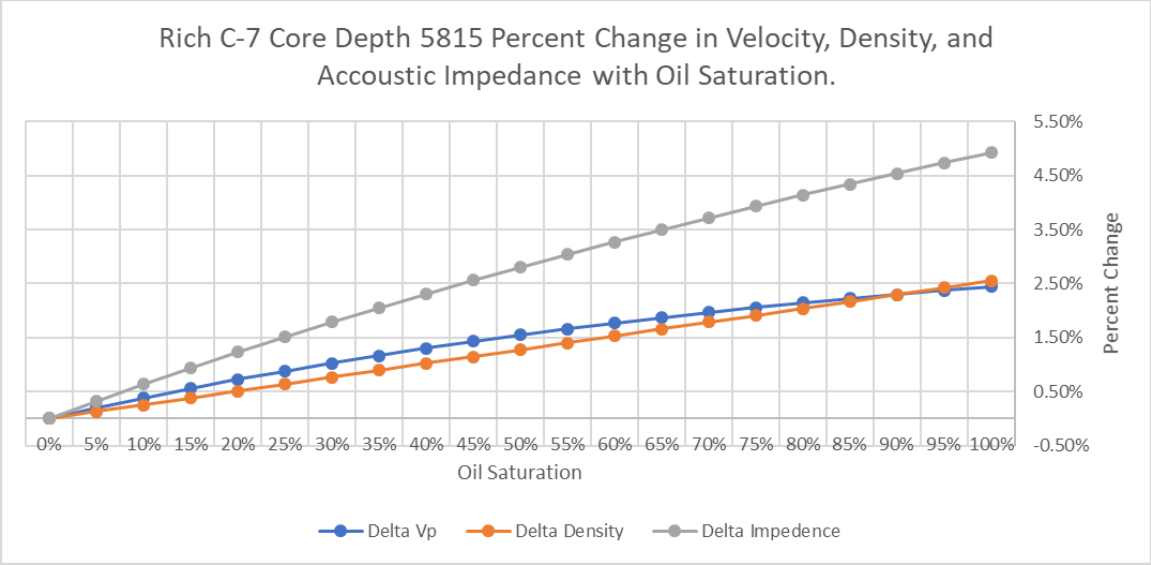

Figure 5-71: Gassmann Fluid Replacement results at 100% Calcite and 24% porosity (in-situ).

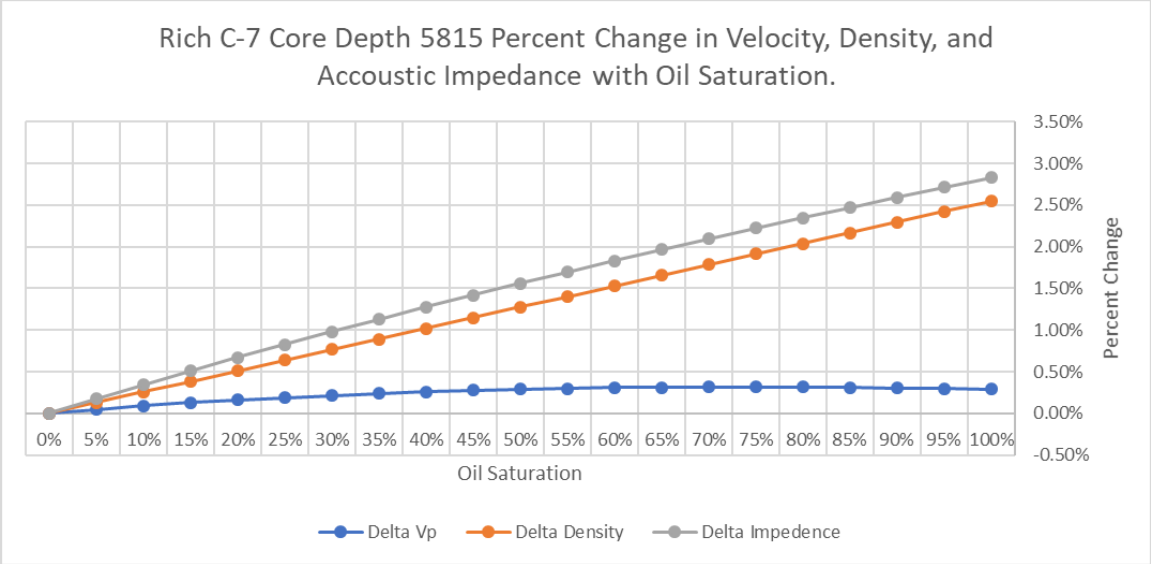

Figure 5-72: Gassmann Fluid Replacement results at 100% Chert and 24% porosity (in-situ).

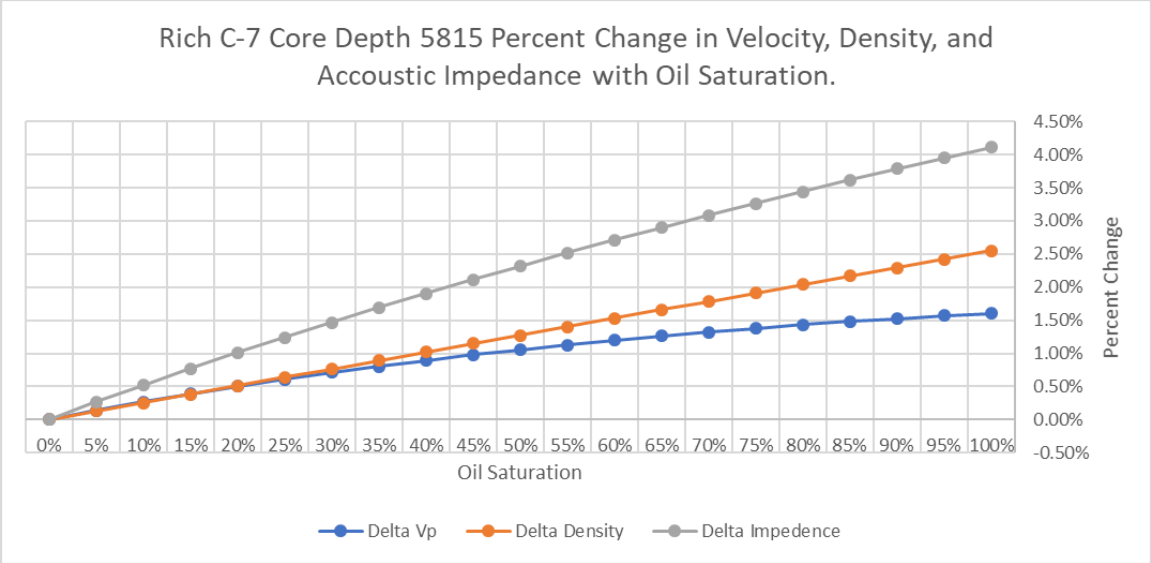

Figure 5-73: Gassmann Fluid Replacement results at 70% Chert, 30% Dolomite, and 24% porosity (in-situ).

At 100% Dolomite and Calcite the relationships of Vp and Rho are almost identical. Both have strong near linear trends, and Vp and Rho converge towards each other at high oil saturation. Vp reduces its rate of change, while Rho increases it. Dolomite and Calcite do not however fully cross (density changing at a faster rate than velocity), whereas effective lithology

does at 80% hydrocarbon saturation. As shown above this could be due to the higher porosity seen in chert rich samples. There is no decisive evidence that calcite or dolomite specifically as lithologies effect fluid replacement directly. Calcite only effect fluid replacement in a secondary manner through lower porosity values. Lastly, dolomite and calcite both have Vp and Rho percent change at around two and a half and impedance at five percent. Effective lithology has similar results with a lower total impedance change, greater density change, and lower velocity change.

Composition of 100% Chert, however, provides clear evidence of its effect on fluid replacement. If the Viola "B" was 100% Chert, density change would be the standout driver of impedance. With over two and a half percent changes in density and below half a percent change in velocity, chert has a clear effect on impedance, Vp and density, but a grand majority change in density compared to velocity. This would not be helpful in seismic exploration but paired with porosity and dolomite composition within the Viola "B". Changes in only density has much less of an effect on seismic than a combined impedance change.

Lastly a 70% Chert and 30% Dolomite lithology is a more exaggerated effective lithology with less total impedance change further solidifying the evidence of chert's effect on fluid replacement.

Lower "B" Zone

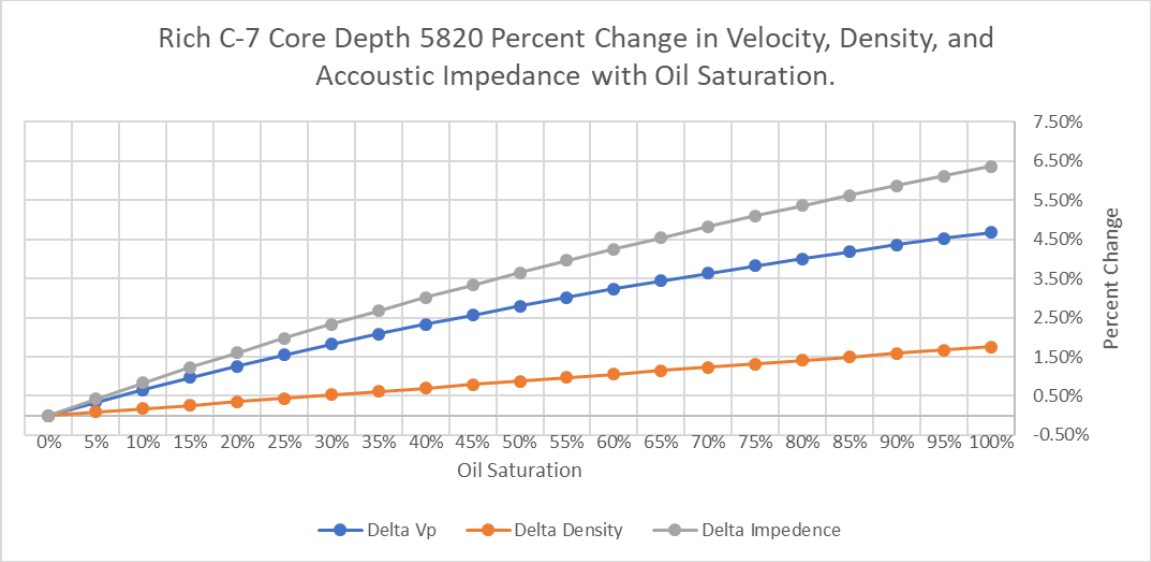

Figure 5-74: Gassmann Fluid Replacement results at effective lithologic composition and 17% porosity (in-situ).

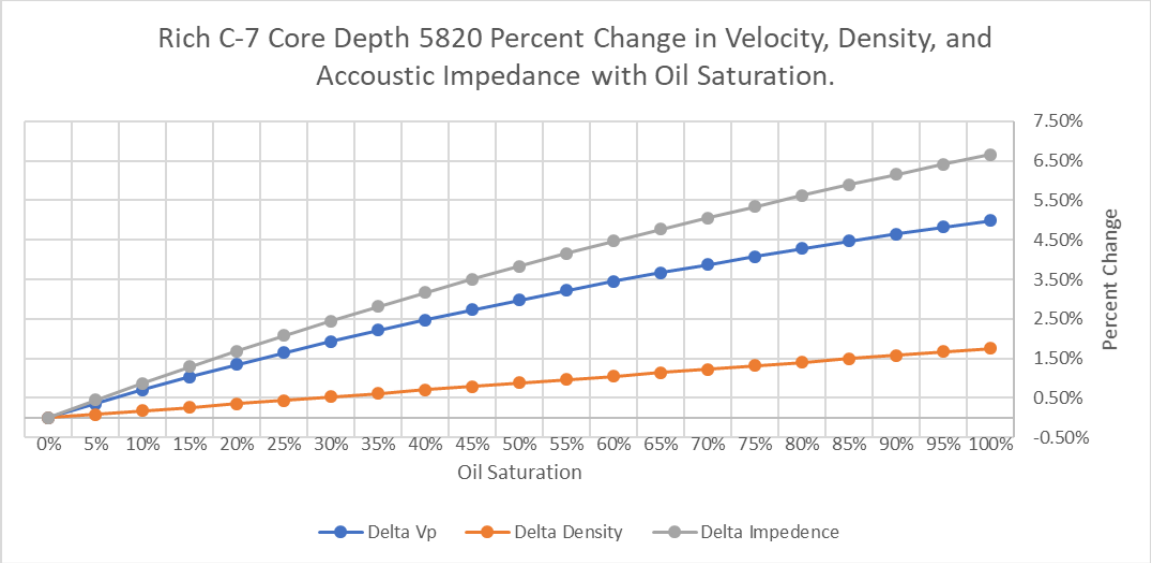

Figure 5-75: Gassmann Fluid Replacement results at 100% Dolomite composition and 17% porosity (in-situ).

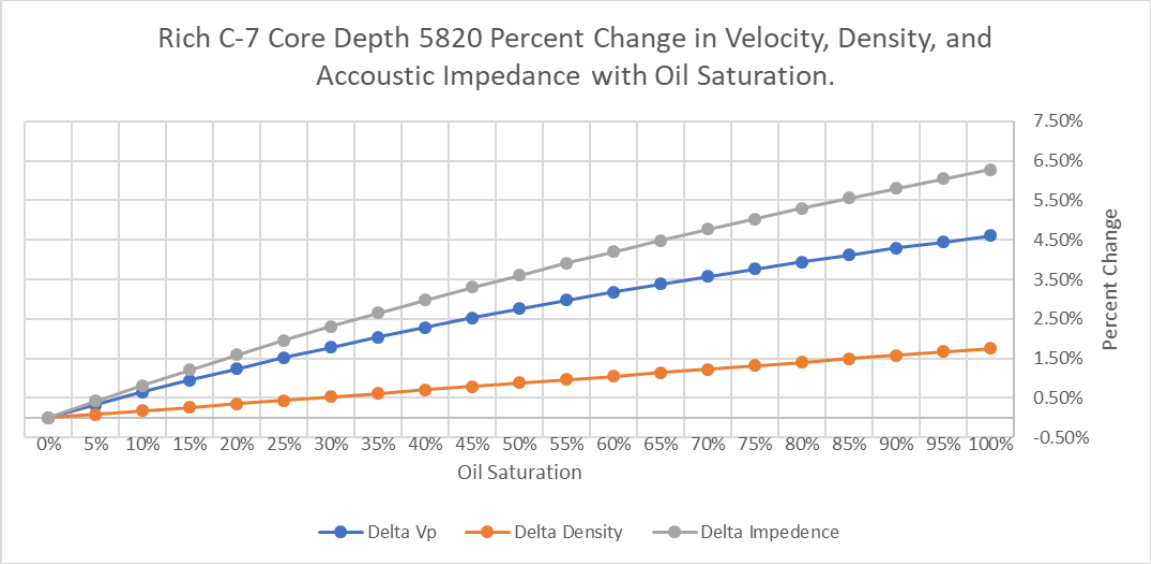

Figure 5-76: Gassmann Fluid Replacement results at 100% Calcite composition and 17% porosity (in-situ).

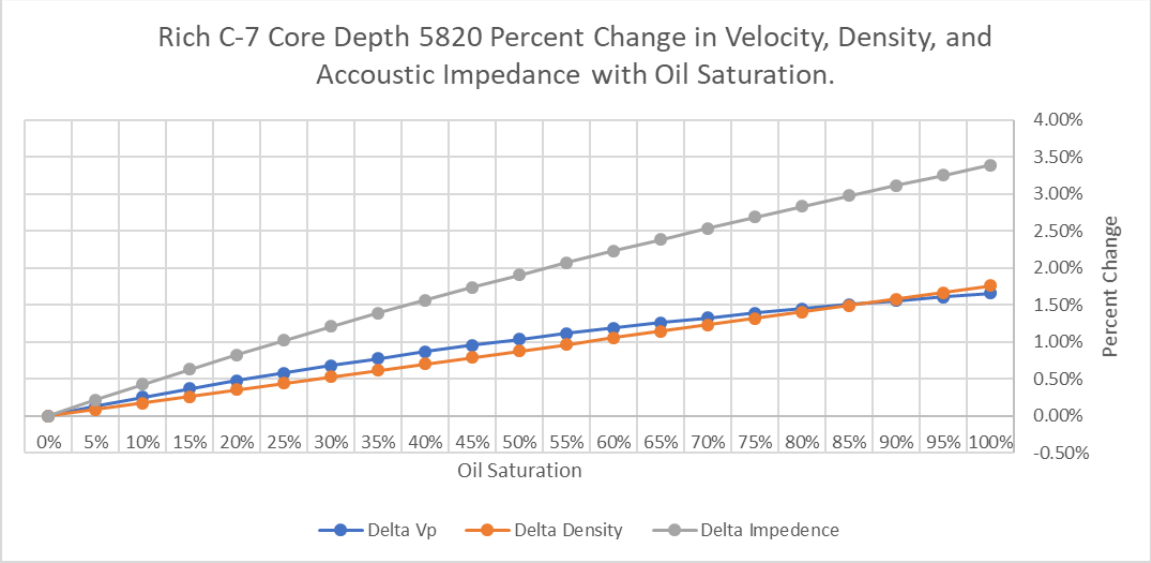

Figure 5-77: Gassmann Fluid Replacement results at 100% Chert composition and 17% porosity (in-situ).

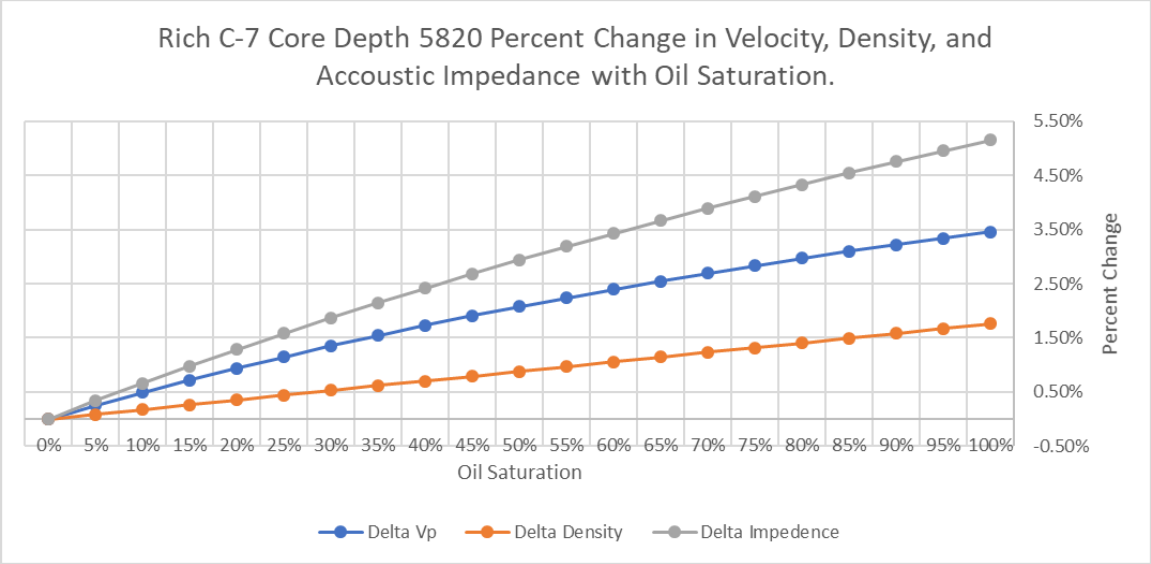

Figure 5-78: Gassmann Fluid Replacement results at 70% Chert, 30% Dolomite, and 17% porosity (in-situ).

In the Lower Viola "B", effective lithology (Table 5-8) mimics the results for 100% Dolomite (Figures 5-74 and 5-75), with very similar slopes for Vp, Rho and Impedance, and near identical percent change values. Porosity its moderately lower in this zone due to lower chert, but still with high dolomite proportions compared to calcite. Comparatively, changes in chert (Figure 5-76) compared to the 70%/30% blend (Figure 5-78) is notable. When dolomite is introduced into the system, the change in density is almost constant but there is a significantly larger change in velocity. Hence, why Viola "B" reservoirs with good dolomite and chert content along with porosity should stand out in seismic. The 100% Chert results (figure 5-77) are vastly different from the effective lithology. Again, as seen in figure 5-72, chert causes density to change at a more rapid rate than Vp. However, compared to the middle Viola "B", the difference between density and P-wave velocities are not nearly as great. This is due to porosities effect on the Viola "B" during fluid replacement, as seen in figure 5-67 and 5-68. When porosity is lower, the Gassman effect on density is more proportional with velocity.

5.5.4 Comparability between Gassmann's and the Viola Well-Logs

Understanding how well-log data from Rich C-7 compares to Gassmann Fluid Replacement results is critical in understanding the accuracy of the results. In addition, comparing Poisson's ratio, P-ave velocity, and bulk density with dry core values is also important. Figures 5-79 and 5-80 show relationships of P-wave velocity and bulk density Gassmann values as they relate to sonic log and bulk density log values. Each color represents a specific tested depth, where circles indicate 100% water-saturated Gassmann values and the squares indicate 100% oil-saturated values. Hence, the graphs show not only Gassmann's values relationships to the Rich C-7 well log, but also to each other. It should be noted, as described above, that ultrasonic measurements are taken at much higher frequencies than sonic log measurements.

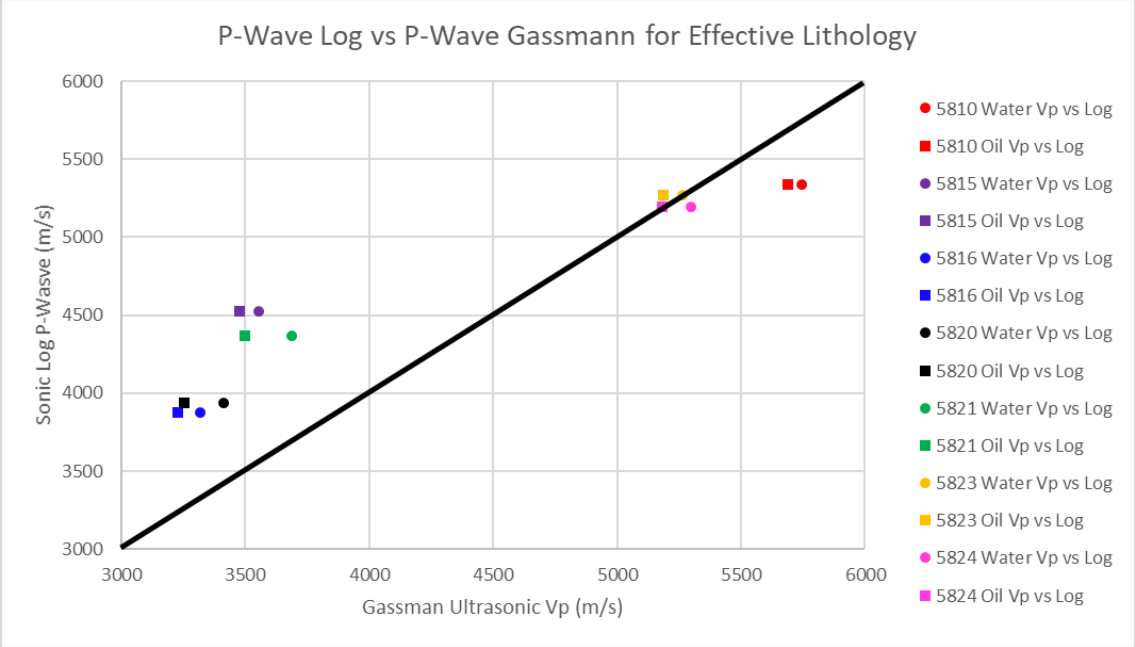

Figure 5-79: Comparison of Gassmann velocity values to Well Log values. The X-Axis represents data from Gassmann data, and the Y-Axis represent data values from well log. The black trend line depicts a slope of 1 providing a linear trend line relationship.

Samples taken at 5810 feet, 5824 feet and 5823 feet show minimal fluid variance, plotting on the trend line. This is likely that, since these samples are out of the "B" zone, they have more calcite and lower porosity. The paucity of fluid and pores in these samples result in almost identical values with well-logs due to their dense lithology. On the contrary, all points from intervals with high porosity (5815, 5816, 5820, and 5821 feet), in the "B" zone, display a separation between water- and hydrocarbon-saturated points, and lie well above the linear trendline. This separation can be observed as the distance on the graph horizontally of the circle (brine) and square (oil) points of the same color. The greater the separation, the larger the Vp change when fluid is replaced from brine to oil.

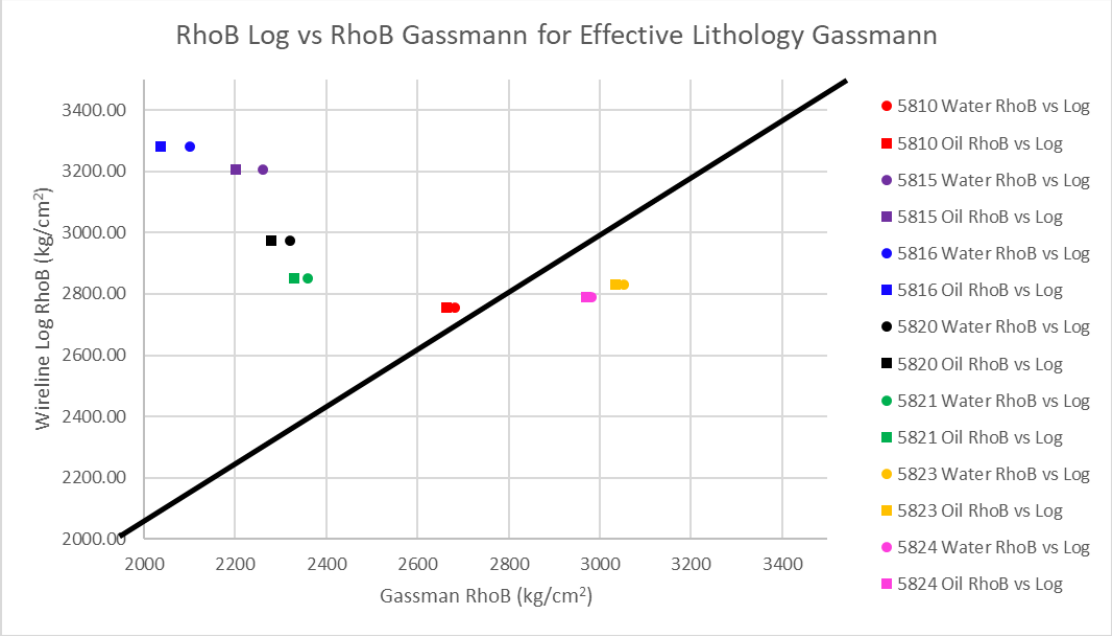

Figure 5-80: Comparison of Gassmann density values to Well Log values. The X-Axis represents data from Gassmann data, and the Y-Axis represent data values from well log. The black trend line depicts a slope of 1 providing a linear trend line relationship.

Figure 5-80 display the correlation between Gassman's and well-log values for density. Again, as seen in Figure 5-79, values for lower-porosity intervals are closer to the trendline and

water- and oil-saturated samples are coincident with each other than intervals with higher porosity. However, samples at 5815 and 5816 feet are significantly slower in wireline logs than in Gassmann calculations. This is most likely due to the presence of hydrocarbons and chert due to chert's low density compared to dolomite and limestone and oil's lower density compared to water. Chert would primarily contribute to this offset, which is then increased with the introduction of hydrocarbons, as seen in the previous sections about the effect of fluid replacement in velocity, density, and acoustic impedance. Density has a greater overall percent change than velocity when hydrocarbons are introduced (Figures 5-81 and 5-82).

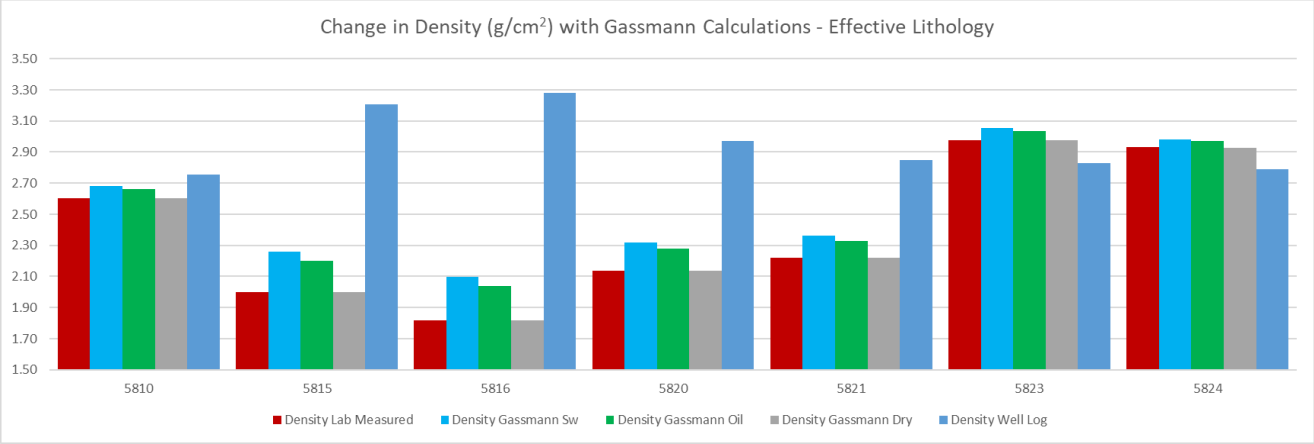

Figure 5-81: Changes in density at all depths between well log values, considering 100% Gassmann oil-saturated, 100% Gassmann brine-saturated, dry-density Gassmann calculated, and dry-density lab measured density.

Lab-measured density (red) and Gassmann calculated dry density (grey) are both in compliance in all depths. Brine- and oil-saturated densities are different from each other, similarly to what is depicted in Figures 5-79 and 5-80. At depths of high porosity, a large gap can be seen between well-logs bulk density and Gassmann-calculated densities. This trend most likely is due to low calcite proportions, high chert proportion, and high porosity. Higher porosity within the Viola did correlate with larger percent changes in density and velocity when hydrocarbons were introduced into the system. Below, figure 5-82 provides the same comparison

but for P-wave velocity. Again, lab-measured dry ultrasonic and Gassmann-calculated dry velocities are in agreement, while there is differentiation between log and Gassmann-calculated, brine- and oil-staurated Vp. However, the magnitude of difference between Gassmann values and log values of P-wave velocity is much less than density. As matrix density decreases in the viola, porosity increases due to an increase in chert. The large proportion of pore spaces being fill with oil will have a greater change in density than velocity due to porosities already majority effect on velocity. Further providing evidence of lithological effects within the Viola and it's expected response on seismic modeling. The greatest impedance changes within the viola would be seen in areas where porosity is high, there is more chert than calcite, and dolomite is the majority mineralogical unit.

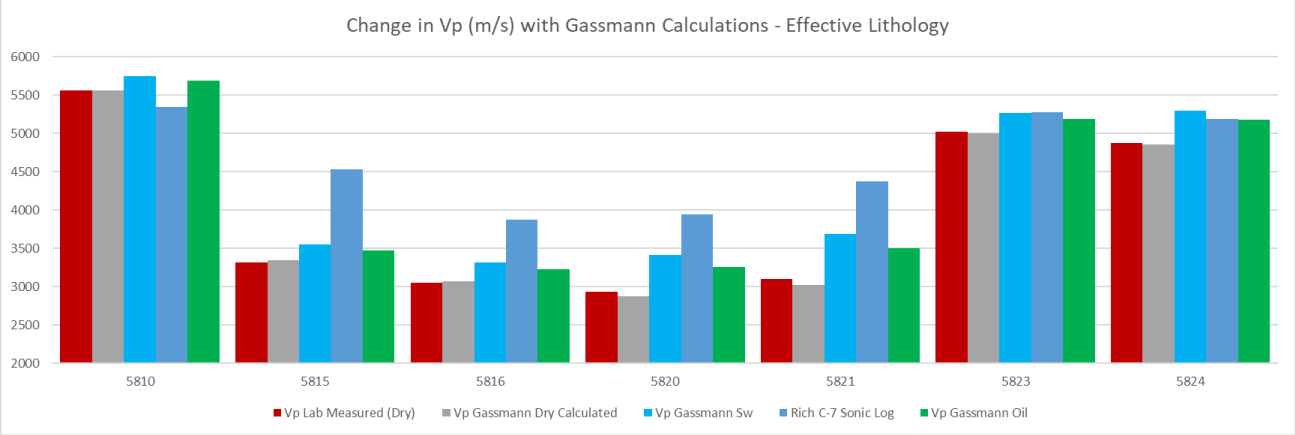

Figure 5-82: Changes in velocity at all depths between well log values, considering 100% Gassmann oil-saturated, 100% Gassmann brine-saturated, dry-density Gassmann calculated, and dry-density lab-measured P-wave velocity.

Lastly, figure 5-83 shows the same comparison for Poisson's coefficient. Using Castagna's Vs transform for well log values from available P-wave velocity values, there is an inverse relation between well logs to dry lab-measured samples compared to velocity and density. Samples with higher porosity (5815, 5816, 5820, and 5821 feet) had lab-measured Poisson's, Gassmann-calculated Poisson's, and well log Poisson's coefficient with lower

variance than those with lower porosities (5810, 5823, and 5824 feet). Poisson's coefficient is minimally affected by fluid and mostly affected by porosity and lithology. Samples with higher porosity and high chert content have overall higher Poisson's values than samples with lower porosity and high calcite content. This observation agrees with the elastic moduli analysis done in section 5.2, showing correlation between porosities and bulk moduli's with porosity, and how the "B" zone was consistently isolated from other lithologies within the Viola.

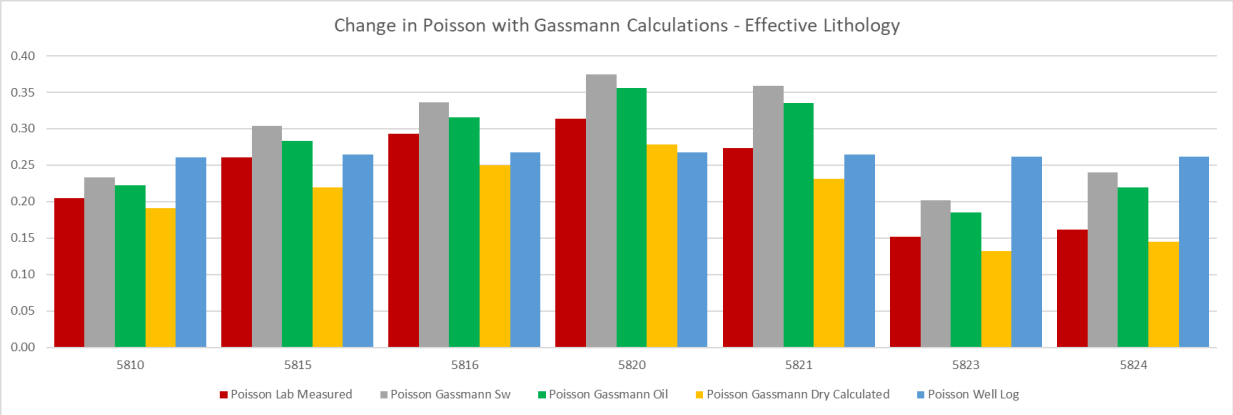

Figure 5-83: Changes in Poisson's Coefficient at all tested depths between well log values, considering 100% Gassmann oil-saturated, 100% Gassmann brine-saturated, dry Gassmann calculated, and lab-measured values.

Chapter 6 - Conclusion

This study investigated the effects on elastic properties (acoustic impedance, density, and velocity) resulting from changing pore-fluid composition, lithology, and porosity within the Viola Limestone. The relationships between elastic moduli, well log signatures, and Gassmann's fluid replacement modeling allow to better understand and characterize reservoir facies within the Viola. Collectively, this multi-faceted study concludes the following;

1. Ultrasonic Poisson's ratio, bulk modulus, P-wave velocity, and shear modulus provide the same trend as sonic and density log variation in response to changes in lithofacies and porosity. Photoelectric assessments confirm changes in lithology, as higher porosity correlates with higher chert and lower porosity correlates with higher calcite in Rich C-7. Due to a lack in dipole sonic data, a Vs transform is acceptable to use.
2. Fluid replacement modeling depicts evidence of distinct impedance, velocity, and density change in response to 100% hydrocarbon saturation within the Viola "B" Zone. However, such response is below 6% change of 100% brine-saturated impedance; thus pore fluid composition is not the main control on seismic impedance variation. Lithofacies and porosity are the main controlling factors of acoustic impedance and thus of seismic response (amplitude variation).
3. This study's fluid replacement model and elastic moduli characterization clearly corroborates Vohs (2016) conclusion about the velocity anomaly at the top of the Viola. The Viola top has a low reflection amplitude that correlates with better reservoir properties (higher porosity, lower calcite, and higher chert).

4. At higher porosity values, fluid effects on acoustic impedance become more pronounced, thus boosting reservoir amplitude-dimming which is induced by lithofacies and porosity.
5. Ultrasonic Poisson's ratio is a viable parameter for correlating and transforming sonic Vp to sonic-frequency Vs due to lithology and porosity being the main drivers of reservoir characteristics.

Chapter 7 - Future Work

The Viola Limestone in South-West Kansas is an economic producer for a variety of engineering and lease holding reasons. Accurately identifying good Viola reservoirs has been a challenge for operators due to the reservoir's thin nature, erratic lithology, and variable porosity throughout the section. Future work should be conducted in collecting more core data to corroborate the results of this study, as well as Vohs (2016) seismic study, and Hagood (2019) sedimentological characterization study. More lab-tested core data can provide further insight on the elastic relationships and porosity of the cherty Viola "B" zone in relation to the rest of the unit. A study should also be conducted directly measuring brine-saturated samples in a lab setting and comparing them to Gassmann fluid replacement data of dry core samples. A study of this kind would provide a better understanding on fluids effect on the Viola, along with how porosities and lithologies truly impact impedance. Lastly, 3-D seismic should be acquired above Rich C-7 and neighboring Viola wells to test the results of this study, along with establishing a practical workflow when exploring for hydrocarbons within the Viola..

References

Adam, L., Batzle, M., & Brevik, I. (2006). Gassmann's fluid substitution and shear modulus variability in carbonates at laboratory seismic and ultrasonic frequencies. Geophysics, 71(6), F173-F183.

Adkison, W. (1972). Stratigraphy and structure of Middle and Upper Ordovician rocks in the Sedgwick Basin and adjacent areas, south-central Kansas (Geological Survey professional paper; 702).

Avseth, P., Mukerji, T., & Mavko, G. (2005). Quantitative seismic interpretation : Applying rock physics tools to reduce interpretation risk. Cambridge, UK ; New York: Cambridge University Press.

Bello, Rasaq, and Yemi Onifade. "Bello, R., & Onifade, Y. (2016). DISCRIMINATION OF RESERVOIR FLUID CONTACTS USING COMPRESSIONAL AND SHEAR WAVE VELOCITY." Global Journal of Pure and Applied Sciences, vol. 22, no. 2, 2016, pp. 177–190

Besheli, S. A., Hendi, S. S., Vali, J. (1998) Reservoir Characterization by Seismic Attributes With Vp & Vs Measurements of Core samples (a "Rock Physics" study).

Bornemann, E., Doveton, J. H., St. Clair, P. N., 1982, Lithofacies Analysis of the Viola Limestone in South-central Kansas: Kansas Geol. Survey, Petrophysical Series 3, 50 p.

Castagna, J., Batzle, M., & Eastwood, R. (1985). Relationships Between Compressional-Wave and Shear-Wave Velocities in Clastic Silicate Rocks. Geophysics, 50(4), 571-581 p.

Chopra, S. and Marfurt, K.J., 2005, Seismic attributes-a historical perspective. Attribute Review Paper, p. 1-71.

Chopra, S. and Marfurt, K.J., 2008, Emerging and future trends in seismic attributes. The Leading Edge, vol. 27, no. 3, p. 298-318.

Choquette, P.W., and Pray, L.C., 1970, Geological nomenclature and classification of porosity in sedimentary carbonates: American Association of Petroleum Geologists Bulletin, v. 54, p. 207-250

Doveton, J. (2017). Geological Log Analysis. Retrieved May 03, 2020, from

http://www.kgs.ku.edu/Publications/Bulletins/LA/index.html

Downton, J. and Gunderson, J. (2005). Fluid substitution without S-wave velocity information in hydrocarbon saturated reservoirs. SEG Annual Meeting Abstract.

El-Bahiry, M., El-Amir, & Abdelhay. (2017). Reservoir characterization using fluid substitution and inversion methods, offshore West Nile Delta, Egypt. Egyptian Journal of Petroleum, 26(2), 351-361.

Fjaer, E. (2008). Petroleum related rock mechanics (2nd ed., Developments in petroleum science).

Greenberg, M., L. and Castagna, J. P., (1992). Shear wave velocity estimation in porous rocks: theoretical formulation, preliminary verification and applications. Geophysical Prospecting, 40, 195-209.

Grochau, M., & Gurevich, B. (2009). Testing Gassmann fluid substitution: Sonic logs versus ultrasonic core measurements. Geophysical Prospecting, 57(1), 75-79.

Hagood, W., (2019). Detailed core and log analysis of a producing Viola dolomite well in Comanche County, Kansas. Master's Thesis Kansas State University.

Hagood, W.K., Cimino, V., Totten, Matthew., Raef, A. (2018). Analysis and Integration of Well Logs and Ultrasoinc Velocities of Productive Facies in the Upper Viola Formation in Southwestern Kansas, AAPG Annual Conference and Expo, Salt Lake City, Utah, May 16, 2018.

Han, D. H., & Batzle, M. L. (2004). Gassmann's equation and fluid-saturation effects on seismic velocities. Geophysics, 69(2), 398-405.

Isham, R., (2012). Integration of in situ and laboratory velocity measurements analysis and calibration for rock formation characterization. Master's Thesis Kansas State University.

Jaeger, J.C., & Cook, M.G.W. (1969). Fundamentals of Rock Mechanics. Methuen, London.

Jaiswal, P., Varacchi, Ebrahimi, Dvorkin, & Puckette. (2014). Can seismic velocities predict sweet spots in the Woodford Shale? A case study from McNeff 2–28 Well, Grady County, Oklahoma. Journal of Applied Geophysics, 104, 26-34.

Kansas Geological Survey (KGS), 2020, <http://www.kgs.ku.edu> Accessed, 2016 - 2020

Linares, A., (2016). Petrographic analysis and diagenetic history of the Viola limestone at Stephen's Ranch, in the Morrison northeast field of Clark County, Kansas. Master's Thesis Kansas State University.

Lueck, A., (2017). Characterizing two carbonate formations for CO_2-EOR and carbon geosequestration applicability of existing rock physics models and implications for feasibility of a time lapse monitoring program in the Wellington Oil Field, Sumner County, Kansas. Master's Thesis Kansas State University.

Mavko, G., Chan, C., & Mukerji, T. (1995). Fluid substitution: Estimating changes in Vp without knowing Vs. Geophysics, 60(6), 1750-1755.

Mavko, G., Mukerji, T., & Dvorkin, J. (1998). The Rock Physics Handbook: Tools for Seismic Analysis in Porous Media (First ed.). United Kingdom: Cambridge University press.

Mavko, G., Mukerji, T., & Dvorkin, J. (2009). The rock physics handbook tools for seismic analysis of porous media (2nd ed.). Cambridge ; New York: Cambridge University Press.

Raef, A., Meek, T., & Totten, M. (2016). Applications of 3D seismic attribute analysis in hydrocarbon prospect identification and evaluation: Verification and validation based on fluvial palaeochannel cross-sectional geometry and sinuosity, Ness County, Kansas, USA. Marine and Petroleum Geology, 73, 21-35.

Raef, A., Totten, M., Vohs, A., & Linares, A. (2017). 3D Seismic Reflection Amplitude and Instantaneous Frequency Attributes in Mapping Thin Hydrocarbon Reservoir Lithofacies: Morrison NE Field and Morrison Field, Clark County, KS. Pure and Applied Geophysics, 174(12), 4379-4394.

Raef, A., Totten, E., Linares, M., & Kamari, W. (2019). Lithofacies Control on Reservoir Quality of the Viola Limestone in Southwest Kansas and Unsupervised Machine Learning Approach of Seismic Attributes Facies-Classification. Pure and Applied Geophysics, 176(10), 4297-4308.

Richardson, L. J., (2013), The Herd Viola Trend, Comanche County, Kansas: AAPG Mid-Continent Section Meeting., 1-32 pp.

Røgen, B., Fabricius, I., Japsen, P., Høier, C., Mavko, G., & Pedersen, J. (2005). Ultrasonic velocities of North Sea chalk samples: Influence of porosity, fluid content and texture. Geophysical Prospecting, 53(4), 481-496.

Sayers, C., & Chopra, S. (2009). Introduction to this special section - Rock physics. Leading Edge (Tulsa, OK), 28(1), 15-16.

Schlumberger 2019 Oilfield Glossary www.glossary.oilfield.slb.com

Simm, R., & Bacon, M. (2014). Seismic amplitude: An interpreter's handbook. Cambridge University Press.

Smith, T., Sondergeld, C., & Rai, C. (2003). Gassmann fluid substitutions: A tutorial. Geophysics, 68(2), 430-440.

Vohs, A., (2016). 3D seismic attributes analysis in reservoir characterization the Morrison NE field & Morrison field, Clark County Kansas. Master’s Thesis Kansas State University.

Xu, S., & Payne, M.A. (2009). Modeling elastic properties in carbonate rocks. The Leading Edge, 28(1), 66-74

Wang, Z. (2001). Fundamentals of seismic rock physics. Geophysics, 66(2), 398-412.

Watt, P. J., Davies, G.F., & O’Connell, R.J. (1976). The elastic properties of composite materials. Rev. Geophys. Space Phys., 14, 541-563.

Widess, M. B. (1973). How Thin is a Thin Bed?. Geophyics , 38(6), 1176-1190.

Zeng, H. (2009). How thin is a thin bed? An alternative perspective. Leading Edge (Tulsa, OK), 28(10), 1192-1197.

Appendix A -

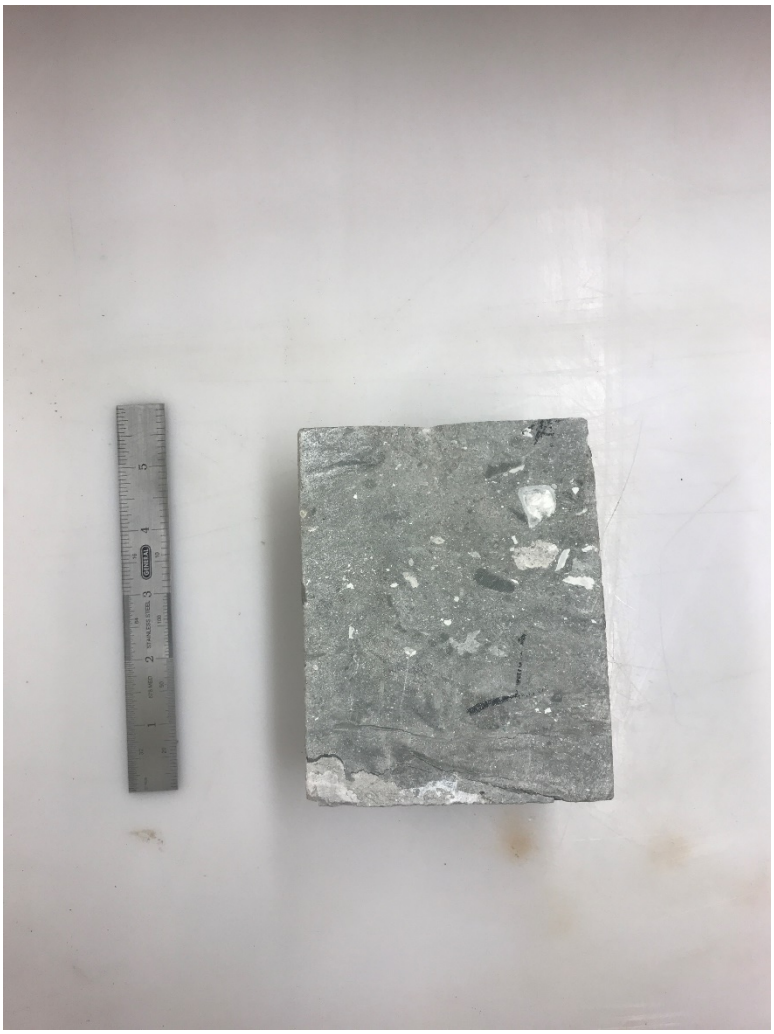

A-7-1. Cross sectional view of dried core from Rich C-7 at 5804 ft.

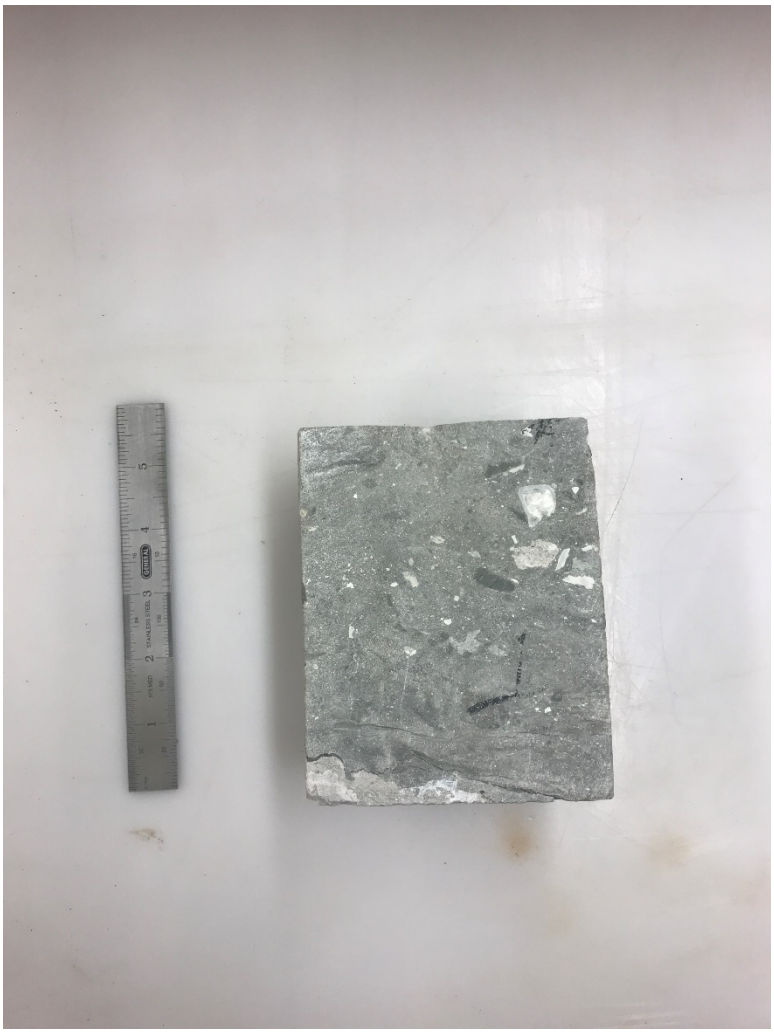

A-7-2. Cross sectional view of dried core from Rich C-7 at 5805 ft.

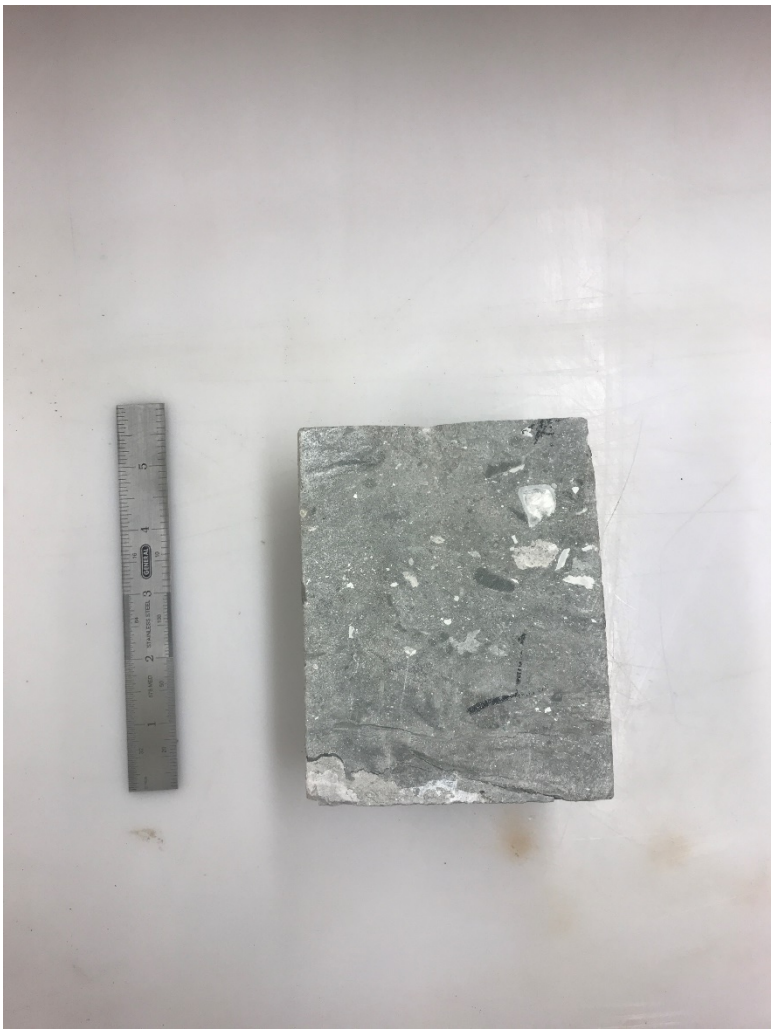

A-7-3. Cross sectional view of dried core from Rich C-7 at 5806 ft.

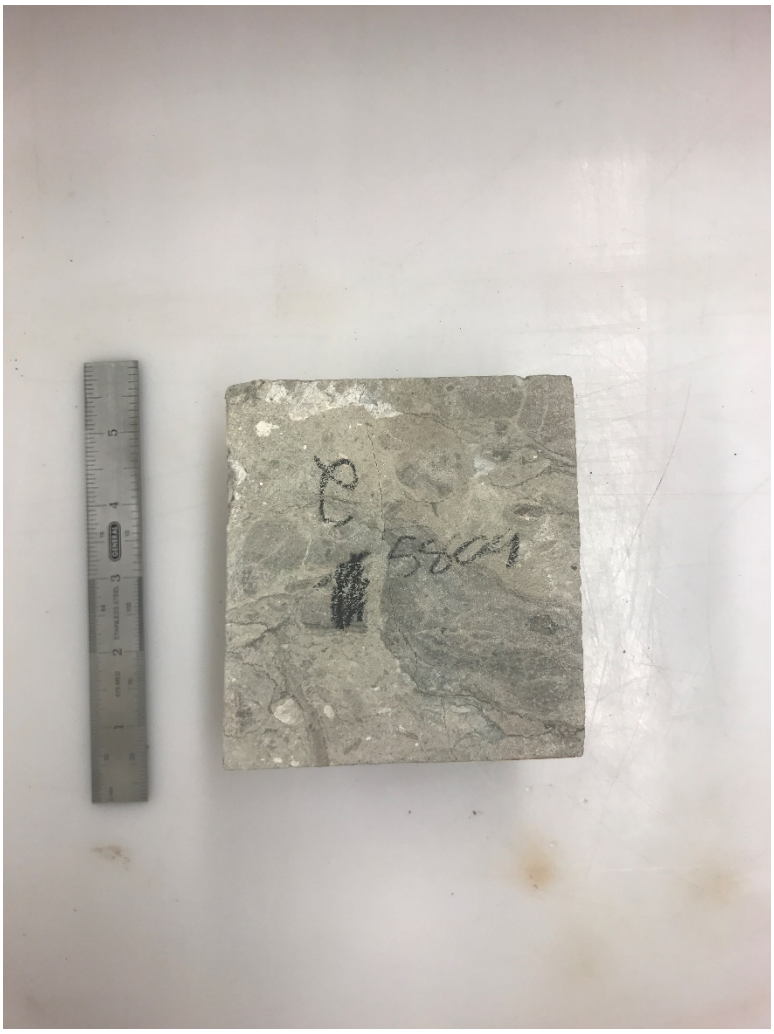

A-7-4. Cross sectional view of dried core from Rich C-7 at 5809 ft.

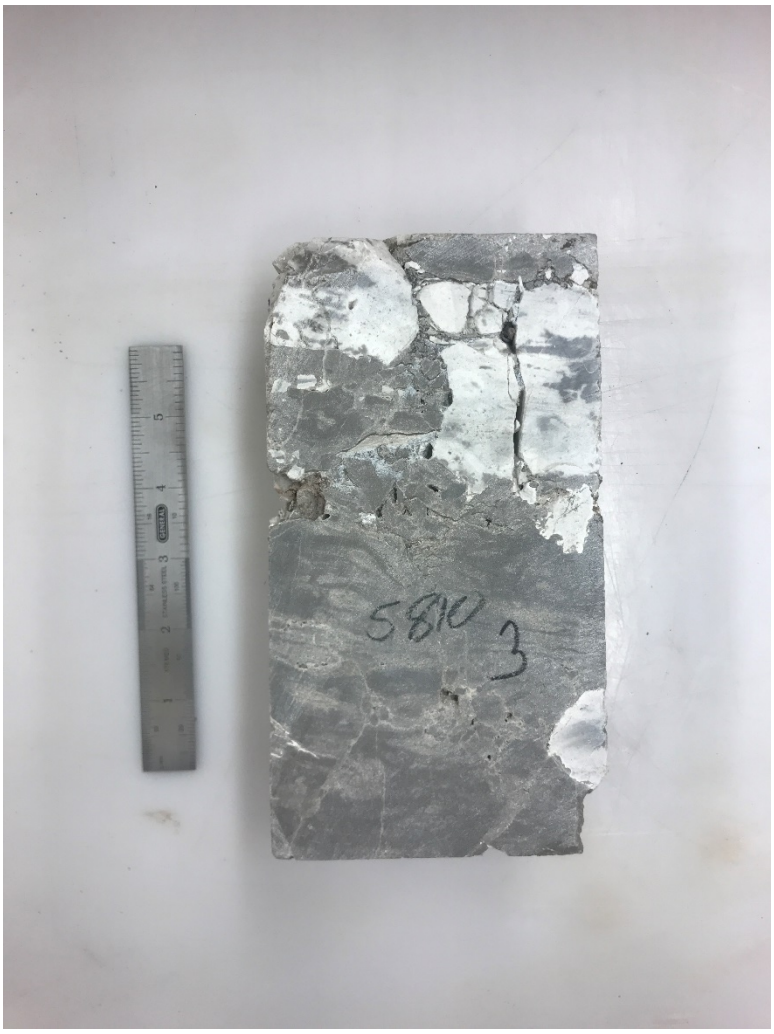

A-7-5. Cross sectional view of dried core from Rich C-7 at 5810 ft.

Sat % SHc	Vp	Vs	Rho	Bulk	Poisson	Shear	Bulk (Gpa)	Impedence	Delta Vp	elta Densit	lta Impeder
0%	5745.711	3389	2681.151	4.75E+10	0.23	30.79	47.45	15.41	0.00%	0.00%	0.00%
5%	5741	3390	2680.311	4.73E+10	0.23	30.79	47.29	15.39	0.08%	0.03%	0.11%
10%	5737	3390	2679.471	4.71E+10	0.23	30.79	47.14	15.37	0.15%	0.06%	0.21%
15%	5733	3391	2678.631	4.7E+10	0.23	30.79	46.99	15.36	0.22%	0.09%	0.31%
20%	5729	3391	2677.791	4.68E+10	0.23	30.79	46.84	15.34	0.29%	0.13%	0.41%
25%	5726	3392	2676.951	4.67E+10	0.23	30.79	46.70	15.33	0.35%	0.16%	0.50%
30%	5722	3392	2676.111	4.66E+10	0.23	30.79	46.57	15.31	0.41%	0.19%	0.60%
35%	5719	3393	2675.271	4.64E+10	0.23	30.79	46.44	15.30	0.47%	0.22%	0.68%
40%	5716	3393	2674.431	4.63E+10	0.23	30.79	46.31	15.29	0.52%	0.25%	0.77%
45%	5713	3394	2673.591	4.62E+10	0.23	30.79	46.20	15.27	0.57%	0.28%	0.85%
50%	5710	3394	2672.751	4.61E+10	0.23	30.79	46.08	15.26	0.62%	0.31%	0.94%
55%	5707	3395	2671.911	4.6E+10	0.23	30.79	45.97	15.25	0.67%	0.34%	1.01%
60%	5704	3395	2671.071	4.59E+10	0.23	30.79	45.86	15.24	0.72%	0.38%	1.09%
65%	5702	3396	2670.231	4.58E+10	0.23	30.79	45.76	15.23	0.76%	0.41%	1.17%
70%	5700	3396	2669.391	4.57E+10	0.22	30.79	45.65	15.21	0.80%	0.44%	1.24%
75%	5697	3397	2668.551	4.56E+10	0.22	30.79	45.56	15.20	0.84%	0.47%	1.31%
80%	5695	3398	2667.711	4.55E+10	0.22	30.79	45.46	15.19	0.88%	0.50%	1.38%
85%	5693	3398	2666.871	4.54E+10	0.22	30.79	45.37	15.18	0.92%	0.53%	1.45%
90%	5691	3399	2666.031	4.53E+10	0.22	30.79	45.28	15.17	0.96%	0.56%	1.51%
95%	5689	3399	2665.191	4.52E+10	0.22	30.79	45.20	15.16	0.99%	0.60%	1.58%
100%	5687	3400	2664.351	4.51E+10	0.22	30.79	45.11	15.15	1.02%	0.63%	1.64%

Table A-7-1. Gassmann Fluid Replacement Results for 5810 ft core sample.

A-7-6. Cross sectional view of dried core from Rich C-7 at 5815 ft.

Sat % SHc	Vp	Vs	Rho	Bulk	Poisson	Shear	Bulk (Gpa)	Impedence
0%	3555.086	1886	2260.2	1.78E+10	0.30	8.04	17.85	8.04
5%	3549	1887	2257.32	1.77E+10	0.30	8.04	17.71	8.01
10%	3543	1888	2254.44	1.76E+10	0.30	8.04	17.57	7.99
15%	3537	1890	2251.56	1.74E+10	0.30	8.04	17.45	7.96
20%	3532	1891	2248.68	1.73E+10	0.30	8.04	17.33	7.94
25%	3526	1892	2245.8	1.72E+10	0.30	8.04	17.21	7.92
30%	3522	1893	2242.92	1.71E+10	0.30	8.04	17.10	7.90
35%	3517	1894	2240.04	1.7E+10	0.30	8.04	16.99	7.88
40%	3513	1896	2237.16	1.69E+10	0.29	8.04	16.89	7.86
45%	3509	1897	2234.28	1.68E+10	0.29	8.04	16.79	7.84
50%	3505	1898	2231.4	1.67E+10	0.29	8.04	16.69	7.82
55%	3501	1899	2228.52	1.66E+10	0.29	8.04	16.60	7.80
60%	3498	1901	2225.64	1.65E+10	0.29	8.04	16.51	7.78
65%	3494	1902	2222.76	1.64E+10	0.29	8.04	16.42	7.77
70%	3491	1903	2219.88	1.63E+10	0.29	8.04	16.34	7.75
75%	3488	1904	2217	1.63E+10	0.29	8.04	16.26	7.73
80%	3486	1906	2214.12	1.62E+10	0.29	8.04	16.18	7.72
85%	3483	1907	2211.24	1.61E+10	0.29	8.04	16.11	7.70
90%	3481	1908	2208.36	1.6E+10	0.29	8.04	16.04	7.69
95%	3478	1909	2205.48	1.6E+10	0.28	8.04	15.97	7.67
100%	3476	1911	2202.6	1.59E+10	0.28	8.04	15.90	7.66

Table A-7-2. Gassmann Fluid Replacement Data for core sample taken at 5815 ft.

A-7-7. Cross sectional view of dried core from Rich C-7 at 5816 ft.

Sat % SHc	Vp	Vs	Rho	Bulk	Poisson	Shear	Bulk (Gpa)	Impedence
0%	3319.28	1649	2099.696	1.55E+10	0.34	5.71	15.52	6.97
5%	3312	1650	2096.576	1.54E+10	0.33	5.71	15.39	6.94
10%	3305	1651	2093.456	1.53E+10	0.33	5.71	15.26	6.92
15%	3299	1653	2090.336	1.51E+10	0.33	5.71	15.13	6.90
20%	3292	1654	2087.216	1.5E+10	0.33	5.71	15.01	6.87
25%	3287	1655	2084.096	1.49E+10	0.33	5.71	14.90	6.85
30%	3281	1656	2080.976	1.48E+10	0.33	5.71	14.79	6.83
35%	3276	1658	2077.856	1.47E+10	0.33	5.71	14.68	6.81
40%	3271	1659	2074.736	1.46E+10	0.33	5.71	14.58	6.79
45%	3266	1660	2071.616	1.45E+10	0.33	5.71	14.49	6.77
50%	3262	1661	2068.496	1.44E+10	0.32	5.71	14.39	6.75
55%	3257	1663	2065.376	1.43E+10	0.32	5.71	14.30	6.73
60%	3253	1664	2062.256	1.42E+10	0.32	5.71	14.22	6.71
65%	3250	1665	2059.136	1.41E+10	0.32	5.71	14.13	6.69
70%	3246	1666	2056.016	1.41E+10	0.32	5.71	14.05	6.67
75%	3243	1668	2052.896	1.4E+10	0.32	5.71	13.97	6.66
80%	3240	1669	2049.776	1.39E+10	0.32	5.71	13.90	6.64
85%	3237	1670	2046.656	1.38E+10	0.32	5.71	13.83	6.62
90%	3234	1672	2043.536	1.38E+10	0.32	5.71	13.76	6.61
95%	3231	1673	2040.416	1.37E+10	0.32	5.71	13.69	6.59
100%	3228	1674	2037.296	1.36E+10	0.32	5.71	13.62	6.58

Table A-7-3. Gassmann Fluid Replacement data for core sample taken at 5816 ft.

A-7-8. Cross sectional view of dried core from Rich C-7 at 5820 ft.

Sat % SHc	Vp	Vs	Rho	Bulk	Poisson	Shear	Bulk (Gpa)	Impedence
0%	3414.028	1527	2320.458	1.98E+10	0.37	5.41	19.83	7.92
5%	3403	1528	2318.418	1.96E+10	0.37	5.41	19.63	7.89
10%	3392	1528	2316.378	1.94E+10	0.37	5.41	19.43	7.86
15%	3381	1529	2314.338	1.92E+10	0.37	5.41	19.24	7.82
20%	3371	1530	2312.298	1.91E+10	0.37	5.41	19.06	7.79
25%	3361	1530	2310.258	1.89E+10	0.37	5.41	18.89	7.77
30%	3352	1531	2308.218	1.87E+10	0.37	5.41	18.72	7.74
35%	3343	1532	2306.178	1.86E+10	0.37	5.41	18.56	7.71
40%	3335	1532	2304.138	1.84E+10	0.37	5.41	18.41	7.68
45%	3326	1533	2302.098	1.83E+10	0.37	5.41	18.26	7.66
50%	3319	1534	2300.058	1.81E+10	0.36	5.41	18.12	7.63
55%	3311	1534	2298.018	1.8E+10	0.36	5.41	17.98	7.61
60%	3304	1535	2295.978	1.78E+10	0.36	5.41	17.85	7.59
65%	3297	1536	2293.938	1.77E+10	0.36	5.41	17.72	7.56
70%	3290	1536	2291.898	1.76E+10	0.36	5.41	17.59	7.54
75%	3283	1537	2289.858	1.75E+10	0.36	5.41	17.47	7.52
80%	3277	1538	2287.818	1.74E+10	0.36	5.41	17.36	7.50
85%	3271	1539	2285.778	1.72E+10	0.36	5.41	17.24	7.48
90%	3265	1539	2283.738	1.71E+10	0.36	5.41	17.14	7.46
95%	3260	1540	2281.698	1.7E+10	0.36	5.41	17.03	7.44
100%	3254	1541	2279.658	1.69E+10	0.36	5.41	16.93	7.42

Table A-7-4. Gassmann Fluid Replacement Data for core sample at a depth of 5820 ft.

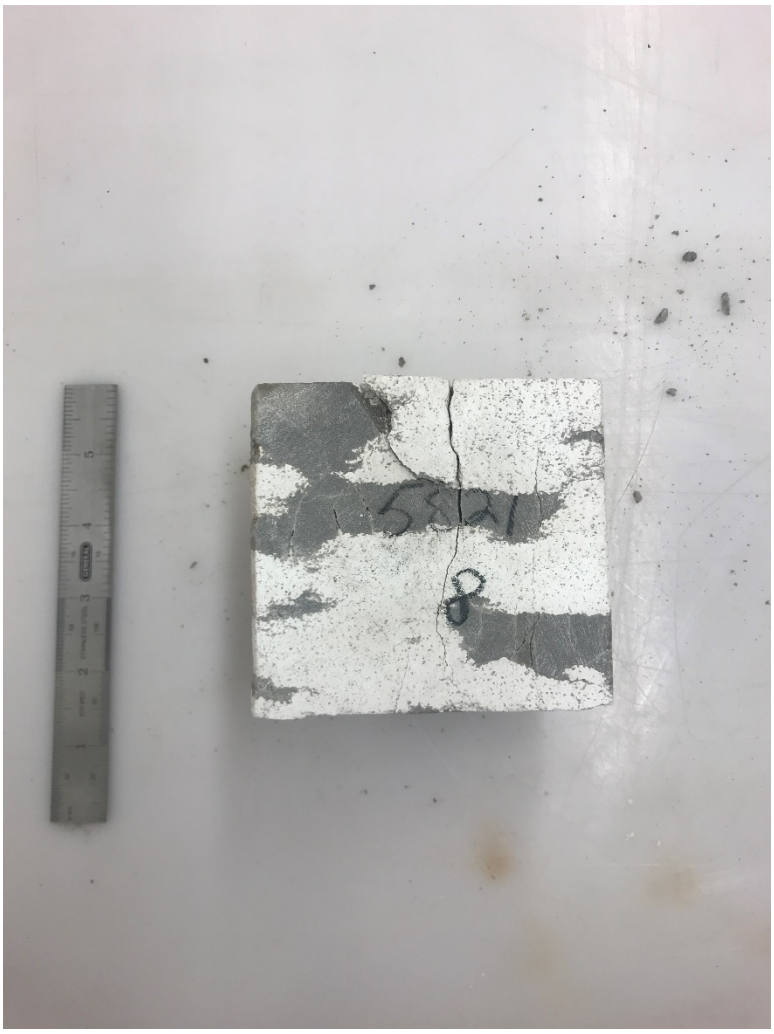

A-7-9. Cross sectional view of dried core from Rich C-7 at 5821 ft.

Sat % SHc	Vp	Vs	Rho	Bulk	Poisson	Shear	Bulk (Gpa)	Impedence
0%	3690.046	1730	2360.37	2.27E+10	0.36	7.06	22.72	8.71
5%	3677	1731	2358.81	2.25E+10	0.36	7.06	22.47	8.67
10%	3664	1731	2357.25	2.22E+10	0.36	7.06	22.23	8.64
15%	3652	1732	2355.69	2.2E+10	0.35	7.06	22.00	8.60
20%	3640	1732	2354.13	2.18E+10	0.35	7.06	21.77	8.57
25%	3629	1733	2352.57	2.16E+10	0.35	7.06	21.56	8.54
30%	3618	1733	2351.01	2.14E+10	0.35	7.06	21.36	8.51
35%	3608	1734	2349.45	2.12E+10	0.35	7.06	21.16	8.48
40%	3598	1735	2347.89	2.1E+10	0.35	7.06	20.97	8.45
45%	3588	1735	2346.33	2.08E+10	0.35	7.06	20.78	8.42
50%	3579	1736	2344.77	2.06E+10	0.35	7.06	20.61	8.39
55%	3569	1736	2343.21	2.04E+10	0.35	7.06	20.44	8.36
60%	3561	1737	2341.65	2.03E+10	0.34	7.06	20.27	8.34
65%	3552	1737	2340.09	2.01E+10	0.34	7.06	20.11	8.31
70%	3544	1738	2338.53	2E+10	0.34	7.06	19.96	8.29
75%	3536	1739	2336.97	1.98E+10	0.34	7.06	19.81	8.26
80%	3529	1739	2335.41	1.97E+10	0.34	7.06	19.66	8.24
85%	3522	1740	2333.85	1.95E+10	0.34	7.06	19.52	8.22
90%	3514	1740	2332.29	1.94E+10	0.34	7.06	19.39	8.20
95%	3508	1741	2330.73	1.93E+10	0.34	7.06	19.26	8.18
100%	3501	1742	2329.17	1.91E+10	0.34	7.06	19.13	8.15

Table A-7-5. Gassmann Fluid Repalcement data for sample at a depth of 5821 ft.

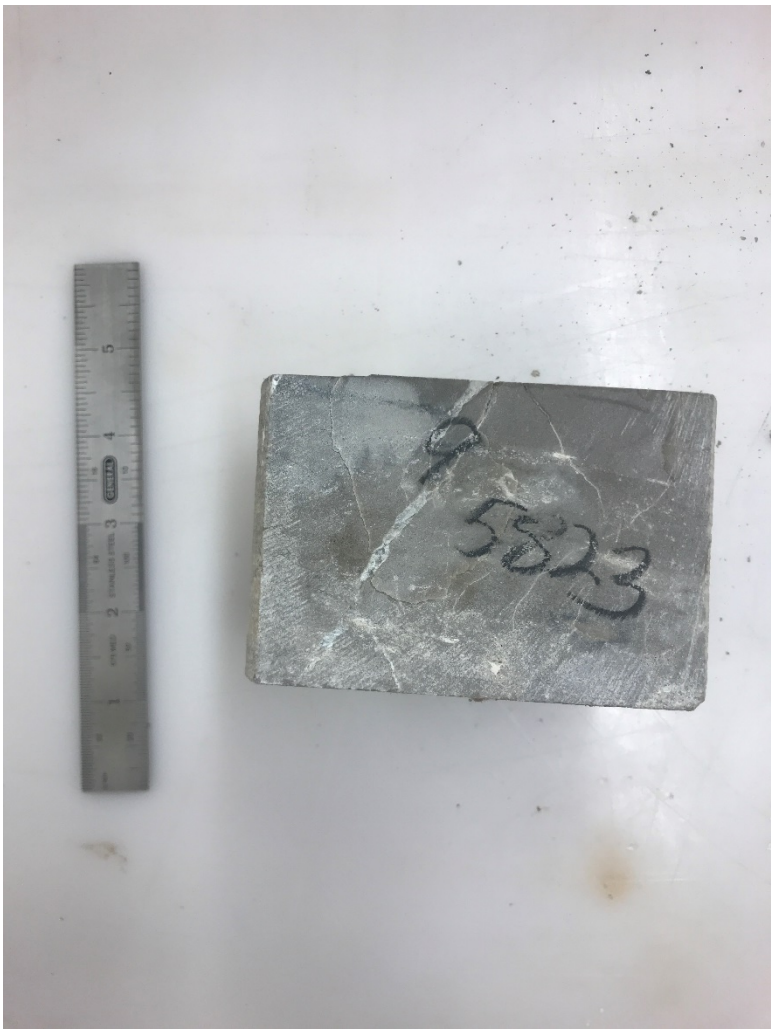

A-7-10. Cross sectional view of dried core from Rich C-7 at 5823 ft.

Sat % SHc	Vp	Vs	Rho	Bulk	Poisson	Shear	Bulk (Gpa)	Impedence
0%	5265.75	3217	3052.216	4.25E+10	0.20	31.59	42.52	16.07
5%	5260	3217	3051.376	4.23E+10	0.20	31.59	42.31	16.05
10%	5255	3218	3050.536	4.21E+10	0.20	31.59	42.12	16.03
15%	5250	3218	3049.696	4.19E+10	0.20	31.59	41.93	16.01
20%	5245	3219	3048.856	4.18E+10	0.20	31.59	41.75	15.99
25%	5240	3219	3048.016	4.16E+10	0.20	31.59	41.58	15.97
30%	5236	3220	3047.176	4.14E+10	0.20	31.59	41.41	15.95
35%	5231	3220	3046.336	4.12E+10	0.19	31.59	41.25	15.94
40%	5227	3221	3045.496	4.11E+10	0.19	31.59	41.09	15.92
45%	5223	3221	3044.656	4.09E+10	0.19	31.59	40.94	15.90
50%	5219	3221	3043.816	4.08E+10	0.19	31.59	40.80	15.89
55%	5216	3222	3042.976	4.07E+10	0.19	31.59	40.66	15.87
60%	5212	3222	3042.136	4.05E+10	0.19	31.59	40.52	15.86
65%	5209	3223	3041.296	4.04E+10	0.19	31.59	40.39	15.84
70%	5205	3223	3040.456	4.03E+10	0.19	31.59	40.26	15.83
75%	5202	3224	3039.616	4.01E+10	0.19	31.59	40.14	15.81
80%	5199	3224	3038.776	4E+10	0.19	31.59	40.02	15.80
85%	5196	3225	3037.936	3.99E+10	0.19	31.59	39.90	15.79
90%	5193	3225	3037.096	3.98E+10	0.19	31.59	39.79	15.77
95%	5190	3225	3036.256	3.97E+10	0.19	31.59	39.68	15.76
100%	5188	3226	3035.416	3.96E+10	0.18	31.59	39.58	15.75

Table A-7-6. Gassmann Fluid Replacement Data at sample taken from a depth of 5823 ft.

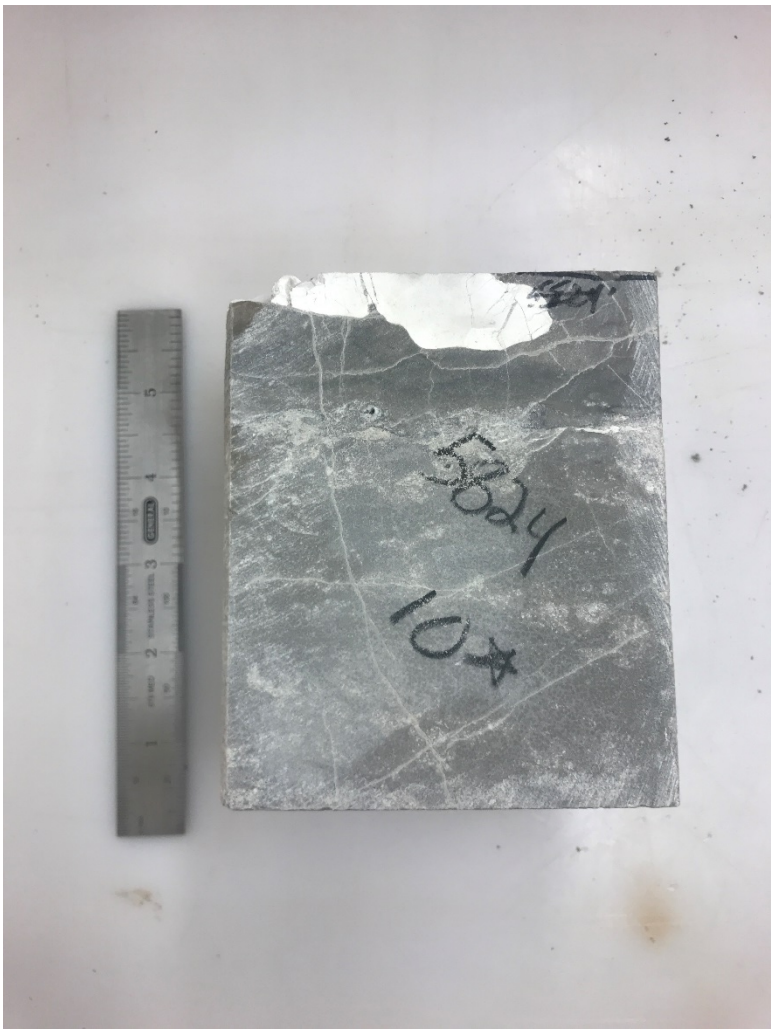

A-7-11. Cross sectional view of dried core from Rich C-7 at 5824 ft.

Sat % SHc	Vp	Vs	Rho	Bulk	Poisson	Shear	Bulk (Gpa)	Impedence
0%	5299.482	3100	2982.867	4.56E+10	0.24	28.67	45.55	15.81
5%	5291	3100	2982.267	4.53E+10	0.24	28.67	45.28	15.78
10%	5284	3101	2981.667	4.5E+10	0.24	28.67	45.02	15.75
15%	5276	3101	2981.067	4.48E+10	0.24	28.67	44.77	15.73
20%	5269	3101	2980.467	4.45E+10	0.23	28.67	44.52	15.70
25%	5262	3102	2979.867	4.43E+10	0.23	28.67	44.29	15.68
30%	5255	3102	2979.267	4.41E+10	0.23	28.67	44.06	15.66
35%	5249	3102	2978.667	4.38E+10	0.23	28.67	43.84	15.63
40%	5242	3102	2978.067	4.36E+10	0.23	28.67	43.63	15.61
45%	5236	3103	2977.467	4.34E+10	0.23	28.67	43.42	15.59
50%	5231	3103	2976.867	4.32E+10	0.23	28.67	43.22	15.57
55%	5225	3103	2976.267	4.3E+10	0.23	28.67	43.03	15.55
60%	5219	3104	2975.667	4.28E+10	0.23	28.67	42.84	15.53
65%	5214	3104	2975.067	4.27E+10	0.23	28.67	42.66	15.51
70%	5209	3104	2974.467	4.25E+10	0.22	28.67	42.48	15.49
75%	5204	3105	2973.867	4.23E+10	0.22	28.67	42.31	15.48
80%	5199	3105	2973.267	4.21E+10	0.22	28.67	42.15	15.46
85%	5194	3105	2972.667	4.2E+10	0.22	28.67	41.99	15.44
90%	5190	3106	2972.067	4.18E+10	0.22	28.67	41.83	15.42
95%	5185	3106	2971.467	4.17E+10	0.22	28.67	41.68	15.41
100%	5181	3106	2970.867	4.15E+10	0.22	28.67	41.53	15.39

Table A-7-7. Gassmann Fluid Replacement data taken at a depth of 5824 ft.

A-7-12 Cross sectional view of dried core from Rich C-7 at 5825 ft.

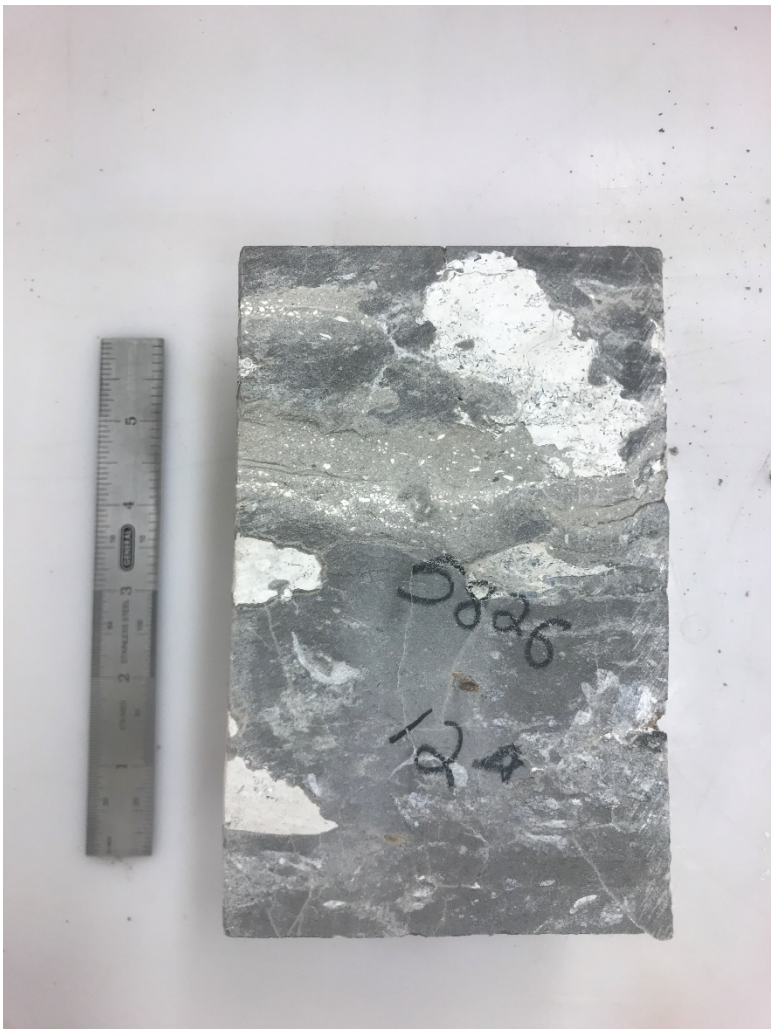

A-7-13. Cross sectional view of dried core from Rich C-7 at 5826 ft.

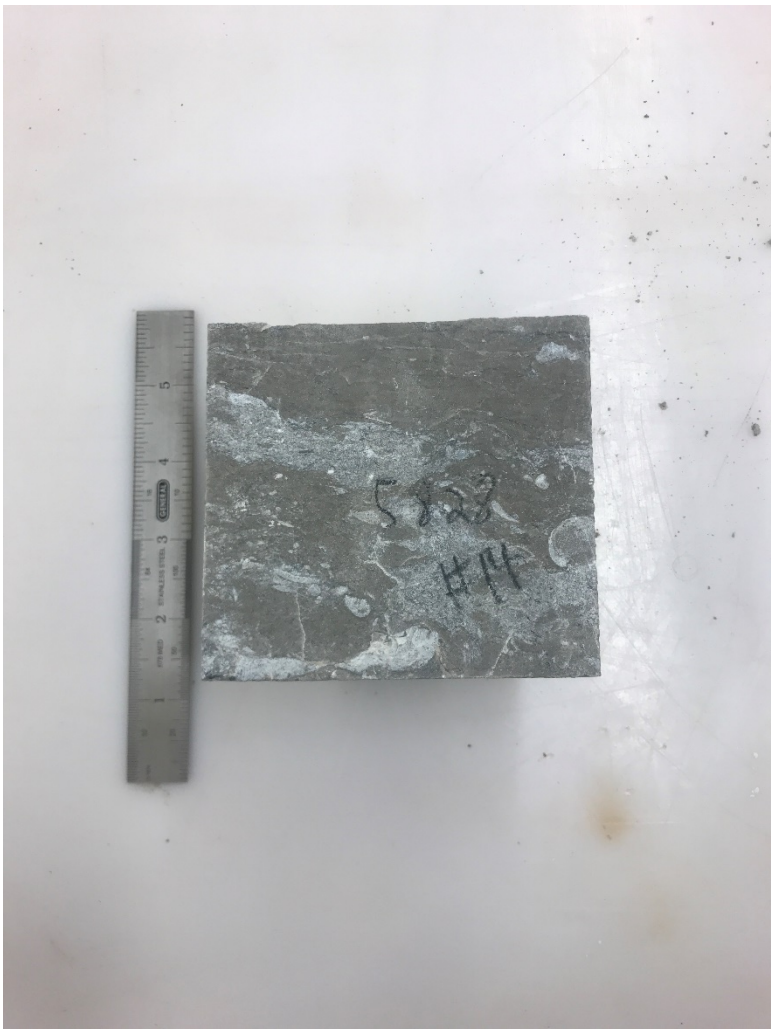

A-7-14. Cross sectional view of dried core from Rich C-7 at 5828 ft.

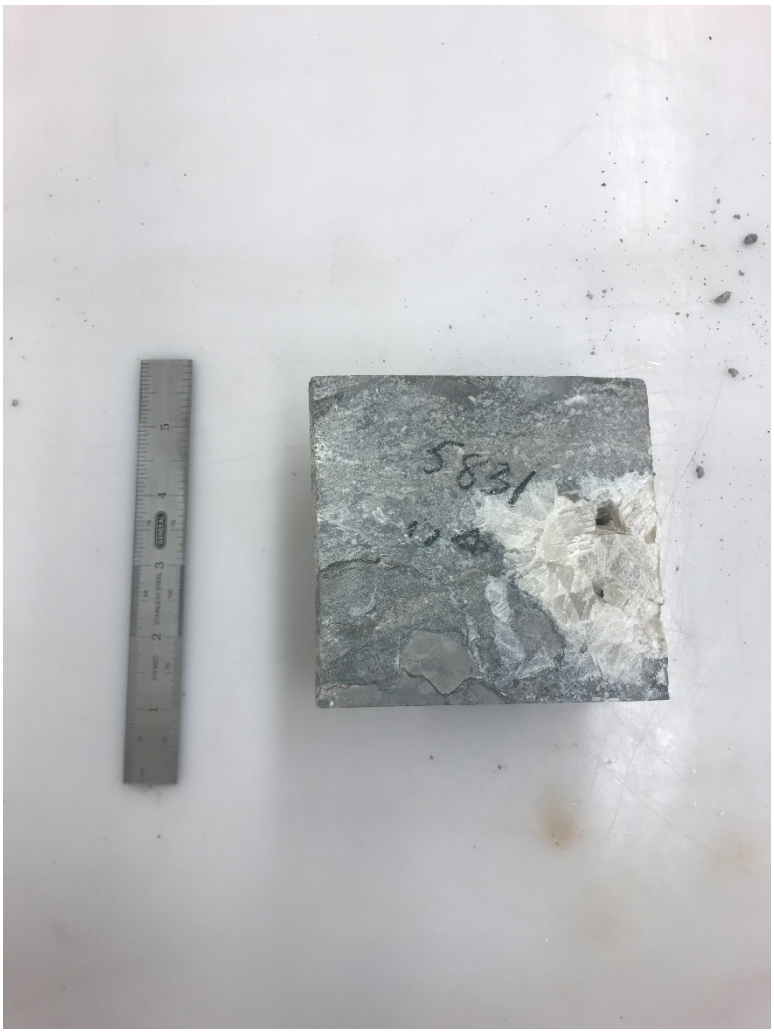

A-7-15. Cross sectional view of dried core from Rich C-7 at 5831 ft.

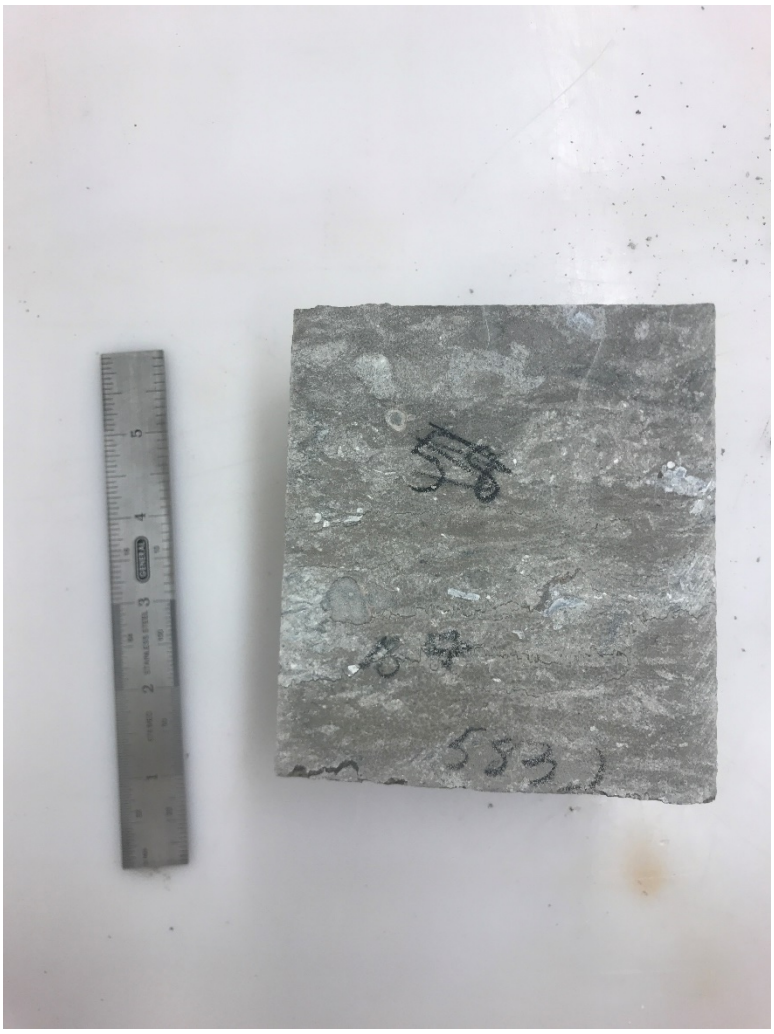

A-7-16. Cross sectional view of dried core from Rich C-7 at 5832 ft.

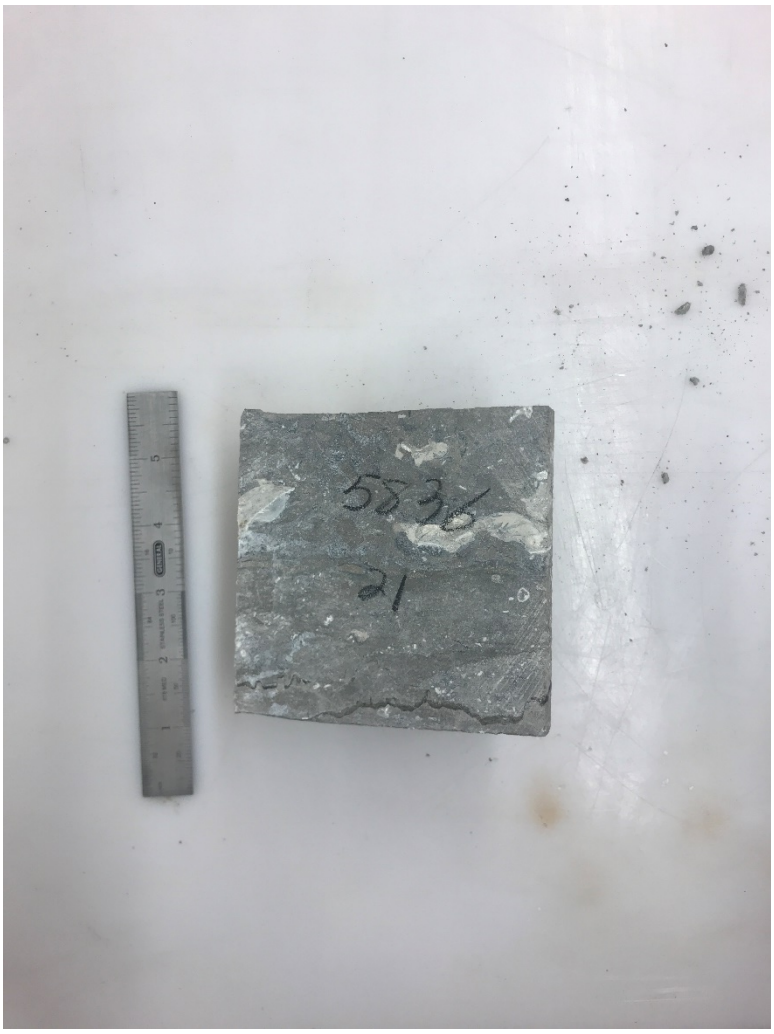

A-7-17. Cross sectional view of dried core from Rich C-7 at 5836 ft.

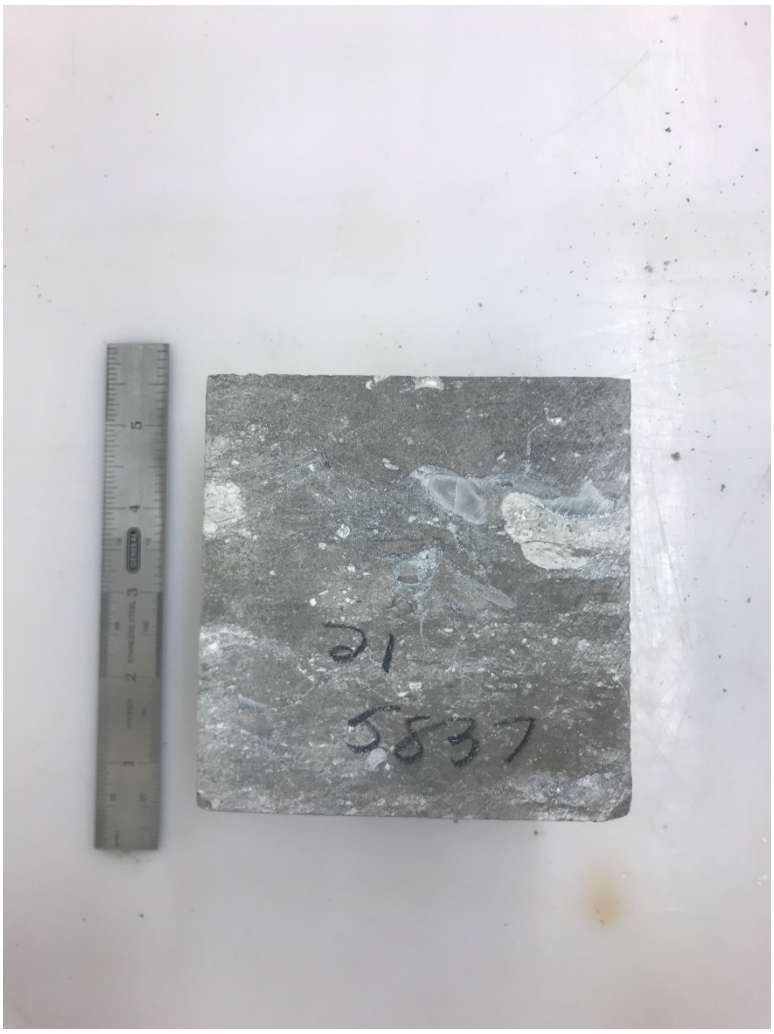

A-7-18. Cross sectional view of dried core from Rich C-7 at 5837 ft.

A-7-19. Cross sectional view of dried core from Rich C-7 at 5838 ft.

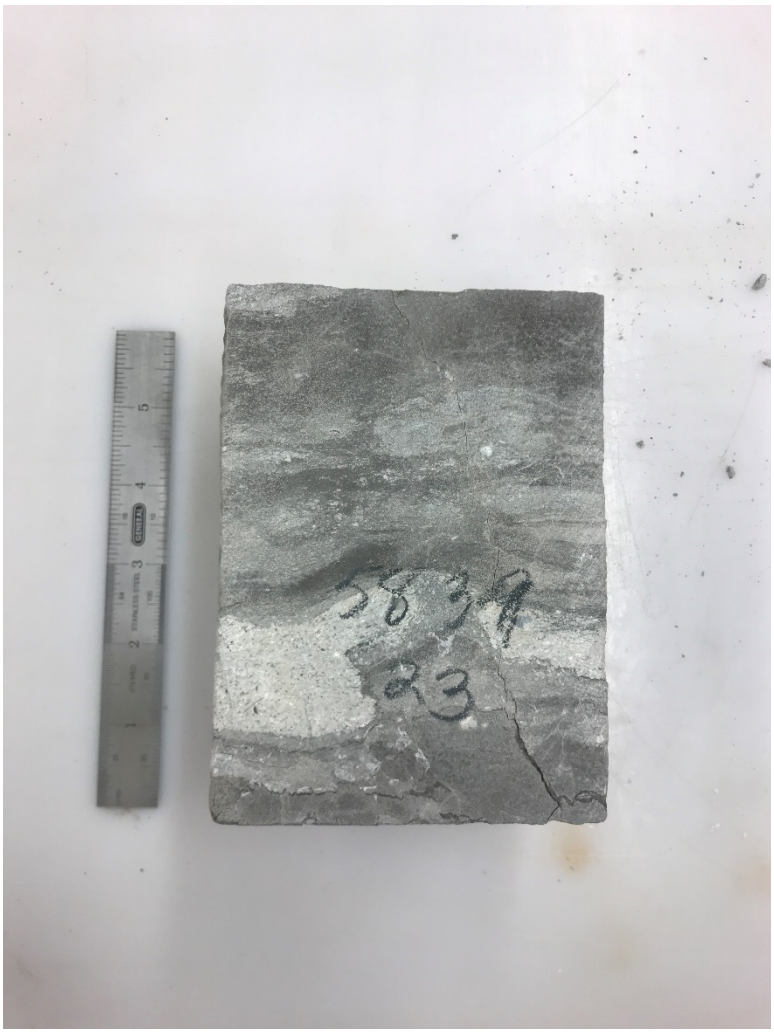

A-7-20. Cross sectional view of dried core from Rich C-7 at 5839 ft.

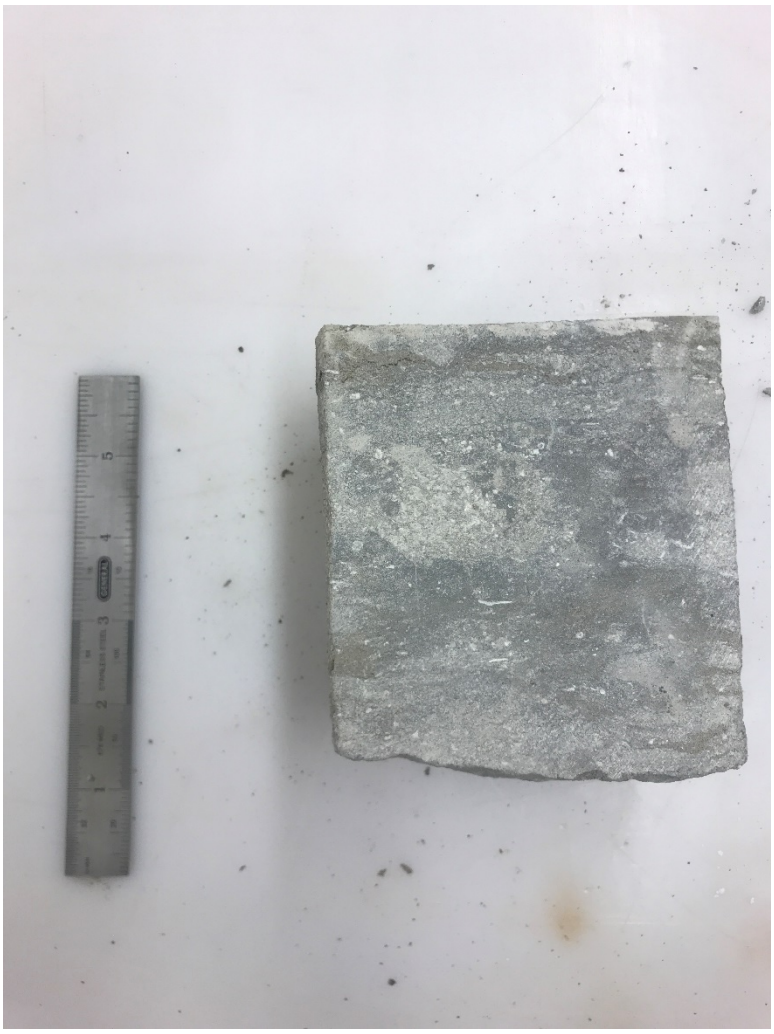

A-7-21. Cross sectional view of dried core from Rich C-7 at 5842 ft.

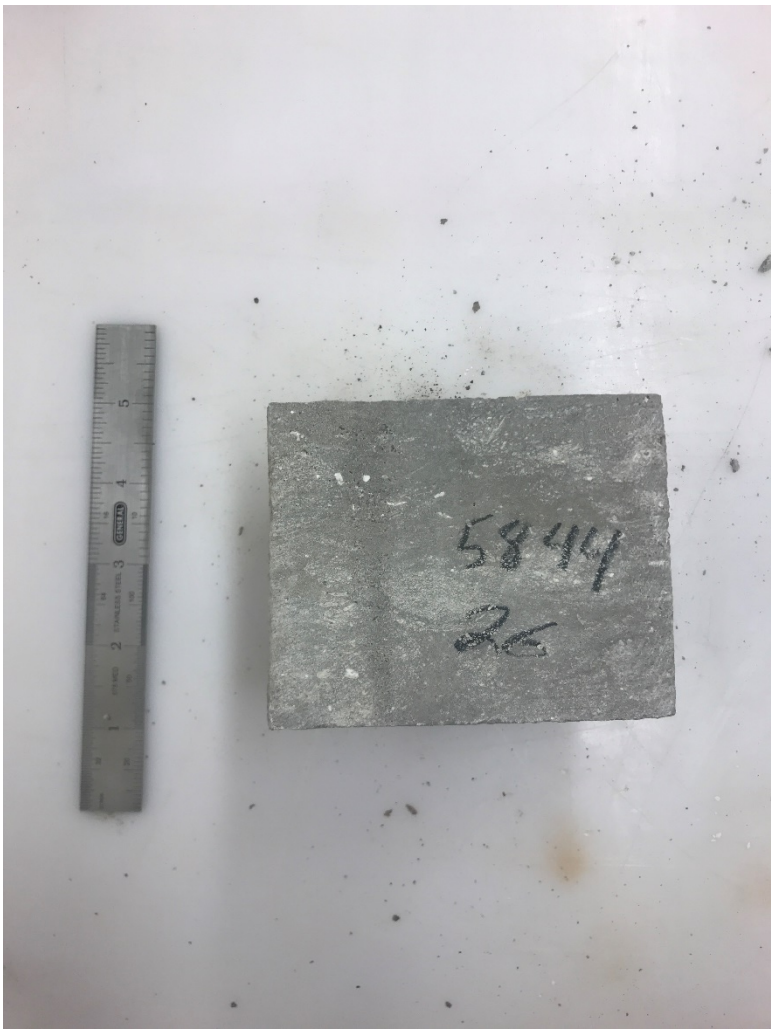

A-7-22. Cross sectional view of dried core from Rich C-7 at 5844 ft.

A-7-23. Cross sectional view of dried core from Rich C-7 at 5845 ft.

A-7-24. Cross sectional view of dried core from Rich C-7 at 5848 ft.

A-7-25. Cross sectional view of dried core from Rich C-7 at 5850 ft.

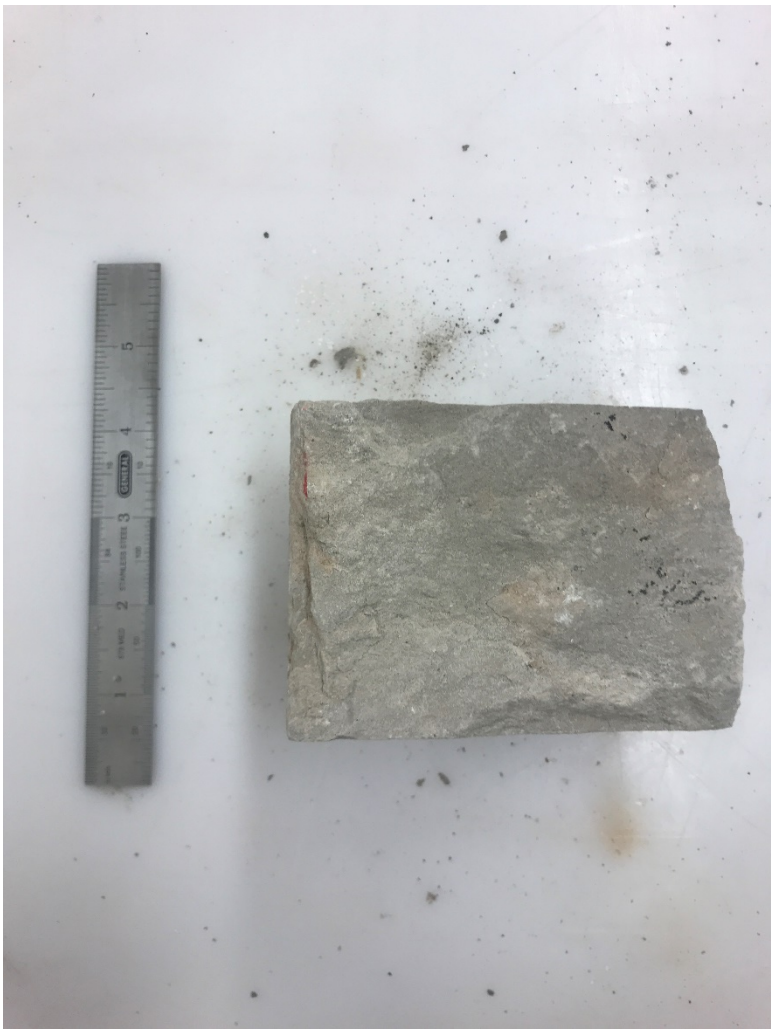

A-7-26. Cross sectional view of dried core from Rich C-7 at 5856 ft.

Depth	Situ Lbs/Ft	Sonic Log	Ult P	Ult S
5808	19160	5158.332	4351	2444
5809	19164	5284.856	4451	2612
5810	19167	5341.054	5562	3389
5815	19183	4528.452	3316	1886
5816	19187	3877.178	3050	1649
5820	19200	3940.775	2931	1527
5821	19203	4370.949	3800	2257
5823	19210	5272.609	5022	3217
5824	19213	5193.922	4878	3100
5825	19216	5105.98	4957	3449
5826	19220	5170.141	4890	2998
5829	19230	5366.343	5017	3062
5831	19236	5246.026	5164	2422
5832	19240	5027.589	4725	3004
5836	19253	5096.165	4969	2971
5837	19256	4982.237	4708	2854
5838	19259	4895.988	4265	2701
5839	19263	4901.261	4366	2914
5842	19273	5037.724	4683	2721
5844	19279	4732.147	4635	2727
5845	19282	4574.246	4589	2918
5846	19286	4512.634	4066	2655
5848	19292	4606.87	4338	2749
5850	19299	4510.431	4186	2353
5853	19309	4349.932	3779	2423
5856	19319	4650.154	4056	2280

Table A-7-8. Ultrasonic and Sonic Data taken at each depth used in this study.